Paul Anton Letnes

Optical Polarization Effects of Rough and Structured Surfaces

Thesis for the degree of Philosophiae Doctor

Trondheim, September 2012

Norwegian University of Science and Technology
Faculty of Natural Sciences and Technology
Department of Physics

NTNU – Trondheim
Norwegian University of
Science and Technology

NTNU
Norwegian University of Science and Technology

Thesis for the degree of Philosophiae Doctor

Faculty of Natural Sciences and Technology
Department of Physics

ISBN 978-82-471-3771-0 (printed ver.)
ISBN 978-82-471-3772-7 (electronic ver.)
ISSN 1503-8181

Doctoral theses at NTNU, 2012:234

Printed by NTNU-trykk

Abstract

The reflection and scattering of light from surfaces is a topic that has been much discussed in the scientific literature. The application of optical methods for the characterization of surfaces and the understanding of natural phenomena is dependent on good models for the optical properties of surfaces and interfaces. In this work, we will examine three different aspects of the optical properties of surfaces and interfaces.

The measurement of polarization effects of surfaces is dependent on well-performing Mueller matrix ellipsometers. While designing Mueller matrix ellipsometers for a single wavelength is trivial, the design of broad-band imaging ellipsometers is a much more challenging problem. We discuss the use of genetic algorithms to optimize such ellipsometers in a very general fashion, and apply them to ellipsometers based on various liquid crystal technologies. The results include an ellipsometer design which was patented, and which outperforms previous designs both in terms of spectral bandwidth and noise propagation.

Recent progress in the ability to manipulate matter on the nanoscale has led to great interest in the biological, chemical, and physical properties of nanoparticles and nano-sized structures. Depositing nanoparticles on top of a surface modifies the optical properties of both the particles as well as the substrate: any optical resonances that the particle(s) possess are modified by the substrate, and the reflectivity of the substrate is changed due to the presence of the particles. The electromagnetic interactions between nanoparticles and substrate are here investigated in the quasistatic regime, with discussion of both small clusters of nanoparticles as well as (infinite) periodic lattices of nanoparticles deposited on a substrate. The results include analysis of the interactions and resonances found in nanoparticle clusters deposited on a substrate.

When light is incident on surfaces possessing random roughness or structure, the light is scattered according to the statistical properties of the surface. While there has been significant progress on surface scattering from

surfaces with one-dimensional surface profile functions, less attention has been devoted to numerical models of surfaces possessing two-dimensional surface profiles. The main reason for this is that the solution of these models requires a large amount of computational power, even by today's standards. We attempt to shed some light on optical effects observed in scattering from two-dimensional rough surfaces, with some focus on polarization effects, which are absent in scattering from one-dimensional surfaces. The Mueller matrix for a rough surface is also calculated, and describes the full polarization effects of rough surface scattering.

Preface

This thesis is a part of the requirements for the degree of *philosophiae doctor* at the Norwegian University of Science and Technology (NTNU[1]). The work described here was performed primarily at NTNU in the period September 2008 to June 2012. The body of this thesis consists of two main parts. The first part is intended as an introduction to and overview of the subjects discussed in the second part. The second part consists of the scientific papers published as a result of the work I have performed, in collaboration with the co-authors of those papers.

This PhD thesis owes a lot to a continuous flow of good ideas and inspiration from my supervisor, Ingve Simonsen. Working together with Ingve for four years has been both interesting and fun, in so many ways.

I would have achieved only half as much if I did not share an office with Tor Nordam. Together, we have written a powerful simulation code, and eaten a lot of sausages.

Some parts of this work were done at the University of California at Irvine (UCI), in March–April 2010 and May–June 2011. During my stays at Irvine, I collaborated closely with Douglas L. Mills on the topic of nanoparticles and their interactions. Doug is also an unbelievable source of great stories and interesting discussions. Unfortunately, Doug passed away in March 2012 after a long period of illness. Doug, I will miss you.

I believe that the secrets of scattering of light from two-dimensional rough surfaces would still lie in darkness if not for the enthusiastic support of Alexei A. Maradudin at UCI. It is a delight discussing physics with someone both so knowledgeable and interested as Alex.

I would also like to thank Ping Chu, at UCI at the time, for her help in verifying the correctness of my results.

Lunchtime discussions would not have been the same without Ingar Stian Nerbø, Lars Martin Sandvik Aas, Pål Gunnar Ellingsen, and Morten

[1] `http://www.ntnu.edu`

Kildemo. Some of these discussions led to a paper on the optimization of Mueller matrices by the use of genetic algorithms, as well as a patent application and a bronze prize in the 2011 "Humies"[2]. For the implementation of genetic algorithms, I also received excellent advice from Keith Downing.

The work done on satellite peaks and light scattering from rough thin films could not have been done without the support and CPU-hours from the EPCC and the HPC Europa 2 program. In particular, I am indebted to Fiona Reid and Catherine Inglis, who facilitated our visit in so many ways, and Chris Johnson, who taught us all about ScaLAPACK and MPI. The same can be said about Jamie Cole and his group who welcomed Tor and me as visitors to the School of Physics at the University of Edinburgh.

The office would not be as much fun without its most recent addition: Jerome Maria. Noone can make you feel warm in winter like a freezing Frenchman. I should also thank Daniel Skåre for keeping Jerome in shape and out of hospital through tireless soccer practice. I am also grateful for the warm welcome I got from Frantz Stabo-Eeg and Eirik Glimsdal when I was a fresh Ph.D. student.

I would still be trying to compile my code if not for the numerous hours of technical support from Yngve Inntjore Levinsen. I owe him many thanks; contrary to popular belief[3], compiling your code is not the same as slacking off.

Thanks to Håvard Granlund for pointing out errors in this manuscript.

I would like to thank employees at the department of physics in general for making NTNU such a nice place to work. Many a Friday cake has been devoured in good company.

Finally, I would like to thank my family and friends for their love and support throughout my period as a Ph.D. student. A special thanks goes to Aleksandra, for tearing me away from the computer screen more often than I like.

Trondheim, August 24, 2012
Paul Anton Letnes

[2] `http://www.genetic-programming.org/hc2011/combined.html`
[3] `http://www.xkcd.com/303/`

List of papers

In this section, the author's contributions to the papers included in the thesis are clarified in detail. This is a requirement according to NTNU's regulations for Ph.D. candidates, paragraph 7.4. For completeness and convenience, the papers are included in full in Appendix A.

The simulation code RAYLEIGH2D used for the numerical simulations of rough surface scattering was developed in close collaboration with Tor Nordam. We contributed (approximately) equally to the simulation code, and it was used in generating results for several of the papers. This is indicated below, where appropriate. The surface generator used in the simulations of rough surface scattering was written by Ingve Simonsen.

Paper 1

P. A. Letnes and I. Simonsen. "Spectrally dependent locations of hot-spots in nanoparticle clusters", pp. 2084–2088. *phys. status solidi (b)* **247** (2010)

My contributions to this paper were in the development of the simulation code, running the numerical simulations, preparation of the figures, and writing large parts of the paper. I. Simonsen contributed by writing the introduction of the paper, as well as with theoretical discussions and editing of the final manuscript.

Paper 2

P. A. Letnes, I. S. Nerbø, L. M. S. Aas, P. G. Ellingsen, and M. Kildemo. "Fast and optimal broad-band Stokes/Mueller polarimeter design by the use of a genetic algorithm", pp. 23095–23103. *Opt. Express* **18** (2010)

Here, I wrote the genetic algorithm used for optimization of Stokes polarimeters. I also created several of the figures, in particular, the figures presenting the scientific results. I contributed significantly to the writing of the text in the paper, especially the chapters presenting the results of the genetic optimization. I.S. Nerbø wrote the other parts of the manuscript and participated in discussion of the theory. M. Kildemo contributed important ideas and theory. L.M. Sandvik

Aas and P.G. Ellingsen contributed to the development of the code by verifying my simulation results against their existing code written for similar purposes.

Paper 3

P. A. Letnes, I. Simonsen, and D. L. Mills. "Substrate influence on the plasmonic response of clusters of spherical nanoparticles", 075426. *Phys. Rev. B* **83** (2011)

In this paper, I developed the analytic formalism used in the numerical calculations. I also wrote the simulation code and generated the figures presenting the results. I also contributed to parts of the text in the paper. D.L. Mills and I. Simonsen contributed theoretical knowledge and suggestions for the paper. D.L. Mills authored significant parts of the manuscripts.

Paper 4

P. A. Letnes, I. Simonsen, and D. L. Mills. "Erratum: Substrate influence on the plasmonic response of clusters of spherical nanoparticles [Phys. Rev. B 83, 075426 (2011)]", 149901. *Phys. Rev. B* **85** (14 Apr. 2012)

An erratum to Paper 3 has been published as the original publication had a figure incorrectly duplicated. For convenience, the erratum is included in Appendix A.

Paper 5

P. A. Letnes, I. S. Nerbø, L. M. S. Aas, P. G. Ellingsen, and M. Kildemo. "Genetic invention of fast and optimal broad-band Stokes / Mueller polarimeter designs". In: *Proceedings of the 13th annual conference companion on genetic and evolutionary computation*. Ed. by N. Krasnogor. Dublin, Ireland: ACM, 2011, pp. 237–238

This paper was a part of the proceedings for the Genetic and Evolutionary Computation Conference (GECCO) 2011 held in Dublin, Ireland. (It did not undergo peer review.) I performed the optimization of the Stokes polarimeters and generated one of the figures (Fig. 2). I also contributed significantly to the writing up of the paper, and presented it as a poster at the conference. I.S. Nerbø wrote parts of the manuscript, and the other co-authors contributed in the same fashion as for Paper 2.

Paper 6

T. A. Leskova, P. A. Letnes, A. A. Maradudin, T. Nordam, and I. Simonsen. "The scattering of light from two-dimensional randomly rough surfaces". *Proc. SPIE* **8172** (2011)

This paper was intended as a broad review of numerical simulations of rough surface scattering. As such, the paper was written in collaboration with all the co-authors, contributing to different parts of the paper. My contribution was to the chapters on numerical solution of the reduced Rayleigh equation. The RAYLEIGH2D simulation code was used in generating these results. I also performed some of the numerical calculations. T.A. Leskova, A.A. Maradudin, and I. Simonsen contributed the remaining parts of the paper, and prepared the manuscript for publication.

Paper 7

P. A. Letnes, A. A. Maradudin, T. Nordam, and I. Simonsen. "Calculation of all elements of the Mueller matrix for scattering of light from a two-dimensional randomly rough metal surface", `http://arxiv.org/abs/1108.2599`. *(accepted, Phys. Rev. A)* (2012)

In this paper, I contributed by performing the numerical simulations. The code for calculating and presenting the Mueller matrices was written by me in collaboration with T. Nordam. The underlying simulation code used in generating the surface scattering results was the RAYLEIGH2D code. I also contributed by creating the figures and by writing parts of the text of the paper. A.A. Maradudin contributed by writing the initial draft of the paper, while T. Nordam and I. Simonsen contributed by writing and editing parts of the paper.

Paper 8

T. Nordam, P. A. Letnes, and I. Simonsen. "Numerical simulations of scattering of light from two-dimensional surfaces using the Reduced Rayleigh Equation", `http://arxiv.org/abs/1204.4984` (2012)

This paper presents the method of using the reduced Rayleigh equation to model the scattering of light from two-dimensional rough surfaces. It describes the numerical solution of the reduced Rayleigh equation in detail, used when implementing the RAYLEIGH2D simu-

lation code. All results presented in the paper were generated from this code, and I performed some of the simulations shown. In addition, I contributed by generating figures for the paper as well as by giving comments to the manuscript, which was mainly prepared by T. Nordam and I. Simonsen.

Paper 9

T. Nordam, P. A. Letnes, I. Simonsen, and A. A. Maradudin. "Satellite peaks in the scattering of light from the two-dimensional randomly rough surface of a dielectric film on a planar metal surface", pp. 11336–11350. *Opt. Express* **20** (2012)

The RAYLEIGH2D simulation code was used to generate the results. I contributed by performing the numerical simulations in collaboration with T. Nordam. I also performed some editing of the manuscript and generated the figures presented in the paper. A.A. Maradudin wrote a draft of the paper and participated in discussions. All co-authors contributed to the finishing of the manuscript.

Paper 10

P. A. Letnes, I. Simonsen, and D. L. Mills. "Plasmonic resonances at interfaces patterned by nanoparticle lattices", `http://arxiv.org/abs/1208.1911` (2012)

In this study, the plasmonic and reflectivity properties of lattices of silver nanoparticles were studied. I wrote the simulation code and performed the numerical simulations, and generated the figures for the paper. I wrote a draft of the paper in cooperation with D.L. Mills, and I. Simonsen participated in the finishing of the manuscript.

Paper 11

P. A. Letnes, T. Nordam, and I. Simonsen. "Coherent effects in the scattering of light from two-dimensional rough metal surfaces". *(unpublished)* (2012)

The RAYLEIGH2D code was used to study effects in surfaces where surface plasmon polaritons can be excited due to surface roughness. The numerical simulations were in part performed by T. Nordam and in part by me. The manuscript was written by me and T. Nordam in collaboration. I. Simonsen contributed important theoretical insight and helped finish the manuscript for publication.

Contents

1. Introduction

”
God made the bulk; the surface was invented by the devil.
— Wolfgang Pauli

Pauli's jest reflects upon the fact that whereas inside the bulk of a material, where symmetries of rotation and translation often can be assumed, these conditions never apply at a surface. Simply the presence of an interface between two materials breaks both rotation and translation symmetry, at least in the vicinity of the surface. Since the sources of polarized light are often linked to anisotropy and the breaking of symmetries, it is perhaps not surprising that the surfaces and interfaces between materials produce effects upon the polarization of light. Interfaces which modify the polarization of light are the broader topic of this thesis.

The simplest example of such phenomena is the Brewster effect [12]. This effect consists of the fact that, for some materials, the reflectivity of p-polarized light drops to zero at a certain angle of incidence called the Brewster angle. This angle can be found by

$$n_1 \tan \theta_B = n_2 \tag{1.1}$$

where n_1 and n_2 are the refractive indices in the two media, θ_B is the Brewster angle (of incidence), and the ray of light is incident from medium 1. Note that p polarization is defined as the polarization of light where the electric field lies in the plane of incidence. The effect can be observed in the reflection of light from planar interfaces, such as those of glass, water, and plastic.

Throughout this thesis, we will shed some light on research done by the author and collaborators on other polarization effects that have their origin in the interplay between light and structured interfaces between materials. First, a discussion of how the polarization of light can be created and measured is in order.

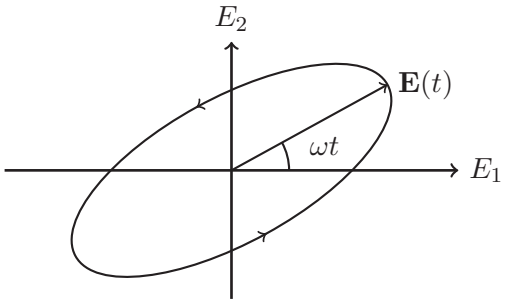

Figure 1.1: The polarization ellipse indicates the shape the electric field "paints" when you look at the electric field vector along the wave vector (or equivalently, the direction of propagation), **k**. As time progresses, the electric field vector rotates with an angular frequency ω.

1.1. Creating polarized light

Everyone is familiar with sources of unpolarized[1] light, such as fire, incandescent lamps, and the Sun. It is less trivial to create light which possesses a specified state of polarization. In general, light is elliptically polarized, as depicted in Fig. 1.1. Special cases include linearly polarized light and circularly polarized light. In the linear case, the polarization ellipse has collapsed to a single line, and the electric field oscillates along a single direction. In the circular case, the phase difference between E_1 and E_2 is exactly $\pi/2$, giving a polarization ellipse of a perfectly circular shape.

Linearly polarized light can be created by a variety of methods. The simplest example from our daily lives is that of polarizing (polaroid) sunglasses. These polarization filters are composed of aligned microscopic anisotropic crystals embedded in a polymer film [13]. These hepathite crystals are capable of conducting electricity at optical frequencies. This means that when light is incident on the microscopic crystals, the electric field along one axis of the crystals sets up a current in the filter which exactly cancels out that component of the electric field. The resulting transmitted light is thus linearly polarized transversely to the alignment axis of the crystals.

[1] Unpolarized light is sometimes referred to as "natural" light. Since light can be polarized by phenomena found in nature, this choice of words is unfortunate.

The Brewster effect [12] can be used to create s-polarized light in reflection. For instance, reflections from the Sun on wet roads are predominantly s-polarized due to the Brewster effect. By using a stack of reflectors at the Brewster angle, one can also create p-polarized light in transmission in an efficient manner. Another everyday source of polarized light is the blue sky. At a 90° angle with respect to the Sun, the light from the sky is partially polarized. The reason is that when light is scattered from molecules in the air, a simple geometric effect causes the light scattered by 90° to be linearly polarized [12].

A birefringent polarizer, such as the historically important Nicol prism, is based on the phenomena of total internal reflection and birefringence [14]. In a birefringent material, the refractive index is different for two independent polarizations. Hence, the two polarizations undergo total internal reflection at different critical angles, meaning that one polarization is (partially) transmitted when the other is totally reflected.

A common technique to construct optical filters with high reflectance or transmittance is to use stacks of thin films. Similar approaches can be used to generate linearly polarized light by employing stacks of birefringent thin films [15]. Essentially, one polarization "sees" a thin film filter optimized for reflection, whereas the other polarization sees it as a transmission filter.

Recently, more exotic techniques for generating polarized light have become possible with the advent of nanotechnology. Work done by the author and co-workers [10] discusses an alternative way of generating light which is predominantly s-polarized in one part of the optical spectrum and predominantly p-polarized in a different part of the spectrum, by the application of surface plasmons in surfaces patterned by nanoparticles. The plasmonic interactions in an anisotropic lattice of nanoparticles shift the resonances in such a way as to produce this effect. Progress has also been made in the theoretical understanding of how surface scattering affects the polarization of light [7]. The ability to control the structure of matter on the nanoscale combined with the ability to model polarization effects in surface scattering could lead to the advent of optical components with interesting polarization effects based on the scattering of light.

1.2. Measuring polarization

The measurement of polarization can, to some extent, be done using relatively primitive instruments. For instance, a linear polarizer combined with an intensity detector can be used to determine the linear degree of polarization. In the simplest case, holding your polarizing sunglasses between you and a source of light while rotating the sunglasses lets you distinguish between linearly polarized sources of light. Photographic polarization filters are used in this fashion.

As light can be elliptically or circularly polarized, such measurements are insufficient to determine the full polarization properties of light. Optical retarders have the capability of adjusting the phase difference δ between the components of the electric field, and thus adjusting the shape of the polarization ellipse (Fig. 1.1). Hence, circularly or elliptically polarized light can be transformed into linearly polarized light. For instance, a quarter wave plate[2] can be used to convert circularly polarized light into linearly polarized light, and vice versa. As linearly polarized light can be measured by the rotating polarizer trick described in the previous paragraph, it is possible to measure the full polarization state of light by combining retarders and linear polarizers.

In general, light can also be unpolarized, meaning that the direction of the electric field varies in a seemingly random fashion from one moment to the next. A typical example is the light coming from the Sun, which is unpolarized due to the random nature of light emitted from glowing gases. To describe the full polarization state of light, four parameters, known as the Stokes parameters, are required. For this reason, measuring the full polarization state of light is referred to as Stokes polarimetry. At this stage the discussion becomes rather technical, and we defer further discussion to Chapter 2.2.

1.3. Applications of polarization phenomena

Polarized light has had many applications throughout history. For instance, there is a long-standing hypothesis that Vikings used birefringent

[2]Simply put, a quarter wave plate delays the propagation of one polarization by 1/4 of an oscillation period relative to the other polarization [14].

crystals, referred to as a "sólarsteinn" or "sunstone", to measure the polarization of light coming from (partially) overcast sky. Recent measurements of the degree of polarization of the sky over the Arctic and over Europe, including in partially overcast weather, shows that the position of the Sun can be revealed through such measurements [16]. Further studies will determine whether the polarization properties of partially overcast skies can be reliably used for navigation [16].

In nature, several species of fish [17] and octopuses [18] are able to detect polarization of light, especially from reflections (the Brewster effect) at air-water interfaces. The same is true of insects [19]. There is also evidence that some bird species [20] and even, to a lesser extent, humans [21] can detect polarization patterns in light.

The measurement of how the polarization of light is modified by reflection from a material, or transmission through it, is used extensively to characterize materials. Examples include medicine, in particular dermatology [22], semiconductors [23], surface structures [24], and many others. One of the more interesting ideas in the search for extraterrestrial life is that most sources of circularly polarized light are biological in nature. Searching for circularly polarized light originating from planets in other solar systems could reveal clues as to whether (not necessarily intelligent) life is present [25].

The use of polarization is widespread in everyday technology as well. For instance, liquid crystal displays (LCD) used in TVs, computers, and other electronic devices employ a liquid crystal whose optical retardance[3] can be adjusted by an electric voltage, sandwiched between two polaroid films, to generate the image shown on the screen. So-called 3D cinema can be achieved by wearing glasses of opposite polarization on each eye, and projecting two images—one of each polarization—onto the screen.

In summary, the polarization of light can both be of great technological use and can reveal much about our universe by careful observation. This thesis will discuss how polarization can be modified by surface structures, including nanoparticles and randomly rough surfaces. Some of the discussion will be devoted to the observation of polarization of light, in particular, how one can optimize polarimeters for optimal performance.

[3]The retardance is the phase shift between the two linear polarizations caused by transmission through e.g. a quarter wave plate.

2. Electromagnetic theory

”
The work of James Clerk Maxwell changed the world forever.
— Albert Einstein

Our understanding of optics was largely based on phenomenological observations of various physical phenomena until the laws of electromagnetism were discovered. For instance, the nature of light was debated for centuries, as different schools of philosophers and physicists argued whether light behaved like particles[1] or waves[2]. By a cruel twist of fate, history has proven both interpretations to be correct, depending on which experiment is conducted. In this thesis, the interpretation of light as (classical) electromagnetic waves is sufficient to describe the phenomena under study. This chapter presents the background theory of the optical phenomena discussed in this thesis with Maxwell's equations as the fundamental basis.

2.1. Maxwell's equations and electromagnetic waves

The whole of classical electromagnetism can be contained in four small equations, who were discovered separately by some of the most brilliant physicists in all of history: Gauss, Faraday, and Ampere. It took the genius of James Clerk Maxwell to organize these into a single framework. Also, significant development of notation was necessary before the equations could take on the modern form.

[1] Newton famously created a theory for the particle nature of light. Although several of his conclusions were later proven to be incorrect, Einstein was awarded the 1921 Nobel prize in physics for showing the particle nature of light.

[2] A successful wave theory of light was published by Huygens in 1690.

As the joke goes: "And God said

$$\nabla \cdot \mathbf{D} = \rho_f, \tag{2.1a}$$
$$\nabla \cdot \mathbf{B} = 0, \tag{2.1b}$$
$$\nabla \times \mathbf{E} = -\partial_t \mathbf{B}, \tag{2.1c}$$
$$\nabla \times \mathbf{H} = \mathbf{J}_f + \partial_t \mathbf{D}, \tag{2.1d}$$

and then there was light."

In Eqs. (2.1), $\mathbf{E}$ denotes the electric field, $\mathbf{H}$ the magnetic field, $\mathbf{D}$ the electric displacement field, and $\mathbf{B}$ the magnetic flux density. The notation $\partial_t \equiv \partial/\partial t$ denotes the partial derivative with respect to time, t. The terms ρ_f and $\mathbf{J}_f$ denote, respectively, the free charge and free current densities. The terms ρ_f and $\mathbf{J}_f$ are often referred to as the *source* terms, since they are the origin of electric and magnetic fields.

When studying optical phenomena, we can (at least for our purposes) neglect the source terms, and Maxwell's equations become correspondingly simpler. It is also advantageous to work in the frequency domain, meaning that we assume that all fields have a time dependence $\exp(-\mathrm{i}\omega t)$, where ω is the angular frequency of the oscillations in the electric and magnetic field. Hence, we can simplify Eqs. (2.1) by letting $\partial_t \to -\mathrm{i}\omega$, $\rho_f \to 0$, and $\mathbf{J}_f \to 0$:

$$\nabla \cdot \mathbf{D} = 0 \tag{2.2a}$$
$$\nabla \cdot \mathbf{B} = 0 \tag{2.2b}$$
$$\nabla \times \mathbf{E} = \mathrm{i}\omega \mathbf{B} \tag{2.2c}$$
$$\nabla \times \mathbf{H} = -\mathrm{i}\omega \mathbf{D}. \tag{2.2d}$$

Under the assumption that the materials under study are local[3], linear, isotropic, and homogeneous, the constitutive relations connecting $\mathbf{E}$ with $\mathbf{D}$ and $\mathbf{H}$ with $\mathbf{B}$ read, in the frequency domain, as

$$\mathbf{D}(\mathbf{x}|\omega) = \varepsilon(\omega)\mathbf{E}(\mathbf{x}|\omega) \tag{2.3a}$$

and

$$\mathbf{B}(\mathbf{x}|\omega) = \mu(\omega)\mathbf{H}(\mathbf{x}|\omega). \tag{2.3b}$$

[3]A local material is one in which the dielectric function does not depend on the wavenumber, $\mathbf{k}$.

By manipulating Eqs. (2.2) while assuming the constitutive relations in Eq. (2.3), it can be shown that the electric and magnetic fields both fulfill the wave equation [12]:

$$\left(\nabla^2 + \varepsilon\mu\omega^2\right)\mathbf{E} = 0, \tag{2.4a}$$

$$\left(\nabla^2 + \varepsilon\mu\omega^2\right)\mathbf{B} = 0. \tag{2.4b}$$

Note that $\mathbf{B}$ can be found from Eq. (2.2c), after determining $\mathbf{E}$. The solutions to Eq. (2.4a) consist of two independent modes, denoted polarizations. If we assume a plane wave travelling along the x_3 axis, we can decompose the electric field along the x_1 and x_2 axes in the following fashion:

$$E_1(\mathbf{x}, t) = E_{0,1}\exp\left(\mathrm{i}k_3x_3 - \mathrm{i}\omega t\right) \tag{2.5a}$$

$$E_2(\mathbf{x}, t) = E_{0,2}\exp\left(\mathrm{i}k_3x_3 - \mathrm{i}\omega t + \mathrm{i}\delta\right). \tag{2.5b}$$

Here, the variables $E_{0,1}$ and $E_{0,2}$ denote the amplitudes of the oscillations in the electric fields along the 1 and 2 directions, respectively, and δ denotes the phase difference between E_1 and E_2.

In the bulk of a homogeneous and isotropic dielectric material, electromagnetic waves propagate freely without being affected by the surroundings. Optics is therefore to a large extent concerned with the interaction of electric and magnetic fields with the interfaces between materials, where the electric and magnetic fields are reflected and transmitted. The equations governing such interactions are known as the boundary conditions, and can be derived from Maxwell's equations [12]. For the electric field and the electric displacement fields, the following conditions have to be met, where we have assumed no free electric charges ($\rho_f = 0$):

$$\lim_{h\to 0^+}\hat{\mathbf{n}}\cdot\mathbf{D}_1 = \lim_{h\to 0^-}\hat{\mathbf{n}}\cdot\mathbf{D}_2 \tag{2.6a}$$

and

$$\lim_{h\to 0^+}\hat{\mathbf{n}}\times\mathbf{E}_1 = \lim_{h\to 0^-}\hat{\mathbf{n}}\times\mathbf{E}_2 \tag{2.6b}$$

where h denotes a small distance from the surface (Fig. 2.1), $\hat{\mathbf{n}}$ is the surface normal, and the subscripts 1 and 2 are labels indicating which

medium we are inside. Similarly, if one assumes the absence of free current ($\mathbf{J}_f = 0$), the magnetic field and the magnetic flux density have to obey

$$\lim_{h\to 0^+} \hat{\mathbf{n}} \cdot \mathbf{B}_1 = \lim_{h\to 0^-} \hat{\mathbf{n}} \cdot \mathbf{B}_2 \tag{2.7a}$$

and

$$\lim_{h\to 0^+} \hat{\mathbf{n}} \times \mathbf{H}_1 = \lim_{h\to 0^-} \hat{\mathbf{n}} \times \mathbf{H}_2. \tag{2.7b}$$

Equations (2.6) and (2.7) govern the interactions between electric and magnetic fields and the interfaces between materials. As an example, Fresnel's equations for reflectance and transmittance can be derived directly from the solutions of the wave equation [Eq. (2.5a)] and the boundary conditions [14].

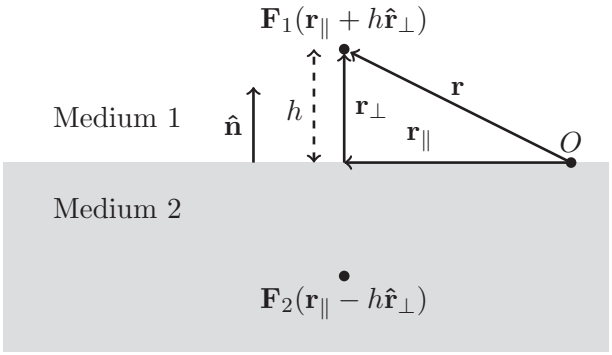

Figure 2.1: The quantity h is defined above, where $\mathbf{F}$ can be any of the four electromagnetic fields ($\mathbf{H}$, $\mathbf{B}$, $\mathbf{E}$, or $\mathbf{D}$).

2.2. Polarized light and the Mueller–Stokes calculus

To describe the polarization state of light, including partially (un)polarized light, the most complete formalism is that of the Stokes (pseudo)vector.

The Stokes vector can be defined as [14, 26]

$$\boldsymbol{S} = \begin{bmatrix} I \\ Q \\ U \\ V \end{bmatrix} = \begin{bmatrix} \langle E_{0,1}^2 \rangle + \langle E_{0,2}^2 \rangle \\ \langle E_{0,1}^2 \rangle - \langle E_{0,2}^2 \rangle \\ \langle 2E_{0,1}E_{0,2}\cos\delta \rangle \\ \langle 2E_{0,1}E_{0,2}\sin\delta \rangle \end{bmatrix}, \tag{2.8}$$

where $\langle x \rangle$ denotes averaging of the quantity x. The averaging can be over e.g. a measurement time or over an ensemble of surface realizations, depending on the context of the (thought) experiment at hand. The variables I, Q, U, and V are referred to as the Stokes parameters, and are used when one does not work with the entire Stokes vector. It is worth noting that all four Stokes parameters are real numbers. It is interesting to note that the Stokes vector $\begin{pmatrix} I_0 & 0 & 0 & 0 \end{pmatrix}^T$ represents fully unpolarized light of intensity I_0. Often, one works with Stokes vectors normalized such that $S_1 = 1$, i.e. the vectors contain the full polarization information but the intensity information is neglected. It is worth observing that the Stokes parameters must obey the relation [26]

$$I^2 \geq Q^2 + U^2 + V^2 \tag{2.9}$$

since the intensity of polarized light cannot be greater than the total intensity. In the case of a normalized Stokes vector, this becomes

$$1 \geq Q^2 + U^2 + V^2. \tag{2.10}$$

The Stokes parameters I, Q, U, and V each denote, respectively, the intensity of the light, the degree of linear horizontal and/or vertical polarization, the degree of $\pm 45°$ polarization, and the degree of left/right-handed circular polarization. Light is usually not purely linearly or circularly polarized, but is more generally elliptically polarized, as depicted in Fig. 1.1. The process of measuring the polarization state of light is usually referred to as polarimetry.

To compactly describe linear interactions between (partially) polarized light and matter, one can associate a matrix called the Mueller matrix to each optical component [26]. Assuming that light with a Stokes vector $\boldsymbol{S}_{\text{in}}$ is incident on a (partially) transparent optical component that can be

modeled by a Mueller matrix $\boldsymbol{M}_\mathrm{c}$, the light being transmitted through the component can be found from the equation

$$\boldsymbol{S}_\mathrm{out} = \boldsymbol{M}_\mathrm{c}\boldsymbol{S}_\mathrm{in}. \tag{2.11}$$

The elements of Mueller matrices are denoted M_{ij}, and the matrix has dimensions 4×4 to match the length of the Stokes vector.

Examples of such matrices and their physical interpretation can be found in any textbook on modern optics [14, 26]. Due to e.g. conservation of energy, there are several conditions a 4×4 matrix must fulfill in order to be a physically realizable Mueller matrix [27]. When focusing on polarization effects, it is common to normalize the Mueller matrix by dividing all elements by M_{11}. This removes the intensity effects of the Mueller matrix, but displays the polarization effects more clearly. Also, a normalized Mueller matrix operating on a normalized Stokes vector produces a new normalized Stokes vector.

Save for nonlinear and quantum effects, Stokes vectors and Mueller matrices are the most powerful tools available when analyzing the polarization state of light and the polarization interactions between light and matter. In this thesis, Mueller matrices are used to model the properties of the optical components used in Stokes polarimeters. The Mueller matrices are also used to describe the polarization effects associated with rough surface scattering, and the interpretation of the Mueller matrices of rough surfaces will be essential in order to extract the maximum possible information from such experimental data.

3. Genetic optimization of spectroscopic polarimeters

”
I love fools' experiments. I am always making them.
— Charles Darwin

The polarization state of light can be fully described by the four Stokes parameters, which are often collected into a vector (cf. Chapter 2.2). In order to determine the full polarization state of light, one uses a Stokes polarimeter, and the measurements are referred to as Stokes polarimetry. Stokes polarimetry is typically used in scenarios when one wants to remotely investigate a light source for some reason. Example applications include astrobiology [25], astronomy [28], and mine detection [29].

For characterization of e.g. semiconductor [23], biological [30], or hybrid [31] materials, one often wishes to measure the effect the material has on the polarization state of light. Performing such measurements is referred to as Mueller matrix ellipsometry, and the interested reader can find a thorough review in Ref. [32]. Mueller matrix polarimetry is used for characterization when one is able to control both the incoming and the outgoing polarization state of light, such as characterization of rough surfaces [7], gratings [33], and nanostructures [34], detection of eye disease [35], and sensitive detection of roughness and particles on semiconductor surfaces [36].

In general, optical components possessing an anisotropic refractive index are used to modulate the polarization state (Fig. 1.1). Several classes of optical components exist for the purpose, including liquid crystal variable retarders (LCVR)[1] and ferroelectric liquid crystals (FLC). Other possibilities (that are not discussed here) include rotating retarders [37] and division of amplitude [38, 39]. The advantage of the LCVR is that the degree

[1]This is the technology used in regular flat screen TVs, giving its name to the well-known LCD (Liquid Crystal Display) acronym.

of anisotropy of the refractive index, and hence the retardance [14], of the material can be tuned through a range of values by adjusting the voltage applied to the crystal. The disadvantage of the LCVR technology is that the time required for the material to switch between two discrete states is typically greater than 15 ms [40]. An FLC based component, however, can switch only between two different orientations, effectively moving the fast axis by 45°. This gives less flexibility in modulating the polarization state, but the switching time of an FLC based component can be as low as 55 µs [40]. This is the background for the suggestion by Gandorfer [41] to use FLCs in fast and hyperspectral (imaging) Stokes polarimeters.

Designing a Stokes polarimeter with optimal performance for a single wavelength is a trivial task, but one is frequently interested in measuring the full Stokes vector for a broader part of the optical spectrum. In this case, the process of producing a good polarimeter design is complicated by the fact that the optical properties of materials are dependent on the (vacuum) wavelength of the light source under analysis. Several techniques have been used to optimize Stokes polarimeters (or Mueller matrix ellipsometers), such as searching the "design space" of polarimeters by partial direct search [42] and Monte Carlo search [43]. We have suggested that genetic algorithms [44] can be employed to perform efficient and automated design of Stokes polarimeters (Mueller matrix ellipsometers) [2].

3.1. Performance assessment of Stokes polarimeters

In order to build a Stokes polarimeter, a polarization state analyzer (PSA) is required. A PSA projects the polarization state of the incident light onto a basis of at least 4 polarization states, and subsequently measures the intensity of each projection state. The measured Stokes vector can then be expressed as $\boldsymbol{S} = \boldsymbol{A}^{-1}\boldsymbol{b}$, where $\boldsymbol{A}$ is a system matrix describing the PSA and $\boldsymbol{b}$ is a vector containing the intensity measurements. $\boldsymbol{A}^{-1}$ denotes the matrix inverse for square (4×4) system matrices, and the Moore–Penrose pseudoinverse for non-square system matrices, which is necessary when more than 4 projection states are used. It can be shown that the noise in the intensity measurements ($\boldsymbol{b}$) is amplified by the condition number [45] of the matrix $\boldsymbol{A}$, denoted $\kappa_{\boldsymbol{A}}$.

For a Mueller matrix polarimeter, the inversion process needed to find the Mueller matrix of the sample involves two matrix inversions, one for the system matrix of the PSA ($\boldsymbol{A}$) and one for the system matrix of the polarization state generator (PSG), denoted $\boldsymbol{W}$. As was shown by Stabo-Eeg et al. [46], the noise amplification of the inversion process is limited by the inequality

$$\frac{\|\Delta \boldsymbol{M}\|}{\|\boldsymbol{M}\|} \lesssim \kappa_{\boldsymbol{W}} \kappa_{\boldsymbol{A}} \frac{\|\Delta \boldsymbol{B}\|}{\|\boldsymbol{B}\|} + \kappa_{\boldsymbol{A}} \frac{\|\Delta \boldsymbol{A}\|}{\|\boldsymbol{A}\|} + \kappa_{\boldsymbol{W}} \frac{\|\Delta \boldsymbol{W}\|}{\|\boldsymbol{W}\|} \tag{3.1}$$

where $\boldsymbol{M}$ is the Mueller matrix that we seek to measure, $\Delta \boldsymbol{M}$ is the measurement error in $\boldsymbol{M}$, and $\boldsymbol{B}$ is the intensity measurement matrix; see Ref. [46] for more details. The notation $\|\boldsymbol{M}\|$ indicates the 2-norm of the matrix $\boldsymbol{M}$. Usually, the PSA and the PSG are built from identical components, meaning that $\kappa_{\boldsymbol{A}} \equiv \kappa_{\boldsymbol{W}} \equiv \kappa$. In this case, the noise amplification of a Mueller matrix ellipsometer is proportional to κ^2.

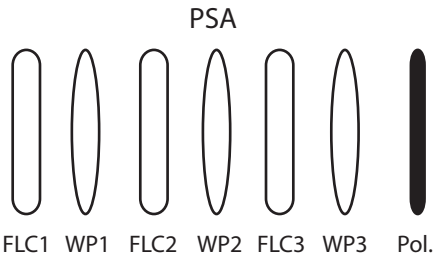

Figure 3.1: Sketch of the polarization state analyzer (PSA) for the polarimeter design published in Ref. [2].

In order to project the measured light onto the basis states, one uses a stack of optical components, as depicted in Fig. 3.1. This stack forms the PSA. A PSA typically consists of a linear polarizer and wave plates with a retardance that can be controlled electronically; often, LVCR or FLC retarders are used [41]. In addition, one can add fixed retarders, e.g. quartz wave plates, to increase the condition number of the system matrix. A sketch of the PSA published in Ref. [2] is shown in Fig. 3.1. This design consists of 3 FLC-based switchable wave plates (FLC1, FLC2, and FLC3

in Fig. 3.1), 3 fixed quartz wave plates (WP1, WP2, and WP3 in Fig. 3.1), and a linear polarizer (Pol.).

The performance of a polarimeter is directly dependent on the condition number, which is a function of the (vacuum) wavelength of light, $\kappa(\lambda)$. Since we want a single figure of merit to quantify the performance of a polarimeter, we define the fitness function f of a polarimeter design as

$$\frac{1}{f} = \frac{1}{N_\lambda} \sum_{n=1}^{N_\lambda} \left[\kappa^{-1}(\lambda_n) - 1/\sqrt{3} \right]^4 . \tag{3.2}$$

where $\lambda_n = \lambda_{\min} + (n-1)\Delta\lambda$, with $n = 1, 2, \ldots, N_\lambda$, are a discrete set of wavelength values. The choice of the power 4 in the fitness function was taken to severely punish large, narrow peaks in the condition number. Such peaks will make the polarimeter unusable for a certain wavelength range, which is undesirable.

3.2. Optimization by genetic algorithms

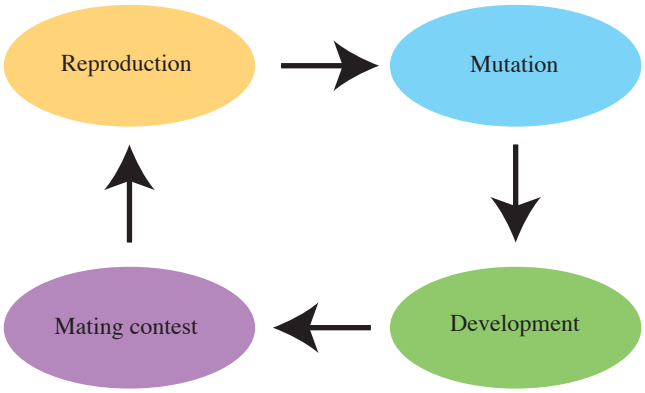

Figure 3.2: The sketch shows the four essential processes of a genetic algorithm: reproduction, mutation, development, and the mating contest.

The genetic algorithm (GA) employed was of a standard type, originally suggested by Holland [44]. A GA performs optimization by simulat-

ing evolution in a population of individuals (here: polarimeter designs). The fitness[2] f increases in the population if the three fundamental properties of evolution are present in the simulation: variation, heritability, and selection.

Variation is the presence of genetic, and thus phenotypic[3], variation in the population: all individuals are not created equal. In our GA, the population is initialized by a set of individuals with randomly generated genomes. If a trait is said to be heritable, it means that the presence of a trait in the parent individuals (e.g. hair color in humans) is transferred to the offspring individuals, possibly with some probability. Finally, selection was first discussed by Darwin [47], where he observed that most offspring do not survive to child-bearing age. Only successful individuals reach adulthood and are able to pass on their genes to the next generation. Thus, the essential components of a GA are variation, heritability, and selection.

The processes included in our GA were those indicated in Fig. 3.2, and were simulated in the following manner. The genome used was a binary genome [44], i.e. a list of bits (0 or 1). Mutation was simulated by randomly introducing bit-flips, i.e. letting $0 \rightarrow 1$ or vice versa, into the genome. Mutation generates new genes during evolution, creating new variation for the GA to improve upon. The development from genotype to phenotype was performed by interpreting the bits in the binary genome as real numbers, giving the values for e.g. orientation angles of the optical components. The Gray code [48] was used for the interpretation of bits into numbers to avoid excessively large changes in the phenotype when the individual undergoes mutation in the genome. The mating contest was performed by one of several standard protocols, but the best performance was achieved by the use of tournament selection with 4 individuals participating in the tournament [49, page 25]. Finally, reproduction was simulated either by asexual reproduction, i.e. by copying the genome, or by sexual reproduction, simulated by two-point genetic crossover. The kind of reproduction was chosen by a random number generator, setting

[2]The fitness function is sometimes referred to as the objective function or energy function in other optimization algorithms.

[3]The genotype is the information encoded in your DNA (e.g. one gene for blue eyes and one for brown eyes), whereas the phenotype is the physical trait that is a result of your DNA (e.g. you have brown eyes).

e.g. a 70% chance for sexual reproduction and a 30% chance for asexual reproduction. Two-point crossover is the process where the genome of each parent is cut at two locations, producing 3 smaller strings of bits. By interchanging and "gluing" together every second bit string, the genomes of the two parents are mixed in a fashion resembling that of real-world sexual reproduction. Further details of the genetic algorithm are discussed in Ref. [2].

Taken together, these processes simulate evolution in a population of polarimeters. As the generations go by, the population will contain polarimeters with a continuously improving condition number, and eventually, several good solutions are found. Although the genetic algorithm makes no promise on finding the globally most optimal polarimeter design, it allows for searching larger design spaces, and will often result in better designs than the optimization approaches used in previous work [43, 46].

3.3. Examples of generated polarimeter designs

In this section, the performance of some polarimeter designs generated by our genetic algorithm is discussed. For the interested reader, the details on the polarimeter design and the design process can be found in Ref. [2]. Here, we will show examples of how the performance of the genetic designs compare to previous designs.

The performance of our most broad-band design is shown in Fig. 3.3. Our design consists of a PSA containing 3 FLCs and 3 fixed quartz waveplates. For comparison, the theoretically optimal value of $\kappa^{-1}_{\text{optimal}} = 1/\sqrt{3}$ and the performance of a recently patented design [50] is indicated. As can be seen from Eq. (3.1), the noise amplification of a Mueller matrix ellipsometer scales as κ^2. The GA based design clearly outperforms the recent patent, especially in the infrared part of the spectrum. The GA based design will probably perform well also further into the infrared part of the spectrum, but to date, no characterization of the optical components has been performed for this part of the spectrum. Hence, there is some uncertainty with respect to if our design is usable in the wavelength range $\lambda > 2000\,\text{nm}$.

An optimization was also performed for polarimeters based on 2 FLC components, similar to designs implemented in the past. The performance

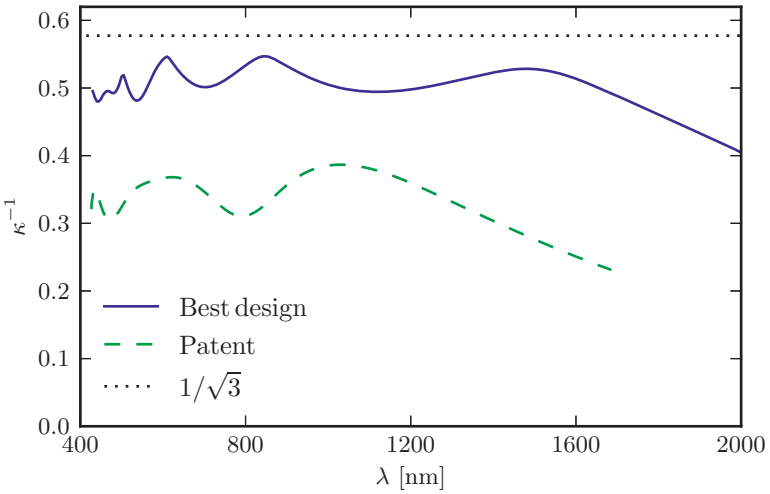

Figure 3.3: The blue solid curve shows the inverse condition number of the most broad-band polarimeter design generated by our genetic algorithm. For comparison, the design by Cattelan et al. [50] is shown as a dashed green line. The theoretically optimal inverse condition number of $1/\sqrt{3}$ is also shown for reference.

of two GA-generated designs is shown in Fig. 3.4, as compared to a commercial design (covering the visible part of the spectrum) and a research design (used for Mueller matrix infrared spectroscopy) currently in use at NTNU. The GA-generated designs outperform the previous designs both in condition number and in the spectral range over which they have usable condition numbers. An inverse condition number below approximately 0.3 is considered to be problematic in a real-world application.

An alternative to FLC based polarimeter designs is to use LCVR retarders. These retarders can be placed in a large number of different states. This is obtained by adjusting the voltage across the crystal, resulting in a voltage dependent retardance. By this method, a Mueller matrix ellipsometer featuring 6 states (one LCVR with 2 and one LCVR with 3 states each) has been designed by our GA code. The resulting design was implemented and characterized, with the resulting condition number shown in Fig. 3.5. The parameters of the LCVR retarders were taken from

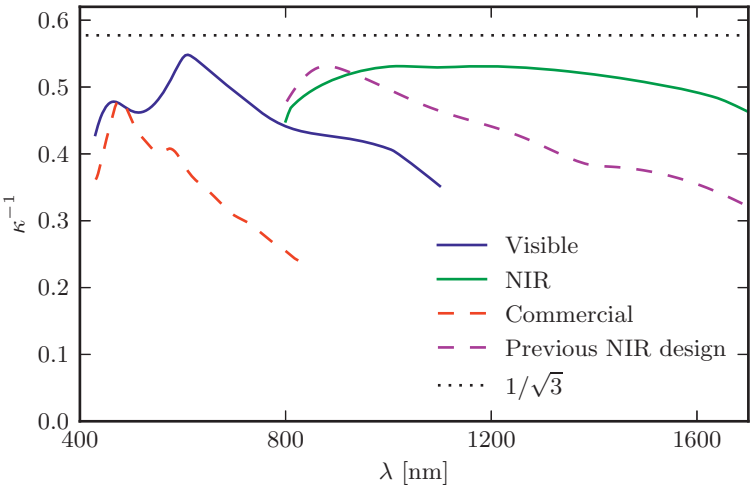

Figure 3.4: The inverse condition number of two GA-generated designs, denoted "Visible" and "NIR" (Near Infra-Red), are shown in green and blue. The performance of a commercially available design and a previous NIR design [42] are shown in dashed lines for comparison.

measured values. As all four LCVRs (two for the PSA and two for the PSG) had slightly different properties, the PSA and PSG were simulated and characterized separately. The correspondence between simulated and measured values is very good, and the system is well conditioned over the entire wavelength range for which it was designed (900 nm to 1700 nm).

To conclude, the problem of designing a well-performing polarimeter can be solved by the use of genetic algorithms. GAs do not promise to find the optimal design, but are good at picking up patterns in large search spaces. This ability allows one to explore a larger variation of possible designs than what is possible by brute force or gradient optimization, including choice of materials or other variables that are incompatible with optimization algorithms relying on the existence of derivatives of all the variables.

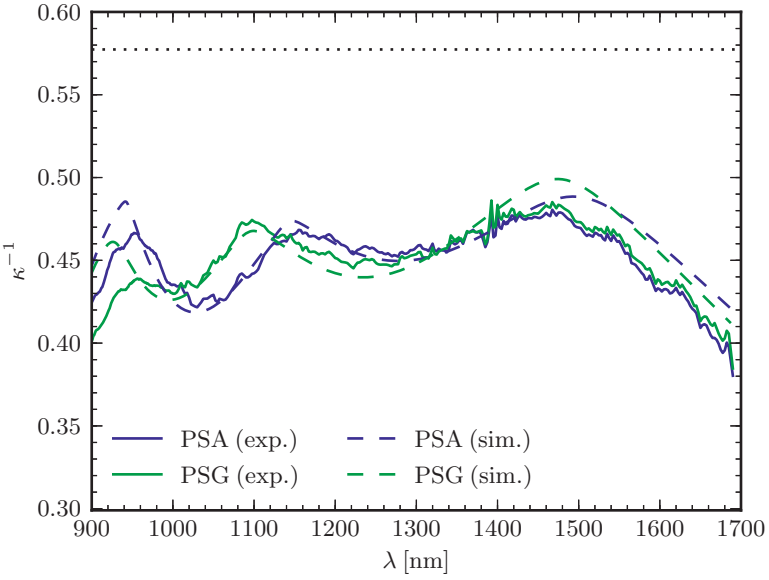

Figure 3.5: The experimentally measured ("exp.") and simulated ("sim.") inverse condition number for a Mueller matrix ellipsometer. Note that the y axis is truncated to show the curves more clearly.

4. Plasmonic polarization in nanoparticle patterned surfaces

”
. . . there is enough room on the head of a pin to put all of
the Encyclopaedia Brittanica.
— Richard P. Feynman

The optical properties of nanoparticles were first discussed by Maxwell Garnett [51] and by Mie [52] as an explanation of the optical properties of metal glasses and metallic colloids, respectively. In these systems, the narrow absorption bands observed were explained by plasmonic resonances, giving rise to the interesting color effects. In later years, other observed phenomena such as gold-ruby glass have been explained [53]. Recently, advances in experimental sciences have given us the possibility to manipulate matter on the nano-scale with unprecedented precision. For instance, the optical response of single Ag particles or pairs of particles of sub-wavelength size has been measured [54]. Both theoretical and experimental studies have been done on the effects nanoparticle have on surface reflectivity and transmission [55, 56]. Some studies indicate that nanoparticles deposited on the surface of photovoltaic cells can increase their light harvesting efficiency through plasmonic resonances [57–59]. As the electromagnetic field from plasmonic resonances feature strong spatial localization, there is also interest in creating plasmonic circuits to replace electronic ones [60]. Furthermore, for several spectroscopic techniques, such as Raman spectroscopy, the signal can be greatly enhanced by the use of an appropriate substrates such as roughened silver [61] or lattices of nanoparticles [62]. A comprehensive review of the properties of metallic nanoparticles, including fabrication, optical characterization, and modelling of their optical properties can be found in Ref. [63].

In this chapter, we will discuss what effects such plasmonic interactions have on the polarization of light. The discussion will be limited to the

quasistatic regime, i.e., we assume that the wavelength of light is much longer than the length scale of our system. The interactions between nanoparticles make the reflection properties of substrates patterned with arrays of nanoparticles depend strongly on the relative orientation of particles and electric fields [10]. In the quasistatic regime, the physical basis for these effects is the frequency shifts of plasmonic resonances, caused by particle-substrate and particle-particle interactions [1, 3]. Especially the particle-substrate interactions have not been studied extensively in the literature. One reason for this is the breaking of symmetries caused by the presence of a substrate. This makes it hard to solve the corresponding analytic models, although some models including substrate interactions have been constructed [55, 64]. Another reason is that manipulating such particles in a controlled manner has been possible only in the last few decades [54, 65]. We will attempt to shed some light on the effects of the presence of a substrate and of the electromagnetic interactions between nanoparticles, while deferring the details of the theoretical treatment to Refs. [1, 3, 10].

4.1. Plasmonic interactions in nanoparticle dimers

In order to examine the fundamental electromagnetic interparticle and particle-substrate interactions, we have studied a model system consisting of two spherical particles of dielectric function $\varepsilon_j(\omega)$ and radius a, hovering a height h above the substrate. The parameter h is introduced in order to avoid singularities in the electric field [66]. The ambient and substrate materials have a dielectric function $\varepsilon_+(\omega)$ and $\varepsilon_-(\omega)$, respectively. The system under study is depicted in Fig. 4.1. The results for nanoparticle interactions shown in this chapter are discussed in full detail in Ref. [3].

The optical response from a single sub-wavelength sized sphere in an ambient dielectric has been known for a long time due to the work of G. Mie [52]. However, the close proximity of the two spheres (i.e. for small d) and the spheres with the substrate (i.e. for small h) cause the optical response to change significantly from the Mie behaviour. In general, the presence of a second nanoparticle or of a substrate can cause significant red-shift of the Mie resonance, and also the stimulation of higher

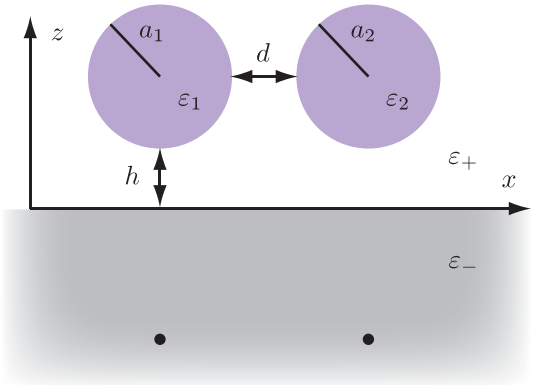

Figure 4.1: The geometry of a nanoparticle dimer. The results discussed here will be restricted to the case $a_1 = a_2 = a$ and $\varepsilon_1(\omega) = \varepsilon_2(\omega) = \varepsilon(\omega)$. A small but finite value of h is kept to avoid the divergence which occurs when the spheres are touching the substrate.

order resonances. To probe these resonances, we study the length of the normalized dipole moment of (one of) the spheres, defined as (in SI units)

$$\bar{p}(\omega) = \frac{|\mathbf{p}(\omega)|}{a^3 \varepsilon_0 E_0}, \tag{4.1}$$

where $\mathbf{p}$ is the (possibly complex) dipole moment of a single sphere, a is the sphere radius, ε_0 is the vacuum permittivity, and E_0 is the strength of the incident electric field. The normalization is such that a perfectly conducting spherical particle in vacuum has $\bar{p}(\omega) \equiv 1$. Note that $\bar{p}(\omega)$ also gives us information on higher order resonances, due to the coupling between the modes caused by intersphere- and particle-substrate interactions.

The normalized dipole moment, $\bar{p}(\omega)$, of a single Ag nanoparticle on top of a dielectric substrate is shown in Fig. 4.2, for different directions of the incident electric field $\mathbf{E}_0$. For the results shown here, $h = 0.05a$. Note that in the quasistatic regime, there are no inherent length scales; as such, there is no explicit length scale in the simulation. The wavelength of the incident light only enters through the frequency dependence of $\varepsilon(\omega)$. The incident electric field was set to point either along $\hat{\mathbf{x}}$ (blue solid line) or along $\hat{\mathbf{z}}$

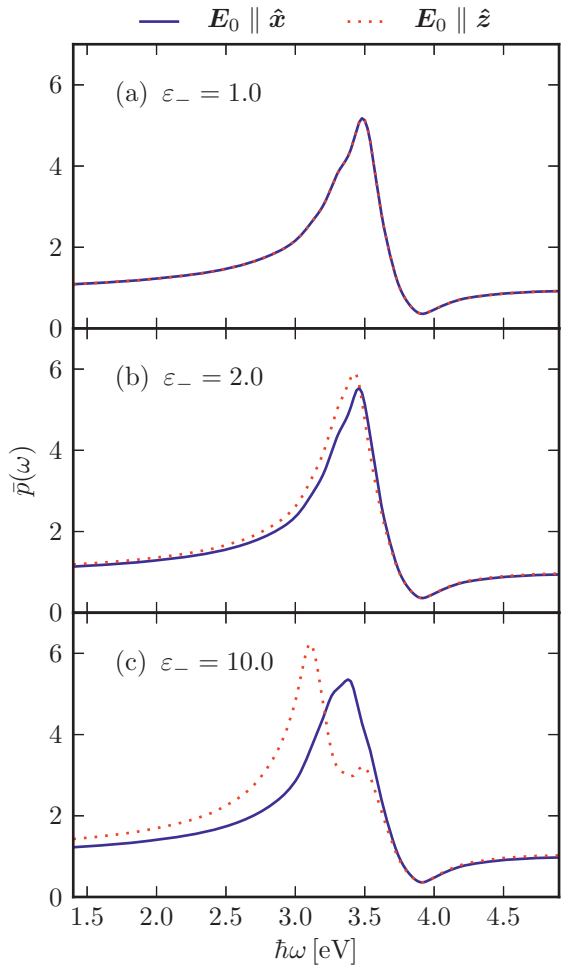

Figure 4.2: The dipole moment of a single Ag nanoparticle over a dielectric substrate with a dielectric function (a) $\varepsilon_-(\omega) \equiv 1$ (i.e. vacuum), (b) $\varepsilon_-(\omega) \equiv 2$, and (c) $\varepsilon_-(\omega) \equiv 10$.

(red dotted line). For the case where $\varepsilon_-(\omega) \equiv 1$, the sphere is essentially hovering in vacuum [Fig. 4.2(a)], and there is full spherical symmetry around the center of the sphere. As ε_- increases, the resonance frequency [the position of the peak in $\bar{p}(\omega)$] red-shifts. Another interesting feature is the fact that, due to the symmetry breaking caused by the substrate, the

resonance peak for $\mathbf{E}_0 \parallel \hat{\mathbf{x}}$ splits relative to the case where $\mathbf{E}_0 \parallel \hat{\mathbf{z}}$. This is an example of how surface interactions can cause polarization effects. It is a reasonable assumption that s- and p-polarized light incident on a surface covered with such particles could be reflected differently, due to the splitting of the resonance.

When considering pairs of nanoparticles, one also breaks the rotational symmetry around the $\hat{\mathbf{z}}$ axis. This causes the resonance peaks for the cases $\mathbf{E}_0 \parallel \hat{\mathbf{x}}$, $\mathbf{E}_0 \parallel \hat{\mathbf{y}}$, and $\mathbf{E}_0 \parallel \hat{\mathbf{z}}$ to split. Simulation results for a nanoparticle dimer, as depicted in Fig. 4.1, are shown in Fig. 4.3. When the substrate is absent [Fig. 4.3(a)], the system is rotationally symmetric around the x axis, which causes the cases $\mathbf{E}_0 \parallel \hat{\mathbf{y}}$ and $\mathbf{E}_0 \parallel \hat{\mathbf{z}}$ to be equivalent. The presence of a second nanoparticle, however, breaks the symmetry with respect to the case where $\mathbf{E}_0 \parallel \hat{\mathbf{x}}$. As the dielectric function of the substrate increases, all three resonances split. The interparticle interactions give rise to the strongest redshift, as can be seen from the fact that the redshift is stronger when $\mathbf{E}_0 \parallel \hat{\mathbf{x}}$. This is fundamentally due to the fact that metallic structures interact more strongly with the electric field than dielectric structures do.

If one assumes that the incident electric field is that of an incident linearly polarized plane wave, the response of the nanoparticles will depend greatly both on the frequency of the incident light as well as the polarization ($\mathbf{E}_0$). The response can be tailored by varying d and by choosing the materials, and hence $\varepsilon(\omega)$, in the system. It is, however, necessary to employ more than two particles in order to get a macroscopic optical response. We therefore turn to the case where the substrate is patterned by a two-dimensional, periodic lattice of nanoparticles. In this case, the plasmonic resonances of the nanoparticles can be observed by the naked eye.

4.2. Reflectivity from lattices of nanoparticles

When a two-dimensional lattice of nanoparticles is imposed on a semi-infinite substrate, the reflectivity of the surface can be significantly influenced by the presence of the particles. The fundament of our treatment is still the theory discussed in Refs. [1, 3]. The only difference is that the cluster of particles is now in principle infinite. In practice, it is necessary

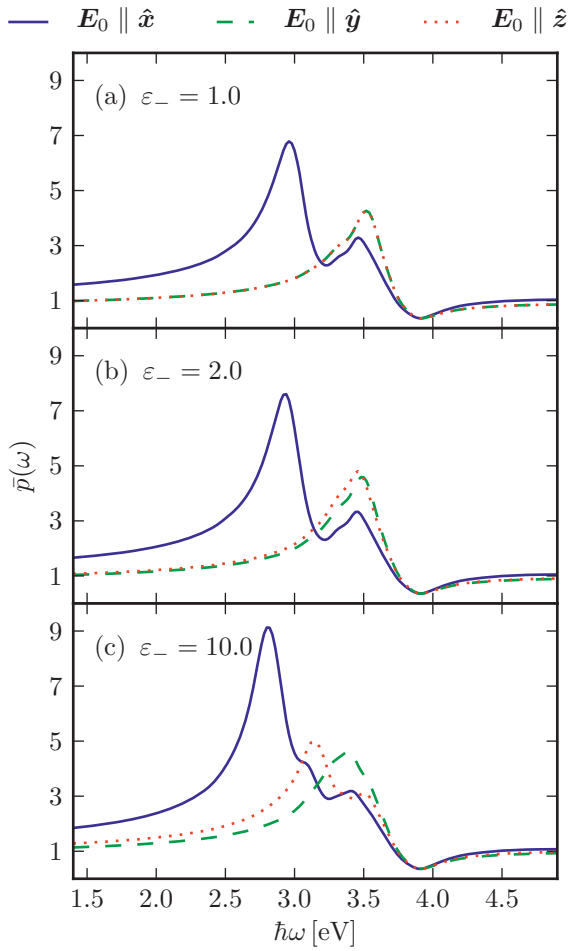

Figure 4.3: The dipole moment of one of the spheres in an Ag nanoparticle dimer over a dielectric substrate. Here, we have assumed that $d = 0.1a$, and the other simulation parameters are identical to the ones used in generating Fig. 4.2.

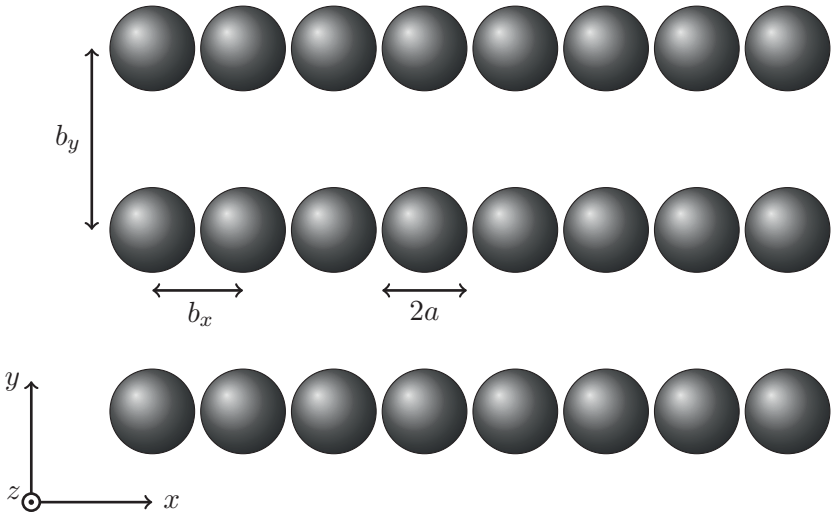

(a) A sketch of the two-dimensional nanoparticle lattice in the xy plane ("from above").

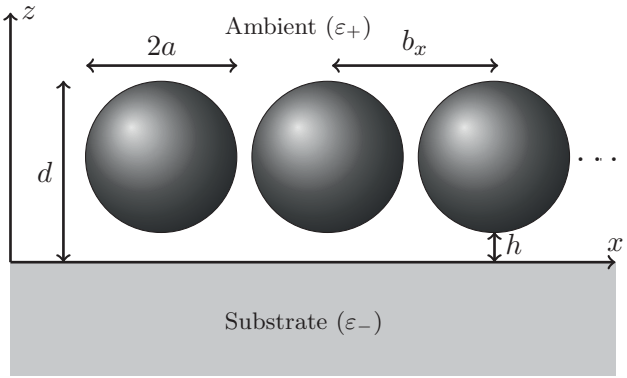

(b) The lattice seen in the xz plane.

Figure 4.4: Sketches of the nanoparticle lattice in the xy and the xz planes, showing the definitions of d, the effective film thickness; a, the sphere radius; b_x and b_y, the lattice constants along $\hat{\mathbf{x}}$ and $\hat{\mathbf{y}}$, respectively; and the parameter h used to obtain convergence. The spheres are all characterized by the dielectric function $\varepsilon(\omega)$. Note that the value of h is exaggerated for clarity: normally, we assume $h = 0.01a$.

to truncate the summation over the contributions from neighbouring particles at some $N_{\max}$ unit cells away. Additional details not discussed here can be found in Ref. [10].

In this chapter, we will be studying two-dimensional lattices of particles deposited on a substrate, as depicted in Fig. 4.4. The lattice is assumed to be rectangular with lattice constants b_x and b_y along the x and y axes, respectively. Each sphere has a radius of a, and a finite value of $h = 0.01a$ is kept for the same reasons as for the nanoparticle dimer case. The exact value of h was found to be unimportant for the reflectivity results, as long as it is sufficiently small and non-zero. Whereas the local potential (and thus, the local electric field) near the bottom of the particles may not necessarily converge fully, the reflectivity results depend mainly on the lower order modes, and thus converge for much lower cutoffs ($L_{\max}$) in the spherical harmonic expansion; see Ref. [10] for details.

The reflectivity of an Al_2O_3 surface patterned with Ag nanoparticles of radius $a = 10\,\text{nm}$ in a square lattice with lattice constant $b_x = b_y = 2.2a$ is shown in Fig. 4.5(a). The angle of incidence was $\theta_0 = 45°$. The plane of incidence was the xz plane, meaning that p-polarized light has an electric field vector parallel to the xz plane, whereas s-polarized light is polarized along the y axis. For the square lattice, the interparticle distance was the same along the x and y axes. This means that the interactions between neighbouring particles is equally strong along both axes, leading to the same red-shift in the Mie resonance for both p- and s-polarized light. When examining Fig. 4.5(a), we observe peaks in R for both polarizations of the incident light at about 2.9 eV, meaning that the redshift is identical for both polarizations due to the lattice isotropy.

In Fig. 4.5(b), the reflectivity at $\theta_0 = 45°$ for an otherwise identical lattice except with $b_y = 2b_x = 4.4a$ is shown. In this case, the s-polarized light excites plasmonic interactions along the $\hat{\mathbf{y}}$ direction, in which the lattice constant is larger than in the $\hat{\mathbf{x}}$ direction ($b_y = 4.4a$). Due to the large lattice constant and the weak substrate interaction when the electric field lies in the xy plane, the Mie resonance undergoes virtually no redshift and is placed at the frequency of the Mie resonance for an isolated sphere in vacuum, which is located at approximately 3.5 eV.

When considering the p-polarized incident light, however, the component of the electric field along $\hat{\mathbf{x}}$ excites interactions along the short axis of the lattice ($b_x = 2.2a$). The small distance between the spheres leads

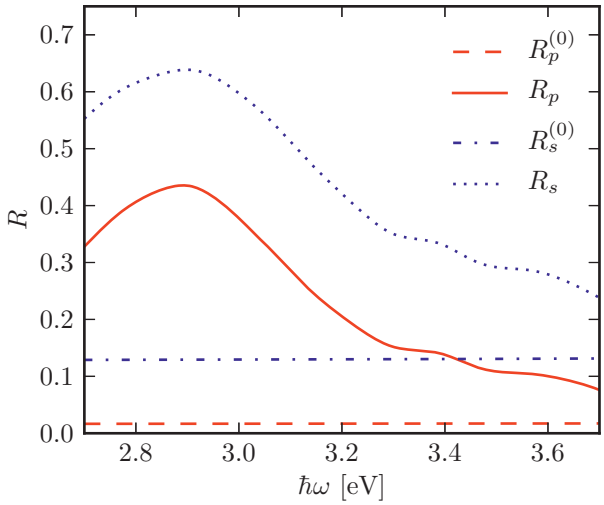

(a) Isotropic lattice with $b_x = b_y = 2.2a$.

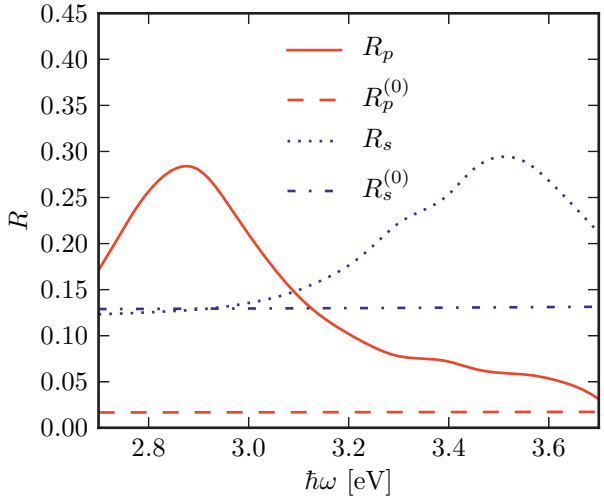

(b) Anisotropic lattice with $b_y = 2b_x = 4.4a$.

Figure 4.5: Reflectivity of an Al_2O_3 substrate patterned with an (a) isotropic and (b) anisotropic lattice of Ag nanoparticles of radius $a = 10\,\text{nm}$. In both cases, the plane of incidence was the xz plane, and the polar angle of incidence was $\theta_0 = 45°$. The (almost) flat lines with superscript (0) indicate the reflectivity of a clean Al_2O_3 surface as calculated from the Fresnel equations.

to strong interparticle interactions and a larger red-shift. The component of $\mathbf{E}_0$ along $\hat{\mathbf{z}}$ causes particle-substrate interactions, which also lead to a red-shift in the Mie resonance. Taken together, this gives a (modified) Mie resonance at around 2.9 eV, similar to the case of the isotropic lattice [Fig. 4.5(a)].

The net effect is that a surface supporting an anisotropic lattice of metallic nanoparticles can work as a sort of spectral plasmonic polarizer. If one imagines that a plane wave of unpolarized light is incident on the surface in the xz plane, the polarization of the reflected beam will be frequency dependent. A reflected beam at $\hbar\omega = 2.9\,\mathrm{eV}$ will be primarily p-polarized, whereas a beam at $\hbar\omega = 3.5\,\mathrm{eV}$ will be primarily s-polarized. At the time of this writing, results are not available for the transmission of light. However, from conservation of energy, the following inequality must hold:

$$T \leq 1 - R, \tag{4.2}$$

where T is the fraction of transmitted energy and R is the fraction of reflected energy. Thus, it is reasonable to assume that a similar but opposite pattern will be observable in transmission.

There is large interest in tuning the optical properties of surfaces and interfaces. In the quasistatic regime, the red-shifts of resonances are independent of the size of the particles. However, the bigger the particles are, the higher the reflectivity; in terms of effective medium theory, the thin film becomes thicker. There are also several other ways to tune the surface properties. For instance, one can employ different materials in both the substrate and in the particles. The particles can also be made in the form of metallic nanoshells with a dielectric core, or vice versa, giving rise to tunability in the ratio between the inner and outer radius of the shell [67]. The particle lattice can be tuned by choosing the lattice parameters b_x and b_y, affecting both the resonance positions and the overall reflectivity. As such, there is a large space of tunability when designing a plasmonic polarizer, and it is reasonable to assume that interesting optical components can be constructed employing the plasmonic properties of surfaces patterned by nanoparticles.

5. Rough surface scattering

”

The work may be hard, and the discipline severe; but the interest never fails, and great is the privilege of achievement.

— Lord Rayleigh

The study of light scattering from randomly rough or structured surfaces was pioneered by Lord Rayleigh [68], who discussed light scattering from rough surfaces where the surface profile is constant along one axis but varies along another axis. In other words, the surface profile can be expressed as a function of one position variable[1]: $\zeta(x_1, x_2) \equiv \zeta(x_1)$. (We note that in this thesis, we will restrict our discussion to surfaces whose profile function is single-valued, i.e. the surface has no overhangs.) Colloquially, we refer to such surfaces as “one-dimensional” surfaces. If the surface profile function depends on both x_1 and x_2, the surface is denoted as a two-dimensional surface. Lord Rayleigh initially studied one-dimensionally periodic surfaces, in particular ones with a sinusoidal surface profile function. He worked under the assumption that

$$\delta \ll a, \tag{5.1}$$

i.e. that the transverse correlation length (a) is much greater than the rms height of the surface profile function (δ), meaning that the mean slope, i.e. the averaged absolute value of the gradient, of the surface is small compared to 1. It was later shown that for the special case of sinusoidal surfaces, the inequality

$$\frac{\delta}{a} \leq 0.448 \tag{5.2}$$

[1] We use the (x_1, x_2, x_3) convention in this chapter to be more in line with the relevant publications, despite the fact that the (x, y, z) convention is used in other chapters in this thesis.

ensures that the Rayleigh hypothesis holds [69, 70]. The Rayleigh hypothesis is an assumption on the form of the electromagnetic field scattered from a rough surface, and will be discussed in more detail in Chapter 5.2. Briefly put, the hypothesis allows for the derivation of a simplified equation for the scattering of light from a rough surface.

It was a long time before the two-dimensional scattering problem[2], which is the focus of this chapter, was tackled. In particular, the inclusion of cross-polarization effects complicates the analysis significantly when compared to the one-dimensional case. Brown et al. derived the reduced Rayleigh equation for scattering from a two-dimensional randomly rough surface [71]. This equation is frequently used as a starting point for small-amplitude perturbation theory. This approach was taken by McGurn and Maradudin, who analyzed the phenomenon of enhanced backscattering from two-dimensional randomly rough metallic surfaces [72]. Similarly, Johnson used the reduced Rayleigh equation as a starting point for developing a systematic third order small-amplitude perturbation theory [73]. Later, Soubret et al. derived the reduced Rayleigh equation using a different approach from that of Brown et al. and used the results to discuss scattering from randomly rough surfaces [74] as well as thin films with random interfaces [75]. Other approaches have also been employed, such as the stochastic functional approach discussed by Kawanishi et al. [76]. More recently, significant work has also been done on the simulation of strongly rough surfaces with both isotropic [77, 78] and anisotropic [79] surface profile functions by the use of rigorous numerical simulations.

In this work, results from the first (to the author's knowledge) simulations that are based on direct solution of the reduced Rayleigh equation for two-dimensional surfaces are presented. Significant findings include the phenomena of enhanced backscattering [8] and satellite peaks [9], as well as the discovery of reduced backscattering in the M_{44} element of the Mueller matrix of a rough metallic surface [7].

Enhanced backscattering is a well-known and theoretically understood effect [80], caused by the constructive interference between a double scattering path and its time-reversed partner [81]. It takes the form of a peak in the scattered intensity appearing in the direction of the incident field.

[2]In the surface scattering community, the scattering problem is regarded as "two-dimensional" if the surface profile function is a function of both x_1 and x_2.

For weak surfaces, the dominating physical effect leading to enhanced backscattering is the interference between propagating surface modes, e.g. surface plasmon polaritons. It has also been observed experimentally. It takes the form of a peak in the differential reflectivity coefficient (DRC) in the direction pointing to the source of illumination, i.e. at $\theta_s = -\theta_0$. The enhanced backscattering effect was observed experimentally by West and O'Donnell [82], using a surface with a particular power spectrum now commonly referred to as the West–O'Donnell spectrum.

The satellite peak (or satellite ring) phenomenon is also caused by interference between propagating surface modes, but with different lateral wave numbers. The satellite peak phenomenon occurs for instance in systems consisting of a dielectric film with a randomly rough interface, deposited on a metallic substrate, with either the film-ambient or film-substrate interface being randomly rough. The interference between two guided modes, propagating in the film, of different wave numbers gives rise to a ring centered at the position of the enhanced backscattering peak. The ring is partially co- and cross-polarized. The satellite peak phenomenon was originally found theoretically for one-dimensional systems [83]. Numerical simulations supported these results [84], as did experimental findings [85]. Kawanishi et al. [76] concluded that this phenomenon does not exist for two-dimensional surfaces, whereas Soubret et al. [74] found that satellite peaks should be observable also in the two-dimensional case. Recently, the direct numerical solution of the reduced Rayleigh equation has confirmed the presence of satellite peaks for two-dimensional film systems [9].

Reduced backscattering is a phenomenon similar to that of enhanced backscattering, but as the name says, it takes on the form of a dip rather than a peak in the absolute value of the M_{44} element (see Chapter 2.2) of the Mueller matrix of a rough surface. An explanation of this phenomenon is unfortunately lacking at the time of writing, but it is reasonable to assume that it is closely related to the enhanced backscattering effect, i.e. that it is a (destructive) interference effect between surface plasmon polaritons excited by the incident light.

5.1. Statistical description of surface roughness

Stochastically rough surfaces cannot be attributed a specific surface profile function. Instead, a statistical description is preferred, where the height variations and the lateral correlations tell us what properties we would expect a rough surface to have in probabilistic terms. In the following we will assume that the surfaces in question are single-valued functions of the coordinates in the plane, i.e. the surface is located at $x_3 = \zeta(\mathbf{x}_\parallel)$ where $\mathbf{x}_\parallel = (x_1, x_2, 0)$. The surface profile function ζ possesses a height distribution which, in our simulations, is assumed to be Gaussian. In all cases we will assume that the process generating $\zeta(\mathbf{x}_\parallel)$ is a stationary, zero-mean process, implying that

$$\left\langle \zeta(\mathbf{x}_\parallel) \right\rangle = 0. \tag{5.3}$$

The height distribution does not specify (even statistically) how the various heights are placed relative to each other in the $\mathbf{x}_\parallel$ plane. This property is specified by the autocorrelation function of the surface,

$$\left\langle \zeta(\mathbf{x}_\parallel)\zeta(\mathbf{x}'_\parallel) \right\rangle = \delta^2 W\left(\mathbf{x}_\parallel - \mathbf{x}'_\parallel\right), \tag{5.4}$$

normalized such that $W(\mathbf{0}) = 1$. Here, δ is the rms height of the surface. Furthermore, it can be shown that $-1 \leq W(\mathbf{x}_\parallel) \leq 1$. In some cases, the autocorrelation function will be isotropic, meaning that

$$W\left(\mathbf{x}_\parallel - \mathbf{x}'_\parallel\right) = W\left(\left|\mathbf{x}_\parallel - \mathbf{x}'_\parallel\right|\right). \tag{5.5}$$

In order to generate randomly rough surfaces with the desired statistical properties, the method described in Refs. [79, 86] was employed. For this algorithm, the quantity that is specified is the power spectrum of the surface, or the Fourier transform of the (normalized) autocorrelation function:

$$g\left(\mathbf{k}_\parallel\right) = \int \mathrm{d}^2\mathbf{x}_\parallel W\left(\mathbf{x}_\parallel\right) \exp\left(-\mathrm{i}\mathbf{k}_\parallel \cdot \mathbf{x}_\parallel\right). \tag{5.6}$$

A power spectrum frequently used in theoretical and experimental studies to date is the Gaussian power spectrum [81],

$$g\left(\mathbf{k}_\parallel\right) = \pi a_1 a_2 \exp\left(-\frac{a_1^2 k_1^2 + a_2^2 k_2^2}{4}\right), \tag{5.7}$$

where the parameters a_1 and a_2 are denoted as the transverse correlation lengths, and the vector $\mathbf{k}_\parallel = (k_1, k_2, 0)$ is the wave number parallel to the surface. If the choice $a_1 = a_2$ is made, the power spectrum becomes isotropic, and depends only on $k_\parallel = \left|\mathbf{k}_\parallel\right|$. Another power spectrum that we will use is referred to as the West–O'Donnell (or cylindrical) power spectrum [72, 82],

$$g(\mathbf{k}_\parallel) = \frac{4\pi}{k_{\max}^2 - k_{\min}^2} \theta\left(k_\parallel - k_{\min}\right) \theta\left(k_{\max} - k_\parallel\right), \tag{5.8}$$

where $\theta(k)$ is the Heaviside unit step function, and $k_{\min}$ and $k_{\max}$ are parameters whose values determine the surface power spectrum. Note that this power spectrum is isotropic (i.e., rotationally symmetric).

5.2. The reduced Rayleigh equation for two-dimensional surfaces

Once the statistical properties of a rough surface has been described, as specified in Chapter 5.1, one can classify surfaces according to their properties. This is necessary as the validity of all techniques for performing simulations of light scattering from rough surfaces depends on the surface properties. For instance, small amplitude perturbation theory, expanded in power series of the surface profile function [72], breaks down for surfaces with all but the lowest values of rms roughness. Solving the scattering problem by a rigorous approach [77, 78] gives good results for surfaces with any rms roughness and arbitrarily steep slopes, but the calculations are both CPU and memory intensive. Due to the memory requirements, only short surface profiles can be simulated without further development of existing codes or theory. An approach which falls between the perturbation theory and the rigorous simulations is the technique of solving the reduced Rayleigh equation (RRE) in a direct manner, without resorting to perturbation theory [8]. This approach will be discussed below, for the systems shown in Figs. 5.1 and 5.2. (Note that in these figures, the interfaces are rendered as flat for the sake of clarity.)

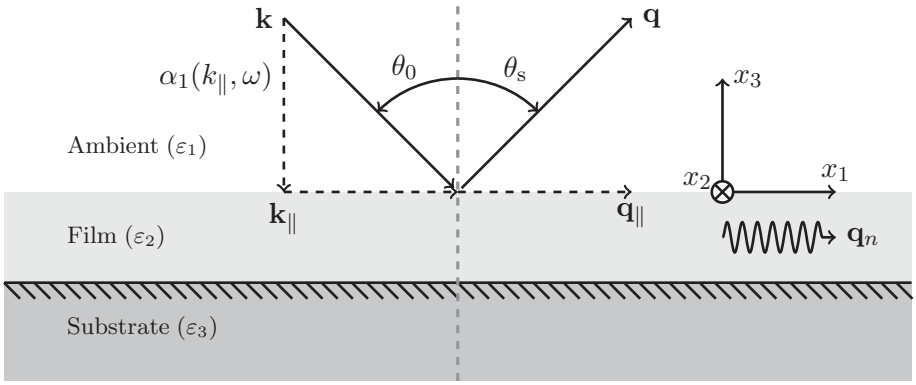

Figure 5.1: The geometry of the scattering problem shown schematically (interface roughness not shown), assuming in-plane scattering $\left(\mathbf{q}_\parallel \parallel \mathbf{k}_\parallel\right)$ and the presence of a thin film on top of the substrate. If one or both of the interfaces of the film are (randomly) rough, guided modes (with wave number $\mathbf{q}_n$, where n is the mode index) can be excited.

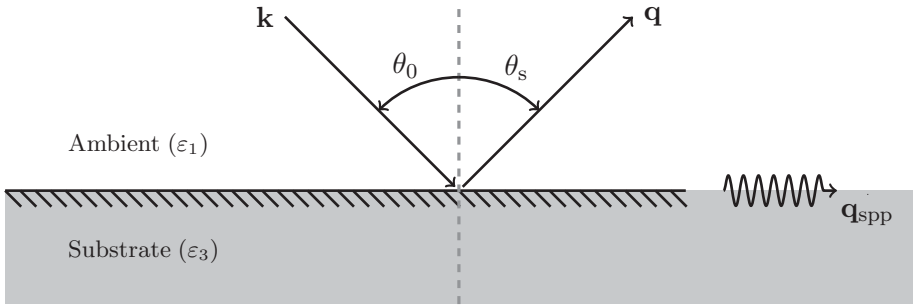

Figure 5.2: The geometry of the scattering problem for a clean, rough surface. To avoid confusion, we denote the dielectric function in the substrate as ε_3 here as well. The surface roughness allows coupling into surface plasmon polaritons with wave number $q_{\mathrm{spp}}(\omega) > \omega/c$, shown schematically.

The incident field is assumed to be a plane wave, expressed as

$$\begin{aligned}\mathbf{E}_0(\mathbf{x}|\omega) = &\left[\hat{\mathbf{e}}_{\mathrm{p}}^{(0)}(\mathbf{k}_\parallel)B_{\mathrm{p}}(\mathbf{k}_\parallel) + \hat{\mathbf{e}}_{\mathrm{s}}^{(0)}(\mathbf{k}_\parallel)B_{\mathrm{s}}(\mathbf{k}_\parallel)\right] \\ &\times \exp\left[\mathrm{i}\mathbf{k}_\parallel \cdot \mathbf{x}_\parallel - \mathrm{i}\alpha_1(k_\parallel,\omega)x_3\right],\end{aligned} \tag{5.9}$$

where $\mathbf{k}_\parallel = (k_1, k_2, 0)$ denotes the component of the incident wave vector parallel to the $\mathbf{x}_\parallel$ plane, and ω being the angular frequency of the incident light. The vectors $\hat{\mathbf{e}}_{\mathrm{p}}$ and $\hat{\mathbf{e}}_{\mathrm{s}}$ are the polarization vectors of the electric field [8]. Finally, the variable B_β is the amplitude of the electric field of β polarization. The scattered field can asymptotically (i.e. as $x_3 \to \infty$) be expressed as a sum of outgoing plane waves:

$$\begin{aligned}\mathbf{E}_{\mathrm{s}}(\mathbf{x}|\omega) = \int \frac{\mathrm{d}^2\mathbf{q}_\parallel}{(2\pi)^2} &\left[\hat{\mathbf{e}}_{\mathrm{p}}^{(\mathrm{s})}(\mathbf{q}_\parallel)A_{\mathrm{p}}(\mathbf{q}_\parallel) + \hat{\mathbf{e}}_{\mathrm{s}}^{(\mathrm{s})}(\mathbf{q}_\parallel)A_{\mathrm{s}}(\mathbf{q}_\parallel)\right] \\ &\times \exp\left[\mathrm{i}\mathbf{q}_\parallel \cdot \mathbf{x}_\parallel + \mathrm{i}\alpha_1(q_\parallel,\omega)x_3\right].\end{aligned} \tag{5.10}$$

Here, the variable A_α is the amplitude of the scattered electric field of α polarization, and $\mathbf{q}_\parallel = (q_1, q_2, 0)$ is the component of the wave vector of the scattered light parallel to the x_1x_2 plane. The transmitted field can be expressed in a similar fashion, but we are not concerned with transmission in this work. The total field above the surface can be written as

$$\mathbf{E}_{\mathrm{tot}}(\mathbf{x}|\omega) = \mathbf{E}_0(\mathbf{x}|\omega) + \mathbf{E}_{\mathrm{s}}(\mathbf{x}|\omega), \tag{5.11}$$

i.e. the sum of the incident and the scattered fields. In Eqs. (5.9) and (5.10), the subscripts p and s correspond to p polarization and s polarization, respectively. The function $\alpha_i(k_\parallel, \omega)$ is defined as

$$\alpha_i\left(k_\parallel, \omega\right) = \left(\varepsilon_i \frac{\omega^2}{c^2} - k_\parallel^2\right)^{1/2} \quad \text{where } \mathrm{Re}(\alpha_i) > 0,\ \mathrm{Im}(\alpha_i) > 0, \tag{5.12}$$

where c is the speed of light in vacuum. Finally, ε_i is the dielectric function in the ambient, film, or substrate, labeled $i = 1, 2, 3$, respectively[3]. The vectors

$$\hat{\mathbf{e}}_{\mathrm{p}}^{(0)}(\mathbf{k}_\parallel) = -\frac{c}{\omega}\left[\alpha_0(k_\parallel,\omega)\hat{\mathbf{k}}_\parallel + k_\parallel \hat{\mathbf{x}}_3\right] \tag{5.13a}$$

[3]When we later will study the reduced Rayleigh equation for a thin film, we will denote the dielectric function in the film with $i = 2$. The use of the subscripts $i = 1, 3$ is intended to cause less confusion at this later stage.

and

$$\hat{\mathbf{e}}_{\mathrm{s}}^{(0)}(\mathbf{k}_{\parallel}) = \hat{\mathbf{k}}_{\parallel} \times \hat{\mathbf{x}}_3 \tag{5.13b}$$

define the polarization vectors of p and s polarization of the incident light, while

$$\hat{\mathbf{e}}_{\mathrm{p}}^{(\mathrm{s})}(\mathbf{q}_{\parallel}) = \frac{c}{\omega}\left[\alpha_0(q_{\parallel},\omega)\hat{\mathbf{q}}_{\parallel} - q_{\parallel}\hat{\mathbf{x}}_3\right] \tag{5.14a}$$

and

$$\hat{\mathbf{e}}_{\mathrm{s}}^{(\mathrm{s})}(\mathbf{q}_{\parallel}) = \hat{\mathbf{q}}_{\parallel} \times \hat{\mathbf{x}}_3 \tag{5.14b}$$

define the polarization vectors for light scattered from the surface. The amplitudes A_α and B_β are assumed to be connected through the linear relation

$$A_\alpha(\mathbf{q}_{\parallel},\omega) = \sum_{\beta=\mathrm{p,s}} R_{\alpha\beta}(\mathbf{q}_{\parallel}|\mathbf{k}_{\parallel})B_\beta(\mathbf{k}_{\parallel},\omega). \tag{5.15}$$

The quantity $R_{\alpha\beta}$ is referred to as the surface scattering amplitude for incident light of β polarization and wave vector $\mathbf{k}$ being scattered into α polarization and wave vector $\mathbf{q}$. This quantity is not directly observable in an experiment; however, the differential reflectivity coefficient can be calculated directly from the scattering amplitude. The differential reflectivity coefficient is defined as the fraction of the total incident power scattered into a solid angle $\partial\Omega_{\mathrm{s}}$ about the scattering direction $(\theta_{\mathrm{s}},\phi_{\mathrm{s}})$ [81]. As we are mainly interested in coherent (non-specular) contributions to the scattering amplitude, we will in this work focus on the incoherent (or diffuse) component of the mean differential reflectivity coefficient, defined as

$$\begin{aligned}\left\langle \frac{\partial R_{\alpha\beta}}{\partial\Omega_{\mathrm{s}}} \right\rangle_{\mathrm{incoh}} &= \left(\frac{\omega}{2\pi cL}\right)^2 \frac{\cos^2\theta_{\mathrm{s}}}{\cos\theta_0} \\ &\quad\times \left(\left\langle \left|R_{\alpha\beta}(\mathbf{q}_{\parallel}|\mathbf{k}_{\parallel})\right|^2 \right\rangle - \left|\left\langle R_{\alpha\beta}(\mathbf{q}_{\parallel}|\mathbf{k}_{\parallel})\right\rangle\right|^2\right).\end{aligned} \tag{5.16}$$

In the expressions above, L is the length of the surface profile, (θ_0,ϕ_0) are the polar angles of the incident wave vectors, and $(\theta_{\mathrm{s}},\phi_{\mathrm{s}})$ are the polar angles of the scattered wave vector. The angles θ_0 and θ_{s} are defined in

Fig. 5.1, while ϕ_0 (ϕ_s) is the angle between $\mathbf{k}_\parallel$ ($\mathbf{q}_\parallel$) and the x_1 axis. In mathematical terms, the relationships between the wave vectors and the polar angles are given by

$$\mathbf{k}_\parallel = \sqrt{\varepsilon_1}\frac{\omega}{c}\sin\theta_0(\cos\phi_0, \sin\phi_0, 0) \tag{5.17a}$$

and

$$\mathbf{q}_\parallel = \sqrt{\varepsilon_1}\frac{\omega}{c}\sin\theta_\mathrm{s}(\cos\phi_\mathrm{s}, \sin\phi_\mathrm{s}, 0). \tag{5.17b}$$

In his efforts to understand surface scattering, Lord Rayleigh made the assumption that the asymptotic expression of the fields [Eq. (5.9)–(5.11)] are valid all the way down to the surface, i.e. at $x_3 = \zeta(\mathbf{x}_\parallel)$. This assumption has later been named "the Rayleigh hypothesis" in his honor. The Rayleigh equation for one-dimensional surfaces was derived by assuming that the Rayleigh hypothesis holds. More recently, Brown et al. [71] derived the reduced Rayleigh equation for light scattering from a two-dimensional surface. Reformulated in the notation of McGurn and Maradudin [72], the equation reads

$$\begin{aligned}\int \frac{\mathrm{d}^2\mathbf{q}_\parallel}{(2\pi)^2}\frac{I\left(\alpha_3(p_\parallel,\omega)-\alpha_1(q_\parallel,\omega)|\mathbf{p}_\parallel-\mathbf{q}_\parallel\right)}{\alpha_3(p_\parallel,\omega)-\alpha_1(q_\parallel,\omega)}\boldsymbol{M}^+(\mathbf{p}_\parallel|\mathbf{q}_\parallel)\boldsymbol{R}(\mathbf{q}_\parallel|\mathbf{k}_\parallel)\\ = \frac{I\left(\alpha_3(p_\parallel,\omega)+\alpha_1(k_\parallel,\omega)|\mathbf{p}_\parallel-\mathbf{q}_\parallel\right)}{\alpha_3(p_\parallel,\omega)+\alpha_1(k_\parallel,\omega)}\boldsymbol{M}^-(\mathbf{p}_\parallel|\mathbf{k}_\parallel),\end{aligned} \tag{5.18a}$$

where the function I is an integral given by

$$I(\gamma|\mathbf{Q}_\parallel) = \int \mathrm{d}^2\mathbf{x}_\parallel \exp(-\mathrm{i}\mathbf{Q}_\parallel\cdot\mathbf{x}_\parallel)\exp\left[-\mathrm{i}\gamma\zeta(\mathbf{x}_\parallel)\right], \tag{5.18b}$$

and the symbol $\boldsymbol{M}^\pm$ refers to the matrix

$$\boldsymbol{M}^\pm(\mathbf{p}_\parallel|\mathbf{q}_\parallel) = \begin{pmatrix} p_\parallel q_\parallel \pm \alpha_3(p_\parallel,\omega)\hat{\mathbf{p}}_\parallel\cdot\hat{\mathbf{q}}_\parallel\alpha_1(q_\parallel,\omega) & -\frac{\omega}{c}\alpha_3(p_\parallel,\omega)(\hat{\mathbf{p}}_\parallel\times\hat{\mathbf{q}}_\parallel)_3 \\ \pm\frac{\omega}{c}(\hat{\mathbf{p}}_\parallel\times\hat{\mathbf{q}}_\parallel)_3\alpha_1(q_\parallel,\omega) & \frac{\omega^2}{c^2}\hat{\mathbf{p}}_\parallel\cdot\hat{\mathbf{q}}_\parallel \end{pmatrix}, \tag{5.18c}$$

where the subscript 3 on the cross products refers to the third component of the resulting vector.

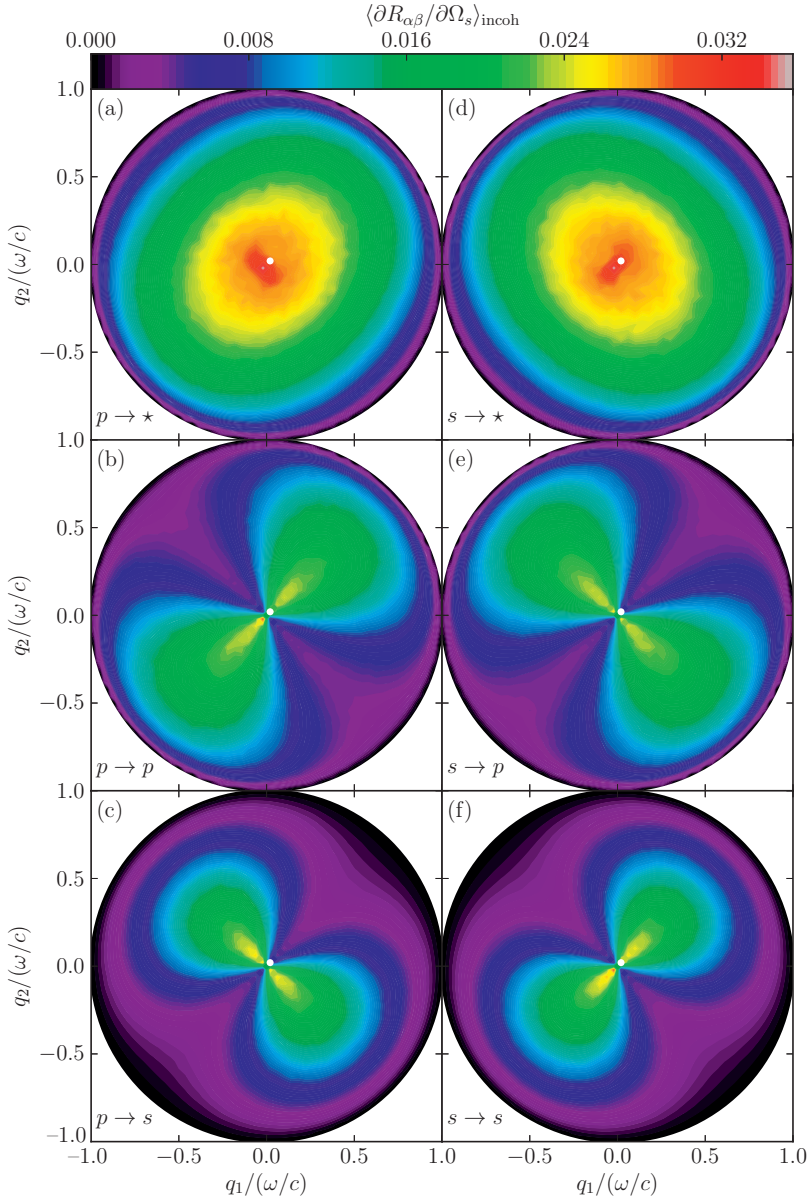

Figure 5.3: The mean differential reflection coefficient for the light scattered from a randomly rough surface, for light incident at $(\theta_0, \phi_0) = (2°, 45°)$. The white dot shows the specular direction.

In order to speed up the numerical calculations, it is desirable to tabulate the integral in Eq. (5.18b) for each combination of $\mathbf{q}_\parallel$ and $\mathbf{p}_\parallel$ in the equation (5.18a). This can be achieved by Taylor expanding the exponential in Eq. (5.18b) as follows:

$$I(\gamma|\mathbf{Q}_\parallel) = \sum_{n=0}^{\infty} \frac{(-\mathrm{i}\gamma)^n}{n!} \hat{\zeta}^{(n)}(\mathbf{Q}_\parallel) \tag{5.19}$$

where

$$\hat{\zeta}^{(n)}(\mathbf{Q}_\parallel) = \int \mathrm{d}^2\mathbf{x}_\parallel \exp\left(\mathrm{i}\mathbf{Q}_\parallel \cdot \mathbf{x}_\parallel\right) \zeta^n(\mathbf{x}_\parallel). \tag{5.20}$$

This integral can be efficiently calculated by use of the fast Fourier transform (FFT) [48].

The details of how one proceeds to obtain the solution to the reduced Rayleigh equation [Eq. (5.18a)] are given in Ref. [8].

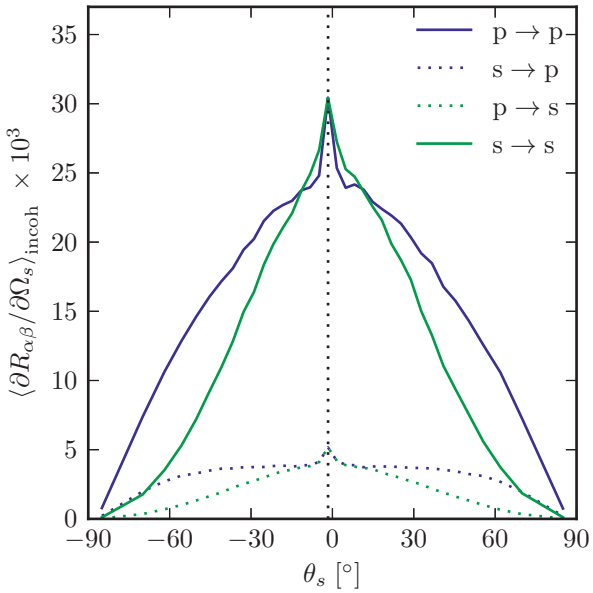

Figure 5.4: In-plane ($\phi_0 = \phi_\mathrm{s}$) cut of the differential reflection coefficient as presented in Fig. 5.3.

The resulting solutions to the reduced Rayleigh equation are most efficiently presented as the incoherent part of the mean differential reflection coefficient [Eq. (5.16)], shown as a contour plot in Fig. 5.3. In generating this figure, light of vacuum wavelength $\lambda = 457.9\,\mathrm{nm}$ was incident on a silver surface profile with an rms height of $\delta = 0.025\lambda$, and an isotropic transverse correlation length of $a = 0.25\lambda$. The realizations of the surface profile functions had a length $L = 25\lambda$ and the resolution of the surface discretization was $\Delta x = 0.078\lambda$. The dielectric function of the substrate was taken to be that of silver at the corresponding wavelength, namely, $\varepsilon_3 = -7.5 + 0.24\mathrm{i}$ [87]. The angles of incidence were $(\theta_0, \phi_0) = (2^\circ, 45^\circ)$, and the DRC shown was found by averaging results from 14 200 surface profile realizations. Note that the specular peak is not present in these results, as only the incoherent (diffuse) contribution to the mean differential reflection coefficient is shown.

Several interesting observations can be made from Fig. 5.3. For instance, one can readily observe that light scattered in-plane ($\phi_\mathrm{s} = \phi_0$) is predominantly co-polarized, i.e. the polarization is unchanged during scattering. Out-of-plane scattering ($\phi_\mathrm{s} = \phi_0 \pm 90^\circ$), however, is predominantly cross-polarized. This is to first approximation a geometric (or single-scattering) effect, which can be explained by a model similar to the Kirchoff model [88] for surface scattering.

The phenomenon of enhanced backscattering which was first discovered in light scattering from one-dimensional surfaces [80] can also be observed in Fig. 5.3. This phenomenon is seen as a sharp peak in the mean differential reflection coefficient in the retroreflection direction [$(\theta_\mathrm{s}, \phi_\mathrm{s}) = (\theta_0, \phi_0 + 180^\circ)$ or, equivalently, $\mathbf{q}_\parallel = -\mathbf{k}_\parallel$]. However, it is more easily seen in an in-plane cut of the differential reflection coefficient, as presented in Fig. 5.4. The specular and backscattering directions are both shown with a vertical dotted line. When comparing plots for different angles of incidence, one sees that the enhanced backscattering peak always occurs at $\theta_\mathrm{s} = -\theta_0$, as one would expect. The enhanced backscattering peak arises from constructive interference between counterpropagating surface plasmon polaritons travelling along the metal-vacuum interface. The observation of the enhanced backscattering effect, as well as the comparison of the results obtained from the reduced Rayleigh equation with a rigorous approach [6, Fig. 9], give confidence in the correctness of these results.

5.3. Satellite peaks

The phenomenon of satellite peaks in the differential reflectivity coefficient is well-known for one-dimensional randomly rough surfaces [83]. However, there has been some controversy over whether this effect exists in surfaces whose profile function is two-dimensional. Kawanishi et al. [76] found no signs of satellite peaks when employing the so-called stochastic functional approach, whereas Soubret et al. [74] observed satellite peaks when solving the reduced Rayleigh equation perturbatively in powers of the surface profile function. We show here and in Ref. [9] that satellite peaks do indeed exist also for systems with a two-dimensional rough surface profile, through the solution of the reduced Rayleigh equation for a system consisting of a dielectric film with a rough interface deposited on a planar metallic substrate.

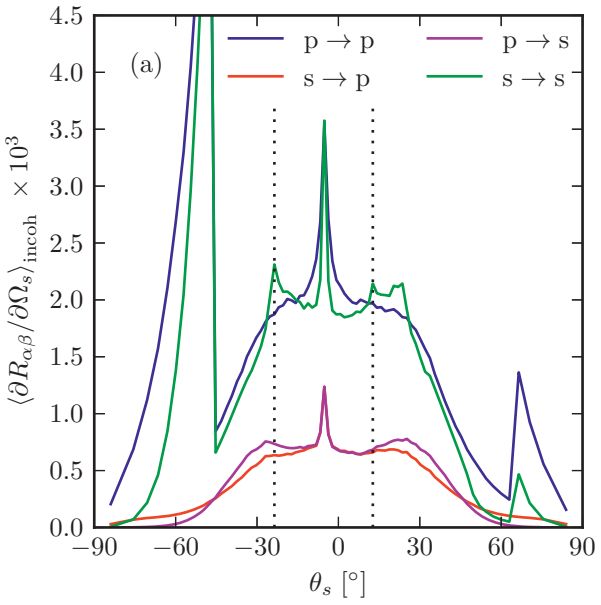

Figure 5.5: The incoherent part of the mean differential reflection coefficient as a function of the polar scattering angle θ_s from the in-plane ($\phi_\mathrm{s} = \phi_0$) co-polarized (p → p, s → s) scattering of light incident on a two-dimensional randomly rough surface of a dielectric film deposited on a planar substrate of silver. The angle of incidence was $\theta_0 = 5°$.

In Fig. 5.5, we show the contributions to the mean differential reflection coefficient as functions of the polar scattering angle θ_s from the in-plane ($\phi_\mathrm{s} = \phi_0$) co-polarized (p $\to$ p, s $\to$ s) and cross-polarized (p $\to$ s, s $\to$ p) scattering of light from a thin, rough film deposited on a planar, metallic substrate. The metal was taken to be silver, whose dielectric constant is $\varepsilon_3 = -18.28 + 0.481\mathrm{i}$ at the vacuum wavelength of $\lambda = 633\,\mathrm{nm}$. The angles of incidence were $(\theta_0, \phi_0) = (0.74^\circ, 45^\circ)$. The dielectric constant of the film was $\varepsilon_2 = 2.6896 + 0.01\mathrm{i}$, and its mean thickness was $d = 478.5$ nm. The roughness of the surface is characterized by the power spectrum in Eq. (5.8), with $k_- = 0.82(\omega/c)$, $k_+ = 1.97(\omega/c)$, and the rms height was $\delta = \lambda/40 = 15.82\,\mathrm{nm}$. This system possesses two guided modes in p-polarization and two guided modes in s-polarization. The p-polarized modes have wave numbers

$$q_{1,\mathrm{p}}(\omega) = 1.4391(\omega/c), \tag{5.21a}$$
$$q_{2,\mathrm{p}}(\omega) = 1.0119(\omega/c), \tag{5.21b}$$

and the s-polarized modes have wave numbers

$$q_{1,\mathrm{s}}(\omega) = 1.5467(\omega/c), \tag{5.21c}$$
$$q_{2,\mathrm{s}}(\omega) = 1.2432(\omega/c). \tag{5.21d}$$

In Fig. 5.5, the satellite peaks are clearly seen symmetrically around the enhanced backscattering peak for s $\to$ s scattering. The dotted vertical lines indicate the angles $\theta_\mathrm{s} = -23.2^\circ$ and $\theta_\mathrm{s} = 12.3^\circ$ for which one would expect satellite peaks to appear, based on the wave numbers in Eq. (5.21). The lack of any satellite peaks in p-polarization can be due to several reasons, including lack of resolution near $\mathbf{q}_\parallel = \omega/c$; the wave number of one of the p-polarized guided modes are very close to ω/c. Other reasons include that there could be weaker coupling into these modes. We refer the reader to Ref. [9] for further discussion and details.

5.4. The Mueller matrix of a rough surface

As discussed in Chapter 2.2, the Mueller matrix describes linear interactions between the polarization of light and matter. In the past, there have been performed few calculations of the Mueller matrix for a rough

surface. Exceptions include the calculations performed by Bruce using the Kirchoff approximation, and his discussion of symmetry properties of the Mueller matrix for light normally incident on a statistically isotropic rough surface [89]. Zhang and Bahar [90] also performed an approximate analytic calculation of the scattering from a randomly rough dielectric surface coated with a thin film composed of a different dielectric material. However, to the author's knowledge, no computer simulation studies published to date show the full angular distribution of the Mueller matrix for arbitrary angles of incidence. Examples of numerical results will be discussed in this chapter, and the interested reader can consult Ref. [7] for a more thorough discussion.

For a complete description of polarization effects of a randomly rough surface, one needs to calculate the Mueller matrix not only for the specular reflection, but for scattering from any incident wave vector ($\mathbf{k}$) into any scattered wave vector ($\mathbf{q}$). In Fig. 5.6, the full angular distribution of the Mueller matrix for light scattering from an isotropic, randomly rough silver surface is given. The incident light, with $\lambda = 457.9\,\text{nm}$, shining upon a silver surface having a dielectric function of $\varepsilon = -7.5 + 0.24\text{i}$ [87]. The surface autocorrelation function is assumed to be isotropic and Gaussian, i.e.

$$W\left(\left|\mathbf{x}_{\parallel}\right|\right) = \exp\left(-\frac{x_{\parallel}^2}{a^2}\right), \tag{5.22}$$

with a correlation length $a = \lambda/4 = 114.5\,\text{nm}$ and rms roughness $\delta = \lambda/40 = 11.5\,\text{nm}$. The angles of incidence were $(\theta_0, \phi_0) = (2^\circ, 45^\circ)$, i.e. nearly normal incidence.

As predicted by Bruce [89], the elements in column 2 and column 3 are identical, save for a 45° rotation about the origin (Fig. 5.6). Intuitively, one might expect the elements of the Mueller matrix to be circularly symmetric at normal incidence for isotropic surfaces. The "cloverleaf" patterns in the center two columns are counterintuitive, as the physical system under study is rotationally symmetric (to a good approximation: $\theta_0 = 2^\circ$). However, the pattern is artificial in the sense that the orientation of the pattern depends only on the orientation of the coordinate system. For instance, the Stokes parameter Q gives the linearly polarized light intensity in the horizontal and vertical directions, but the labeling of certain directions as

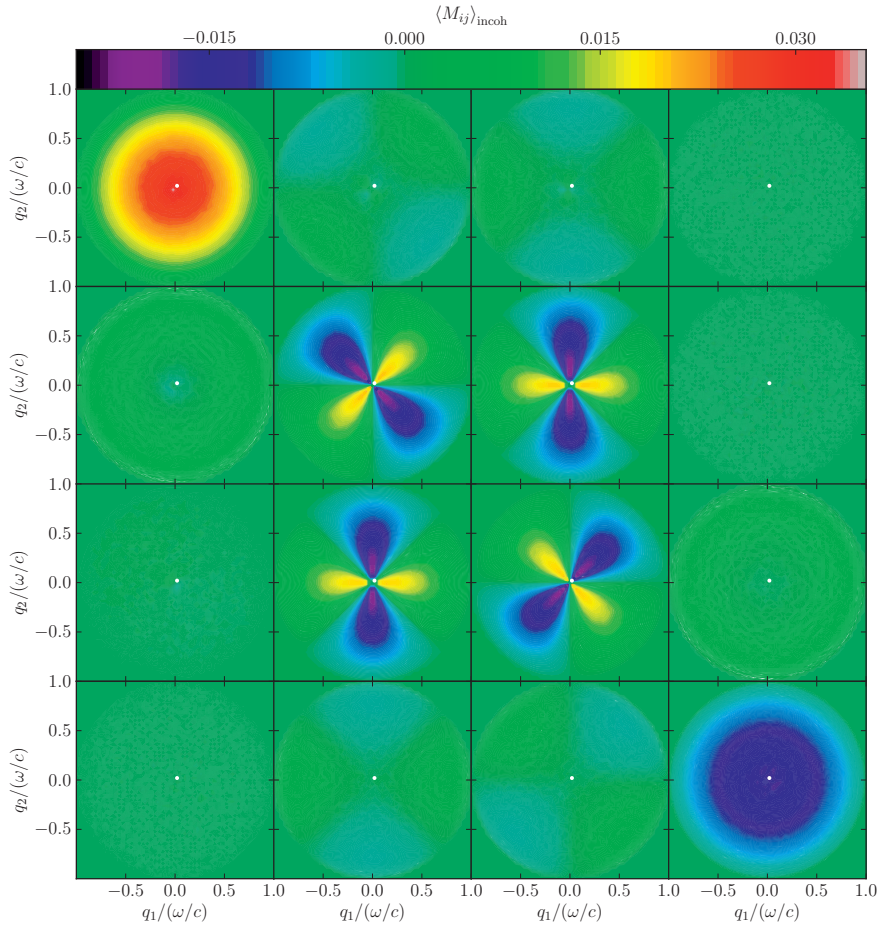

Figure 5.6: The Mueller matrix of a rough surface for angles of incidence $(\theta_0, \phi_0) = (2°, 45°)$. The position of the specular direction is indicated by a white dot.

horizontal or vertical is simply a choice of coordinate system. Rotating the polarization vectors $\hat{\mathbf{e}}_\mathrm{p}$ and $\hat{\mathbf{e}}_\mathrm{s}$ of the incident light thus results in a rotation of the "cloverleaf" pattern.

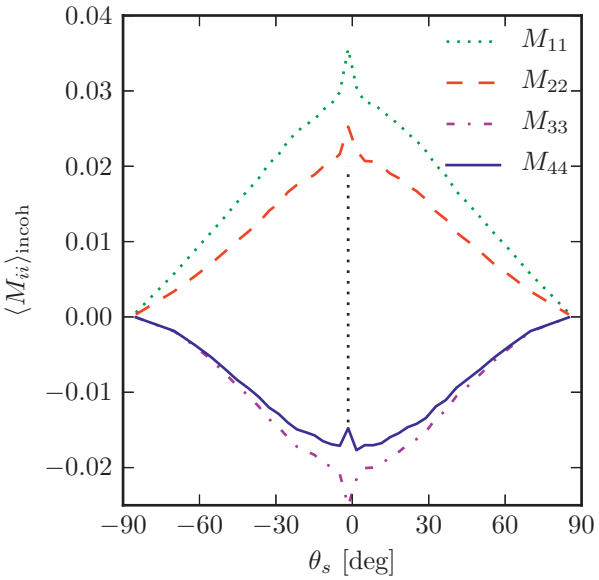

Figure 5.7: In-plane cut ($\phi_\mathrm{s} = \phi_0$) of the diagonal elements of the Mueller matrix for simulation parameters identical to those used in generating Fig. 5.6. The vertical dashed line shows the enhanced backscattering direction ($\theta_\mathrm{s} = -\theta_0 = -2°$). Note in particular the reduced absolute value of M_{44} in the enhanced backscattering direction; this result has not been reported previously.

The full Mueller matrix contains some interesting physical phenomena, for instance enhanced backscattering [80]. This effect is not easily observed directly in Fig. 5.6, but can be seen more readily by plotting the in-plane cut (i.e. the plane $\phi_\mathrm{s} = \phi_0$) of the diagonal elements in the Mueller matrix (Fig. 5.7). It is observed that the absolute value for three of the elements has a peak in the backscattering direction, where $\mathbf{q}_\parallel = -\mathbf{k}_\parallel$, or equivalently, $(\theta_\mathrm{s}, \phi_\mathrm{s}) = (\theta_0, \phi_0 + 180°)$. The M_{44} element, however, has a dip in its absolute value, contrary to the other elements. This corresponds to *reduced backscattering* for circular polarization, which has previously

not been reported.

The full angular distribution of the Mueller matrix for angles of incidence $(\theta_0, \phi_0) = (25°, 45°)$ is shown in Fig. 5.8. Interestingly, the elements M_{31}, M_{41}, M_{14}, and M_{24} are no longer (to numerical precision) zero, but exhibit interesting structure in the angular distribution. The symmetry of the patterns in the center two columns is also broken, although the patterns remain similar. The enhanced backscattering peak in M_{11}, M_{22}, and M_{33} can be observed as a small dot, as can the reduced backscattering peak in M_{44}. The results for non-normal incidence complement the results for normal incidence, showing how the rough surface exhibits different polarization effects for normal and non-normal incidence.

Simulations of the Mueller matrix for (randomly) rough or structured surfaces may facilitate both the design of surfaces with desirable polarization properties, as well as the interpretation of experimental data. There is in general a lack of scattering models for polarization effects, which come into play in a wide range of applications. Simulation approaches like the one sketched here can hopefully be useful in the advancement of both fundamental science, as well as in technological applications.

5.5. Summary

In summary, the surface scattering of light from two-dimensional surfaces has both similarities to and differences from scattering from one-dimensional surfaces. Several phenomena, which were well known from one-dimensional surfaces, have been observed in the numerically generated results for two-dimensional surface scattering, including enhanced backscattering and satellite peaks. The most significant difference lies in the polarization effects, which are not present in one-dimensional surface scattering. Such effects are most efficiently described in terms of Mueller matrices, whose full angular distribution has been calculated.

The surface scattering of light is a classical problem with many aspects to it, and much work remains before all aspects of it are understood. For instance, there is a need for better understanding of which polarization effects can occur in anisotropic and chiral surfaces. Such understanding is necessary if surface scattering is to be an effective experimental characterization technique. It would also be of interest to examine the effects of

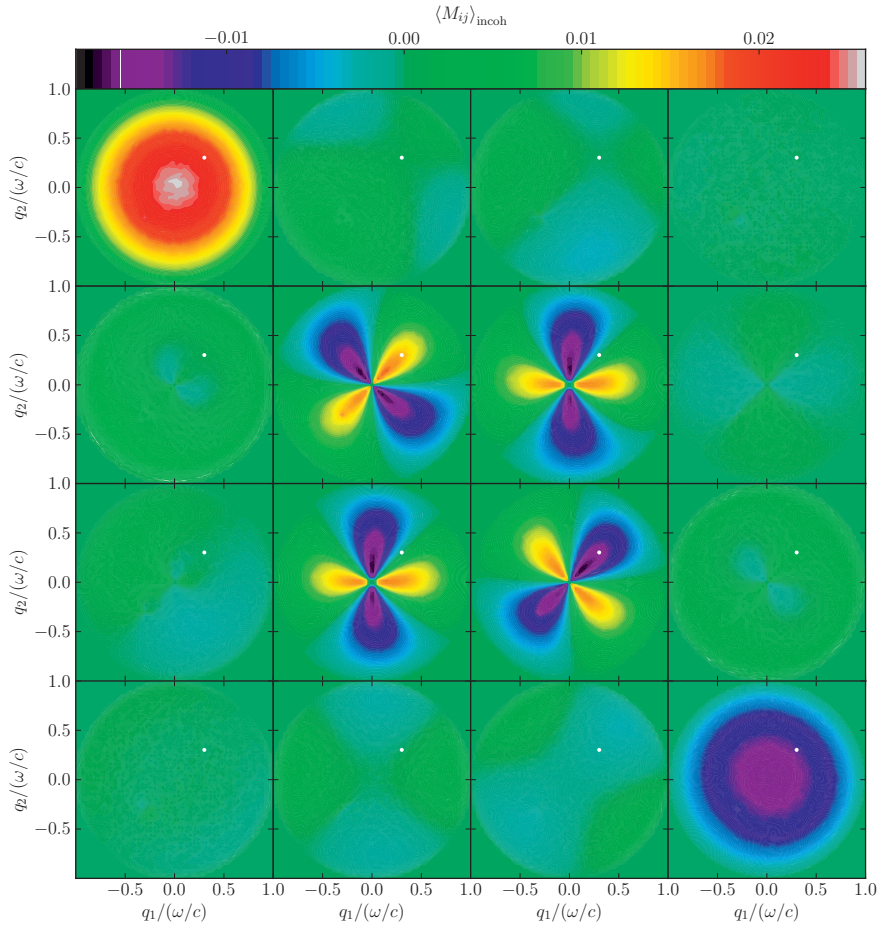

Figure 5.8: The Mueller matrix of the same rough surface as in Fig. 5.6, but with angles of incidence $(\theta_0, \phi_0) = (25°, 45°)$. The position of the specular peak is shown by a white dot. The enhanced (or reduced) backscattering peak can be seen as a faint dot in each of the diagonal elements, located at $\mathbf{q}_\parallel = -\mathbf{k}_\parallel$.

different height distribution functions and lateral correlation functions in a more systematic fashion.

6. Summary

This thesis has discussed polarization effects observed due to the properties of rough and structured interfaces, as well as how one can optimize polarimeters for measuring polarization effects. The systems studied include nanoparticle patterned surfaces, stochastically rough surfaces, and stochastically rough films deposited on planar substrates.

In order to study surfaces patterned with nanoparticles, a simulation code was written which uses multipole expansions [1] and the image multipole method [3, 10] to take particle-particle and particle-substrate effects into account. The code is capable of simulating both small clusters of nanoparticles, as well as two-dimensional infinite arrays of nanoparticles. Simulations of single nanoparticles and nanoparticle dimers on top of substrates show the importance of taking the substrate into account to high order. Conveniently, some variables (e.g. the reflectivity of a nanoparticle lattice) achieve good convergence at lower cutoffs in the spherical harmonic expansion ($L_{\max}$) than the local fields—that is, the fulfillment of the boundary conditions—do.

By employing a form of effective medium theory which takes the environment of the particle into account, the reflectivity from a surface patterned with a lattice of sub-wavelength particles has been simulated. This was done by approximating a rectangular lattice of nanoparticles as an anisotropic thin film, and using standard theory to calculate the reflectance from the surface. The results show some interesting features, including the wavelength dependent polarization of light reflected from the surface [10].

By direct solution of the reduced Rayleigh equation [8], the scattering of light from two-dimensionally rough surfaces has been simulated. The simulation code, named RAYLEIGH2D, takes the polarization effects of the scattering process into account. In order to obtain the most complete description of the polarization effects, the Mueller matrix was constructed from the simulation results [7]. The results exhibit the effect of enhanced

backscattering, well known from studies using perturbation theory to calculate the scattering amplitude. Interestingly, a new effect denoted reduced backscattering was observed in the M_{44} element of the Mueller matrix.

A controversy over whether the phenomenon of satellite peaks, taking the form of peaks (or a ring) placed symmetrically around the enhanced backscattering peak, exists in the scattering of light from two-dimensional (as opposed to one-dimensional) surfaces, was resolved. Our simulation results clearly show satellite peaks at the positions predicted by the dispersion relation, and thus resolve the controversy in the literature [9].

A long-standing problem in Mueller matrix ellipsometry is the issue of optimizing an (imaging) polarization state analyzer (or, equivalently, a polarization state generator) for both speed of operation and noise. Hence, we attempted to generate a polarimeter design with good performance over a broad spectrum using a genetic algorithm. The resulting polarimeter design, based on ferroelectric liquid crystals, features excellent performance [2, 5] over the wavelength range from 430 nm to 2000 nm. This work also received 3rd prize in the 2011 annual "Humies" awards[1] at the GECCO 2011 conference.

The same approach was used again to design a Mueller matrix ellipsometer using liquid crystal variable retarders. This design was subsequently implemented, and the achieved performance was compared to the theoretical design. The predicted performance was achieved to good precision, proving both that our simulation of the ellipsometer was realistic, as well as the efficiency of the optimization algorithm.

To finalize, this thesis describes several models of surface optical phenomena, and especially polarization effects. This includes a quasistatic model of nanoparticles deposited on surfaces, a model of surface scattering from single rough interfaces, and a similar model for scattering from rough thin films deposited on a planar interface. With respect to the measurement of polarization effects, a general approach for the optimization of Stokes/Mueller polarimeters has been described. Together, the papers presented in Appendix A give more details for the interested reader, and complement each other nicely.

[1] `http://www.genetic-programming.org/hc2011/combined.html`

6.1. Suggested future work

As usual, the work described in this thesis not only answers questions, it also opens up for new venues of research. For example, preliminary results indicate that the RAYLEIGH2D simulation code can simulate truncated nanoparticles of low aspect ratio deposited on planar interfaces. The system can be modeled as a thin film where the height of the surface profile function describes the top surface of the particles. This may allow for the comparison of the optical effects of spherical nanoparticles to that of truncated spheres or other types of particles with low aspect ratio and no overhangs. Also, one can attempt to determine at which point retardation effects become important, by simulation of nanoparticles of increasing size.

As the efficiency of genetic algorithms for the design of polarimeters has been established, it would be advantageous to explore new applications of this approach. For example, it is of interest to design even more broad-band polarimeters, and in particular for the ultra violet part of the spectrum. The main challenge here is to find and characterize suitable materials and components. It is also possible that other broad-band optical components could be optimized using similar approaches.

Finally, the simulation of lattices of nanospheres could be expanded to include truncated nanospheres. This requires some analytical work, as the naive approach requires the calculation of an extremely large amount of double integrals. The symmetries of rectangular and triangular lattices may lend itself to the simplification or elimination of some of these integrals, which may facilitate numerical solution of this problem.

Bibliography

[1] P. A. Letnes and I. Simonsen. "Spectrally dependent locations of hot-spots in nanoparticle clusters", pp. 2084–2088. *phys. status solidi (b)* **247** (2010).

[2] P. A. Letnes, I. S. Nerbø, L. M. S. Aas, P. G. Ellingsen, and M. Kildemo. "Fast and optimal broad-band Stokes/Mueller polarimeter design by the use of a genetic algorithm", pp. 23095–23103. *Opt. Express* **18** (2010).

[3] P. A. Letnes, I. Simonsen, and D. L. Mills. "Substrate influence on the plasmonic response of clusters of spherical nanoparticles", 075426. *Phys. Rev. B* **83** (2011).

[4] P. A. Letnes, I. Simonsen, and D. L. Mills. "Erratum: Substrate influence on the plasmonic response of clusters of spherical nanoparticles [Phys. Rev. B 83, 075426 (2011)]", 149901. *Phys. Rev. B* **85** (14 Apr. 2012).

[5] P. A. Letnes, I. S. Nerbø, L. M. S. Aas, P. G. Ellingsen, and M. Kildemo. "Genetic invention of fast and optimal broad-band Stokes / Mueller polarimeter designs". In: *Proceedings of the 13th annual conference companion on genetic and evolutionary computation*. Ed. by N. Krasnogor. Dublin, Ireland: ACM, 2011, pp. 237–238.

[6] T. A. Leskova, P. A. Letnes, A. A. Maradudin, T. Nordam, and I. Simonsen. "The scattering of light from two-dimensional randomly rough surfaces". *Proc. SPIE* **8172** (2011).

[7] P. A. Letnes, A. A. Maradudin, T. Nordam, and I. Simonsen. "Calculation of all elements of the Mueller matrix for scattering of light from a two-dimensional randomly rough metal surface", `http://arxiv.org/abs/1108.2599`. *(accepted, Phys. Rev. A)* (2012).

[8] T. Nordam, P. A. Letnes, and I. Simonsen. "Numerical simulations of scattering of light from two-dimensional surfaces using the Reduced Rayleigh Equation", `http://arxiv.org/abs/1204.4984` (2012).

[9] T. Nordam, P. A. Letnes, I. Simonsen, and A. A. Maradudin. "Satellite peaks in the scattering of light from the two-dimensional randomly rough surface of a dielectric film on a planar metal surface", pp. 11336–11350. *Opt. Express* **20** (2012).

[10] P. A. Letnes, I. Simonsen, and D. L. Mills. "Plasmonic resonances at interfaces patterned by nanoparticle lattices", `http://arxiv.org/abs/1208.1911` (2012).

[11] P. A. Letnes, T. Nordam, and I. Simonsen. "Coherent effects in the scattering of light from two-dimensional rough metal surfaces". *(unpublished)* (2012).

[12] J. D. Jackson. *Classical Electrodynamics*. 3rd ed. New York: John Wiley, 1998.

[13] E. H. Land. "Some aspects of the development of sheet polarizers", pp. 957–962. *J. Opt. Soc. Am. A* **41** (1951).

[14] E. Hecht. *Optics*. 4th ed. Boston, Massachusetts: Addison Wesley, 1998.

[15] I. Hodgkinson and Q. H. Wu. "Birefringent thin-film polarizers for use at normal incidence and with planar technologies", pp. 1794–1796. *Appl. Phys. Lett.* **74** (1999).

[16] G. Horváth, A. Barta, I. Pomozi, B. Suhai, R. Hegedüs, S. Åkesson, B. Meyer-Rochow, and R. Wehner. "On the trail of Vikings with polarized skylight: experimental study of the atmospheric optical prerequisites allowing polarimetric navigation by Viking seafarers", pp. 772–782. *Philos. T. R. Soc. B* **366** (2011).

[17] C. Hawryshyn. "Polarization vision in fish", pp. 164–175. *Am. Sci.* **80** (1992).

[18] N. Shashar and T. W. Cronin. "Polarization contrast vision in Octopus.", pp. 999–1004. *J. Exp. Biol.* **199** (1996).

[19] H. Gábor. "Reflection-polarization patterns at flat water surfaces and their relevance for insect polarization vision", pp. 27–37. *J. Theor. Biol.* **175** (1995).

[20] K. P. Able. "Skylight polarization patterns at dusk influence migratory orientation in birds", pp. 550–551. *Nature* **299** (1982).

[21] W. K. von Haidinger. "Über das direkte Erkennen des polarisierten Lichts", pp. 29–38. *Annalen der Physik und Chemie* **3** (1844).

[22] M. H. Smith, P. D. Burke, A. Lompado, E. A. Tanner, and L. W. Hillman. "Mueller matrix imaging polarimetry in dermatology", pp. 210–216. *Proc. SPIE* **3911** (2000).

[23] T. A. Germer. "Measurement of roughness of two interfaces of a dielectric film by scattering ellipsometry", pp. 349–352. *Phys. Rev. Lett.* **85** (2000).

[24] I. S. Nerbo, S. L. Roy, M. Kildemo, and E. Sondergard. "Real-time in situ spectroscopic ellipsometry of GaSb nanostructures during sputtering", 213105. *Appl. Phys. Lett.* **94** (2009).

[25] W. E. Martin, E. Hesse, J. H. Hough, W. B. Sparks, C. S. Cockell, Z. Ulanowski, T. A. Germer, and P. H. Kaye. "Polarized optical scattering signatures from biological materials", pp. 2444–2459. *J. Quant. Spectrosc. Ra.* **111** (2010).

[26] R. A. Chipman. *Handbook of Optics*. New York: McGraw–Hill, 1994.

[27] S. R. Cloude. "Conditions for the physical realisability of matrix operators in polarimetry", pp. 177–185. *Proc. SPIE* **1166** (1989).

[28] P. Collins, R. M. Redfern, and B. Sheehan. "Design, Construction and Calibration of The Galway Astronomical Stokes Polarimeter (GASP)", pp. 241–246. *AIP Conference Proceedings* **984** (2008).

[29] J. D. Howe, M. A. Miller, R. V. Blumer, T. E. Petty, M. A. Stevens, D. M. Teale, and M. H. Smith. "Polarization sensing for target acquisition and mine detection", pp. 202–213. *Proc. SPIE* **4133** (2000).

[30] P. G. Ellingsen, M. B. Lilledahl, L. M. S. Aas, C. de Lange Davies, and M. Kildemo. "Quantitative characterization of articular cartilage using Mueller matrix imaging and multiphoton microscopy", 116002. *J. Biomed. Opt.* **16** (2011).

[31] D. Schmidt, C. Müller, T. Hofmann, O. Inganäs, H. Arwin, E. Schubert, and M. Schubert. "Optical properties of hybrid titanium chevron sculptured thin films coated with a semiconducting polymer", pp. 2645–2649. *Thin Solid Films* **519** (2011).

[32] R. M. A. Azzam. "Mueller-matrix ellipsometry: a review", pp. 396–405. *Proc. SPIE* **3121** (1997).

[33] M. Foldyna, A. D. Martino, R. Ossikovski, E. Garcia-Caurel, and C. Licitra. "Characterization of grating structures by Mueller polarimetry in presence of strong depolarization due to finite spot size", pp. 735–741. *Opt. Commun.* **282** (2009).

[34] I. S. Nerbø, S. Le Roy, M. Foldyna, M. Kildemo, and E. Søndergård. "Characterization of inclined GaSb nanopillars by Mueller matrix ellipsometry", 014307. *J. Appl. Phys.* **108** (2010).

[35] R. N. Weinreb, S. Shakiba, and L. Zangwill. "Scanning laser polarimetry to measure the nerve fiber layer of normal and glaucomatous eyes", pp. 627–636. *Am. J. Ophthalmol.* **119** (1995).

[36] T. A. Germer. "Measuring Interfacial Roughness by Polarized Optical Scattering". In: *Light Scattering and Nanoscale Surface Roughness*. Ed. by A. A. Maradudin. Berlin: Springer, 2007, pp. 259–284.

[37] D. S. Sabatke, M. R. Descour, E. L. Dereniak, W. C. Sweatt, S. A. Kemme, and G. S. Phipps. "Optimization of retardance for a complete Stokes polarimeter", pp. 802–804. *Opt. Lett.* **25** (2000).

[38] R. M. A. Azzam and A. De. "Optimal beam splitters for the division-of-amplitude photopolarimeter", pp. 955–958. *J. Opt. Soc. Am. A* **20** (2003).

[39] R. M. A. Azzam. "Photopolarimetric measurement of the Mueller matrix by Fourier analysis of a single detected signal", pp. 148–150. *Opt. Lett.* **2** (1978).

[40] J. Ladstein, M. Kildemo, G. K. Svendsen, I. S. Nerbø, and F. Stabo-Eeg. "Characterisation of liquid crystals for broadband optimal design of Mueller matrix ellipsometers". *Proc. SPIE* **6587** (2007).

[41] A. M. Gandorfer. "Ferroelectric retarders as an alternative to piezoelastic modulators for use in solar Stokes vector polarimetry", pp. 1402–1408. *Opt. Eng.* **38** (1999).

[42] J. Ladstein, F. Stabo-Eeg, E. Garcia-Caurel, and M. Kildemo. "Fast near-infrared spectroscopic Mueller matrix ellipsometer based on ferroelectric liquid crystal retarders", pp. 1097–1100. *phys. status solidi (c)* **5** (2008).

[43] S. Tomczyk, R. Casini, A. G. de Wijn, and P. G. Nelson. "Wavelength-diverse polarization modulators for Stokes polarimetry", pp. 3580–3586. *Appl. Opt.* **49** (2010).

[44] J. H. Holland. *Adaptation in natural and artificial systems: an introductory analysis with applications to biology, control, and artificial intelligence*. 2nd ed. Cambridge, Massachusetts: MIT press, 1992.

[45] G. Strang. *Introduction to linear algebra*. Wellesley, Massachusetts: Wellesley Cambridge Press, 2003.

[46] F. Stabo-Eeg, M. Kildemo, I. S. Nerbø, and M. Lindgren. "Well-conditioned multiple laser Mueller matrix ellipsometer", 073604. *Opt. Eng.* **47** (2008).

[47] C. Darwin. *On the origin of species by means of natural selection*. London: John Murray, 1859.

[48] W. H. Press, S. A. Teukolsky, W. T. Vetterling, and B. P. Flannery. *Numerical Recipes: The Art of Scientific Computing*. Cambridge University Press, 2007.

[49] D. Floreano and C. Mattiussi. *Bio-Inspired Artificial Intelligence: Theories, Methods, and Technologies*. Cambridge, Massachusetts: MIT Press, 2008.

[50] D. Cattelan, E. Garcia-Caurel, A. De Martino, and B. Drevillon. "Device and method for taking spectroscopic polarimetric measurements in the visible and near-infrared ranges". *Patent application 2937732, France* (2010).

[51] J. C. Maxwell Garnett. "Colours in metal glasses and in metallic films", pp. 385–420. *Phil. Trans. R. Soc. Lond. A* **203** (1904).

[52] G. Mie. "Beitrage zur Optik truber Medien, speziell kolloidaler Metallösungen", pp. 377–445. *Annalen der Physik* **330** (1908).

[53] F. E. Wagner, S. Haslbeck, L. Stievano, S. Calogero, Q. A. Pankhurst, and K. P. Martinek. "Before striking gold in gold-ruby glass — The chemistry of the magic ingredient in this ancient glass is no longer a mystery.", pp. 691–692. *Nature* **407** (2000).

[54] H. Tamaru, H. Kuwata, H. T. Miyazaki, and K. Miyano. "Resonant light scattering from individual Ag nanoparticles and particle pairs", pp. 1826–1828. *Appl. Phys. Lett.* **80** (2002).

[55] D. Bedeaux and J. Vlieger. *Optical Properties of Surfaces*. London: Imperial College Press, 2004.

[56] I. Simonsen, R. Lazzari, J. Jupille, and S. Roux. "Numerical modeling of the optical response of supported metallic particles", pp. 7722–7733. *Phys. Rev. B* **61** (2000).

[57] S. Pillai, K. R. Catchpole, T. Trupke, and M. A. Green. "Surface plasmon enhanced silicon solar cells", *Journal of Applied Physics* **101** (2007).

[58] H. A. Atwater and A. Polman. "Plasmonics for improved photovoltaic devices", pp. 205–213. *Nat Mater* **9** (2010).

[59] Y. Nishijima, L. Rosa, and S. Juodkazis. "Surface plasmon resonances in periodic and random patterns of gold nano-disks for broadband light harvesting", pp. 11466–11477. *Opt. Express* **20** (May 2012).

[60] E. Ozbay. "Plasmonics: Merging Photonics and Electronics at Nanoscale Dimensions", pp. 189–193. *Science* **311** (2006).

[61] M. Moskovits. "Surface-enhanced spectroscopy", pp. 783–826. *Rev. Mod. Phys.* **57** (1985).

[62] F. Le, D. W. Brandl, Y. A. Urzhumov, H. Wang, J. Kundu, N. J. Halas, J. Aizpurua, and P. Nordlander. "Metallic Nanoparticle Arrays: A Common Substrate for Both Surface-Enhanced Raman Scattering and Surface-Enhanced Infrared Absorption", pp. 707–718. *ACS Nano* **2** (2008).

[63] M. Pelton, J. Aizpurua, and G. Bryant. "Metal-nanoparticle plasmonics", pp. 136–159. *Laser Photonics Rev.* **2** (2008).

[64] T. Yamaguchi, S. Yoshida, and A. Kinbara. "Optical effect of the substrate on the anomalous absorption of aggregated silver films", pp. 173–187. *Thin Solid Films* **21** (1974).

[65] J. Tang, E. V. Ponizovskaya, A. M. Bratkovsky, D. R. Stewart, Z. Li, and R. S. Williams. "Metallic nanocrystals near ultrasmooth metallic films for surface-enhanced Raman scattering application", 415702. *Nanotechnology* **19** (2008).

[66] I. Romero, J. Aizpurua, G. W. Bryant, and F. J. García de Abajo. "Plasmons in nearly touching metallic nanoparticles: singular response in the limit of touching dimers", pp. 9988–9999. *Opt. Express* **14** (2006).

[67] E. Prodan, C. Radloff, N. J. Halas, and P. Nordlander. "A Hybridization Model for the Plasmon Response of Complex Nanostructures", pp. 419–422. *Science* **302** (2003).

[68] L. Rayleigh. "On the Dynamical Theory of Gratings", pp. 399–416. *Proc. R. Soc. London A* **79** (1907).

[69] R. F. Millar. "On the Rayleigh assumption in scattering by a periodic surface", pp. 773–791. *Proc. Cambridge Philos. Soc.* **65** (1969).

[70] R. F. Millar. "On the Rayleigh assumption in scattering by a periodic surface. II", pp. 217–225. *Proc. Cambridge Philos. Soc* **69** (1971).

[71] G. C. Brown, V. Celli, M. Haller, and A. Marvin. "Vector theory of light scattering from a rough surface: Unitary and reciprocal expansions", pp. 381–397. *Surf. Sci.* **136** (1984).

[72] A. R. McGurn and A. A. Maradudin. "Perturbation theory results for the diffuse scattering of light from two-dimensional randomly rough metal surfaces", pp. 251–267. *Wave. Random Media* **6** (1996).

[73] J. T. Johnson. "Third-order small-perturbation method for scattering from dielectric rough surfaces", pp. 2720–2736. *J. Opt. Soc. Am. A* **16** (Nov. 1999).

[74] A. Soubret, G. Berginc, and C. Bourrely. "Application of reduced Rayleigh equations to electromagnetic wave scattering by two-dimensional randomly rough surfaces", 245411. *Phys. Rev. B* **63** (2001).

[75] A. Soubret, G. Berginc, and C. Bourrely. "Backscattering enhancement of an electromagnetic wave scattered by two-dimensional rough layers", pp. 2778–2788. *J. Opt. Soc. Am. A* **18** (2001).

[76] T. Kawanishi, H. Ogura, and Z. L. Wang. "Scattering of an electromagnetic wave from a slightly random dielectric surface: Yoneda peak and Brewster angle in incoherent scattering", pp. 351–384. *Wave. Random Media* **7** (1997).

[77] I. Simonsen, A. A. Maradudin, and T. A. Leskova. "Scattering of Electromagnetic Waves from Two-Dimensional Randomly Rough Penetrable Surfaces", 223904. *Phys. Rev. Lett.* **104** (2010).

[78] I. Simonsen, A. A. Maradudin, and T. A. Leskova. "Scattering of electromagnetic waves from two-dimensional randomly rough perfectly conducting surfaces: The full angular intensity distribution", 013806. *Phys. Rev. A* **81** (2010).

[79] I. Simonsen, J. B. Kryvi, A. A. Maradudin, and T. A. Leskova. "Light scattering from anisotropic, randomly rough, perfectly conducting surfaces", pp. 1904–1908. *Comput. Phys. Commun.* **182** (2011).

[80] A. R. McGurn, A. A. Maradudin, and V. Celli. "Localization effects in the scattering of light from a randomly rough grating", pp. 4866–4871. *Phys. Rev. B* **31** (1985).

[81] I. Simonsen. "Optics of surface disordered systems", pp. 1–103. *Eur. Phys. J.–Spec. Top.* **181** (2010).

[82] C. S. West and K. A. O'Donnell. "Observations of backscattering enhancement from polaritons on a rough metal surface", pp. 390–397. *J. Opt. Soc. Am. A* **12** (1995).

[83] V. Freilikher, E. Kanzieper, and A. A. Maradudin. "Coherent scattering enhancement in systems bounded by rough surfaces", pp. 127–204. *Phys. Rep.* **288** (1997).

[84] I. Simonsen and A. A. Maradudin. "Numerical simulation of electromagnetic wave scattering from planar dielectric films deposited on rough perfectly conducting substrates", pp. 99–111. *Opt. Commun.* **162** (1999).

[85] E. R. Méndez, E. I. Chaikina, and H. M. Escamilla. "Observation of satellite peaks and dips in the scattering of light in a double-pass geometry", pp. 705–707. *Opt. Lett.* **24** (1999).

[86] A. A. Maradudin, T. Michel, A. R. McGurn, and E. R. Méndez. "Enhanced backscattering of light from a random grating", pp. 255–307. *Ann. Phys.* **203** (1990).

[87] P. B. Johnson and R. W. Christy. "Optical Constants of the Noble Metals", pp. 4370–4379. *Phys. Rev. B* **6** (1972).

[88] F. G. Bass and I. M. Fuks. *Wave scattering from statistically rough surfaces.* Oxford: Pergamon Press, 1979.

[89] N. Bruce. "Calculations of the Mueller matrix for scattering of light from two-dimensional surfaces", pp. 15–28. *Wave. Random Media* **8** (1998).

[90] Y. Zhang and E. Bahar. "Mueller matrix elements that characterize scattering from coated random rough surfaces", pp. 949–955. *IEEE Trans. Antennas Propag.* **47** (1999).

A. Papers

P. A. Letnes and I. Simonsen. "Spectrally dependent locations of hot-spots in nanoparticle clusters", pp. 2084–2088. *phys. status solidi (b)* 247 (2010)

Paper 1

Is not included due to copyright

P. A. Letnes, I. S. Nerbø, L. M. S. Aas, P. G. Ellingsen, and M. Kildemo. "Fast and optimal broad-band Stokes/Mueller polarimeter design by the use of a genetic algorithm", pp. 23095–23103. *Opt. Express* 18 (2010)

Paper 2

Fast and optimal broad-band Stokes/Mueller polarimeter design by the use of a genetic algorithm

Paul Anton Letnes,* Ingar Stian Nerbø, Lars Martin Sandvik Aas, Pål Gunnar Ellingsen, and Morten Kildemo

Department of Physics, The Norwegian University of Science and Technology (NTNU), N-7491 Trondheim, Norway

**paul.anton.letnes@gmail.com*

Abstract: A fast multichannel Stokes/Mueller polarimeter with no mechanically moving parts has been designed to have close to optimal performance from $430 - 2000$ nm by applying a genetic algorithm. Stokes (Mueller) polarimeters are characterized by their ability to analyze the full Stokes (Mueller) vector (matrix) of the incident light (sample). This ability is characterized by the condition number, κ, which directly influences the measurement noise in polarimetric measurements. Due to the spectral dependence of the retardance in birefringent materials, it is not trivial to design a polarimeter using dispersive components. We present here both a method to do this optimization using a genetic algorithm, as well as simulation results. Our results include fast, broad-band polarimeter designs for spectrographic use, based on 2 and 3 Ferroelectric Liquid Crystals, whose material properties are taken from measured values. The results promise to reduce the measurement noise significantly over previous designs, up to a factor of 4.5 for a Mueller polarimeter, in addition to extending the spectral range.

OCIS codes: (120.2130) Ellipsometry and polarimetery; (120.4570) Optical design of instruments; (300.0300) Spectroscopy.

References and links

1. A. M. Gandorfer, "Ferroelectric retarders as an alternative to piezoelastic modulators for use in solar Stokes vector polarimetry," Opt. Eng. **38**, 1402–1408 (1999).
2. P. Collins, R. Redfern, and B. Sheehan, "Design, construction and calibration of the Galway astronomical Stokes polarimeter (GASP)," in *AIP Conference Proceedings,* D. Phelan, O. Ryan, and A. Shearer, eds. (AIP, Edinburgh (Scotland), 2008), vol. 984, p. 241.
3. A. Alvarez-Herrero, V. Martínez-Pillet, J. del Toro Iniesta, and V. Domingo, "The IMaX polarimeter for the solar telescope SUNRISE of the NASA long duration balloon program," in *Proceedings of API'09,* E. Garcia-Caurel, ed. (EPJ Web of Conferences, 2010), vol. 5, p. 05002.
4. J. D. Howe, M. A. Miller, R. V. Blumer, T. E. Petty, M. A. Stevens, D. M. Teale, and M. H. Smith, "Polarization sensing for target acquisition and mine detection," in *Polarization Analysis, Measurement, and Remote Sensing III,* D. B. Chenault, M. J. Duggin, W. G. Egan, and D. H. Goldstein, eds., Proc. SPIE **4133**, 202–213 (2000).
5. M. H. Smith, P. D. Burke, A. Lompado, E. A. Tanner, and L. W. Hillman, "Mueller matrix imaging polarimetry in dermatology," in *Biomedical Diagnostic, Guidance, and Surgical-Assist Systems II,* T. Vo-Dinh, W. S. Grundfest, and D. A. Benaron, eds., Proc. SPIE **3911**, 210–216 (2000).
6. R. N. Weinreb, S. Shakiba, and L. Zangwill, "Scanning laser polarimetry to measure the nerve fiber layer of normal and glaucomatous eyes," Am. J. Ophthalmol. **119**, 627–636 (1995).

#134880 - $15.00 USD Received 9 Sep 2010; revised 5 Oct 2010; accepted 5 Oct 2010; published 18 Oct 2010

7. M. Foldyna, A. D. Martino, R. Ossikovski, E. Garcia-Caurel, and C. Licitra, "Characterization of grating structures by Mueller polarimetry in presence of strong depolarization due to finite spot size," Opt. Commun. **282**, 735–741 (2009).
8. I. S. Nerbø, S. Le Roy, M. Foldyna, M. Kildemo, and E. Søndergård, "Characterization of inclined GaSb nanopillars by Mueller matrix ellipsometry," J. Appl. Phys. **108**, 014307 (2010).
9. L. Jin, M. Kasahara, B. Gelloz, and K. Takizawa, "Polarization properties of scattered light from macrorough surfaces," Opt. Lett. **35**, 595–597 (2010).
10. T. A. Germer, "Polarized light scattering by microroughness and small defects in dielectric layers." J. Opt. Soc. Am. A **18**, 1279–1288 (2001).
11. T. Germer, "Measurement of roughness of two interfaces of a dielectric film by scattering ellipsometry," Phys. Rev. Lett. **85**, 349–352 (2000).
12. F. Stabo-Eeg, M. Kildemo, I. Nerbø, and M. Lindgren, "Well-conditioned multiple laser Mueller matrix ellipsometer," Opt. Eng. **47**, 073604 (2008).
13. J. S. Tyo, "Noise equalization in Stokes parameter images obtained by use of variable-retardance polarimeters," Opt. Lett. **25**, 1198–1200 (2000).
14. D. S. Sabatke, M. R. Descour, E. L. Dereniak, W. C. Sweatt, S. A. Kemme, and G. S. Phipps, "Optimization of retardance for a complete Stokes polarimeter," Opt. Lett. **25**, 802–804 (2000).
15. R. M. A. Azzam and A. De, "Optimal beam splitters for the division-of-amplitude photopolarimeter," J. Opt. Soc. Am. A **20**, 955–958 (2003).
16. R. M. A. Azzam, "Photopolarimetric measurement of the Mueller matrix by Fourier analysis of a single detected signal," Opt. Lett. **2**, 148 (1978).
17. J. M. Bueno, "Polarimetry using liquid-crystal variable retarders: theory and calibration," J. Opt. A: Pure Appl. Opt. **2**, 216–222 (2000).
18. E. Garcia-Caurel, A. D. Martino, and B. Drévillon, "Spectroscopic Mueller polarimeter based on liquid crystal devices," Thin Solid Films **455-456**, 120–123 (2004).
19. J. Ladstein, M. Kildemo, G. Svendsen, I. Nerbø, and F. Stabo-Eeg, "Characterisation of liquid crystals for broadband optimal design of Mueller matrix ellipsometers," in *Liquid Crystals and Applications in Optics,* M. Glogarova, P. Palffy-Muhoray, and M. Copic, eds. Proc. SPIE **6587**, 65870D (2007).
20. L. M. S. Aas, P. G. Ellingsen, M. Kildemo, and M. Lindgren, "Dynamic Response of a fast near infra-red Mueller matrix ellipsometer," J. Mod. Opt. **(accepted)** (2010).
21. D. Cattelan, E. Garcia-Caurel, A. De Martino, and B. Drevillon, "Device and method for taking spectroscopic polarimetric measurements in the visible and near-infrared ranges," Patent application 2937732, France (2010).
22. J. H. Holland, "Genetic algorithms," Scientific American **267**, 44–50 (1992).
23. D. Floreano and C. Mattiussi, *Bio-Inspired Artificial Intelligence: Theories, Methods, and Technologies* (The MIT Press, 2008).
24. A. Kudla, "Application of the genetic algorithms in spectroscopic ellipsometry," Thin Solid Films **455-456**, 804–808 (2004).
25. G. Cormier and R. Boudreau, "Genetic algorithm for ellipsometric data inversion of absorbing layers," J. Opt. Soc. Am. A **17**, 129–134 (2000).
26. V. R. Fernandes, C. M. S. Vicente, N. Wada, P. S. André, and R. A. S. Ferreira, "Multi-objective genetic algorithm applied to spectroscopic ellipsometry of organic-inorganic hybrid planar waveguides," Opt. Express **18**, 16580–16586 (2010).
27. F. Stabo-Eeg, M. Kildemo, E. Garcia-Caurel, and M. Lindgren, "Design and characterization of achromatic 132° retarders in CaF_2 and fused silica," J. Mod. Opt. **55**, 2203–2214 (2008).
28. W. H. Press, S. A. Teukolsky, W. T. Vetterling, and B. P. Flannery, *Numerical Recipes: The Art of Scientific Computing* (Cambridge University Press, 2007).
29. E. Compain, S. Poirier, and B. Drevillon, "General and self-consistent method for the calibration of polarization modulators, polarimeters, and Mueller-matrix ellipsometers," Appl. Opt. **38**, 3490–3502 (1999).
30. J. Ladstein, F. Stabo-Eeg, E. Garcia-Caurel, and M. Kildemo, "Fast near-infra-red spectroscopic Mueller matrix ellipsometer based on ferroelectric liquid crystal retarders," Phys. Status Solidi C **5**, 1097–1100 (2008).

1. Introduction

Polarimeters are applied in a wide range of fields, from astronomy [1–3], remote sensing [4] and medical diagnostics [5, 6] to applications in ellipsometry such as characterizing gratings [7], nanostructures [8] and rough surfaces [9–11]. As all polarimeters are based on inverting so-called system matrices, it is well known that the measurement error from independent Gaussian noise is minimized when the condition number (κ) of these system matrices is minimized [12, 13]. It has been shown that $\kappa = \sqrt{3}$ is the best condition number that can be achieved for such a system, and that this optimal condition number can be achieved by several different

#134880 - $15.00 USD Received 9 Sep 2010; revised 5 Oct 2010; accepted 5 Oct 2010; published 18 Oct 2010

approaches using various optical components (*e.g.* rotating retarders [14], division of amplitude [15, 16], and liquid-crystal variable retarders [17]). In many applications it is necessary to perform fast spectroscopic measurements (*e.g.* by using a Charge-Coupled Device (CCD) based spectrograph) [18]. In that case, the wavelength dependence of the optical elements will cause the polarimeter not to be optimally conditioned over the full range simultaneously. A system based on two Ferroelectric Liquid Crystals (FLC) has been reported to be fast and reasonably well conditioned over the visible or near infrared spectral range [18–20]. By introducing a third FLC a similar system has been proposed to have an acceptable condition number from the visible to the near infra-red ($430-1700$ nm) [21]. The design of a system having the best possible condition number over a broad spectrum is a challenging optimization problem due to the large number of parameters; many optimization algorithms are prone to return local optimums, and a direct search is too time consuming. To avoid this time-consuming exhaustive search, we decided to employ the Genetic Algorithm (GA). A GA simulates evolution on a population of individuals in order to find an optimal solution to the problem at hand. Genetic Algorithms were pioneered by Holland [22], and are discussed in detail in *e.g.* Ref. [23]. GAs have previously been applied in ellipsometry to solve the inversion problem for the thickness and dielectric function of multiple thin layers, see *e.g.* Ref. [24–26].

2. Overdetermined polarimetry

A Stokes polarimeter consists of a polarization state analyzer (PSA) capable of measuring the Stokes vector of a polarization state, see Fig. 1. The PSA is based on performing at least 4 different measurements along different projection states. A measured Stokes vector $\mathbf{S}$ can then be expressed as $\mathbf{S} = \mathbf{A}^{-1}\mathbf{b}$, where $\mathbf{A}$ is a system matrix describing the PSA and $\mathbf{b}$ is a vector containing the intensity measurements. $\mathbf{A}^{-1}$ denotes the matrix inverse of $\mathbf{A}$, which in the case of overdetermined polarimetry with more than 4 projection states will denote the Moore–Penrose *pseudoinverse*. The analyzing matrix $\mathbf{A}$ is constructed from the first rows of the Mueller matrices of the PSA for the different states. The noise in the measurements of $\mathbf{b}$ will be amplified by the condition number of $\mathbf{A}$, $\kappa_\mathbf{A}$, in the inversion to find $\mathbf{S}$. Therefore $\kappa_\mathbf{A}$ should be as small as possible, which correspond to do as independent measurements as possible (*i.e.* to use projection states that are as orthogonal as possible).

A Mueller matrix $\mathbf{M}$ describes how an interaction changes the polarization state of light, by transforming an incoming Stokes vector $\mathbf{S}_\text{in}$ to the outgoing Stokes vector $\mathbf{S}_\text{out} = \mathbf{M}\mathbf{S}_\text{in}$. To measure the Mueller matrix of a sample it is necessary to generate at least 4 different polarization states by a polarization state generator (PSG) and measure the outgoing Stokes vector by at least 4 measurements for each generated state. The measured intensities can then be arranged in a matrix $\mathbf{B} = \mathbf{A}\mathbf{M}\mathbf{W}$, where the system matrix $\mathbf{W}$ of the PSG contains the generated Stokes vectors as its columns. These generated Stokes vectors are found simply as the first column of the Mueller matrix of the PSG in the respective states. $\mathbf{M}$ can then be found by inversion as $\mathbf{M} = \mathbf{A}^{-1}\mathbf{B}\mathbf{W}^{-1}$. The error $\Delta\mathbf{M}$ in $\mathbf{M}$ is then bounded by the condition numbers according to [27]

$$\frac{\|\Delta\mathbf{M}\|}{\|\mathbf{M}\|} \lesssim \kappa_\mathbf{W}\kappa_\mathbf{A}\frac{\|\Delta\mathbf{B}\|}{\|\mathbf{B}\|} + \kappa_\mathbf{A}\frac{\|\Delta\mathbf{A}\|}{\|\mathbf{A}\|} + \kappa_\mathbf{W}\frac{\|\Delta\mathbf{W}\|}{\|\mathbf{W}\|}. \tag{1}$$

The condition number is given as $\kappa_\mathbf{A} = \|\mathbf{A}\|\|\mathbf{A}^{-1}\|$, which for the the 2-norm can be calculated from the ratio of the largest to the smallest singular value [28]. $\Delta\mathbf{A}$ and $\Delta\mathbf{W}$ are calibration errors, which increase with κ when calibration methods using matrix inversion are applied. The PSG can be constructed from the same optical elements as the PSA, placed in the reverse order, which would give $\kappa_\mathbf{A} = \kappa_\mathbf{W} \equiv \kappa$. As the error in Mueller matrix measurements is proportional

#134880 - $15.00 USD Received 9 Sep 2010; revised 5 Oct 2010; accepted 5 Oct 2010; published 18 Oct 2010

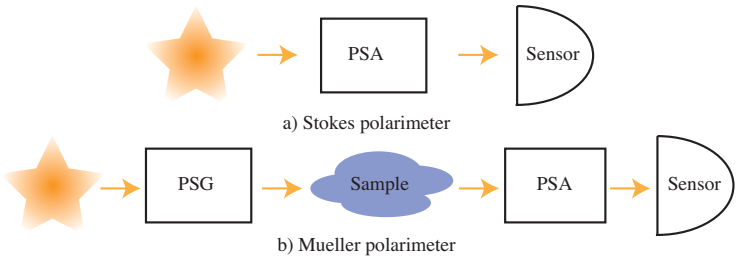

Fig. 1. (a) A Stokes polarimeter measures the polarization state of an arbitrary light source using a Polarization State Analyzer (PSA). (b) A Mueller polarimeter measures how the polarization state of light, generated by with a Polarization State Generator (PSG), is changed by a sample.

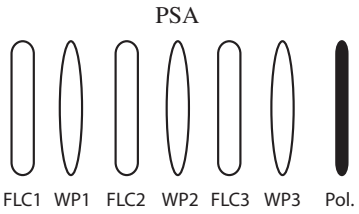

Fig. 2. Sketch of a PSA consisting of 3 FLC's, 3 waveplates (WP), each with a retardance δ and an orientation θ relative to the transmission axis of a polarizer.

to κ^2, it is very important to keep this value as low as possible.

If 4 optimal states can be achieved (giving $\kappa = \sqrt{3}$), no advantage is found by doing a larger number of measurements with different states, compared to repeated measurements with the 4 optimal states [14]. If, however, these optimal states can not be produced ($\kappa > \sqrt{3}$), the condition number, and hence the error, can be reduced by performing more than 4 measurements. For a FLC based polarimeter this can be done by using 3 FLCs followed by a polarizer as PSA, with up to 3 waveplates (WP) between the FLCs to increase the condition number (see Fig. 2). A PSG can be constructed with the same elements in the reverse order. Since each FLC can be switched between two states (this switching can be described as a rotation of the fast axis of a retarder by $+45°$), $2^3 = 8$ different states can be analyzed (generated) by the PSA (PSG). To accurately measure the Stokes vector, the system matrix $\mathbf{A}$ needs to be well known. For a Mueller polarimeter generating and analyzing 4 states in the PSG and PSA, the eigenvalue calibration method (ECM) [29] can be applied. The ECM allows the measuring of the actual produced states by the PSA and PSG ($\mathbf{A}$ and $\mathbf{W}$), without relying on exact knowledge or modeling of the optical components. However, the ECM is based on the inversion of a product of measured intensity matrices $\mathbf{B}$ for measurements on a set of calibration samples. This product becomes singular for a system analyzing and generating more than four states. A workaround of this problem is to choose the subset of 4 out of 8 states which gives the lowest κ value, and build a $\mathbf{B}$ matrix of those states to find 4 of the 8 rows (columns) of $\mathbf{A}$ ($\mathbf{W}$). More rows (columns) of $\mathbf{A}$ ($\mathbf{W}$) can then be found by calibrating on a different subset of the 8 states, giving the second lowest κ value, and so on. By repeating the calibration on different subsets of states, all the 8 rows (columns) of $\mathbf{A}$ ($\mathbf{W}$) can be found with low relative error $\|\Delta\mathbf{A}\|/\|\mathbf{A}\|$ ($\|\Delta\mathbf{W}\|/\|\mathbf{W}\|$).

#134880 - $15.00 USD Received 9 Sep 2010; revised 5 Oct 2010; accepted 5 Oct 2010; published 18 Oct 2010

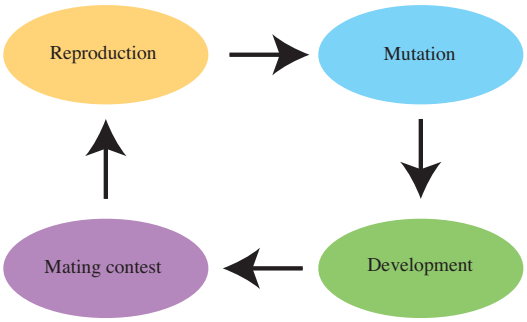

Fig. 3. The four essential processes in a genetic algorithm are shown above. Sexual reproduction is performed by multi-point genetic crossover, giving rise to the next generation of individuals. Mutation can be simulated with simple bit negation (*e.g.* $0 \rightarrow 1$ and *vice versa*). Development is the process where a genotype is interpreted into its phenotype, *i.e.* the binary genome is interpreted as a polarimeter design. In the mating contest, one evaluates the fitness of each individual's phenotype, and let the more fit individuals reproduce with higher probability than the less fit individuals.

3. Genetic optimization

In order to optimize $\kappa(\lambda)$, one can conceivably employ a variety of optimization algorithms, from simple brute-force exhaustive search to more advanced algorithms, such as *e.g.* Levenberg–Marquardt, simulated annealing, and particle swarm optimization. Our group has previously performed optimization of a polarimeter design based on fixed components, namely, two FLCs and two waveplates. In this case, the optimization problem reduces to searching the space of 4 orientation angles. With a resolution of 1° per angle, this gives a search space consisting of $180^4 \approx 10^9$ states to evaluate; on modern computer hardware, this direct search can be performed. In order to optimize the retardances of the components as well, the total number of states increases to about $\left(10^9\right)^2 = 10^{18}$. Obviously, brute force exhaustive search is unfeasible for such large search spaces.

A GA performs optimization by simulating evolution in a population of individuals (here: simulated polarimeters). The three pillars of evolution are variation, heritability, and selection. Our initial population must have some initial genetic variation between the individuals; hence, we initialize our population by generating random individuals. Heritability means that the children have to carry on some of the traits of their parents. We simulate this by either cloning parents into children (asexual reproduction) or by performing genetic crossover (sexual reproduction) in a manner that leave children with some combination of the traits of their parents. Finally, selection is done by giving more fit individuals a larger probability of survival. For this purpose, we used the tournament selection protocol, described in Ref. [23]. For a sketch of the essential processes involved in a GA, see Fig. 3.

Our GA builds directly on the description given by Holland [22], using a binary genome as the genetic representation. In this representation, a string of 0s and 1s represent the genome of the individual. To simulate mutation in our genetic algorithm, we employ logical bit negation; *i.e.* $0 \rightarrow 1$ or vice versa. Sexual reproduction is simulated by using multi-point crossover, *i.e.* simply cutting and pasting two genomes together, as described by Holland [22].

The interpretation of the genome into a phenotype (development), in this case a polarimeter design, is done in a straightforward way. For each variable in the polarimeter's configuration,

#134880 - $15.00 USD Received 9 Sep 2010; revised 5 Oct 2010; accepted 5 Oct 2010; published 18 Oct 2010

i.e. for each orientation angle and each retardance, we select m bits in the genome (typically, $m = 8$) and interpret this number as an integer in the range from 1 to 2^m. The integer is subsequently interpreted as a real number in a predefined range, *e.g.*, $\theta \in [0°, 180°]$. In order to avoid excessively large jumps in the search space due to mutations, we chose to implement the interpretation of bits into integers by using the Gray code, also known as the reflected binary code. The most important parameter values in our GA are shown in Table 2. Making good choices for each of these parameters is often essential in order to ensure good convergence.

After determining the phenotype, we must assign to each simulated polarimeter individual a fitness function (also known as the objective function). In order to do this, we first calculate $\kappa(\lambda)$. As discussed, $\kappa^{-1}(\lambda)$ maximally takes on the value $1/\sqrt{3}$. Hence, we define an error function, e, as

$$e = \frac{1}{N_\lambda} \sum_{n=1}^{N_\lambda} \left(\kappa^{-1}(\lambda_n) - 1/\sqrt{3} \right)^4 . \tag{2}$$

In Eq. (2), $\lambda_n = \lambda_{\min} + (n-1)\Delta\lambda$, with $n = 1, 2, \ldots, N_\lambda$ and $\Delta\lambda = 5$ nm. $\lambda_{\min}$ and N_λ are determined by the wavelength range we are interested in. The choice of taking the difference between $\kappa^{-1}(\lambda)$ and the optimal value to power 4 is done in order to "punish" peaks in the condition number more severely. As GAs conventionally seek to maximize the fitness function, we define an individual's fitness as

$$f = \frac{1}{e}. \tag{3}$$

This definition is convenient because f takes on real and positive values where higher values represents more optimal polarimeter designs.

4. Results

For the case of a polarimeter based on 3 FLCs and 3 WPs, we have minimized $\kappa(\lambda)$ by varying the orientation angle, θ, and the retardance, δ, of all the elements. This yields a 12-dimensional search space, *i.e.*, 6 retardances and 6 orientation angles. θ is the angle between the fast axis of the retarder (WP or FLC) and the transmission axis of the polarizer (see Fig. 2), taken to be in the range $\theta \in [0°, 180°]$. The retardance, δ, is modeled using a modified Sellmeier equation,

$$\delta \approx 2\pi L \left[\frac{A_{UV}}{(\lambda^2 - \lambda_{UV}^2)^{1/2}} - \frac{A_{IR}}{(\lambda_{IR}^2 - \lambda^2)^{1/2}} \right], \tag{4}$$

where A_{UV}, A_{IR}, λ_{UV}, and λ_{IR} are experimentally determined parameters for an FLC ($\lambda/2$@510 nm, Displaytech Inc.) and a Quartz zero order waveplate ($\lambda/4$@465 nm) taken directly from Refs. [19] (for the FLCs, $A_{IR} = 0$). L is a normalized thickness, with $L = 1$ corresponding to a retardance of $\lambda/2$@510 nm for the FLCs and $\lambda/4$@465 nm for the waveplates. Each L and θ are represented by 8 bits each in the genome. We use experimental values to ensure that our design is based on as realistic components as possible.

The 3-FLC polarimeter design scoring the highest fitness function is shown in Table 1. The wavelength range for which we optimized the polarimeter was from 430 to 2000 nm. To visualize the performance of this design, we show a plot of $\kappa^{-1}(\lambda)$ in Fig. 4. The inverse condition number, κ^{-1}, is larger than 0.5 over most parts of the spectrum, which is close to the optimal inverse condition number ($\kappa^{-1} = 1/\sqrt{3} = 0.577$). This is a great improvement compared to the earlier reported 3-FLC design [21], which oscillates around $\kappa^{-1} \approx 0.33$. The new design promise a decrease in noise amplification by up to a factor of 2.1 for a Stokes polarimeter, and up to factor of 4.5 for a Mueller polarimeter. In addition the upper spectral limit is extended

#134880 - $15.00 USD Received 9 Sep 2010; revised 5 Oct 2010; accepted 5 Oct 2010; published 18 Oct 2010

Table 1. Orientation angles, θ, and normalized thicknesses L, of the components of the best 3-FLC polarimeter. (WP = (fixed) waveplate)

Component	$\theta[^\circ]$	L
FLC1	56.5	2.44
WP1	172.9	1.10
FLC2	143.3	1.20
WP2	127.1	1.66
FLC3	169.4	1.42
WP3	110.1	4.40

from 1700 nm to 2000 nm. Shorter wavelengths than 430 nm were not considered as the FLC material will be degraded by exposure to UV light. Previous designs often suffer from $\kappa^{-1}(\lambda)$ oscillating as a function of wavelength, whereas our solution is more uniform over the wavelength range we are interested in. This uniformity in $\kappa(\lambda)$ will, according to Eq. (1), give a more uniform noise distribution over the spectrum.

To give some idea of how fast the GA converges, a plot of f [see Eq. (3)] as a function of the generation number is shown in Fig. 5. The mean population fitness (μ) and standard deviation (σ) is also shown. As so often happens with genetic algorithms, we see that the maximal and average fitness increases dramatically in the first few generations. Following this fast initial progress, evolution slows down considerably, before it finally converges after 600 generations. The parameters used in our GA to obtain these results are shown in Table 2.

A design using fewer components, in particular 2 FLCs and 2 waveplates, does have advantages. These advantages include increased transmission of light, as well as reduced cost and complexity with respect to building and maintaining the instrument. In addition some applications have weight and volume restrictions [3]. For these reasons, we have performed genetic optimization of the 2-FLC design. In Fig. 6, we show the performance of two polarimeter designs for the wavelength ranges $430-1100$ nm (compatible with an Si detector) and $800-1700$ nm. Both of these polarimeter designs show condition numbers which are considerably better

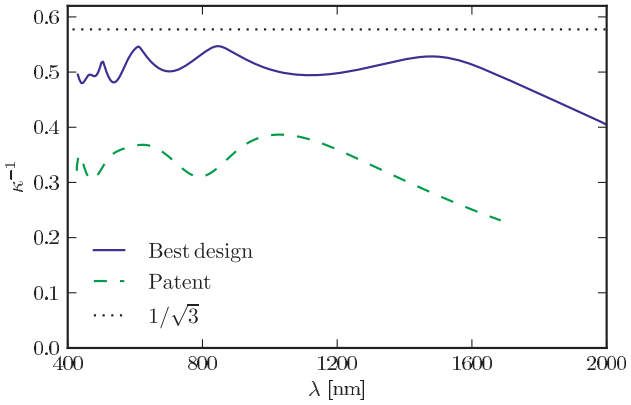

Fig. 4. Inverse condition number for the best GA-generated 3-FLC design. For comparison, we show the inverse condition number of the patented 3-FLC design [21].

#134880 - $15.00 USD Received 9 Sep 2010; revised 5 Oct 2010; accepted 5 Oct 2010; published 18 Oct 2010

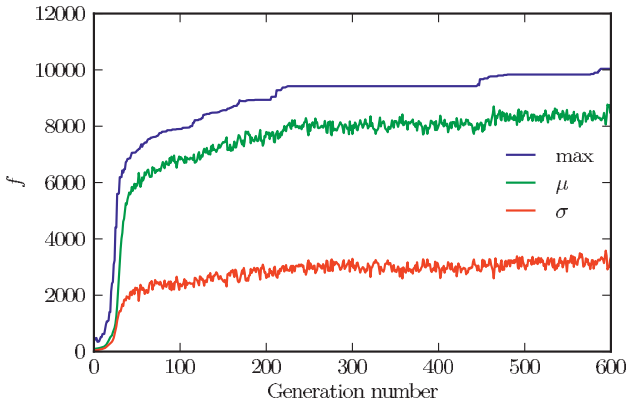

Fig. 5. Convergence of fitness as a function of generation number. μ and σ refer to the average and standard deviation of the population's fitness, respectively. The best result from this simulation is the one shown in Fig. 4.

Table 2. Genetic Algorithm parameters. The "crossover rate" is the probability for two parents to undergo sexual reproduction (the alternative being asexual reproduction). The parameter "crossover points" refer to the number of points where we cut the genome during crossover (sexual reproduction). "Mutation rate" is the probability for any given individual to undergo one or several bit flip mutations in one generation

Parameter	Value
Crossover rate	0.7
Crossover points	2
Mutation rate	0.2
Population size	500

Table 3. Orientation angle, θ, and normalized thickness, L, of the 2-FLC polarimeters shown in Fig. 6

	Visible design		NIR design	
Component	θ[°]	L	θ[°]	L
FLC 1	90.4	1.17	177.9	2.60
WP 1	3.5	3.58	112.9	2.94
FLC 2	92.5	1.02	74.8	1.75
WP 2	19.8	3.52	163.1	4.71

than previously reported designs. The numerical parameters of the two designs based on 2 FLCs are shown in Table 3.

Our optimization algorithm can, with little effort, be applied to a wider range of polarimeter design. Any optical component can be included into our GA; for example, one can include fixed waveplates of different materials, prisms, mirrors, and other types of liquid crystal devices. The material of each component could also be a variable, which could help alleviate the dispersion problem. The only requirement is that the retardance of the component in question must be

#134880 - $15.00 USD Received 9 Sep 2010; revised 5 Oct 2010; accepted 5 Oct 2010; published 18 Oct 2010

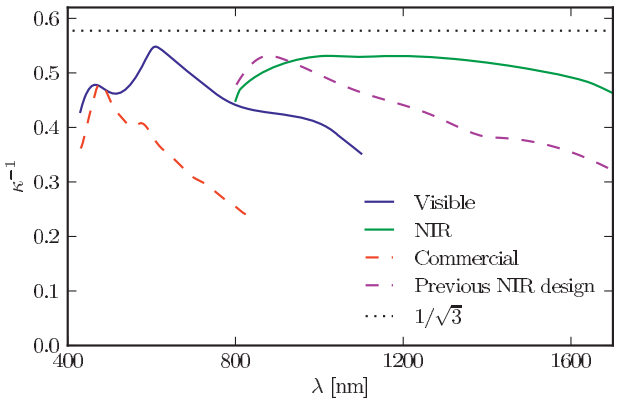

Fig. 6. Condition number for two designs using 2 FLC retarders and 2 waveplates. By optimizing $\kappa(\lambda)$ over a narrower part of the spectrum, we can design good polarimeters with fewer components. The polarimeter designs labeled "Visible" and "IR" show our two designs, optimized for 430 nm $< \lambda <$ 1100 nm and 800 nm $< \lambda <$ 1700 nm, respectively. For comparison with our "NIR" design, we show the previous simulated design from Ref. [30]. The curve labeled "Commercial" shows the measured condition number of a commercial instrument (MM16, Horiba, 2006) based on the same (FLC) technology.

possible to either model theoretically or measure experimentally. It is possible to optimize a polarimeter for a different wavelength range, simply by changing program inputs. Focusing on a wavelength range which is as narrow as possible typically results in higher condition numbers than reported here. Evaluating different technologies, materials and components for polarimetry should thus be relatively straightforward. The task is not computationally formidable: we have used ordinary desktop computers in all our calculations.

5. Conclusion

In conclusion, we have used genetic algorithms to optimize the design of a fast multichannel spectroscopic Stokes/Mueller polarimeter, using fast switching ferroelectric liquid crystals. We have presented three polarimeter designs which promise significant improvement with respect to previous work in terms of noise reduction and spectral range. Our approach requires relatively little computational effort. One can easily generate new designs if one should wish to use other components and materials, or if one wishes to focus on a different part of the optical spectrum. We hope that our designs will make polarimetry in general, and ellipsometry in particular, a less noisy and more efficient measurement technique.

Acknowledgements

The authors would like to thank professor Keith Downing at the Department of Computer and Information Science at NTNU for helpful discussions regarding genetic algorithms and their implementation.

#134880 - $15.00 USD Received 9 Sep 2010; revised 5 Oct 2010; accepted 5 Oct 2010; published 18 Oct 2010

P. A. Letnes, I. Simonsen, and D. L. Mills. "Substrate influence on the plasmonic response of clusters of spherical nanoparticles", 075426. *Phys. Rev. B* 83 (2011)

Paper 3

PHYSICAL REVIEW B **83**, 075426 (2011)

Substrate influence on the plasmonic response of clusters of spherical nanoparticles

P. A. Letnes* and I. Simonsen
Department of Physics, The Norwegian University of Science and Technology (NTNU), NO-7491 Trondheim, Norway

D. L. Mills
Department of Physics and Astronomy, University of California, Irvine, California 92697, USA
(Received 16 November 2010; published 23 February 2011)

The plasmonic response of nanoparticles is exploited in many subfields of science and engineering to enhance optical signals associated with probes of nanoscale and subnanoscale entities. We develop a numerical algorithm based on previous theoretical work that addresses the influence of a substrate on the plasmonic response of collections of nanoparticles of spherical shape. Our method is a real-space approach within the quasistatic limit that can be applied to a wide range of structures. We illustrate the role of the substrate through numerical calculations that explore single nanospheres and nanosphere dimers fabricated from either a Drude model metal or from silver on dielectric substrates and from dielectric spheres on silver substrates.

DOI: 10.1103/PhysRevB.83.075426 PACS number(s): 78.67.Bf

I. INTRODUCTION

Currently there is great interest in the use of the plasmonic response of tailored metallic substrates and other structures for the purpose of enhancing electric fields of laser beams in their near vicinity. Enhancements with an origin in the excitation of collective plasmon modes can increase the field intensity by many orders of magnitude in the near vicinity of diverse systems. This phenomenon was first explored in the context of surface-enhanced Raman scattering (SERS), wherein it was found that the Raman cross section of pyridine adsorbed on electrochemically roughened Ag surfaces can be enhanced by approximately 6 orders of magnitude relative to that realized for pyridine in solution.[1] The field has evolved to the point where the Raman spectrum of single molecules can be detected through the use of plasmon-enhanced Raman probes.[2,3] Plasmonic enhancements can be used not only in the context of Raman spectroscopy, but also, more generally, to enhance the cross section of diverse nonlinear optical processes.[4,5]

In the theoretical literature, one finds numerous studies of the plasmonic response of isolated nanoparticles of diverse shape[6,7] along with metallic arrays of nanoparticles.[8,9] So far as we know, virtually all such discussions explore nanoparticles and their arrays in free space.[10,11] Treatments of the free-space response are appropriate for clusters of nanoparticles in solution, but commonly, one is interested in particles and particle arrays on substrates. Then, an issue is the influence of the nanoparticle-substrate interaction on the plasmonic response of the nanoparticles that reside on it. Papers addressing particle-substrate interactions include the work of Yamaguchi *et al.*,[12] which discussed particles above substrates in the dipole approximation. Work done by Ruppin[13] and by Román-Velázquez *et al.*[14] and Noguez[15] also deal with sphere-substrate interactions but only for a single nanoparticle. Mayergoyz *et al.* have studied the plasmon eigenfrequencies of nanosphere dimers and also cylindrical structures on a substrate.[7] Moreover, a recent study on the plasmonic response of cubical nanoparticle dimers[16] reports on the dimer-substrate interactions in the SERS context.

Since the early 1970s, Bedeaux and Vlieger have conducted numerous theoretical and numerical studies on the effects of particle-substrate and particle-particle interactions.[17] These studies have been concentrated around spherical or spheroidal particles on top of a substrate or *truncated* particles of such shapes on a substrate (used to model a finite contact angle). In a paper based on the formalism of Bedeaux and Vlieger, the particle-substrate interactions were taken into account to high multipolar order, while the particle-particle interactions were only calculated to dipolar or quadrupolar order, since their main concern was systems where the particle coverage is low.[18]

More recently, numerical studies based on Bedeaux and Vlieger's work have been carried out by Lazzari and coworkers for the purpose of *in situ* inversion of experimental optical spectra obtained from growing thin granular metal films.[18–21]

In this paper, we present a description of the influence of a substrate on the plasmonic response of nonperiodic nanosphere arrays; through the use of the Bloch theorem, one may address periodic systems as well. We employ the quasistatic description of the response of the system. This proves adequate for objects whose linear dimensions are small compared to the wavelength of light.[22] In contrast to previous work, we consistently take into account higher-order interactions between the nanospheres.

After we describe the formalism, we turn our attention to calculations that explore the influence of the substrate on the response of nanospheres and nanosphere dimers. Of interest is the discussion of hot-spot regions where, at selected excitation frequencies, one realizes very large field enhancements by virtue of the excitation of collective plasmon modes. For the case of two spheres in free space that are nearly in contact, one realizes a hot spot at the point of closest contact between the spheres.[23,24] In this paper, for a nanosphere dimer near a dielectric substrate, we find moving hot spots. A small change in excitation frequency can cause the hot spot to move from the point of nearest contact between the spheres to the south poles of the spheres—the points on the spheres closest to the substrate. In recent work, two of the authors have discussed moving hot spots in nanosphere clusters.[25]

This paper illustrates the role of the substrate in creating new hot spots. We find that, if a dielectric sphere is in close proximity to a plasmonic active metallic substrate, the region

around the south pole of the dielectric sphere becomes a hot spot. A spatially localized potential well that can trap substrate plasmons is formed just under the dielectric sphere. Also, if a metallic sphere is placed close to a dielectric substrate, we find a collective plasmon localized near the south pole of the sphere. Thus, the interaction of nanospheres and structured arrays of such objects placed on substrates creates new hot spots that can be exploited in diverse nonlinear optical spectral probes of nanoscale and subnanoscale matter.

In this paper, Sec. II is devoted to setting up a formalism that may be applied to any nonperiodic structure of spherical nanoparticles that are located on, or near, a substrate, and Sec. III presents the results of our numerical studies of isolated nanospheres and nanosphere dimers on substrates. Section IV contains concluding remarks.

II. THEORY

Even if the numerical calculations to be performed in this paper will focus on one or two nanoparticles, we will, however, present a more general formalism valid for a cluster of N nanoparticles. For the case of the dimer, the geometry is illustrated in Fig. 1. The substrate is located in the half space $z < 0$, and it is characterized by the dielectric function $\varepsilon_-(\omega)$. The region above the substrate, $z > 0$, is assumed to be a nonabsorbing dielectric characterized by the dielectric function $\varepsilon_+(\omega)$.

We consider a system consisting of N nonoverlapping nanospheres, located at arbitrary positions. For each such sphere, we embed a coordinate system $\mathcal{S}_j$, $j = 1,2,\ldots N$ so that the origin of $\mathcal{S}_j$ is located at the center of sphere j. With each coordinate system $\mathcal{S}_j$, we associate a position vector $\boldsymbol{r}_j = (r_j,\theta_j,\phi_j)$.

Our interest is in nanosphere arrays whose extent is small compared to the wavelength of light, so the electrostatic approximation suffices to describe the electric fields in its vicinity. Under this assumption, the Maxwell equations are equivalent to the Laplace equation. Thus, our task is to solve Laplace's equation for the electrostatic potential ψ,

$$\nabla^2\psi = 0,$$

subject to the appropriate boundary conditions on the surface of each sphere and at the interface between the substrate and the rest of the system. As usual, the electric field is given by[22] $\boldsymbol{E} = -\boldsymbol{\nabla}\psi$.

We will assume that a spatially uniform electric field $\boldsymbol{E}_0$ of angular frequency ω is applied to the system, and we analyze its response to this field. In what follows, all dielectric functions that enter the analysis are the complex dielectric functions appropriate for the frequency ω, although we suppress any explicit reference to ω in what follows. Hence, the electrostatic potential in the half space $z > 0$ can be written as

$$\psi_+(\boldsymbol{r}) = -\boldsymbol{r}\cdot\boldsymbol{E}_0 + \sum_{j=1}^{N}\psi_j(\boldsymbol{r}_j) + \sum_{\bar{j}=1}^{N}\psi_{\bar{j}}(\boldsymbol{r}_{\bar{j}}), \tag{1}$$

where ψ_j is the electrostatic potential produced by the polarization charges in sphere j and $\psi_{\bar{j}}$ is the potential produced by its image, located in the half space $z < 0$. In the substrate ($z < 0$), the electrostatic potential takes the form

$$\psi_-(\boldsymbol{r}) = -\boldsymbol{r}\cdot\boldsymbol{E}_0^T + \sum_{j=1}^{N}\psi_j^T(\boldsymbol{r}_j), \tag{2}$$

where ψ_j^T is the electrostatic potential of sphere j as seen by an observer in the region $z < 0$, and $\boldsymbol{E}_0^T$ is the applied field in the substrate. The various single-sphere potential functions that enter Eqs. (1) and (2) may be expanded in the spherical harmonics. Using the shorthand notation $\sum_{lm} = \sum_{l=0}^{\infty}\sum_{m=-l}^{l}$, we have

$$\psi_j(\boldsymbol{r}_j) = \begin{cases} \sum_{lm} A_{lm}^{(j)} r_j^{-l-1} Y_l^m(\theta_j,\phi_j), & r_j \geqslant a_j, \\ \sum_{lm} B_{lm}^{(j)} r_j^{l} Y_l^m(\theta_j,\phi_j), & r_j < a_j, \end{cases} \tag{3a}$$

$$\psi_{\bar{j}}(\boldsymbol{r}_{\bar{j}}) = \sum_{lm} A_{lm}^{(j,R)} r_{\bar{j}}^{-l-1} Y_l^m(\theta_{\bar{j}},\phi_{\bar{j}}), \tag{3b}$$

and

$$\psi_j^T(\boldsymbol{r}_j) = \textstyle\sum_{lm} A_{lm}^{(j,T)} r_j^{-l-1} Y_l^m(\theta_j,\phi_j), \tag{3c}$$

where the various A_{lm} and B_{lm} are expansion coefficients to be determined and a_j refers to the radius of sphere j. The symbol Y_l^m refers to the spherical harmonic functions as described in Ref. 22. As discussed in Refs. 17 and 19, the coefficients $A_{lm}^{(j,R)}$ and $A_{lm}^{(j,T)}$ are related to $A_{lm}^{(j)}$ through the boundary conditions at the interface $z = 0$. Simple image arguments supply the relation between these quantities. In particular, one finds that[17,19]

$$A_{lm}^{(j,R)} = (-1)^{l+m}\frac{\varepsilon_+ - \varepsilon_-}{\varepsilon_+ + \varepsilon_-}A_{lm}^{(j)}, \tag{4a}$$

and

$$A_{lm}^{(j,T)} = \frac{2\varepsilon_+}{\varepsilon_+ + \varepsilon_-}A_{lm}^{(j)}. \tag{4b}$$

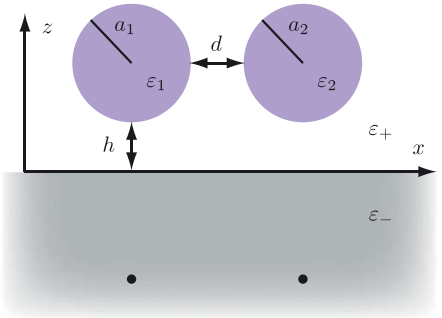

FIG. 1. (Color online) An illustration of the system we consider in this paper, for the case where we have a nanosphere dimer. The substrate occupies the half space $z < 0$, h is the distance between the south poles of the spheres and the substrate, and d is their surface-surface separation. Sphere j of the dimer has dielectric function $\varepsilon_j(\omega)$ and radius a_j. The medium above the substrate has dielectric function $\varepsilon_+(\omega)$ while that of the substrate is $\varepsilon_-(\omega)$. The two black dots schematically represent image multipoles in the substrate seen by an observer in the half space $z > 0$.

Equation (4) ensures that the boundary conditions on the substrate ($z = 0$) are automatically satisfied for any $A_{lm}^{(j)}$. Thus, in what follows, we seek to solve for the coefficients $A_{lm}^{(j)}$ and $B_{lm}^{(j)}$ using the equations that follow from the boundary conditions at the surface of each nanosphere, i.e., where $r_j = a_j$. Through rearrangement of the equations following from the boundary conditions on the sphere surfaces, one can eliminate the coefficients $B_{lm}^{(j)}$. In the Appendix, the linear set of equations determining $A_{lm}^{(j)}$ and $B_{lm}^{(j)}$ are derived [cf. Eq. (A4)].

In Sec. III, we present a series of numerical studies of plasmon resonance phenomena for nanosphere monomers and dimers placed on a substrate. To this end, we must solve Eq. (A4). In order to do so, we truncate the summations in Eq. (3) and also the equation system in Eq. (A4) at $l = L$. The number of unknown coefficients in Eq. (A4) is then $N(L+1)^2 - 1$. We use the same truncation limit for both the nanosphere-nanosphere interactions as well as for the nanosphere-substrate interactions. The nanosphere-substrate interactions include both the interaction of a given nanosphere with its own image and the images of the other nanospheres. Note that all particle-substrate *and* particle-particle interactions consistently have been taken into account (to a given order). In several previous studies, the interaction with the substrate has been taken into account to a high order, while the particle-particle interactions have been accounted for at dipolar or quadrupolar order.[17–21] In Sec. III, we will see that the use of the dipole approximation (retention of only the terms with $l = 1$) in the particle-substrate interaction is very inaccurate from a quantitative point of view save for the case when the nanospheres are quite far from the substrate.

In passing, we note that the formalism presented in this paper can be applied to extend the formalism used in Ref. 9 to incorporate interactions of periodic structures with a substrate. One then has plasmon normal modes characterized by a wave vector $\boldsymbol{k}_\parallel$ parallel to the surface; one encounters only $(L+1)^2$ coefficients in this case because the expansion coefficients of different nanoparticles are linked by the Bloch theorem. The quasistatic limit developed in this paper can be applied to the description of collective excitations whose wave vector is large compared to ω/c with ω as the angular frequency of an excitation of interest and c as the velocity of light in vacuum.

III. RESULTS AND DISCUSSION

In this section, we present a series of studies of the influence of a dielectric substrate on the plasmonic response of isolated nanospheres and nanosphere dimers. In addition, we find hot spots created by plasmonic resonances between dielectric spheres and metallic substrates, as noted before. We will also see that termination of the hierarchy of equations at the dipole ($L = 1$, see Ref. 12) or quadrupole ($L = 2$) order provides a very poor quantitative description of interactions between particles and between the particles and the substrate. We remark that it is evident from earlier studies, which utilize a different methodology,[24] that higher-order harmonics must be included in the description of particle-particle interaction, since the fields associated with hot spots are highly localized around the points of nearest contact. Thus, one must retain spherical harmonics at high order to describe these features.

For the purpose of studying particle-substrate interactions, we first consider nanoparticles modeled by a dielectric function of the Drude form,[22]

$$\varepsilon(\omega) = 1 - \frac{\omega_P^2}{\omega(\omega + \mathrm{i}\gamma)}, \tag{5}$$

where ω_P is the plasma frequency and γ is the inverse of the free carrier relaxation time. For the ambient material, we have chosen vacuum, i.e., $\varepsilon_+ = 1$ and a dielectric substrate of $\varepsilon_- > 0$. The virtue of model studies based on the form of Eq. (5) is that we may choose the relaxation rate γ sufficiently small so that much detail is evident in the calculated results. For the Drude model parameters, we assume $\omega_P = 3$ eV and $\gamma = 0.03$ eV. After our discussion of nanospheres consisting of Drude metal, we present results for geometries incorporating silver (Ag) nanoparticles. Among metals that exhibit plasmonic response in the visible part of the optical spectrum, the damping rate in Ag is modest, and numerous experiments employ Ag-based structures.[26] It should be remarked that the optical response of aluminum (Al) is described very well by the Drude model. Unfortunately, the plasma frequency is very high, close to 15 eV, so the interesting plasmonic resonances in Al-based materials lie well into the ultraviolet. In our view, it would be of great interest to see experimental probes of structures that incorporate Al nanoparticles, with attention to the appropriate spectral range.

One possible indicator of plasmonic activity is the total dipole moment of one of our spherical objects. With $\boldsymbol{p}(\omega)$ being the dipole moment of a nanosphere at angular frequency ω, we define the dimensionless dipole moment as

$$\bar{\boldsymbol{p}} = \frac{\boldsymbol{p}}{a^3 \varepsilon_0 E_0},$$

where a is the radius of the sphere in question and ε_0 is the vacuum permeability. In terms of our expansion coefficients A_{lm}, the three Cartesian components of the dimensionless dipole moment are given by

$$\bar{p}_x = \sqrt{\frac{3}{8\pi}} \frac{A_{1,-1} - A_{1,1}}{a^2},$$

$$\bar{p}_y = -\mathrm{i}\sqrt{\frac{3}{8\pi}} \frac{A_{1,-1} + A_{1,1}}{a^2},$$

and

$$\bar{p}_z = \sqrt{\frac{3}{4\pi}} \frac{A_{10}}{a^2}.$$

Since the dipole moment in general is a complex vector quantity, the quantity we display in the figures that follow is the modulus of the total dipole moment given by

$$\bar{p}(\omega) \equiv |\bar{\boldsymbol{p}}(\omega)| = \sqrt{\bar{\boldsymbol{p}}^\dagger \bar{\boldsymbol{p}}},$$

where $\dagger$ symbolizes the Hermitian transpose. In our studies of the interaction of a single sphere with the substrate, we will display the total dimensionless dipole moment, along with field-enhancement factors for applied fields perpendicular to the substrate ($\boldsymbol{E}_0 \parallel \hat{\boldsymbol{z}}$) as well as parallel to the substrate ($\boldsymbol{E}_0 \parallel \hat{\boldsymbol{x}}$). Moreover, for the dimer illustrated in Fig. 1, we will present results for all three Cartesian components of the applied field.

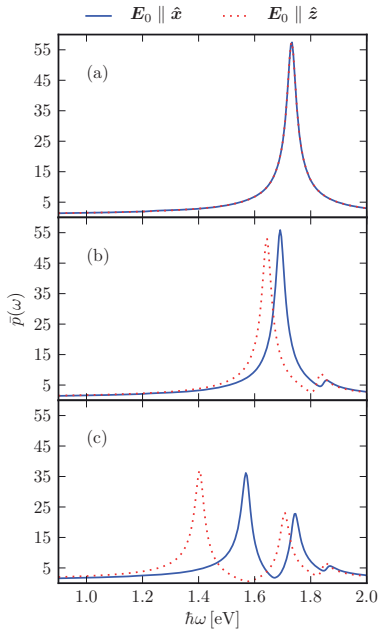

FIG. 2. (Color online) The dimensionless dipole moment $\bar{p}(\omega)$, for a Drude metal particle on a substrate of dielectric function (a) $\varepsilon_- = 1$, (b) $\varepsilon_- = 2$, and (c) $\varepsilon_- = 10$. For the vacuum case, i.e., $\varepsilon_- = 1$, we obtain the Mie result at $\hbar\omega = \hbar\omega_P/\sqrt{3} \approx 1.73$ eV. For all plots, we have $h = 0.05a$, $\omega_P = 3$ eV, $\gamma = 0.03$ eV, and $L = 50$.

A. The Drude monomer and dimer

We begin by considering a single Drude sphere in vacuum ($\varepsilon_+ = 1$) located a distance $h = 0.05a$ above a substrate. In Fig. 2, we present numerical calculations of the dimensionless dipole moment for three choices of the dielectric function of the substrate, $\varepsilon_- = 1$, 2, and 10. The choice $\varepsilon_- = 1$ corresponds physically to the case where no substrate is present. We present results for two choices of the applied field: (i) perpendicular to the substrate (z direction, red dotted curves) and (ii) parallel to the substrate (x direction, blue solid curves). Since the system is invariant with respect to rotation about the z axis, the response to an applied field parallel to the y axis is identical to that shown for x polarization.

In Fig. 2(a), we present the response of the sphere in free space, from which the Mie resonance at the frequency $\hbar\omega_P/\sqrt{3} \approx 1.73$ eV is readily observed. While an isolated Drude metal sphere has a spectrum of multipole modes at angular frequencies $\omega_l = \omega_P\,[l/(2l+1)]^{1/2}$ with $l = 1,2,3,\ldots$, only the dipole mode with $l = 1$ is excited by an applied field whose wavelength is large compared to the radius of the sphere. In the presence of a substrate, higher-order modes may be excited by a spatially uniform applied field, as we will see. These will appear at higher frequencies than the Mie resonance, as suggested by the fact that $\omega_{l+1} > \omega_1$ for $l \geqslant 1$.

When the dielectric function of the substrate is $\varepsilon_- > \varepsilon_+$, the spectral response of the nanosphere is altered significantly. First, for the case of modest dielectric function $\varepsilon_- = 2$, the (former) Mie resonance remains the dominant spectral feature, and it is redshifted by the proximity of the dielectric substrate to the nanosphere [Fig. 2(b)]. A substantial splitting of the modes is observed when the response to a field parallel to the substrate is compared to the response to a field perpendicular to it. We also see activation of a higher-frequency mode. One might be tempted to associate this with excitation of the quadrupolar mode with $l = 2$, but when the sphere is so close to the substrate, classification of the mode by the angular momentum quantum number is no longer accurate since a large number of l modes are mixed together. We require L, the cutoff used in the hierarchy of equations displayed in Eq. (A4), to be on the order of 30 (or more) to obtain converged results.

If the substrate has a large dielectric function ($\varepsilon_- = 10$), then the response of the sphere is modified dramatically relative to the free-space case [Fig. 2(c)]. The splitting of the low-frequency resonances, for parallel and perpendicular excitations, is now very large. For both orientations of the applied field, the oscillator strength of the next highest mode is comparable to the low-frequency (dipole) mode. We also see a third mode in the spectrum, so the symmetry breaking provided by the substrate now asserts itself prominently in the response of the sphere.

The appearance of these higher-order modes can be intuitively understood as follows. When we apply an electric field $\boldsymbol{E}_0$ to a nanosphere, it will generate local evanescent fields. When h is small, some of the evanescent fields are reflected from the substrate, resulting in a nonuniform field around the sphere. This causes the simultaneous excitation of many different l modes, meaning that the notion of discussing modes in multipolar terminology breaks down badly. The cross talk between different l modes is also the reason why we see higher-order modes (e.g., quadrupole modes) in the dipole moment [$\bar{p}(\omega)$] of the spheres.

We now turn our attention to a discussion of the response of a Drude dimer, as shown in Fig. 1. The radii of the two spheres are both assumed to be equal to a. The distance between the spheres is $d = 0.1a$, and they are both placed a distance $h = 0.05a$ above the substrate. In Fig. 3, we depict the dimensionless dipole moment of one of the spheres in a dimer whose axis is parallel to the x axis and, hence, to the substrate.

When the dimer is placed in free space [Fig. 3(a)] and the applied field is perpendicular to the dimer axis, there is one dominant resonance. This is the Mie resonance of the single sphere, slightly blueshifted due to the particle-particle interactions. In addition, a second weak mode shows up at higher frequencies. In contrast, when the dimer is excited by a field parallel to the dimer axis (blue solid curve), we see a sequence of collective modes redshifted by large amounts from the isolated sphere Mie resonance. These results are in agreement with previous work on nanoparticle dimers in free space.[24] As for the case of the single sphere on a substrate, the fields generated from one sphere cause higher-order modes to be excited in the other sphere, and vice versa.

For a substrate with modest dielectric function [$\varepsilon_- = 2$, Fig. 3(b)], we see a splitting between the dominant collective modes excited by a field parallel to $\hat{\boldsymbol{z}}$ (red dotted curve) and that excited by a field parallel to $\hat{\boldsymbol{y}}$ (green dashed curve). This is to be expected since the presence of the substrate will break

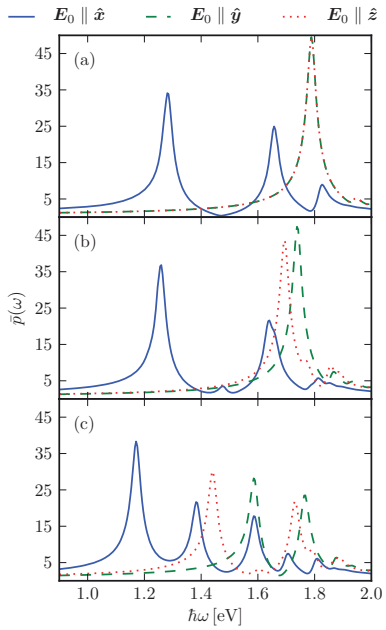

FIG. 3. (Color online) The dimensionless dipole moment $\bar{p}(\omega)$, for one of the particles in a Drude metal dimer, on top of a substrate of dielectric function (a) $\varepsilon_- = 1$, (b) $\varepsilon_- = 2$, and (c) $\varepsilon_- = 10$. For all plots, we have $h = 0.05a$, $d = 0.1a$, $\omega_P = 3$ eV, $\gamma = 0.03$ eV, and $L = 50$.

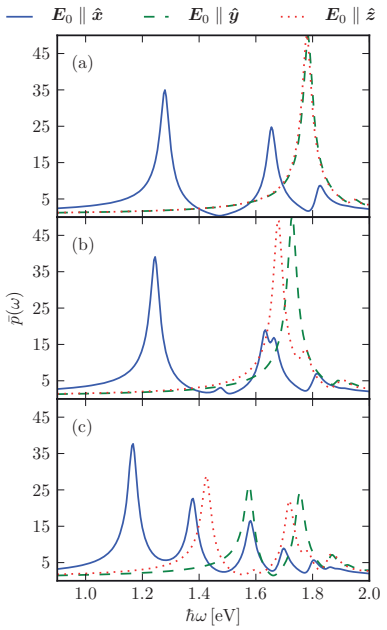

FIG. 4. (Color online) The plots show $\bar{p}(\omega)$ for one of the particles in a Drude metal dimer for (a) $h = 2a$, (b) $h = 0.3a$, and (c) $h = 0.05a$. For all plots, we have $\varepsilon_- = 10$, $d = 0.1a$, $\omega_P = 3$ eV, $\gamma = 0.03$ eV, and $L = 30$.

the rotational symmetry around the x axis. If the dielectric function of the substrate is substantial [$\varepsilon_- = 10$, Fig. 3(c)], we observe dramatic differences between the spectral response for the three directions of the applied field. The shift of the lowest-frequency mode for $\boldsymbol{E}_0 \parallel \hat{\boldsymbol{x}}$ from the Mie resonance of the isolated sphere is particularly dramatic.

These results demonstrate that placing metallic nanosphere dimers over a substrate with a large dielectric function will give rise to substantial field enhancements. Also, strong dipole moment enhancements can be achieved over a very large spectral range compared to that realized for a single isolated nanosphere. Thus, as this example illustrates, the interaction between structured nanoparticle arrays and a substrate of substantial dielectric function can allow one to design objects with a broad plasmonic spectral response.

Figure 4 shows how the response of the dimer depends on the distance h above the substrate. A substrate dielectric function $\varepsilon_- = 10$ was assumed in order to emphasize the influence of the substrate on the response of the dimer. In Fig. 4(a), where $h = 2a$, the spectral response is very close to that of the isolated dimer, shown in Fig. 3(a). We see clear interaction effects with the substrate when $h = 0.3a$ [Fig. 4(b)], but it remains true that the spectrum is qualitatively similar to that of the free dimer. The dimer has to be close to the substrate for the interaction effects to modify the spectrum even for the large substrate dielectric function used in these calculations [Fig. 4(c)].

We pause for a moment to comment on issues of convergence. It is common to employ the dipole approximation to describe intersphere interactions and interactions of nanoparticles with substrates using the image method.[12] In Fig. 5, we present how the position of the lowest-energy collective mode for the case $\boldsymbol{E}_0 \parallel \hat{\boldsymbol{z}}$ depends on L, which determines the number of unknown A_{lm} coefficients in Eq. (A4). The frequently used dipole approximation corresponds to $L = 1$, and from Fig. 5, one observes that it is inaccurate even when the dimer is far above the substrate ($h = 2a$) and becomes gradually worse as h is decreased. The cutoff L must be on the order of 30 to obtain converged results for the parameter ranges explored in this paper. One may appreciate the reason for this from earlier work.[24] When two spheres are quite close to each other, one encounters collective modes wherein the fields are concentrated in a small angular range near the points of closest contact. Similarly, when one or more nanospheres are very close to a dielectric substrate, one encounters collective modes localized around the south pole of the spheres—the points closest to the substrate. One requires large values of the cutoff L if one wishes to describe such modes accurately. Notice, by the way, that the mode frequency is significantly redshifted when the dimer comes very close to touching the substrate. In passing, we note that convergent results do not guarantee correctness of the calculated potentials. In order to do so, one has to explicitly make sure that the boundary conditions are satisfied for the required accuracy at all points on all interfaces.[19]

In Fig. 6, we examine the nature of the enhanced fields in the Drude dimer at the two points indicated in the inset. Again, we

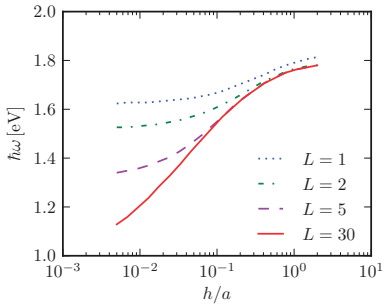

FIG. 5. (Color online) Position of the lowest-energy resonance as a function of h, in the case where $\boldsymbol{E}_0 \parallel \hat{\boldsymbol{z}}$. The blue dotted curve shows the result when the calculation is done in the dipole approximation (i.e., $L = 1$), while the red solid curve $L = 30$ shows the converged results. For all cases, a Drude dimer with $d = 0.1a$ was assumed, and the substrate dielectric function was $\varepsilon_- = 10$.

have assumed $d = 0.1a$ and $h = 0.05a$ in these calculations. For most of the spectrum, the largest field enhancement is found at point 2, the hot spot where the two spheres nearly touch. Notice, however, that we also have very large field enhancements between the south pole of the spheres and the dielectric substrate, in particular, at 1.35 eV [see Figs. 6 and 7(a)]. In our view, the region where the dielectric substrate is very close to the bottom of the sphere acts like an effective potential well that traps surface plasmons at the south pole. The surface plasmons sense the presence of the dielectric through the fields associated with them in the region outside the sphere.

From Fig. 6, we can see that points 1 and 2 are hot simultaneously at roughly the same frequency. However, as one scans through a given resonance peak, near $\hbar\omega = 1.4$ eV in Fig. 6, the hot spot moves from point 1 to point 2 and conversely, depending on the precise value of the frequency. Thus, we have another example of the phenomenon of the moving hot spots discussed in a recent publication.[25] We illustrate this behavior in Fig. 7, where we plot $|\boldsymbol{E}|/|\boldsymbol{E}_0|$ on a contour map.[27] A small energy shift of 0.1 eV is enough to change the shape of the field enhancement considerably and move the hot spot from point 1 to point 2.

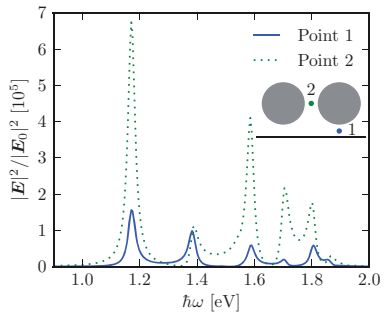

FIG. 6. (Color online) The square of the electric field $|\boldsymbol{E}|^2/|\boldsymbol{E}_0|^2$, at point 1 (blue solid curve) and point 2 (green dotted curve) as a function of frequency, for the Drude dimer. The results are for the case where $\boldsymbol{E}_0 \parallel \hat{\boldsymbol{x}}$, and the substrate dielectric function is $\varepsilon_- = 10$. The other parameters are the same as in Fig. 3.

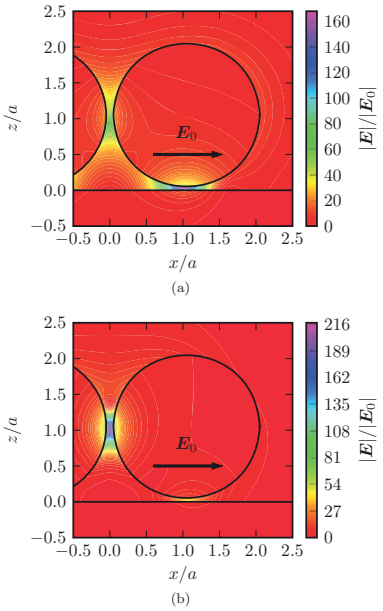

FIG. 7. (Color online) The field enhancement $|\boldsymbol{E}|/|\boldsymbol{E}_0|$ in the xz plane. At (a) $\hbar\omega = 1.35$ eV, the highest field enhancement is found between the sphere and the substrate; at (b) $\hbar\omega = 1.45$ eV, the highest field enhancement is found on the line connecting the two spheres. As shown in the figure, $\boldsymbol{E}_0 \parallel \hat{\boldsymbol{x}}$. The system parameters are $\varepsilon_- = 10$, $h = 0.05a$, $d = 0.1a$, and $L = 50$. Of particular interest is the area between the two lowest-frequency peaks, where the location of maximum field enhancement flips between the two points indicated.

B. Ag monomers and dimers

The Drude model discussed in Sec. III A is useful to examine, since one may model metals in which the plasmons are damped very lightly. Thus, one can explore detailed structure in the response of the model system. In practice, however, interest resides in realistic metals that display plasmonic response in the visible. In this respect, silver (Ag) and gold (Au) are the two metals most studied experimentally. While Au is indeed plasmon active, the plasmons in this material are, in fact, rather heavily damped. Ag is a much better material in principle, even though in experiments oxide can form on its surface.

This section is devoted to studies of the plasmon resonance properties of Ag monomers and dimers. Figure 8 shows calculations of the reduced dipole moment for a single Ag nanosphere placed a distance $h = 0.05a$ over a dielectric substrate. For a free-standing Ag sphere in vacuum, the Mie resonance at $\hbar\omega = 3.5$ eV is readily observed [Fig. 8(a)]. The response of the sphere is modest for $\varepsilon_- = 2$ [Fig. 8(b)]. However, when $\varepsilon_- = 10$ [Fig. 8(c)], we see a substantial splitting of the main resonance and activation of higher-frequency modes occur.

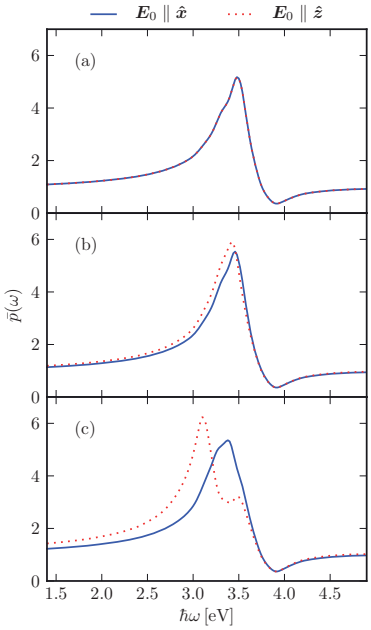

FIG. 8. (Color online) The dimensionless dipole moment for an Ag sphere placed a distance $h = 0.05a$ above a dielectric substrate of (a) $\varepsilon_- = 1$, (b) $\varepsilon_- = 2$, and (c) $\varepsilon_- = 10$. The equation system was truncated at $L = 50$.

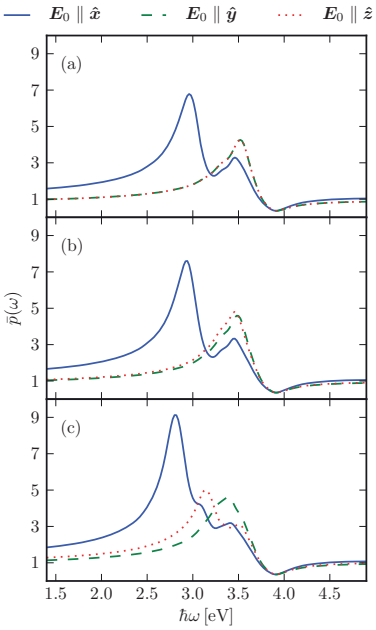

FIG. 9. (Color online) The response for an Ag dimer close to a substrate, as described by the dimensionless dipole moment of one of the spheres. As in previous cases, $d = 0.1a$, $h = 0.05a$, and $L = 50$ were used. (a) $\varepsilon_- = 1$, (b) $\varepsilon_- = 2$, (c) $\varepsilon_- = 10$.

In Fig. 9, we show the response of an Ag dimer with its axis parallel to the substrate. As previously, we have assumed $h = 0.05a$ and $d = 0.1a$. The strong interaction between the two spheres of a free-standing dimer in vacuum can be seen from Fig. 9(a) by noting the pronounced difference in response to an applied field parallel ($\boldsymbol{E}_0 \parallel \hat{\boldsymbol{x}}$) or perpendicular ($\boldsymbol{E}_0 \parallel \hat{\boldsymbol{y}}$ or $\boldsymbol{E}_0 \parallel \hat{\boldsymbol{z}}$) to the dimer axis. At least from the perspective of the dipole moment of each sphere, the influence of the substrate is not significant for $\varepsilon_- = 2$ [Fig. 9(b)], but we see substantial effects for the larger dielectric function $\varepsilon_- = 10$ [Fig. 9(c)].

While the dipole moment of the Ag spheres shows substrate effects to be weaker than those of the corresponding Drude monomer and dimer, the field-enhancement effects are still substantial. When the spheres are either close to each other and/or close to the substrate, the resonances are highly localized in space and form so-called hot spots. This is illustrated by Fig. 10, which shows the enhancement in the electric field intensity ($|\boldsymbol{E}|^2/|\boldsymbol{E}_0|^2$) for an Ag dimer. Hence, one can have local regions where the fields are strongly enhanced while their effect on the total dipole moment of the sphere is more modest.

Regarding the field enhancement in the Ag dimer, depicted in Fig. 10, we see considerable enhancement between the sphere and the substrate. This enhancement is caused by the proximity of the sphere to the dielectric substrate that creates a potential well where surface plasmons can be trapped near the south pole of the sphere. On resonance, the enhancement in the square of the field is close to 5×10^3 [Fig. 10]. If one has SERS in mind, where the cross section is enhanced by roughly the fourth power of the field, then in this case, the Raman cross section would be enhanced by 25×10^6. Thus, the influence of the dielectric substrate on the enhanced fields realized for the dimer is very substantial. Although we observed full reversal of hot-spot positions for a dimer made from Drude metal, it appears that the larger attenuation of silver $\{\mathrm{Im}[\varepsilon_j(\omega)]\}$ prohibits this phenomena in the Ag dimer. Hence, the dominant hot spot is for all frequencies of the incident light located at point 2 in the gap between the two spheres.

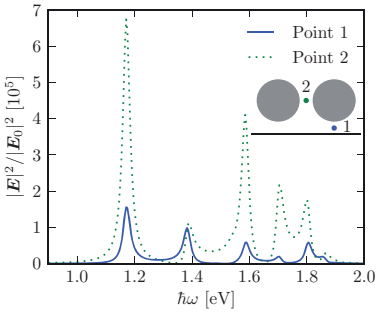

FIG. 10. (Color online) Intensity enhancement $|\boldsymbol{E}|^2/|\boldsymbol{E}_0|^2$, as a function of frequency of the applied field at points 1 and 2 for the Ag dimer on a substrate of dielectric function $\varepsilon_- = 10$. The remaining parameters are the same as in Fig. 9.

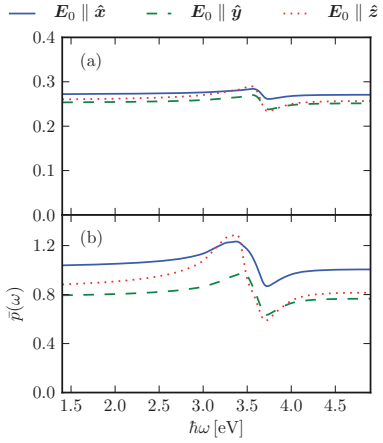

FIG. 11. (Color online) The dimensionless dipole moment of a member of a dielectric dimer placed in close proximity to an Ag surface. The dielectric functions for the two spheres forming the dimer are both (a) $\varepsilon_j = 2$ and (b) $\varepsilon_j = 10$. In both cases, we have $d = 0.1a$, $h = 0.05a$, and $L = 50$.

C. Dielectric dimer on an Ag substrate

In the literature, primary attention is directed toward nanoscale objects fabricated from plasmon-active metals. We find that dielectric particles create localized evanescent fields that stimulate the formation of localized plasmons in a nearby metallic substrate. These surface plasmons are not excited on a flat metallic surface. In this section, we consider a dielectric dimer with a frequency-independent, real, and positive dielectric function ε_j placed close to an Ag surface.

Figure 11 depicts the dimensionless dipole moment of the dielectric dimers placed very close to an Ag substrate. As before, the separation between the two spheres is $d = 0.1a$, and the height above the substrate is $h = 0.05a$. Dipole activity in the dielectric sphere is observed in the frequency range near the surface plasmon resonance of the Ag surface. Since the dielectric function of the sphere (ε_j) is frequency independent, this plasmonic activity has its origin in the Ag substrate. As expected, the effect is enhanced when the dielectric function of the spheres ε_j is increased [Fig. 11].

Figure 12 illustrates the frequency dependence of the intensity enhancement at a position between the dielectric spheres and the substrate (point 1) and between the spheres (point 2). Between the spheres (point 2), the plasmonic response of the substrate plays only a minor role in the intensity enhancement, whereas, just below the south pole of the spheres, the plasmonic activity plays a more important role, producing higher intensity enhancement for a narrow part of the spectrum. The proximity of the dielectric spheres to the substrate converts the incoming plane wave to an evanescent wave that excites surface plasmons in the Ag substrate. The consequence is that substantial intensity enhancements appear below the nanospheres near the surface plasmon frequency of the Ag surface. The physics is quite similar to the formation of a hot spot between a metal sphere and a dielectric substrate.

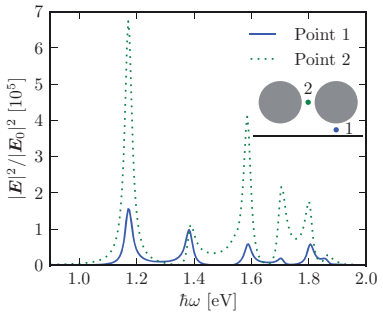

FIG. 12. (Color online) Intensity enhancements at two selected points for a dielectric dimer placed in the near vicinity of an Ag surface. The dielectric function of the spheres is $\varepsilon = 10$, and other parameters are the same as in Fig. 11.

The structure of the field enhancement near the plasmon resonance is shown in detail in Fig. 13. This figure is qualitatively similar to Fig. 7. Again, we are faced with the moving hot-spot phenomenon, since the hot spot moves from between the spheres to below the spheres as the frequency of the incident light changes.

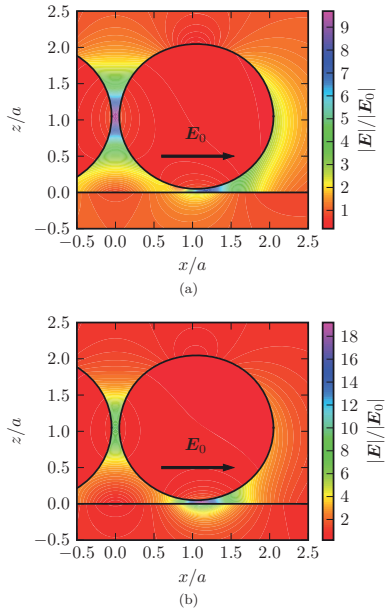

FIG. 13. (Color online) The field enhancement $|\boldsymbol{E}|/|\boldsymbol{E}_0|$ in the xz plane for a dielectric dimer above an Ag substrate. At (a) $\hbar\omega = 3.02$ eV, the highest field enhancement is found between the spheres; at (b) $\hbar\omega = 3.39$ eV, the highest field enhancement is found on the line connecting the two spheres. As shown in the figure, $\boldsymbol{E}_0 \parallel \hat{\boldsymbol{x}}$. The parameters are $\varepsilon_j = 10$, $h = 0.05a$, $d = 0.1a$, and $L = 50$.

IV. CONCLUDING REMARKS

We have formulated the theory of the interaction of nonperiodic nanosphere arrays with a substrate, and for the case of monomers and dimers, we have provided numerical studies of electric dipole moments induced by a uniform driving field and field enhancement generated by excitation of plasmon resonances. While the focus usually is placed on the interaction of metallic nanoscale objects with metallic substrates or surroundings, our emphasis has been on the interaction between metallic and dielectric materials: metallic nanoparticles on dielectric substrates or dielectric nanoparticles on metallic substrates. Such systems are, in our view, better suited for experimental examination.

For both these configurations, we find hot spots (i.e., local regions of high intensity) that are localized between the south pole of the nanosphere and the substrate. The physical origin of this behavior is an effective potential well created by the dielectric that traps and localizes plasmons in the nearby metallic component. Consider, for example, a semi-infinite slab of a model metal described by the Drude model, Eq. (5). Let the metal lie in the half space $z < 0$, and let the half space $z > 0$ be vacuum. The surface supports surface plasmons, and in electrostatic theory, these have frequency $\omega_P/\sqrt{2}$ independent of the wave vector. Instead, suppose we fill the upper half space $z > 0$ with a dielectric material whose dielectric constant is $\varepsilon_+ > 1$. This lowers the frequency of surface plasmons on the metal surface to $\omega_P(1+\varepsilon_+)^{-1/2}$. Then, if we imagine that the dielectric covers only a finite area on the metallic surface, clearly an attractive potential well is formed that can trap surface plasmons bound to the region where the dielectric is found. The frequency of these modes lies below the frequency band associated with those on the metal/vacuum interface. In our studies, we have a rather different geometry. For instance, in one configuration, we explored a dielectric sphere that is placed just a bit above the metallic substrate. The surface plasmons on the metal surface sense the presence of the dielectric through their evanescent field that extends above the metal surface. We then find plasmon modes localized in the near vicinity of the south pole of the sphere. In the case of dimers, of interest is the moving hot-spot phenomenon illustrated in Fig. 7. Small changes in excitation frequency result in a hot spot that moves from one point in the structure to another. An earlier discussion provided an example of this behavior in a rather different structure.[25]

The hot spots localized between metallic spheres and dielectric substrates and between dielectric spheres and metallic substrates, suggests that strongly enhanced nonlinear optical studies may be carried out on diverse systems, not just those where all constituents are plasmon-active metals. It would be of interest to explore field enhancements not just for spheres placed near flat substrates, but for other nanoscale objects of diverse shape as well. It should be possible to engineer structures in which large field enhancements are realized that can be exploited to study, for instance, adsorbates on insulating surfaces.

ACKNOWLEDGMENTS

We used the freely available software archive SHTOOLS authored by Mark Wieczorek (available at http://www.ipgp.fr/~wieczor/SHTOOLS/SHTOOLS.html) to evaluate the associated Legendre functions.

P.A.L. and I.S. would like to thank the Department of Physics and Astronomy, University of California at Irvine for its kind hospitality. P.A.L. would like to thank Ping Chu and Tor Nordam for interesting discussions. He would also like to thank NTH-fondet for its support of his research. The research of D.L.M. has been supported by the U. S. National Science Foundation, through Grant No. CHE-0533162. I.S. acknowledges the support from the Research Council of Norway under the program Småforsk and the NTNU Mobility program.

APPENDIX: CONSTRUCTION OF THE EQUATION SYSTEM

The expression for the electrostatic potential $\psi(\boldsymbol{r})$ is shown in Eqs. (1) and (3). This expansion is of no use before one has determined the expansion coefficients $A_{lm}^{(j)}$ and $B_{lm}^{(j)}$. To do so, we combine the series expansion of ψ and require the fulfillment of the boundary conditions at the surface of the spheres, i.e., the continuity of ψ and $\varepsilon\,\partial_n\psi$ over any interface (where $\partial_n = \hat{\boldsymbol{n}}\cdot\nabla$ denotes the normal derivative).[22] Note that the boundary conditions at the interface at $z = 0$ are already fulfilled through Eq. (4). For instance, we may consider continuity of the electrostatic potential at the surface of sphere j. This gives the condition

$$\lim_{r_j\to a_j^-}\psi_j(\boldsymbol{r}_j) = \lim_{r_j\to a_j^+}\left\{-\boldsymbol{r}\cdot\boldsymbol{E}_0 + \sum_{i=1}^{N}\psi_i(\boldsymbol{r}_i) + \sum_{i=1}^{N}\psi_{\bar{i}}(\boldsymbol{r}_i)\right\}, \quad \text{(A1)}$$

where the notation $a_j^{\pm}$ means $a_j \pm \eta$, where η is infinitesimally small and positive. For this condition to be useful, and similarly, for the equation following from the continuity of the normal components of the displacement field $\boldsymbol{D} = -\varepsilon\varepsilon_0\nabla\psi$, we need to express the potentials ψ_i and $\psi_{\bar{i}}$ for $i \neq j$ in terms of the coordinate system $\mathcal{S}_j$ centered on sphere j. One can do this by using an identity employed by Bedeaux and Vlieger.[17] This reads

$$r_i^{-l_i-1}Y_{l_i}^{m_i}(\theta_i,\phi_i) = \sum_{l_j=0}^{\infty}\sum_{m_j=-l_j}^{l_j} H(l_j,m_j,|l_i,m_i) \times \frac{Y_{l_i+l_j}^{m_i-m_j}(\theta_{ij},\phi_{ij})}{R_{ij}^{l_j+l_i+1}} r_j^{l_j}Y_{l_j}^{m_j}(\theta_j,\phi_j), \quad \text{(A2)}$$

where $\boldsymbol{R}_{ij}$ is the vector between the center of the sphere i and j, and θ_{ij} and ϕ_{ij} are the polar and azimuthal angles, respectively, which describe the direction of $\boldsymbol{R}_{ij}$. In writing Eq. (A2), we have used

$$H(l_j,m_j,|l_i,m_i) = \sqrt{4\pi}(-1)^{l_i+m_j} \times \left[\frac{2l_i+1}{(2l_j+1)(2l+1)}\right]^{1/2} \times \left[\binom{l+m}{l_i+m_i}\binom{l-m}{l_j+m_j}\right]^{1/2}, \quad \text{(A3)}$$

where $l = l_j + l_i$ and $m = m_i - m_j$. Moreover, the notation $\binom{a}{b}$ denotes the binomial coefficient. The expansion described by Eqs. (A2) and (A3) can also be applied to the image multipoles located in the substrate ($z < 0$).

We now have the electrostatic potential on each side of the surface of sphere j expressed in terms of the coordinates of system $\mathcal{S}_j$. One may generate a system of equations for the unknown amplitudes by equating the coefficients of $Y_{l_j}^{m_j}(\theta_j,\phi_j)$. When Eq. (A1) is combined with the condition that the normal components of the electric displacement field $\boldsymbol{D}$ should be continuous across the surface of sphere j, it is possible to eliminate the coefficients $B_{lm}^{(j)}$ and to generate a linear system of equations that involves only $A_{lm}^{(j)}$. When this is done, the following linear system of equations results:

$$\begin{aligned} -b_{1m_j}\delta_{1,l_j} = A_{l_jm_j}^{(j)} \frac{l_j\varepsilon_j + \varepsilon_+(l_j+1)}{l_j(\varepsilon_j - \varepsilon_+)} a_j^{-2l_j-1} \\ - \sum_{l_j,m_j} A_{l_im_i}^{(j)} H(l_j,m_j|l_i,m_i) \frac{Y_{l_i+l_j}^{m_i-m_j}(\theta_{ij},\phi_{ij})}{R_{ij}^{l_j+l_i+1}} \\ + \sum_{i\neq j}\sum_{l_i,m_i} A_{l_im_i}^{(i)} H(l_j,m_j|l_i,m_i) \Bigg[\frac{Y_{l_i+l_j}^{m_i-m_j}(\theta_{ij},\phi_{ij})}{R_{ij}^{l_j+l_i+1}} \\ + (-1)^{l_i+m_i}\beta \frac{Y_{l_i+l_j}^{m_i-m_j}(\theta_{\tilde{i}j},\phi_{\tilde{i}j})}{R_{\tilde{i}j}^{l_j+l_i+1}} \Bigg], \end{aligned} \tag{A4}$$

where $\beta = (\varepsilon_+ - \varepsilon_-)/(\varepsilon_+ + \varepsilon_-)$ and $l_j = 1,2,3,\ldots,L$ and $m_j = 0, \pm 1, \pm 2, \ldots, \pm l_j$. The coefficients b_{lm} are the expansion coefficients of the applied field $\boldsymbol{E}_0$ in terms of the spherical harmonics. The nonzero b_{lm} coefficients (in the case of uniform $\boldsymbol{E}_0$) are given by[17,19]

$$b_{10} = -E_0\sqrt{\frac{4\pi}{3}}\cos\theta_0, \tag{A5a}$$

$$b_{1\pm1} = \pm E_0\sqrt{\frac{2\pi}{3}}\sin\theta_0 e^{\mp i\phi_0}, \tag{A5b}$$

where θ_0 is the angle between the external field and the positive z axis and ϕ_0 is the azimuthal angle that describes the angle between the projection of the external field onto the xy plane and the positive x axis. As the Laplace equation is linear, we only need to solve for three different directions of $\boldsymbol{E}_0$ ($\boldsymbol{E}_0$ parallel to $\hat{\boldsymbol{x}}$, $\hat{\boldsymbol{y}}$, and $\hat{\boldsymbol{z}}$). The response to an applied field pointing in any other direction can be constructed through superposition of these three cases.

Equation (A4) gives us $N(L+1)^2 - 1$ linear equations in the expansion coefficients $A_{lm}^{(j)}$, and we have $N(L+1)^2$ unknowns. The final equation results from the continuity of the normal component of $\boldsymbol{D}$ at the spherical interfaces. Taking the normal (i.e., radial) derivative of the B_{00} term, we see that this term vanishes [$\partial_{r_j} B_{00}\, Y_0^0(\theta_j,\phi_j) = 0$]. This means that $A_{00} = 0$, related to the fact that the nanoparticles are assumed to carry no charge. Hence, the equation system is closed, and we can expect to find a unique solution.

Finally, the resonances for an isolated sphere in a homogeneous background of dielectric function ε_+ can be obtained from Eq. (A4). By neglecting all contributions from other particles and image multipoles, i.e., to keep only the first term on the right-hand side of Eq. (A4), one is essentially left with the isolated sphere case. Under this assumption, the resulting equation can readily be solved to give

$$A_{lm} \propto \frac{1}{l\varepsilon + \varepsilon_+(l+1)},$$

where ε is the dielectric function of the sphere. Hence, the resonance positions are determined by the zeros of the real part of the denominator of A_{lm}:

$$\mathrm{Re}\,[l\varepsilon + \varepsilon_+(l+1)] = 0.$$

If we assume for ε the Drude model with $\gamma = 0$ ($\varepsilon = 1 - \omega_P^2/\omega^2$), which in our case, is a good approximation, we get the following resonance frequencies for the isolated sphere:

$$\omega_l = \omega_P\sqrt{\frac{l}{2l+1}}.$$

For systems containing more than a single isolated sphere, such as the ones discussed in this paper, these resonance frequencies are typically modified due to particle-particle or particle-substrate interactions.

*paul.anton.letnes@gmail.com

[1] M. Moskovits, Rev. Mod. Phys. **57**, 783 (1985).
[2] S. Nie and S. R. Emory, Science **275**, 1102 (1997).
[3] J. Jiang, K. Bosnick, M. Maillard, and L. Brus, J. Phys. Chem. B **107**, 9964 (2003).
[4] D. S. Chemla, J. P. Heritage, P. F. Liao, and E. D. Isaacs, Phys. Rev. B **27**, 4553 (1983).
[5] T. Ichimura, N. Hayazawa, Y. Inouye, and S. Kawata, J. Raman Spectrosc. **34**, 651 (2003).
[6] D. R. Fredkin and I. D. Mayergoyz, Phys. Rev. Lett. **91**, 253902 (2003).
[7] I. D. Mayergoyz, D. R. Fredkin, and Z. Zhang, Phys. Rev. B **72**, 155412 (2005).
[8] S. Zou and G. C. Schatz, Nanotechnology **17**, 2813 (2006).
[9] R. Arias and D. L. Mills, Phys. Rev. B **68**, 245420 (2003).
[10] G. Bachelier, I. Russier-Antoine, E. Benichou, C. Jonin, N. Del Fatti, F. Vallée, and P.-F. Brevet, Phys. Rev. Lett. **101**, 197401 (2008).
[11] J. M. Gérardy and M. Ausloos, Phys. Rev. B **22**, 4950 (1980).
[12] T. Yamaguchi, S. Yoshida, and A. Kinbara, Thin Solid Films **21**, 173 (1974).
[13] R. Ruppin, Surf. Sci. **127**, 108 (1983).
[14] C. E. Román-Velázquez, C. Noguez, and R. G. Barrera, Phys. Rev. B **61**, 10427 (2000).
[15] C. Noguez, J. Phys. Chem. C **111**, 3806 (2007).
[16] S. Y. Lee, L. Hung, G. S. Lang, J. E. Cornett, I. D. Mayergoyz, and O. Rabin, ACS Nano **4**, 5763 (2010).
[17] D. Bedeaux and J. Vlieger, *Optical Properties of Surfaces* (Imperial College Press, London, 2004).

[18]R. Lazzari, I. Simonsen, and J. Jupille, Europhys. Lett. **61**, 541 (2003).
[19]I. Simonsen, R. Lazzari, J. Jupille, and S. Roux, Phys. Rev. B **61**, 7722 (2000).
[20]R. Lazzari, S. Roux, I. Simonsen, J. Jupille, D. Bedeaux, and J. Vlieger, Phys. Rev. B **65**, 235424 (2002).
[21]R. Lazzari and I. Simonsen, Thin Solid Films **419**, 124 (2002).
[22]J. D. Jackson, *Classical Electrodynamics*, 3rd ed. (Wiley, New York, 1999).
[23]P. Chu and D. L. Mills, Phys. Rev. Lett. **99**, 127401 (2007).
[24]P. Chu and D. L. Mills, Phys. Rev. B **77**, 045416 (2008).
[25]P. A. Letnes and I. Simonsen, Phys. Status Solidi B **247**, 2084 (2010).
[26]H. Tamaru, H. Kuwata, H. T. Miyazaki, and K. Miyano, Appl. Phys. Lett. **80**, 1826 (2002).
[27]Note that we do not plot the square of $|\boldsymbol{E}|/|\boldsymbol{E}_0|$, as the enhancement then becomes very large, in which case, it is difficult to synthesize a nicely color-coded figure.

P. A. Letnes, I. Simonsen, and D. L. Mills. "Erratum: Substrate influence on the plasmonic response of clusters of spherical nanoparticles [Phys. Rev. B 83, 075426 (2011)]", 149901. *Phys. Rev. B* 85 (14 Apr. 2012)

Paper 4

PHYSICAL REVIEW B **85**, 149901(E) (2012)

Erratum: Substrate influence on the plasmonic response of clusters of spherical nanoparticles [Phys. Rev. B 83, 075426 (2011)]

P. A. Letnes,* I. Simonsen,† and D. L. Mills

(Received 12 April 2012; published 23 April 2012)

DOI: 10.1103/PhysRevB.85.149901 PACS number(s): 78.67.Bf, 99.10.Cd

A technical mistake in our original paper led to Fig. 6 being duplicated as Fig. 10 and Fig. 12. For this reason, we publish revised versions of Fig. 10 and Fig. 12 in this erratum. The captions in the original paper are reproduced without modification for the reader's convenience.

To the best of our knowledge, the original paper is otherwise technically correct.

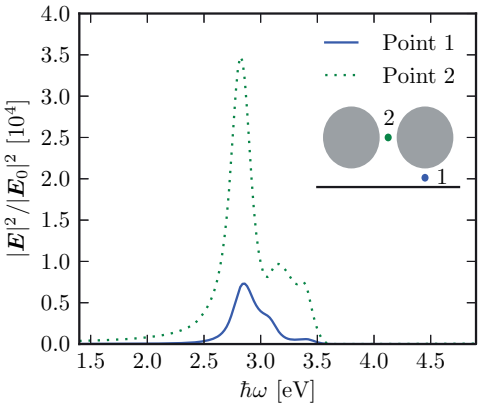

FIG. 10. (Color online) Intensity enhancement, $|\boldsymbol{E}|^2/|\boldsymbol{E}_0|^2$, as a function of frequency of the applied field at point 1 and point 2, for the Ag dimer on a substrate of dielectric function $\varepsilon_- = 10$. The remaining parameters are the same as in Fig. 9.

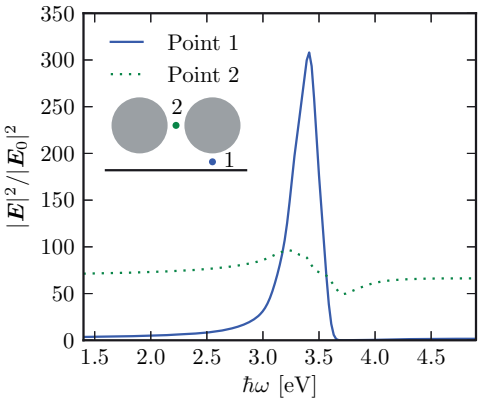

FIG. 12. (Color online) Intensity enhancements at two selected points for a dielectric dimer placed in the near vicinity of an Ag surface. The dielectric function of the spheres is $\varepsilon = 10$, and other parameters are the same as in Fig. 11.

*paul.anton.letnes@gmail.com
†Ingve.Simonsen@ntnu.no

P. A. Letnes, I. S. Nerbø, L. M. S. Aas, P. G. Ellingsen, and M. Kildemo. "Genetic invention of fast and optimal broad-band Stokes / Mueller polarimeter designs". In: *Proceedings of the 13th annual conference companion on genetic and evolutionary computation*. Ed. by N. Krasnogor. Dublin, Ireland: ACM, 2011, pp. 237–238

Paper 5

Is not included due to copyright

T. A. Leskova, P. A. Letnes, A. A. Maradudin, T. Nordam, and I. Simonsen. "The scattering of light from two-dimensional randomly rough surfaces". *Proc. SPIE* 8172 (2011)

Paper 6

Keynote Paper

The scattering of light from two-dimensional randomly rough surfaces

T.A. Leskova[a], P.A. Letnes[b], A.A. Maradudin[a], T. Nordam[b] and I. Simonsen[b]

[a]Department of Physics and Astronomy and Institute for Surface and Interface Science
University of California, Irvine CA 92697, U.S.A.
[b]Department of Physics, Norwegian University of Science and Technology (NTNU)
NO-7491 Trondheim, Norway

ABSTRACT

We present results, obtained by rigorous computational approaches, for light of p- and s-polarization scattered from two-dimensional, randomly rough, perfectly conducting, lossy metallic, and dielectric surfaces. The perfectly conducting surfaces we study are characterized by an isotropic power spectrum of the surface roughness and by an anisotropic power spectrum. The mean differential reflection coefficient and the full angular distribution of the intensity of the scattered light are calculated for the perfectly conducting and metal surfaces. From the latter calculations it is found that the computational approach used in these calculations conserves energy in the scattering from a perfectly conducting and from a lossless metal surface with an error that is smaller than 0.5%. Finally, we presents results obtained by a numerical, nonperturbative, solution of the reduced Rayleigh equation for the scattering of p- and s-polarized light from two-dimensional randomly rough, metallic and dielectric surfaces. We show that the results for the metallic surface are in good agreement with results for the same metallic surface obtained by the rigorous computational approach.

Keywords: randomly rough surfaces; mean differential reflection coefficient; impedance boundary condition; reduced Rayleigh equation; Müller integral equations; Franz formulas; Stratton–Chu equation; scattering

1. INTRODUCTION

Despite the significant advances that have been made in the last 15 years or so in approaches to the calculation of the scattering of light from two-dimensional randomly rough perfectly conducting[1–8] and penetrable[6,9–14] surfaces, such calculations remain computationally intensive, and need further improvements in the methods used in carrying them out. In this paper we review some of our recent work devoted to this problem, and present some new results. The emphasis will be on the results obtained and their significance, but the methods by which the results were obtained will be sketched out.

The physical system we consider in this paper consists of vacuum in the region $x_3 > \zeta(\mathbf{x}_\parallel)$, where $\mathbf{x}_\parallel = (x_1, x_2, 0)$, and the scattering medium in the region $x_3 < \zeta(\mathbf{x}_\parallel)$ (Fig. 1). The latter will be a perfect conductor, a metal, or a dielectric. The surface profile function $\zeta(\mathbf{x}_\parallel)$ is assumed to be a single-valued function of $\mathbf{x}_\parallel$ that is at least twice differentiable with respect to x_1 and x_2, and constitutes a stationary, zero-mean, Gaussian random process defined by $\left\langle \zeta(\mathbf{x}_\parallel)\zeta(\mathbf{x}'_\parallel)\right\rangle = \delta^2 W(\mathbf{x}_\parallel - \mathbf{x}'_\parallel)$. The angle brackets here denote an average over the ensemble of realizations of the surface profile function, and $\delta = \left\langle \zeta^2(\mathbf{x}_\parallel)\right\rangle^{\frac{1}{2}}$ is the rms height of the surface. The power spectrum of the surface roughness is defined by

$$g(\mathbf{k}_\parallel) \;=\; \int \mathrm{d}^2 x_\parallel \, W(\mathbf{x}_\parallel) \exp\left(-\mathrm{i}\mathbf{k}_\parallel \cdot \mathbf{x}_\parallel\right), \tag{1}$$

where $\mathbf{k}_\parallel = (k_1, k_2, 0)$. Each realization of the surface profile function is generated numerically by a two-dimensional version of the filtering method used in [15], which is based on the power spectrum (1).

This paper is organized as follows. Scattering from two-dimensional randomly rough perfectly conducting surfaces will be discussed in Section 2, both when the surface roughness is characterized by an an isotropic power spectrum and when it is characterized by an anisotropic power spectrum. In Section 3 scattering from a

Optical Complex Systems: OCS11, edited by Gérard Berginc, Proc. of SPIE Vol. 8172
817209 · © 2011 SPIE · CCC code: 0277-786X/11/$18 · doi: 10.1117/12.899304

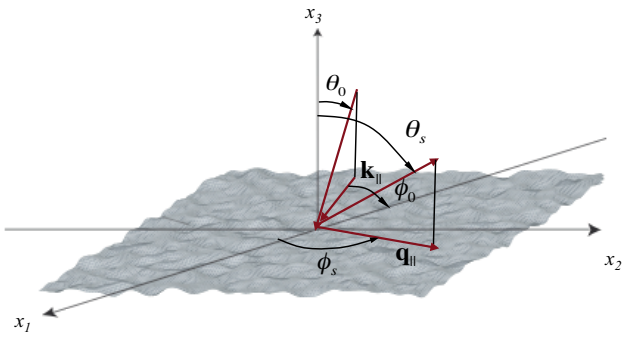

Figure 1. A sketch of the studied scattering geometry. The figure also shows the coordinate system used, angles of incidence (θ_0, ϕ_0) and scattering (θ_s, ϕ_s), and the corresponding transverse wavevectors $\mathbf{k}_\parallel$ and $\mathbf{q}_\parallel$, respectively.

two-dimensional randomly rough penetrable surface is considered, specifically scattering from a metallic surface and from a dielectric surface. Section 4 is devoted to a presentation of results obtained from a purely numerical, nonperturbative, solution of the reduced Rayleigh equation for the scattering of polarized light from a two-dimensional, randomly rough, penetrable surface. A discussion of the results obtained, and conclusions drawn from them, in Section 5, concludes this paper.

2. A PERFECTLY CONDUCTING SURFACE

2.1 Mathematical Formulation

The starting point for the calculation of the electromagnetic field scattered from a two-dimensional rough perfectly conducting surface is the Stratton–Chu formula[16] for the magnetic field in the vacuum

$$\theta(x_3 - \zeta(\mathbf{x}_\parallel))\,\mathbf{H}^{>}(\mathbf{x}|\omega) = \mathbf{H}(\mathbf{x}|\omega)_{\rm inc} + \frac{1}{4\pi}\int \mathrm{d}^2 x'_\parallel \;\; [\boldsymbol{\nabla} g_0(\mathbf{x}|\mathbf{x}')]|_{x'_3=\zeta(\mathbf{x}'_\parallel)} \times \mathbf{J}_H(\mathbf{x}'_\parallel|\omega), \tag{2}$$

where $\theta(z)$ is the Heaviside unit step function, and $\mathbf{H}(\mathbf{x}|\omega)_{\rm inc}$ is the magnetic component of the incident field. In writing Eq. (2) we have assumed the time dependence $\exp(-\mathrm{i}\omega t)$ for the field, but have not indicated this explicitly.

The function $g_0(\mathbf{x}|\mathbf{x}')$ is the scalar free-space Green's function,

$$g_0(\mathbf{x}|\mathbf{x}') = \frac{\exp\left[\mathrm{i}\frac{\omega}{c}\,|\mathbf{x}-\mathbf{x}'|\right]}{|\mathbf{x}-\mathbf{x}'|} \tag{3a}$$

$$= \int \frac{\mathrm{d}^2 q_\parallel}{(2\pi)^2}\,\frac{2\pi\mathrm{i}}{\alpha_0(q_\parallel)} \exp\left[\mathrm{i}\mathbf{q}_\parallel\cdot(\mathbf{x}_\parallel - \mathbf{x}'_\parallel)\right] \exp\left[\mathrm{i}\alpha_0(q_\parallel)|x_3 - x'_3|\right], \tag{3b}$$

where ω and c are the angular frequency and speed of light in vacuum, respectively, while $\alpha_0(q_\parallel) = [(\omega/c)^2 - q_\parallel^2]^{\frac{1}{2}}$, with $\mathrm{Re}\,\alpha_0(q_\parallel) > 0$, $\mathrm{Im}\,\alpha_0(q_\parallel) > 0$. The electric surface current $\mathbf{J}_H(\mathbf{x}_\parallel|\omega)$ is defined by $\mathbf{J}_H(\mathbf{x}_\parallel|\omega) = [\mathbf{n} \times \mathbf{H}^{>}(\mathbf{x}|\omega)]_{x_3=\zeta(\mathbf{x}_\parallel)}$, where $\mathbf{n} = (-\zeta_1(\mathbf{x}_\parallel), -\zeta_2(\mathbf{x}_\parallel), 1)$ and $\zeta_j(\mathbf{x}_\parallel) \equiv \partial\zeta(\mathbf{x}_\parallel)/\partial x_j$ $(j = 1, 2)$. On evaluating Eq. (2) at $x_3 = \zeta(\mathbf{x}_\parallel) + \eta$ and at $x_3 = \zeta(\mathbf{x}_\parallel) - \eta$, where η is a positive infinitesimal, adding the resulting two equations, and taking the vector cross product of the sum with $\mathbf{n}$, we obtain the integral equation satisfied by $\mathbf{J}_H(\mathbf{x}_\parallel|\omega)$,

$$\mathbf{J}_H(\mathbf{x}_\parallel|\omega) = 2\mathbf{J}_H^{(i)}(\mathbf{x}_\parallel|\omega) + \frac{1}{2\pi} P \int \mathrm{d}^2 x'_\parallel \; \mathbf{n} \times \left\{ [\![\boldsymbol{\nabla} g_0(\mathbf{x}|\mathbf{x}')]\!] \times \mathbf{J}_H(\mathbf{x}'_\parallel|\omega) \right\}, \tag{4}$$

where $\mathbf{J}_H^{(i)}(\mathbf{x}_\parallel|\omega)_{\rm inc} = \mathbf{n}\times\mathbf{H}(\mathbf{x}|\omega)_{\rm inc}|_{x_3=\zeta(\mathbf{x}_\parallel)}$, P denotes the Cauchy principal value, and we have introduced the definition

$$[\![f(\mathbf{x}|\mathbf{x}')]\!] \;=\; f(\mathbf{x}|\mathbf{x}')\Big|_{\substack{x_3=\zeta(\mathbf{x}_\parallel)\\ x_3'=\zeta(\mathbf{x}_\parallel')}}. \tag{5}$$

Because $\mathbf{n}\cdot\mathbf{J}_H(\mathbf{x}_\parallel|\omega)=0$, only two components of $\mathbf{J}_H(\mathbf{x}_\parallel|\omega)$ are independent. We choose them to be $J_H(\mathbf{x}_\parallel|\omega)_1$ and $J_H(\mathbf{x}_\parallel|\omega)_2$, and obtain $J_H(\mathbf{x}_\parallel|\omega)_3$ from

$$J_H(\mathbf{x}_\parallel|\omega)_3 = \zeta_1(\mathbf{x}_\parallel)J_H(\mathbf{x}_\parallel|\omega)_1 + \zeta_2(\mathbf{x}_\parallel)J_H(\mathbf{x}_\parallel|\omega)_2. \tag{6}$$

The two coupled, inhomogeneous, two-dimensional integral equations satisfied by $J_H(\mathbf{x}_\parallel|\omega)_{1,2}$ are solved by converting them into matrix equations. This is done by generating a realization of the surface profile function on a grid of N^2 points within a square region of the x_1x_2 plane of edge L, where the discretization intervals for both directions are $\Delta x = L/N$. The integrals over this region are carried out by means of a two-dimensional version of the extended midpoint method,[17] and the values of $J_H(\mathbf{x}_\parallel|\omega)_1$ and $J_H(\mathbf{x}_\parallel|\omega)_2$ are calculated at the points of this grid. The resulting matrix equations are solved by means of the biconjugate gradient stabilized method.[18] The values of $J_H(\mathbf{x}_\parallel|\omega)_3$ are then obtained by the use of Eq. (6).

In these calculations the incident electric field has the form of a p- or s-polarized Gaussian beam, propagating in the direction of $\mathbf{k} = (\omega/c)(\sin\theta_0\cos\phi_0, \sin\theta_0\sin\phi_0, -\cos\theta_0)$. In the case that $\mathbf{k}_\parallel = k_\parallel\hat{\mathbf{x}}_1$, it is given by

$$\mathbf{E}_\nu(\mathbf{x}|\omega)_{\rm inc} \;=\; \int\limits_{q_\parallel<\frac{\omega}{c}} \mathrm{d}^2q_\parallel\; \hat{\boldsymbol{\mathcal{E}}}_\nu^{(i)}(\mathbf{q}_-|\omega)\exp\left[\mathrm{i}\mathbf{q}_-\cdot\mathbf{x}\right]\; W(\mathbf{q}_\parallel|\mathbf{k}_\parallel), \tag{7}$$

where $\nu = p$ or s, $\mathbf{q}_\pm(\mathbf{q}_\parallel,\omega) = \mathbf{q}_\parallel \pm \alpha_0(q_\parallel)\hat{\mathbf{x}}_3$, and $W(\mathbf{q}_\parallel|\mathbf{k}_\parallel)$ is

$$W(\mathbf{q}_\parallel|\mathbf{k}_\parallel) = \frac{w^2}{2\pi}\exp\left[-\frac{w^2}{2}(\mathbf{q}_\parallel-\mathbf{k}_\parallel)^2\right]. \tag{8}$$

For an incident field that is p polarized

$$\hat{\boldsymbol{\mathcal{E}}}_p^{(i)}(\mathbf{q}_-|\omega) \;=\; \frac{\alpha_0(q_\parallel)\hat{\mathbf{x}}_1 + q_1\hat{\mathbf{x}}_3}{[q_1^2+\alpha_0^2(q_\parallel)]^{\frac{1}{2}}}, \tag{9a}$$

while for an incident field that is s polarized

$$\hat{\boldsymbol{\mathcal{E}}}_s^{(i)}(\mathbf{q}_-|\omega) \;=\; \frac{q_1q_2\hat{\mathbf{x}}_1 - [q_1^2+\alpha_0^2(q_\parallel)]\hat{\mathbf{x}}_2 - q_2\alpha_0(q_\parallel)\hat{\mathbf{x}}_3}{\frac{\omega}{c}[q_1^2+\alpha_0^2(q_\parallel)]^{\frac{1}{2}}}. \tag{9b}$$

The scattered electric field, written in terms of $\mathbf{J}_H(\mathbf{x}_\parallel|\omega)$, is

$$\mathbf{E}(\mathbf{x}|\omega)_{\rm sc} \;=\; \int\frac{\mathrm{d}^2q_\parallel}{(2\pi)^2}\;\left[\mathcal{E}_p(\mathbf{q}_+|\omega)\hat{\boldsymbol{\gamma}}_p(\mathbf{q}_+|\omega) + \mathcal{E}_s(\mathbf{q}_+|\omega)\hat{\boldsymbol{\gamma}}_s(\mathbf{q}_+|\omega)\right]\exp\left[\mathrm{i}\mathbf{q}_+\cdot\mathbf{x}\right], \tag{10}$$

where

$$\hat{\boldsymbol{\gamma}}_p(\mathbf{q}_+|\omega) \;=\; \frac{-\alpha_0(q_\parallel)\hat{\mathbf{q}}_\parallel + q_\parallel\hat{\mathbf{x}}_3}{\omega/c} \tag{11a}$$

$$\hat{\boldsymbol{\gamma}}_s(\mathbf{q}_+|\omega) \;=\; \hat{\mathbf{q}}_\parallel\times\hat{\mathbf{x}}_3, \tag{11b}$$

and ($\nu = p, s$)

$$\mathcal{E}_\nu(\mathbf{q}_+|\omega) \;=\; -\frac{(\omega/c)}{2\alpha_0(q_\parallel)}\int\mathrm{d}^2x_\parallel\;\hat{\boldsymbol{\gamma}}_\nu(\mathbf{q}_+|\omega)\cdot\mathbf{J}_H(\mathbf{x}_\parallel|\omega)\exp\left[-\mathrm{i}\mathbf{q}_\parallel\cdot\mathbf{x}_\parallel - \mathrm{i}\alpha_0(q_\parallel)\zeta(\mathbf{x}_\parallel)\right]. \tag{12}$$

The differential reflection coefficient $(\partial R/\partial\Omega_s)$ is defined such that $(\partial R/\partial\Omega_s)\mathrm{d}\Omega_s$ is the fraction of the total time-averaged flux incident on the surface that is scattered into the element of solid angle $\mathrm{d}\Omega_s$ about the scattering direction (θ_s, ϕ_s). Since we are studying the scattering of light from a randomly rough surface, it is the average of this quantity over the ensemble of realizations of the surface profile function that we need to calculate. The mean differential reflection coefficient for the scattering of light of polarization β, the projection of whose wave vector on the mean scattering surface is $\mathbf{k}_\parallel$, into light of polarization α, the projection of whose wave vector on the mean scattering surface is $\mathbf{q}_\parallel$, is given by

$$\left\langle \frac{\partial R_{\alpha\beta}}{\partial\Omega_s} \right\rangle = \frac{1}{4\pi^2}\left(\frac{\omega}{c}\right)^3 \cos^2\theta_s \frac{\left\langle |\mathcal{E}_\alpha(\mathbf{q}_+|\omega)|^2 \right\rangle}{p_{\mathrm{inc}}}, \tag{13}$$

where for both polarizations of the incident light,

$$p_{\mathrm{inc}} = w^4 \int\limits_{q_\parallel < \frac{\omega}{c}} \mathrm{d}^2 q_\parallel \; \alpha_0(q_\parallel) \exp\left[-w^2(\mathbf{q}_\parallel - \mathbf{k}_\parallel)^2\right]. \tag{14}$$

The dependence of the right-hand side of this equation on the polarization index β is through the dependence of the amplitude $\mathcal{E}_\alpha(\mathbf{q}_+|\omega)$ on the surface current $\mathbf{J}_H(\mathbf{x}_\parallel|\omega)$ in Eq. (12). The surface current satisfies Eq. (4) in which the inhomogeneous term depends on the incident field and hence on its polarization $\beta = p, s$. Therefore $\mathcal{E}_\alpha(\mathbf{q}_+|\omega)$ depends implicitly on the polarization β of the incident field and consequently so does the mean differential reflection coefficient.

If one is interested in nonspecular effects, it is the contribution to the mean differential reflection coefficient from the light that has been scattered incoherently (diffusely) that is of interest. It is given by

$$\left\langle \frac{\partial R_{\alpha\beta}}{\partial\Omega_s} \right\rangle_{\mathrm{incoh}} = \frac{1}{4\pi^2}\left(\frac{\omega}{c}\right)^3 \cos^2\theta_s \frac{\left\langle |\mathcal{E}_\alpha(\mathbf{q}_+|\omega)|^2 \right\rangle - \left|\left\langle \mathcal{E}_\alpha(\mathbf{q}_+|\omega) \right\rangle\right|^2}{p_{\mathrm{inc}}}. \tag{15}$$

We now turn to some results obtained on the basis of this method.

2.2 Results for a Perfectly Conducting Surface

2.2.1 An Isotropic Roughness Power Spectrum

The first set of calculations were carried out for a two-dimensional randomly rough perfectly conducting surface defined by an isotropic surface height autocorrelation function, *i.e.* one that depends on the vector $\mathbf{x}_\parallel$ only through its magnitude. We have chosen for it the Gaussian form $W(\mathbf{x}_\parallel) = \exp(-x_\parallel^2/a^2)$. The characteristic length a is called the transverse correlation length of the surface roughness. The power spectrum of the surface, given by Eq. (1), in this case has the form

$$g(\mathbf{k}_\parallel) = \pi a^2 \exp\left(-\frac{k_\parallel^2 a^2}{4}\right). \tag{16}$$

We have carried out calculations of the scattering of p-polarized light from such a surface with an rms height $\delta = \lambda$ and a transverse correlation length $a = 2\lambda$, where λ is the wavelength of the incident field in vacuum. The incident field had the form of a Gaussian beam, Eq. (7), with $w = 4\lambda$. The surface, covering an area $L^2 = 16\lambda \times 16\lambda$ in the mean surface plane, was generated at the points of a 112×112 grid of mesh size $\Delta x = \lambda/7$ for both directions.

In Fig. 2 we plot the mean differential reflection coefficients as functions of the polar scattering angle θ_s for the in-plane $(\phi_s = 0^\circ, 180^\circ)$ and out-of-plane $(\phi_s = \pm 90^\circ)$ co-$(p \to p)$ and cross-$(p \to s)$ polarized scattering when a p-polarized Gaussian beam is incident on the surface at angles of incidence (θ_0, ϕ_0) given by $(0^\circ, 0^\circ)$ and $(20^\circ, 0^\circ)$. Results obtained for 12 000 realizations of the surface profile function were averaged to obtain these figures. The calculations for each realization of the surface profile function required 76 CPU seconds on an Intel Core 2 CPU (Q9550) operating at 2.83 GHz and running the Linux operating system. For the roughness

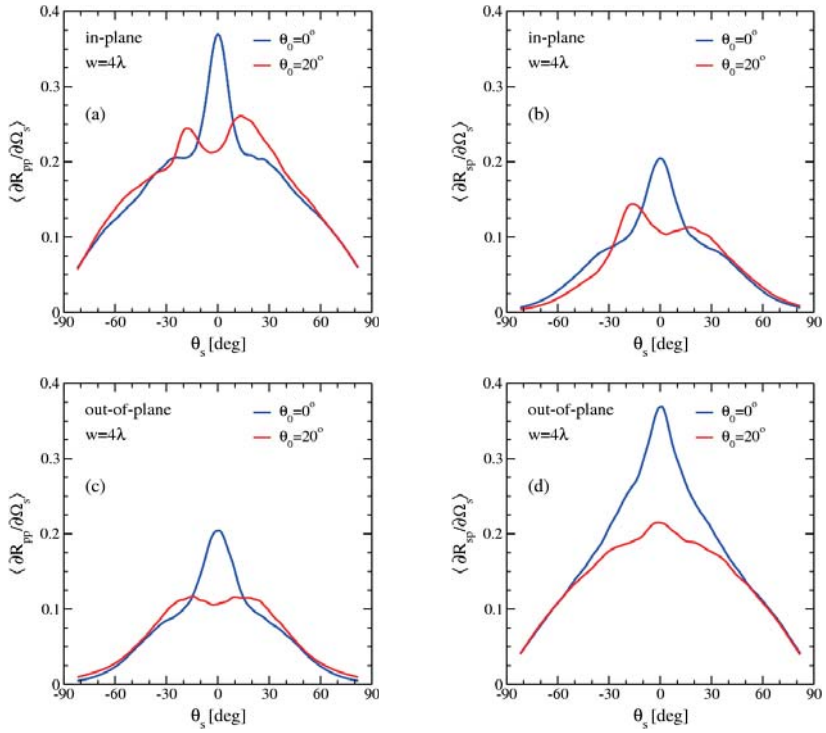

Figure 2. The mean differential reflection coefficients, $\langle \partial R_{\alpha\beta}/\partial\Omega_s \rangle$ ($\beta \to \alpha$), as functions of the polar scattering angle θ_s for the in-plane ($\phi_s = \phi_0$ or $\phi_s = \phi_0 + 180^\circ$) (a) co-polarized ($p \to p$) and (b) cross-polarized scattering ($p \to s$), and the out-of-plane ($\phi_s = \phi_0 \pm 90^\circ$) (c) co-polarized ($p \to p$) and (d) cross-polarized scattering ($p \to s$) of a p-polarized incident beam ($\beta = p$) of width $w = 4\lambda$ ($\theta_0 = 0^\circ$ and $\theta_0 = 20^\circ$; $\phi_0 = 0^\circ$) scattered from a Gaussian randomly rough perfectly conducting surface. The Gaussian correlated surface had a correlation length $a = 2\lambda$ and an rms height $\delta = \lambda$. To facilitate comparison between the various configurations presented in this figure, notice that we have used similar scales for all ordinate axes. Moreover, to simplify the presentation of the figures, a convention was adopted where negative (positive) values of θ_s correspond to $\phi_s = \phi_0 + 180^\circ$ ($\phi_s = \phi_0$). (After Ref. 7).

parameters assumed in these calculations the contribution to the mean differential reflection coefficient from the light scattered coherently is smaller than the contribution from the light scattered incoherently by a factor of approximately 10^{-4}.

There is no single scattering contribution to the mean differential reflection coefficient in the cases of in-plane cross-polarized [Fig. 2(b)] and out-of-plane co-polarized [Fig. 2(c)] scattering.[1] What is plotted in these figures therefore is due to multiple scattering only. The results plotted in Figs. 2(a) and 2(d) contain a contribution from single-scattering processes.

The peaks in the retroreflection directions in the results for in-plane co-polarized scattering [Fig. 2(a)] are enhanced backscattering peaks.[19–22] However, as we will see from the full angular distribution of the intensity of the scattered light, the structures seen as peaks in the results for in-plane cross-polarized scattering [Fig. 2(b)] are not real peaks. The results that the out-of-plane co- and cross-polarized scattering [Figs. 2(c) and 2(d)] are even functions of θ_s are consequences of the scattering geometry, namely that $\phi_0 = 0^\circ$, $\phi_s = \pm 90^\circ$, and the isotropy of the power spectrum of the surface roughness.

The full angular distribution of the intensity of the scattered light is presented as contour plots in Fig. 3,

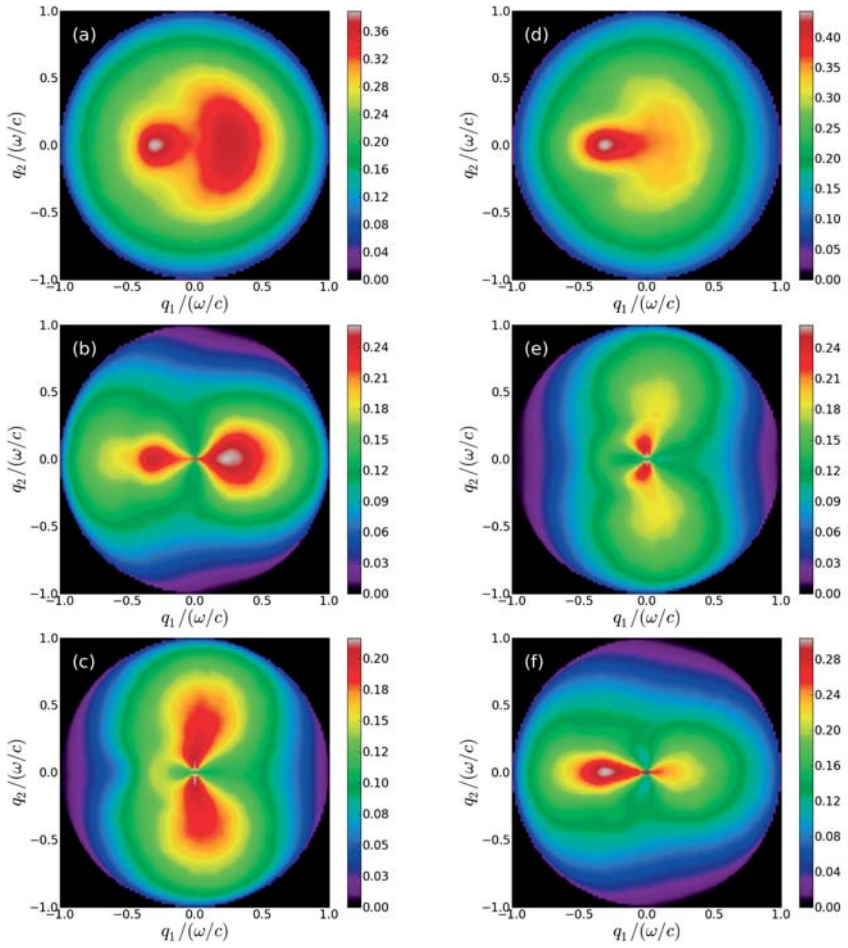

Figure 3. The complete angular distributions of the mean differential reflection coefficient, $\langle \partial R_{\alpha\beta}/\partial\Omega_s \rangle$, for the scattering of an β-polarized Gaussian beam incident on the surface at polar angle $\theta_0 = 20^\circ$ and azimuthal angle $\phi_0 = 0^\circ$. The perfectly conducting rough surface was characterized by a Gaussian height distribution of rms-value $\delta = \lambda$ and a Gaussian correlation function of transverse correlation length $a = 2\lambda$. The incident beam was p polarized in Figs. 3(a)–(c) [left column], and s polarized in Figs. 3(d)–(f) [right column]. Moreover, in the top two figures [Figs. 3(a) and (d)] the polarization of the scattered light was not recorded; in Figs. 3(b) and (e) [central row] only p-polarized scattered light was recorded; while the bottom two figures correspond to recording only s-polarized scattered light [Figs. 3(c) and (f)]. The rough surface, covering an area $16\lambda \times 16\lambda$, was discretized at a grid of 112×112 points corresponding to a discretization interval $\lambda/7$ for both directions. The presented figures were obtained by averaging results for the differential reflection coefficient obtained for 12 000 surface realizations. (After Ref. 7).

which correspond to polar and azimuthal angles of incidence $(\theta_0, \phi_s) = (20^\circ, 0^\circ)$, when the incident beam is p polarized and the scattered light is p and s polarized. In Fig. 3(a) we present a contour plot of the mean differential reflection coefficient for the scattering of p-polarized light into both p- and s-polarized scattered light, *i.e.* the polarization state of the scattered light was not recorded. It is seen that there is a pronounced enhanced backscattering peak in the retroreflection direction at $\theta_s = 20^\circ$ and $\phi_s = 180^\circ$. From Figs. 3(b) and 3(c),

where only p-polarized light or s-polarized scattered light is recorded, respectively, we see that the co-polarized scattering displays a structure that is elongated along the plane of incidence, while the cross-polarized scattering has a scattering pattern that is elongated perpendicular to this plane. In principle an enhanced backscattering peak should be present in the retroreflection direction in both co- and cross-polarized scattering.[20–22] However, for the roughness parameters assumed in this work, instead of a well-defined peak in the retroreflection direction we see a ridge of constant enhanced intensity in parts of the region $q_1 < 0$, forming a semicircle of constant polar scattering angle $\theta_s \approx \theta_0 = 20°$, with $90° < \phi_s < 270°$ [Fig. 3(c)]. In precisely the retroreflection direction, $\theta_s = 20°$ and $\phi_s = 180°$, there is little, if any, additional enhancement in the cross-polarized scattering compared to the intensities at other values of ϕ_s in the interval $[90°, 270°]$. We speculate that the enhancement ridge seen in Fig. 3(c) is a constructive interference effect similar to the effect underlying enhanced backscattering.

We note that if we had examined only the in-plane and out-of-plane results for the same angle of incidence, the peak observed in Fig. 2(b) for $\theta_0 = 20°$ could easily have been interpreted as the well-localized feature in the retroreflection direction similar to the one present for co-polarized scattering in Fig. 3(b). Thus the angular distributions of the intensities of the scattered light, such as those presented in Fig. 3, can provide information that helps in better understanding multiple scattering phenomena.

When the incident beam was s polarized, we obtain the results presented in Figs. 3(d)–(f). Also here an enhanced backscattering peak is observed, and the intensity distributions of the co- and cross-polarized scattered light are oriented along and perpendicular to the plane of incidence, respectively.

A necessary, but not sufficient, criterion for the accuracy of a scattering calculation is that energy be conserved in the scattering process. In scattering from a perfectly conducting surface this requires that the total time-averaged scattered flux must equal the total time-averaged incident flux. This requirement can be stated as

$$U_\beta(\theta_0, \phi_0) = \sum_{\alpha=p,s} \int \mathrm{d}\Omega_s \left\langle \frac{\partial R_{\alpha\beta}}{\partial \Omega_s} \right\rangle = 1 \qquad \beta = p, s. \tag{17}$$

Under the conditions assumed in obtaining the results presented in Figs. 2 and 3, the value of $U_p(\theta_0, \phi_0)$ and $U_s(\theta_0, \phi_0)$ were calculated to be 0.9962 and 0.9966, respectively. Consequently, the computational approach outlined in Section 2 conserves energy in the scattering process with an error that is smaller than 0.5%. This error is expected to be reduced further by decreasing the sampling interval Δx and/or by increasing the area (L^2) of the the mean surface.

2.2.2 An Anisotropic Roughness Power Spectrum

The existing computational studies of the scattering of light from two-dimension randomly rough perfectly conducting surfaces[1–7] have been based on the assumption that the surface profile function $\zeta(\mathbf{x}_\parallel)$ is a stationary, zero-mean, *isotropic*, Gaussian random process. Very little work has been devoted to the case where $\zeta(\mathbf{x}_\parallel)$ is an *anisotropic* random process. In this section we present results obtained by the rigorous computational approach described in Section 2.1 for the light scattered from a two-dimensional, randomly rough, perfectly conducting surface defined by a surface profile function that is a stationary, zero-mean, anisotropic, Gaussian random process.

The surface we assume in these calculations is defined by a surface height autocorrelation function that has an anisotropic Gaussian form, $W(\mathbf{x}_\parallel) = \exp[-(x_1/a_1)^2 - (x_2/a_2)^2]$ where, for specificity, we assume that $a_1 < a_2$. Thus, we will refer to the x_1 and x_2 axes as the minor and major axes of the anisotropy, respectively. The power spectrum of the surface roughness, defined by Eq. (1), in the present case has the form

$$g(\mathbf{k}_\parallel) \quad = \quad \pi a_1 a_2 \exp\left[-\frac{k_1^2 a_1^2}{4} - \frac{k_2^2 a_2^2}{4}\right], \tag{18}$$

and is elongated along the minor anisotropy axis.

To provide a reference against which results for the angular distribution of the fields scattered from an anisotropic random surface can be compared, we first present, in Fig. 4, contour plots of the angular distributions of the fields scattered from an *isotropic* random surface. The incident field is a p-polarized beam with the width

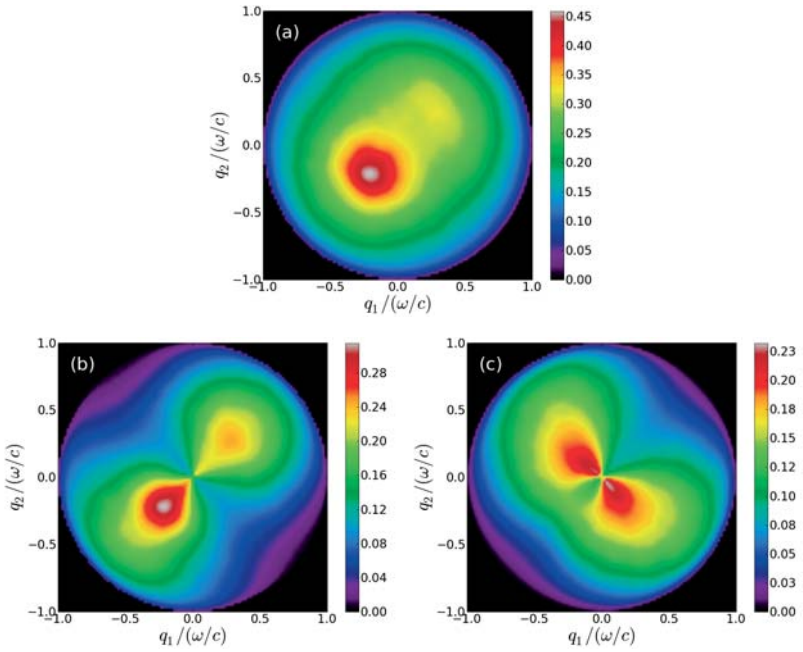

Figure 4. A p-polarized beam of wavelength λ and width $w = 4\lambda$ is scattered from an *isotropic* perfectly conducing rough surface characterized by a Gaussian height distribution of rms-value $\delta = \lambda/2$ and a Gaussian correlation function of correlation lengths $a_1 = a_2 = \lambda$. The panels show contour plots of the full angular distributions of the mean differential reflection coefficient, $\langle \partial R_{\alpha p}/\partial \Omega_s \rangle$, obtained by a rigorous computer simulation approach for the scattering of the beam incident on the rough surface at a polar angle $\theta_0 = 20^\circ$ and an azimuthal angle $\phi_0 = 45^\circ$. The three panels correspond to various configurations for the polarization of the scattered light. They are: (a) the polarization of the scattered light is not recorded [$\alpha = p, s$]; (b) only p-polarized scattered light is measured [$\alpha = p$]; and (c) only s-polarized scattered light is recorded [$\alpha = s$]. The rough surface, covering an area $16\lambda \times 16\lambda$, was discretized on a grid of 112×112 points corresponding to a discretization interval $\lambda/7$ for both directions. The presented figures were obtained by averaging results for the differential reflection coefficient obtained for 6 000 surface realizations. (After Ref. 8).

parameter $w = 4\lambda$, where λ is the wavelength of the field. The polar and azimuthal angles of incidence are $(\theta_0, \phi_0) = (20^\circ, 45^\circ)$. The surface is characterized by the Gaussian power spectrum (16), with a correlation length $a = \lambda$. The rms height of the surface is $\delta = \lambda/2$. The surface was generated on the same grid as the surface studied in Section 2.2.1. The mean differential reflection coefficient was obtained as the arithmetic average of results obtained for 6000 realizations of the surface profile function. The three panels in this figure correspond to different choices for the polarization of the scattered light. Thus, in obtaining Fig. 4(a) the polarization of the scattered light was not recorded; in obtaining Fig. 4(b) only the p-polarized component of the scattered light was recorded; while in obtaining Fig. 4(c) only the s-polarized component of the scattered light was recorded.

We see from these results that the co-polarized ($p \to p$) scattering has a dipole-like angular distribution with the main intensity oriented parallel to the plane of incidence [Fig. 4(b)]. In contrast the cross-polarized ($p \to s$) scattering has its main intensity distribution oriented perpendicular to the plane of incidence [Fig. 4(c)]. In both cases the intensity distributions are symmetric with respect to the plane of incidence, and the scattered intensity patterns simply rotate as the azimuthal angle of incidence ϕ_0 is changed. When the polarization of the scattered light is not recorded [Fig. 4(a)], the pronounced peak in the retroreflection direction ($\theta_s = \theta_0, \phi_s = \phi_0 + 180^\circ$) is the enhanced backscattering peak.

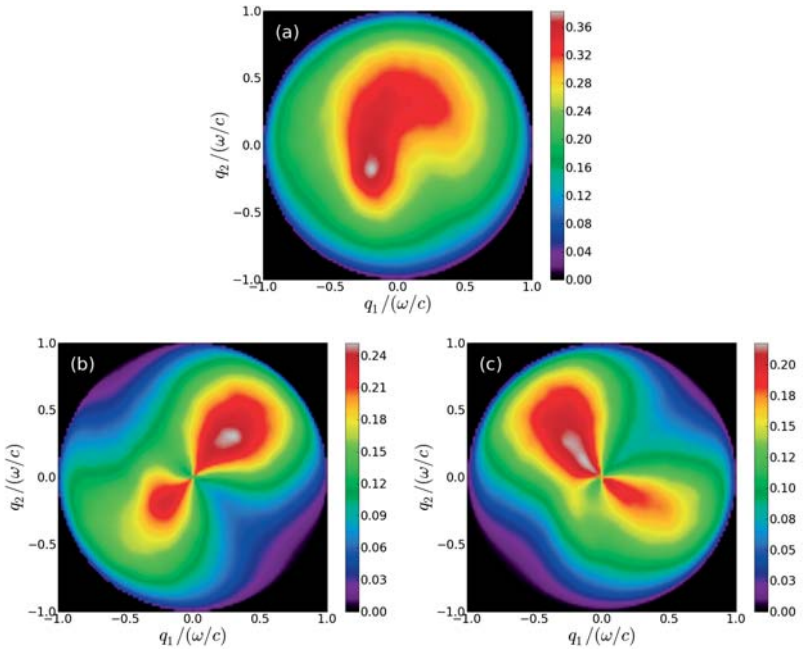

Figure 5. Same as Fig. 4 with the only difference that now the rough surface is *weakly anisotropic* and characterized by the correlation lengths $a_1 = \lambda$ and $a_2 = 1.5\lambda$. (After Ref. 8).

Turning now to the scattering from an anisotropic surface, in Fig. 5 we present contour plots of the full angular distributions of the mean differential reflection coefficients when the randomly rough surface is defined by the power spectrum (18) with $a_1 = \lambda$ and $a_2 = 1.5\lambda$. The remaining experimental and computational parameters have the values used in obtaining the results presented in Fig. 4. The three panels correspond to different choices for the polarization of the scattered light. In obtaining Fig. 5(a) the polarization of the scattered light was not recorded; in obtaining Fig. 5(b) only the p-polarized component of the scattered light was recorded; while in obtaining Fig. 5(c) only the s-polarized component of the scattered light was recorded. Unlike in the scattering of light from an isotropic surface, the intensity distribution of light scattered from an anisotropic surface in general is not symmetric with respect to the plane of incidence. It is only when the plane of incidence is parallel to either the minor or the major axis of the anisotropy that this type of symmetry obtains.

The dipole-like angular intensity patterns in Figs. 5(b) and 5(c) are no longer symmetric with respect to the plane of incidence, as their isotropic equivalents are. This asymmetry is particularly pronounced in the cross-polarized scattering [Fig. 5(c)]. It is explained by the fact that the cross-polarized component of the mean differential reflection coefficient to the lowest (second) order in the surface profile function is proportional to $g(\mathbf{q}_\parallel - \mathbf{k}_\parallel)\ [(\hat{\mathbf{q}}_\parallel \times \hat{\mathbf{k}}_\parallel)_3]^2$, where $\mathbf{q}_\parallel = (\omega/c)\sin\theta_s(\cos\phi_s \sin\phi_s, 0)$.[23] When the power spectrum $g(\mathbf{k}_\parallel)$ is given by Eq. (18), this function is not symmetric with respect to the plane of incidence.

The co-polarized scattering pattern [Fig. 5(b)] is explained in a similar fashion. In this case the contribution to the mean differential reflection coefficient of the lowest order in the surface profile function contains terms proportional to $g(\mathbf{q}_\parallel - \mathbf{k}_\parallel)(\hat{\mathbf{q}}_\parallel - \hat{\mathbf{k}}_\parallel)^m$ with $m = 1, 2$.[23] The maxima of these functions are in the forward scattering direction and, for an anisotropic surface, move away from the plane of incidence toward the minor axis of the anisotropy.

3. A PENETRABLE SURFACE

3.1 Mathematical Formulation

In calculating the electromagnetic field scattered from a two-dimensional randomly rough surface a convenient starting point are the Franz formulas of electromagnetic scattering theory.[24,25] These formulas for the magnetic and electric fields in the vacuum region $x_3 > \zeta(\mathbf{x}_\parallel)$ can be written as

$$\begin{aligned}\mathbf{H}^{>}(\mathbf{x}|\omega) &= \mathbf{H}(\mathbf{x}|\omega)_{\rm inc} + \frac{1}{4\pi}\boldsymbol{\nabla}\times\int \mathrm{d}^2x'_\parallel\; g_0(\mathbf{x}|\mathbf{x}')|_{x'_3=\zeta(\mathbf{x}'_\parallel)}\mathbf{J}_H(\mathbf{x}'_\parallel|\omega)\\ &\quad -\frac{\mathrm{i}c}{4\pi\omega}\boldsymbol{\nabla}\times\boldsymbol{\nabla}\times\int \mathrm{d}^2x'_\parallel\; g_0(\mathbf{x}|\mathbf{x}')|_{x'_3=\zeta(\mathbf{x}'_\parallel)}\mathbf{J}_E(\mathbf{x}'_\parallel|\omega) \qquad (19a)\end{aligned}$$

$$\begin{aligned}\mathbf{E}^{>}(\mathbf{x}|\omega) &= \mathbf{E}(\mathbf{x}|\omega)_{\rm inc} + \frac{1}{4\pi}\boldsymbol{\nabla}\times\int \mathrm{d}^2x'_\parallel\; g_0(\mathbf{x}|\mathbf{x}')|_{x'_3=\zeta(\mathbf{x}'_\parallel)}\mathbf{J}_E(\mathbf{x}'_\parallel|\omega)\\ &\quad +\frac{\mathrm{i}c}{4\pi\omega}\boldsymbol{\nabla}\times\boldsymbol{\nabla}\times\int \mathrm{d}^2x'_\parallel\; g_0(\mathbf{x}|\mathbf{x}')|_{x'_3=\zeta(\mathbf{x}'_\parallel)}\mathbf{J}_H(\mathbf{x}'_\parallel|\omega). \qquad (19b)\end{aligned}$$

The Franz formulas for the magnetic and electric fields in the scattering medium $x_3 < \zeta(\mathbf{x}_\parallel)$ can be written as

$$\begin{aligned}\mathbf{H}^{<}(\mathbf{x}|\omega) &= -\frac{1}{4\pi}\boldsymbol{\nabla}\times\int \mathrm{d}^2x'_\parallel\; g_\varepsilon(\mathbf{x}|\mathbf{x}')|_{x'_3=\zeta(\mathbf{x}'_\parallel)}\mathbf{J}_H(\mathbf{x}'_\parallel|\omega)\\ &\quad +\frac{\mathrm{i}c}{4\pi\omega}\boldsymbol{\nabla}\times\boldsymbol{\nabla}\times\int \mathrm{d}^2x'_\parallel\; g_\varepsilon(\mathbf{x}|\mathbf{x}')|_{x'_3=\zeta(\mathbf{x}'_\parallel)}\mathbf{J}_E(\mathbf{x}'_\parallel|\omega) \qquad (20a)\end{aligned}$$

$$\begin{aligned}\mathbf{E}^{<}(\mathbf{x}|\omega) &= -\frac{1}{4\pi}\boldsymbol{\nabla}\times\int \mathrm{d}^2x'_\parallel\; g_\varepsilon(\mathbf{x}|\mathbf{x}')|_{x'_3=\zeta(\mathbf{x}'_\parallel)}\mathbf{J}_E(\mathbf{x}'_\parallel|\omega)\\ &\quad -\frac{\mathrm{i}c}{4\pi\omega\varepsilon(\omega)}\boldsymbol{\nabla}\times\boldsymbol{\nabla}\times\int \mathrm{d}^2x_\parallel\; g_\varepsilon(\mathbf{x}|\mathbf{x}')|_{x'_3=\zeta(\mathbf{x}'_\parallel)}\mathbf{J}_H(\mathbf{x}'_\parallel|\omega). \qquad (20b)\end{aligned}$$

In writing these equations we have introduced the vectors

$$\begin{aligned}\mathbf{J}_H(\mathbf{x}_\parallel|\omega) &= \left[\mathbf{n}\times\mathbf{H}^{>}(\mathbf{x}|\omega)\right]\big|_{x_3=\zeta(\mathbf{x}_\parallel)}, \qquad (21a)\\ &= \left[\mathbf{n}\times\mathbf{H}^{<}(\mathbf{x}|\omega)\right]\big|_{x_3=\zeta(\mathbf{x}_\parallel)}, \qquad (21b)\end{aligned}$$

and

$$\begin{aligned}\mathbf{J}_E(\mathbf{x}_\parallel|\omega) &= \left[\mathbf{n}\times\mathbf{E}^{>}(\mathbf{x}|\omega)\right]\big|_{x_3=\zeta(\mathbf{x}_\parallel)}, \qquad (22a)\\ &= \left[\mathbf{n}\times\mathbf{E}^{<}(\mathbf{x}|\omega)\right]\big|_{x_3=\zeta(\mathbf{x}_\parallel)}. \qquad (22b)\end{aligned}$$

The vector $\mathbf{n}$ has been defined in Section 2.1. The scalar free-space Green's function for an infinite scattering medium is defined by

$$\begin{aligned}g_\varepsilon(\mathbf{x}|\mathbf{x}') &= \frac{\exp\left[-\left|\mathbf{x}-\mathbf{x}'\right|/d(\omega)\right]}{\left|\mathbf{x}-\mathbf{x}'\right|} \qquad (23a)\\ &= \int\frac{\mathrm{d}^2k_\parallel}{(2\pi)^2}\,\frac{2\pi}{\beta(k_\parallel)}\exp\left[\mathrm{i}\mathbf{k}_\parallel\cdot(\mathbf{x}_\parallel-\mathbf{x}'_\parallel)\right]\exp\left[-\beta(k_\parallel)|x_3-x'_3|\right], \qquad (23b)\end{aligned}$$

where

$$\beta(k_\parallel) = \left[k_\parallel^2+\frac{1}{d^2(\omega)}\right]^{\frac{1}{2}}, \qquad \mathrm{Re}\,\beta(k_\parallel)>0, \mathrm{Im}\,\beta(k_\parallel)<0, \qquad (24)$$

and $d(\omega) = (c/\omega)[-\varepsilon(\omega)]^{-\frac{1}{2}}$, $\mathrm{Re}\, d(\omega) > 0$, $\mathrm{Im}\, d(\omega) > 0$, while $\varepsilon(\omega)$ is the dielectric function of the scattering medium.

To obtain the equations satisfied by $\mathbf{J}_H(\mathbf{x}_\parallel|\omega)$ and $\mathbf{J}_E(\mathbf{x}_\parallel|\omega)$ we proceed as follows. We take the vector cross product of Eqs. (19a) and (20a) with the vector $\mathbf{n}$, evaluate each product at $x_3 = \zeta(\mathbf{x}_\parallel) + \eta$, and $x_3 = \zeta(\mathbf{x}_\parallel) - \eta$, respectively, where η is a positive infinitesimal, and add the resulting equations. In this way we obtain the equation

$$\begin{aligned}\mathbf{J}_H(\mathbf{x}_\parallel|\omega) &= \mathbf{J}_H(\mathbf{x}_\parallel|\omega)_{\mathrm{inc}} + \frac{1}{4\pi} P \int \mathrm{d}^2 x'_\parallel \, [\![\mathbf{n} \times \{\boldsymbol{\nabla} \times [g_0(\mathbf{x}|\mathbf{x}') - g_\varepsilon(\mathbf{x}|\mathbf{x}')]\mathbf{J}_H(\mathbf{x}'_\parallel|\omega)\}]\!] \\ &\quad - \frac{\mathrm{i}c}{4\pi\omega} \int \mathrm{d}^2 x'_\parallel \, [\![\mathbf{n} \times \{\boldsymbol{\nabla} \times \boldsymbol{\nabla} \times [g_0(\mathbf{x}|\mathbf{x}') - g_\varepsilon(\mathbf{x}|\mathbf{x}')]\mathbf{J}_E(\mathbf{x}'_\parallel|\omega)\}]\!], \end{aligned} \tag{25a}$$

where $\mathbf{J}_H(\mathbf{x}_\parallel|\omega)_{\mathrm{inc}} = \mathbf{n} \times \mathbf{H}(\mathbf{x}|\omega)_{\mathrm{inc}}|_{x_3 = \zeta(\mathbf{x}_\parallel)}$, and P denotes the Cauchy principal value.

If we next take the vector cross product of Eq. (19b) and of $\varepsilon(\omega)$ times Eq. (20b) with the vector $\mathbf{n}$, evaluate each product at $x_3 = \zeta(\mathbf{x}_\parallel) + \eta$, and at $x_3 = \zeta(\mathbf{x}_\parallel) - \eta$, respectively, and add the resulting equations, we obtain

$$\begin{aligned}\mathbf{J}_E(\mathbf{x}_\parallel|\omega) &= 2\frac{\mathbf{J}_E(\mathbf{x}_\parallel|\omega)_{\mathrm{inc}}}{1+\varepsilon(\omega)} + \frac{2}{4\pi[1+\varepsilon(\omega)]} P \int \mathrm{d}^2 x'_\parallel \, [\![\mathbf{n} \times \{\boldsymbol{\nabla} \times [g_0(\mathbf{x}|\mathbf{x}') - \varepsilon(\omega) g_\varepsilon(\mathbf{x}|\mathbf{x}')]\mathbf{J}_E(\mathbf{x}'_\parallel|\omega)\}]\!] \\ &\quad + \frac{2\mathrm{i}c}{4\pi\omega[1+\varepsilon(\omega)]} \int \mathrm{d}^2 x'_\parallel \, [\![\mathbf{n} \times \{\boldsymbol{\nabla} \times \boldsymbol{\nabla} \times [g_0(\mathbf{x}|\mathbf{x}') - g_\varepsilon(\mathbf{x}|\mathbf{x}')]\mathbf{J}_H(\mathbf{x}'_\parallel|\omega)\}]\!], \end{aligned} \tag{25b}$$

where $\mathbf{J}_E(\mathbf{x}_\parallel|\omega)_{\mathrm{inc}} = \mathbf{n} \times \mathbf{E}(\mathbf{x}|\omega)_{\mathrm{inc}}|_{x_3 = \zeta(\mathbf{x}_\parallel)}$.

In obtaining Eq. (25) we have used the results

$$\begin{aligned}\lim_{\eta \to 0^+} \int \mathrm{d}^2 x'_\parallel \, \mathbf{n}(\mathbf{x}_\parallel) \times &\left\{ \boldsymbol{\nabla} \times \left[g(\mathbf{x}|\mathbf{x}') \Big|_{\substack{x_3 = \zeta(\mathbf{x}_\parallel) \\ x'_3 = \zeta(\mathbf{x}'_\parallel) \pm \eta}} \mathbf{J}(\mathbf{x}'_\parallel|\omega) \right] \right\} \\ &= \pm 2\pi \, \mathbf{J}(\mathbf{x}_\parallel|\omega) + P \int \mathrm{d}^2 x'_\parallel \, \mathbf{n}(\mathbf{x}_\parallel) \times \left\{ [\![\boldsymbol{\nabla} \times [g(\mathbf{x}|\mathbf{x}')]\!] \, \mathbf{J}(\mathbf{x}'_\parallel|\omega)] \right\}, \end{aligned} \tag{26}$$

where $g(\mathbf{x}|\mathbf{x}')$ is either $g_0(\mathbf{x}|\mathbf{x}')$ or $g_\varepsilon(\mathbf{x}|\mathbf{x}')$, $\mathbf{J}(\mathbf{x}_\parallel|\omega)$ is either $\mathbf{J}_H(\mathbf{x}_\parallel|\omega)$ or $\mathbf{J}_E(\mathbf{x}_\parallel|\omega)$, and P denotes the Cauchy principal value. Equations of the type of Eq. (25) are called Müller integral equations.[26,27] These equations are convenient for numerical calculations. Because $g_0(\mathbf{x}|\mathbf{x}')$ and $g_\varepsilon(\mathbf{x}|\mathbf{x}')$ have the same limiting behavior as $\mathbf{x}' \to \mathbf{x}$, the most divergent terms in the integrands, associated with the second derivatives of these Green's functions, cancel, rendering the resulting integrals integrable. The terms containing the first derivatives of the Green's functions possess integrable singularities.

From the definitions of $\mathbf{J}_{H,E}(\mathbf{x}_\parallel|\omega)$ it follows that $\mathbf{n} \cdot \mathbf{J}_{H,E}(\mathbf{x}_\parallel|\omega) = 0$. Therefore $\mathbf{J}_{H,E}(\mathbf{x}_\parallel|\omega)$ have only two independent elements, which we choose to be $J_{H,E}(\mathbf{x}_\parallel|\omega)_1$ and $J_{H,E}(\mathbf{x}_\parallel|\omega)_2$. The elements $J_{H,E}(\mathbf{x}_\parallel|\omega)_3$ are then obtained from the analogues of Eq. (6). Equations (25) thus provide a system of four coupled, inhomogeneous two-dimensional integral equations for $J_{H,E}(\mathbf{x}_\parallel|\omega)_{1,2}$.

By the use of a local impedance boundary condition,[28]

$$J_E(\mathbf{x}_\parallel|\omega)_i = K_{ij}(\mathbf{x}_\parallel|\omega) J_H(\mathbf{x}_\parallel|\omega)_j \qquad (i = 1, 2), \tag{27}$$

the dependence on $J_E(\mathbf{x}_\parallel|\omega)_{1,2}$ can be removed from Eq. (25a), yielding a pair of coupled, inhomogeneous, two-dimensional, integral equations for $J_H(\mathbf{x}_\parallel|\omega)_{1,2}$. These equations are converted into matrix equations in the manner described in Section 2, which are then solved by the biconjugate gradient stabilized method. The solutions are used to calculate the contribution to the mean differential reflection coefficient from the light scattered incoherently, by the use of the expressions obtained in Section 2.

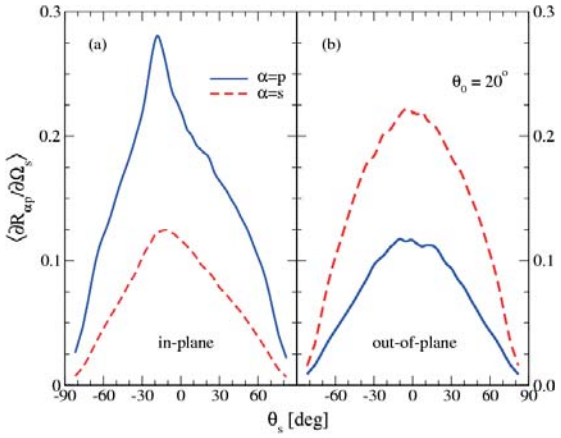

Figure 6. The mean differential reflection coefficients, $\langle \partial R_{\alpha p}/\partial \Omega_s \rangle$ $(p \to \alpha)$ for a p-polarized incident beam of wavelength $\lambda = 632.8$nm and width $w = 4\lambda$, whose polar angle of incidence is $\theta_0 = 20°$, as functions of the polar scattering angle θ_s for the (a) in-plane and (b) out-of-plane scattering. Negative values for θ_s are interpreted as in the caption to Fig. 2. The scattering system assumed in obtaining these results consisted of a silver substrate ($\varepsilon(\omega) = -16 + \mathrm{i}1.088$) separated from vacuum by a Gaussian-correlated randomly rough surface of rms-height $\delta = \lambda/4$ and correlation length $a = \lambda/2$. The randomly rough surface covered an area of $16\lambda \times 16\lambda$ and the discretization length used in the numerical calculations was $\Delta x = \lambda/7$ thus resulting in a 112×112 grid of $\mathbf{x}_\parallel$ values. A total of 5 000 surface realizations were used to calculate $\langle \partial R_{\alpha p}/\partial \Omega_s \rangle$. (After Ref. 14).

3.2 Results for a Penetrable Surface

3.2.1 A Metallic Surface

We first present results for scattering from a metallic surface. We have carried out numerical simulations for the scattering of a p-polarized beam of light of wavelength $\lambda = 632.8$ nm and width parameter $w = 4\lambda$, incident on a randomly rough silver surface. The dielectric function of silver at this wavelength is $\varepsilon(\omega) = -16.00 + \mathrm{i}1.088$.[29] The surface roughness is characterized by the Gaussian power spectrum (16) with a correlation length $a = \lambda/2$, and an rms height $\delta = \lambda/4$. The rough surface was assumed to cover an area $16\lambda \times 16\lambda$ on the mean scattering surface, and the discretization length Δx was $\lambda/7$ on a 112×112 grid of $\mathbf{x}_\parallel$ values.

In Fig. 6 we present the mean differential reflection coefficients as functions of the polar scattering angle θ_s for the in-plane [Fig. 6(a)] and out-of-plane ($\phi_s = \pm 90°$) [Fig. 6(b)], co-(p→p) and cross-(p→s) scattering of the beam when the polar and azimuthal angles of incidence (θ_0, ϕ_0) are $(20°, 0°)$. The results obtained from $N_p = 5\,000$ realizations of the surface profile function were averaged to obtain these results. The calculations required 96 CPU seconds on a 2.67 GHz Intel i7 CPU for each realization of the surface profile function. The peak at $\theta_s = -20°$ in the mean differential reflection coefficient for in-plane co-polarized scattering plotted in Fig. 6(a) is the enhanced backscattering peak.

For the same parameters we present in Figs. 7(a)–(c) the full angular distribution of the mean differential reflection coefficient when the polarization state of the scattered light is not recorded [Fig. 7(a)], when only the p-polarized component of the scattered light is recorded [Fig. 7(b)], and when only the s-polarized component of the scattered light is recorded [Fig. 7(c)]. Similar results, but for an s-polarized incident beam, are presented in Figs. 7(d)–(f). The peaks observed in Figs. 7(a), 7(b), 7(d), and 7(f) in the retroreflection direction ($\theta_s = \theta_0, \phi_s = \phi_0 + 180°$) are the enhanced backscattering peaks.

From a knowledge of the full angular distribution of the mean differential reflection coefficient, the conservation of energy in the scattering process can be checked by means of Eq. (17). For this purpose the full angular distribution of the mean differential reflection coefficient was calculated for "nonabsorbing" silver, *i.e.* for the

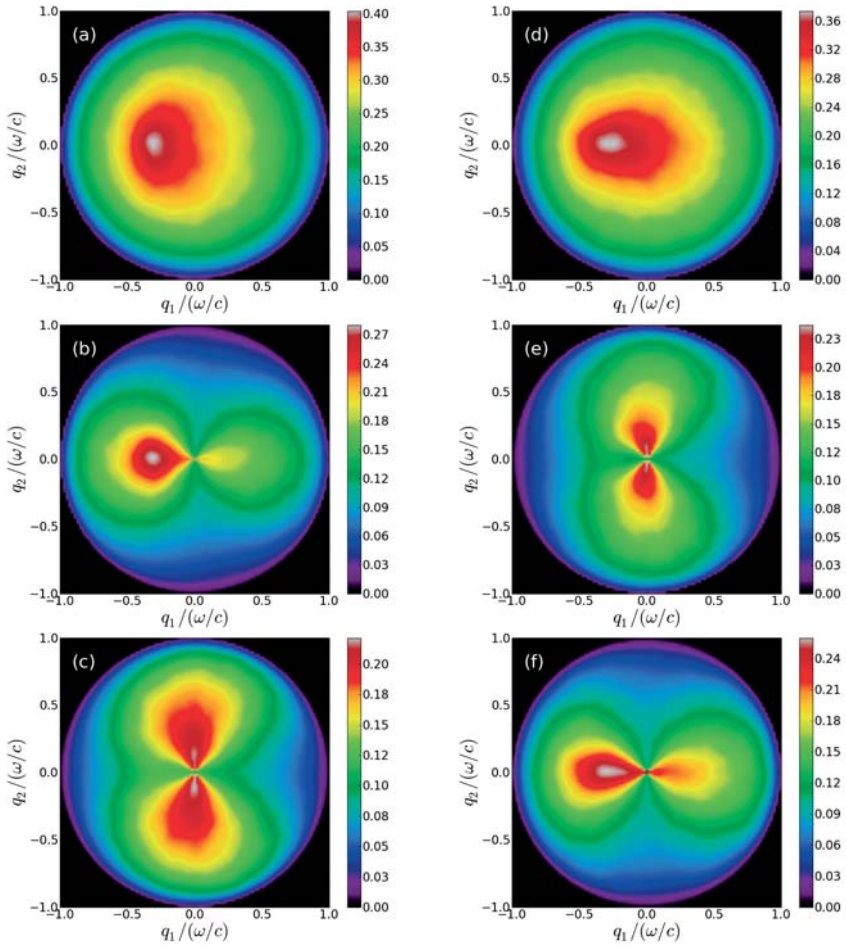

Figure 7. Similar to Fig. 3, but now the scattering medium is silver, and therefore penetrable. The roughness and numerical parameters assumed in obtaining these results are identical to those used to obtain the results of Fig. 6.

case in which the imaginary part of its dielectric function was set equal to zero, so that $\varepsilon(\omega) = -16.00$. For the parameters used in obtaining the results presented in Figs. 6 and 7 it was found that $U_{p,s}(20°, 0°) > 0.995$, a result that demonstrates the accuracy of our computational approach.

In order to obtain such a good unitarity value it was necessary to treat not only the diagonal elements of the matrix versions of Eq. (25) accurately, but also close-to-diagonal elements, because of the singular behavior of the Green's functions for small arguments. The need to treat close-to-diagonal matrix elements more accurately than matrix elements between more widely separated points in the solution of the volume integral equation arising in scattering from finite-sized objects has also been noted.[30] If the extended midpoint method was used in calculating the off-diagonal matrix elements, while the diagonal elements were treated exactly, as in [6] and [9], a value of $U_p(20°, 0°) = 0.834$ was obtained. The ability to calculate unitarity values, and the need to treat close-to-diagonal matrix elements accurately to obtain good unitarity values, are some of the main results of this work.

4. SOLUTION OF THE REDUCED RAYLEIGH EQUATIONS

4.1 Mathematical Formulation

The calculation of the electromagnetic field scattered from a randomly rough surface of a penetrable medium is greatly simplified if the field in the scattering medium does not need to be taken into account. The use of an impedance boundary condition at the interface between the medium of incidence and the scattering medium accomplishes this, so that only the field in the medium of incidence needs to be determined.

The same result can also be achieved by the use of the reduced Rayleigh equation for calculating the scattered field. In this section we present this equation and describe its numerical solution.

We begin by writing the electric field in the vacuum region $x_3 > \zeta(\mathbf{x}_\parallel)$ as the sum of an incident and a scattered field, $\mathbf{E}(\mathbf{x};t) = \left[\mathbf{E}^{(i)}(\mathbf{x}|\omega) + \mathbf{E}^{(s)}(\mathbf{x}|\omega)\right]\exp(-\mathrm{i}\omega t)$, where

$$\mathbf{E}^{(i)}(\mathbf{x}|\omega) = \left\{\frac{c}{\omega}\left[\alpha_0(k_\parallel)\hat{\mathbf{k}}_\parallel + k_\parallel\hat{\mathbf{x}}_3\right]\mathcal{E}_p^{(i)}(\mathbf{k}_\parallel) + [\hat{\mathbf{k}}_\parallel\times\hat{\mathbf{x}}_3]\,\mathcal{E}_s^{(i)}(\mathbf{k}_\parallel)\right\}\exp\left[\mathrm{i}\mathbf{k}_\parallel\cdot\mathbf{x}_\parallel - \mathrm{i}\alpha_0(k_\parallel)x_3\right], \tag{28a}$$

$$\mathbf{E}^{(s)}(\mathbf{x}|\omega) = \int\frac{\mathrm{d}^2q_\parallel}{(2\pi)^2}\left\{\frac{c}{\omega}\left[-\alpha_0(q_\parallel)\hat{\mathbf{q}}_\parallel + q_\parallel\hat{\mathbf{x}}_3\right]\mathcal{E}_p^{(s)}(\mathbf{q}_\parallel) + [\hat{\mathbf{q}}_\parallel\times\hat{\mathbf{x}}_3]\,\mathcal{E}_s^{(s)}(\mathbf{q}_\parallel)\right\}\exp\left[\mathrm{i}\mathbf{q}_\parallel\cdot\mathbf{x}_\parallel + \mathrm{i}\alpha_0(q_\parallel)x_3\right]. \tag{28b}$$

Note that the factors appearing in Eq. (28) in front of $\mathcal{E}_\alpha^{(i)}(\mathbf{k}_\parallel)$ and $\mathcal{E}_\alpha^{(s)}(\mathbf{q}_\parallel)$ ($\alpha = p, s$) are the polarization vectors as defined previously in Section 2.1, but now written out explicitly. Maxwell's equations imply a linear relation between the amplitudes $\mathcal{E}_\alpha^{(s)}(\mathbf{q}_\parallel)$ and $\mathcal{E}_\beta^{(i)}(\mathbf{k}_\parallel)$ of the form ($\alpha = p, s$, $\beta = p, s$)

$$\mathcal{E}_\alpha^{(s)}(\mathbf{q}_\parallel) = \sum_\beta R_{\alpha\beta}(\mathbf{q}_\parallel|\mathbf{k}_\parallel)\mathcal{E}_\beta^{(i)}(\mathbf{k}_\parallel). \tag{29}$$

The contribution to the mean differential reflection coefficient from the incoherent (diffuse) component of the scattered light, when incident light of β polarization (whose wave vector has the projection $\mathbf{k}_\parallel$ on the mean scattering surface) into light of α polarization (whose wave vector has the projection $\mathbf{q}_\parallel$ on the mean scattering surface), is given by

$$\left\langle\frac{\partial R_{\alpha\beta}}{\partial\Omega_s}\right\rangle_{\mathrm{incoh}} = \frac{1}{S}\left(\frac{\omega}{2\pi c}\right)^2\frac{\cos^2\theta_s}{\cos\theta_0}\left[\left\langle\left|R_{\alpha\beta}(\mathbf{q}_\parallel|\mathbf{k}_\parallel)\right|^2\right\rangle - \left|\left\langle R_{\alpha\beta}(\mathbf{q}_\parallel|\mathbf{k}_\parallel)\right\rangle\right|^2\right], \tag{30}$$

where S is the area of the plane $x_3 = 0$ covered by the rough surface.

It was shown by Celli and his colleagues[32] by the use of the Rayleigh hypothesis,[33] the extinction theorem,[34] and the vectorial equivalent of the Kirchhoff integral,[35] that the scattering amplitudes $R_{\alpha\beta}(\mathbf{q}_\parallel|\mathbf{k}_\parallel)$ satisfy the matrix integral equation

$$\int\frac{\mathrm{d}^2q_\parallel}{(2\pi)^2}\,\frac{I(\alpha(p_\parallel)-\alpha_0(q_\parallel)|\mathbf{p}_\parallel-\mathbf{q}_\parallel)}{\alpha(p_\parallel)-\alpha_0(q_\parallel)}\,\mathbf{M}(\mathbf{p}_\parallel|\mathbf{q}_\parallel)\mathbf{R}(\mathbf{q}_\parallel|\mathbf{k}_\parallel) = -\frac{I(\alpha(p_\parallel)+\alpha_0(k_\parallel)|\mathbf{p}_\parallel-\mathbf{k}_\parallel)}{\alpha(p_\parallel)+\alpha_0(k_\parallel)}\mathbf{N}(\mathbf{p}_\parallel|\mathbf{k}_\parallel), \tag{31}$$

with R_{pp} and R_{ps} forming the first row of the matrix $\mathbf{R}$, where

$$I(\gamma|\mathbf{Q}_\parallel) = \int\mathrm{d}^2x_\parallel\exp\left[-\mathrm{i}\gamma\zeta(\mathbf{x}_\parallel)\right]\exp\left[-\mathrm{i}\mathbf{Q}_\parallel\cdot\mathbf{x}_\parallel\right], \tag{32}$$

and $\alpha(p_\parallel) = [\varepsilon(\omega)(\omega/c)^2 - p_\parallel^2]^{\frac{1}{2}}$, with $\mathrm{Re}\,\alpha(p_\parallel) > 0$, $\mathrm{Im}\,\alpha(p_\parallel) > 0$. The matrices $\mathbf{M}(\mathbf{p}_\parallel|\mathbf{q}_\parallel)$ and $\mathbf{N}(\mathbf{p}_\parallel|\mathbf{k}_\parallel)$ are given by

$$\mathbf{M}(\mathbf{p}_\parallel|\mathbf{q}_\parallel) = \begin{pmatrix}[p_\parallel q_\parallel + \alpha(p_\parallel)\hat{\mathbf{p}}_\parallel\cdot\hat{\mathbf{q}}_\parallel\alpha_0(q_\parallel)] & -\frac{\omega}{c}\alpha(p_\parallel)\,[\hat{\mathbf{p}}_\parallel\times\hat{\mathbf{q}}_\parallel]_3\\ \frac{\omega}{c}[\hat{\mathbf{p}}_\parallel\times\hat{\mathbf{q}}_\parallel]_3\,\alpha_0(q_\parallel) & \frac{\omega^2}{c^2}\hat{\mathbf{p}}_\parallel\cdot\hat{\mathbf{q}}_\parallel\end{pmatrix} \tag{33a}$$

and

$$\mathbf{N}(\mathbf{p}_\parallel|\mathbf{k}_\parallel) = \begin{pmatrix}[p_\parallel k_\parallel - \alpha(p_\parallel)\hat{\mathbf{p}}_\parallel\cdot\hat{\mathbf{k}}_\parallel\alpha_0(k_\parallel)] & -\frac{\omega}{c}\alpha(p_\parallel)\,[\hat{\mathbf{p}}_\parallel\times\hat{\mathbf{k}}_\parallel]_3\\ -\frac{\omega}{c}[\hat{\mathbf{p}}_\parallel\times\hat{\mathbf{k}}_\parallel]_3\,\alpha_0(k_\parallel) & \frac{\omega^2}{c^2}\hat{\mathbf{p}}_\parallel\cdot\hat{\mathbf{k}}_\parallel\end{pmatrix}. \tag{33b}$$

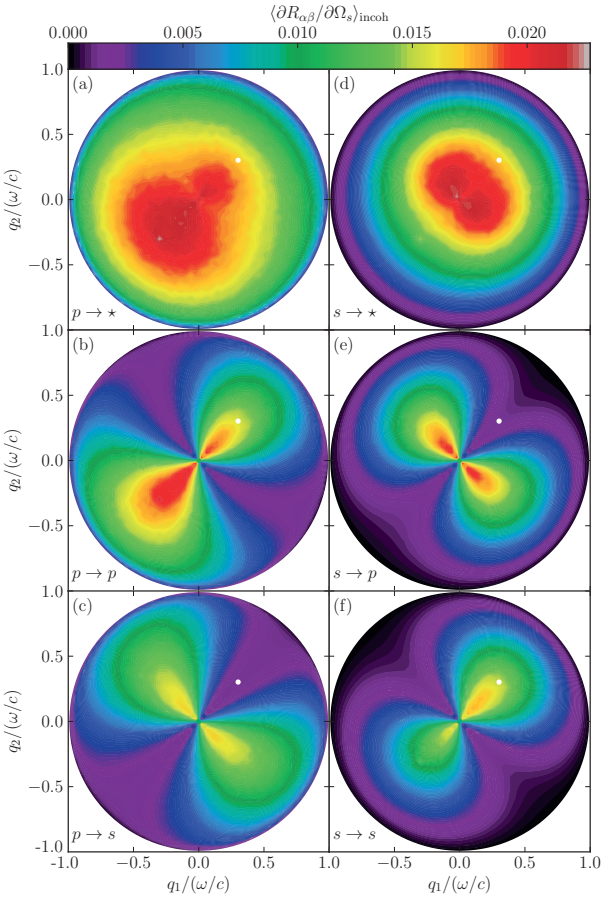

Figure 8. Full angular intensity distribution of the light scattered incoherently from a two-dimensional randomly rough silver surface calculated by solving the reduced Rayleigh equations. Light of either p (left column) or s polarization (right column) is incident on the surface at angles of incidence $(\theta_0, \phi_0) = (25^\circ, 45^\circ)$. The wavelength (in vacuum) of the incident light is $\lambda = 632.8\,\text{nm}$ for which frequency $\omega = 2\pi/\lambda$ the dielectric function of silver is $\varepsilon(\omega) = -16.0 + 1.088\text{i}$. The white dots indicate the position of the specular direction. The surface parameters assumed in these calculations are $L = 25\lambda$; $\delta = \lambda/40$; and $a = \lambda/4$. The surface was discretized so that $Q = 6.4\omega/c$ or equivalently $\Delta x = \pi/Q \approx 0.0781\lambda$. Figures 8(a)–(c) correspond to a p-polarized plane incident wave, while in Figs. 8(d)–(f) the incident plane wave is s polarized. In Figs. 8(a) and (d) all scattered light is recorded, *i.e.* no distinction is made between scattered p- and s-polarized light. However, in Figs. 8(b) and (e) only the scattered p-polarized light is recorded, while Figs. 8(c) and (f) include only s-polarized scattered light. The presented figures were obtained by averaging the results for the differential reflection coefficient obtained for $N_p = 10\,000$ surface realizations.

Although purely numerical, nonperturbative solutions of the reduced Rayleigh equations for the scattering of light from one-dimensional randomly rough clean metal surfaces[36,37] and coated perfectly conducting surfaces[38,39] have been carried out, up to now Eq. (31) has been solved only by small-amplitude perturbation theory through terms of third order in the surface profile fuction.[23,40,41] Here we present some preliminary results for the mean differential reflection coefficient obtained by a purely numerical, nonperturbative solution of Eqs. (31)–(33). This was done by generating a realization of the surface profile as this was done in the preceding two sections, and evaluating the function $I(\gamma|\mathbf{Q}_\parallel)$ by expanding the integrand in Eq. (32) in powers of $\zeta(\mathbf{x}_\parallel)$, and

calculating the Fourier transform of $\zeta^n(\mathbf{x}_\parallel)$ by the Fast Fourier Transform. As in previous sections, the random surface covered a square region of the x_1x_2 plane of edge L, and a grid of N^2 points was created within this square so that the (linear) sampling interval is $\Delta x = L/N$. The infinite limits of integration in Eq. (31) were replaced by finite ones: $|q_1| < Q/2$, $|q_2| < Q/2$ where $Q = \pi/\Delta x$. A quadratic grid within the square region of the q_1q_2 plane of edge Q was constructed with a grid constant $\Delta q = 2\pi/L$. The integral over this region in Eq. (31) was carried out by a two-dimensional version of the extended midpoint method, and the values of $R_{\alpha\beta}(\mathbf{q}_\parallel|\mathbf{k}_\parallel)$ were calculated for values of $\mathbf{q}_\parallel$ at the points of this grid for a given value of $\mathbf{k}_\parallel$, which was a point on the same grid. The resulting matrix equations were solved by LU factorization. This is a slower solution method than the biconjugate gradient stabilized method, but has the advantage of being able to handle multiple right-hand sides, *i.e.* different angles of incidence, more-or-less with no extra addition to the computational time. With the reflection amplitudes, $R_{\alpha\beta}(\mathbf{q}_\parallel|\mathbf{k}_\parallel)$, available, the differential reflection coefficient was then calculated by the use of Eq. (30).

4.2 Results Obtained by the Solution of the Reduced Rayleigh Equations

4.2.1 A Metallic Surface

As the first example of the application of this approach to the scattering of light from a penetrable surface we apply it to the scattering of a p- or s-polarized plane wave of wavelength $\lambda = 632.8$ nm incident on a silver surface. The dielectric function of silver at this wavelength is $\varepsilon(\omega) = -16 + \mathrm{i}1.088$.[29] The roughness of the surface was characterized by the Gaussian power spectrum, Eq. (16), where the transverse correlation length was given the value $a = \lambda/4$, while the rms height of the surface was $\delta = \lambda/40$. In the calculations the rough surface was assumed to cover an area of $25\lambda \times 25\lambda$ of the plane $x_3 = 0$, while for the wavenumber cut-off we assumed $Q = 6.4\omega/c$, which corresponds to a spatial discretization interval of $\Delta x = \pi/Q \approx 0.0781\lambda$ (for both directions).

In Fig. 8 we present contributions to the mean differential reflection coefficients from the light scattered incoherently as functions of q_1 and q_2 when a plane wave is incident on the surface at angles $(\theta_0, \phi_0) = (25^\circ, 45^\circ)$. Figure 8(a) corresponds to a p-polarized incident plane wave being scattered by the rough surface into both p- and s-polarized light, *i.e.* the polarization state of the scattered light was not recorded. However, in Figs. 8(b) and 8(c) contour plots of the same quantity are presented for the cases where only p-polarized or s-polarized scattered light, respectively, are recorded. Similar results are presented in Figs. 8(d)–(f) for the case when the incident light is s-polarized. An arithmetic average of results obtained for $N_p = 10\,000$ realizations of the surface profile function was carried out to produce Fig. 8.

By artificially putting the imaginary part of the dielectric constant of the metal to zero, $\mathrm{Im}\,\varepsilon(\omega) \equiv 0$, so that there is no absorption in the scattering system, it has been found that the numerical method used to solve the reduced Rayleigh equation, Eq. (31), conserves energy with an error smaller than 0.5% for the parameters assumed here.

The numerical calculations used to obtain the results of Fig. 8 required for each realization of the surface profile function approximately 8.8 cpu hours on a single 12-core 2.4 GHz AMD Opteron computer node and using approximately 20 GB of memory.

The calculations whose results are presented in Fig. 8 and which were performed by solving numerically the reduced Rayleigh equations (31), could also have been done by solving the Müller equations, as was discussed in Section 3. In order to compare the two approaches, we present in Fig. 9 the results obtained by these two methods for the contributions to the mean differential reflection coefficients from the light scattered incoherently as functions of the polar scattering angle θ_s for the in-plane ($\phi_s = 0^\circ, 180^\circ$) and out-of-plane ($\phi_s = \pm 90^\circ$) co-($s \to s$) and cross-($s \to p$) polarized scattering when an s-polarized wave is incident on the surface at angles of incidence $(\theta_0, \phi_0) = (25^\circ, 0^\circ)$. The roughness parameters assumed in obtaining these results are identical to those assumed in obtaining Fig. 8. The numerical parameters used to obtain these results were those of Fig. 8 when using the reduced Rayleigh equation. However, when solving the Müller equations, a Gaussian beam of width ($w = 4\lambda$) was assumed to be incident on the surface, which was discretized with an interval $\Delta x = \lambda/7$ (in both directions). It is observed from Fig. 9 that the two approaches produce quantitatively similar results. The minor differences between the results of the two approaches we believe are due to the differences in the areas covered by the rough surfaces, and to the differences in the discretization intervals, assumed in the two sets of calculations, which have not been optimized as yet.

From the results presented in Figs. 8 and 9, we can draw the conclusions that a purely numerical, nonperturbative solution of the reduced Rayleigh equation yields accurate results for the mean differential reflection coefficient that are in good agreement with those obtained by the use of the Müller equations.

4.2.2 A Dielectric Surface

The reduced Rayleigh equation (31) can also be used for calculating the field scattered from a dielectric surface. We apply it here to calculate the contribution to the mean differential reflection coefficient from the incoherent component of the scattered light when a p- or s-polarized plane wave whose wavelength in vacuum is $\lambda = 632.8$ nm is incident at $(\theta_0, \phi_0) = (27.5°, 45°)$ on the surface of a dielectric medium whose dielectric constant is assumed to be $\varepsilon_d = 2.64$ (photoresist). The results are presented in Fig. 10. The randomly rough surface had an rms roughness of $\delta = 3\lambda/200 = 0.015\lambda$ and it covered a $20\lambda \times 20\lambda$ area in the $x_3 = 0$ plane. Moreover, the wavenumber cut-off assumed in these calculations was $Q = 8\omega/c$, corresponding to a discretization interval of $\Delta x = \pi/Q = 0.0625\lambda$. Except for these differences, the remaining roughness and computational parameters were the same as the ones assumed in the calculations that produced Fig 8.

By comparing Figs. 8 and 10 it is observed that the overall structure of the angular distributions of the intensity of the light scattered from a metal and dielectric is rather similar, and that, as expected, the scattered intensity for the metallic surface is stronger (by a factor of about 70) than that for the dielectric surface.

5. DISCUSSION AND CONCLUSIONS

We have shown that the use of the method of moments and the biconjugate gradient stabilized method provides a formally exact solution to the scattering of p- and s-polarized light from a two-dimensional randomly rough perfectly conducting surface, with a modest expenditure of computational time. The addition of an impedance boundary condition on a two-dimensional rough surface to these two methods has been shown to provide a formally exact solution to the scattering of polarized light from two-dimensional randomly rough metallic surfaces, also with a modest expenditure of computational time.

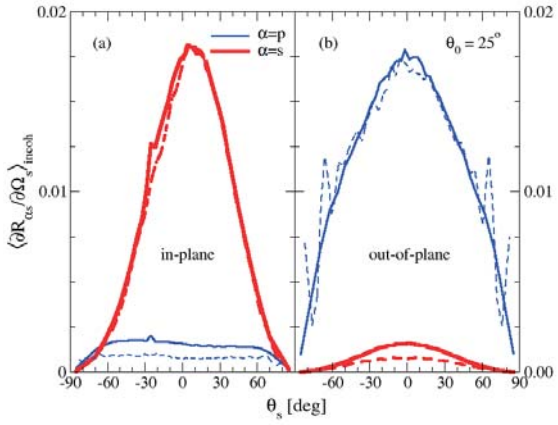

Figure 9. Comparison of the mean differential reflection coefficients for the scattering of s polarized waves from a rough silver surface with the roughness parameters given in the caption of Fig. 8. The results were obtained by two different numerical approaches: the solution of the reduced Rayleigh equation (solid lines), and by the use of the rigorous approach (dashed lines). The numerical parameters and number of surface realizations assumed when using the former approach were those used to obtain the results presented in Fig. 8. However, when using the rigorous approach, the parameters given in the caption to Fig. 6 were assumed with the exception that now $\theta_0 = 25°$, $L = 20\lambda$, and only a small number of surface realizations were used ($N_p = 750$) to obtain these results.

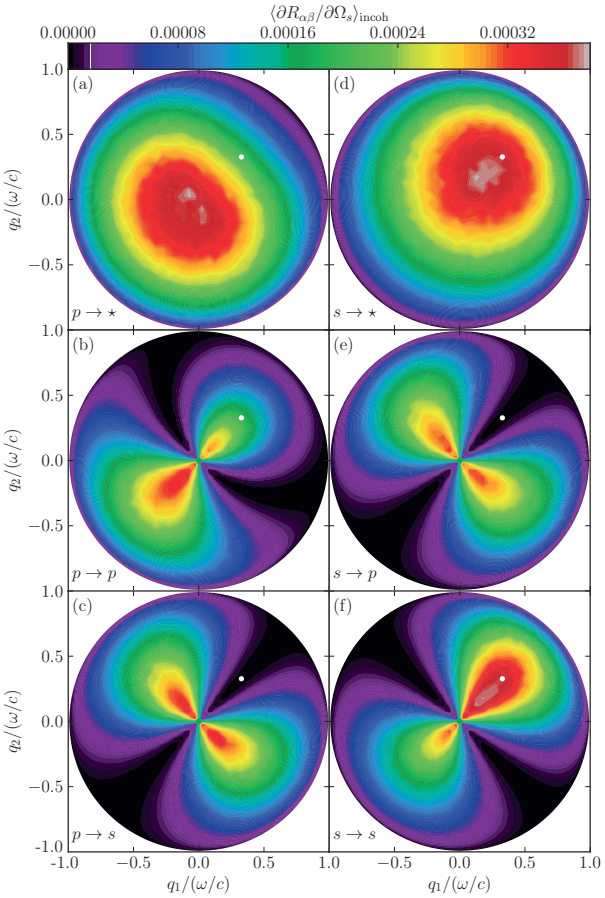

Figure 10. Full angular intensity distribution of the light scattered incoherently from a two-dimensional randomly rough dielectric surface calculated by solving the reduced Rayleigh equations. The dielectric substrate was taken to be photoresist which at the frequency of the incident light $\lambda = 632.8\,\text{nm}$ is characterized by a dielectric constant $\varepsilon(\omega) = 2.64$. The angles of incidence assumed are $(\theta_0, \phi_0) = (27.5^\circ, 45^\circ)$, and the white dots indicate the position of the specular direction. These figures were obtained by averaging results for the scattered intensity obtained for $N_p = 6\,000$ surface realizations. The surface parameters assumed in these calculations were $L = 20\lambda$; $\delta = 3\lambda/200 = 0.015\lambda$; and $a = \lambda/4$. The surface discretization was done so that $Q = 8\omega/c$, or equivalently, $\Delta x = \pi/Q = 0.0625\lambda$. The remaining parameters and the organization of the sub-figures are identical to those of Fig. 8.

The computational methods employed in these calculations have made it possible to obtain a formally exact full angular distribution of the intensity of the light scattered from a strongly rough random surface. In the case of scattering from a perfectly conducting surface, and from a metallic surface when the imaginary part of its dielectric function is set equal to zero, knowledge of the full angular distribution of the intensity of the scattered light enables the conservation of energy in the scattering process to be checked. It was found to be satisfied with an error smaller than 0.5%, a result that testifies to the accuracy of the methods used in our calculations and the adequacy of the discretization of the mean scattering surface employed in them.

We have also presented results obtained from a rigorous numerical solution of the reduced Rayleigh equation for the scattering of p- and s-polarized light from a penetrable surface. These results demonstrate the feasibility

of using this equation in studies of the scattering of light from weakly rough surfaces. The good agreement between the results obtained by the solution of the reduced Rayleigh equation and those obtained by the use of the rigorous computational method indicates that the simpler approach yields accurate results for scattering from surfaces that are not very rough. The limits of validity of this equation have yet to be determined.

The success of the methods used in carrying out the calculations described here opens the door to rigorous computational studies of other properties of electromagnetic waves scattered from two-dimensional randomly rough surfaces. These include calculations of the ellipsometric parameters of metallic and dielectric surfaces, transmission through dielectric surfaces, and all of the elements of the Mueller matrix for scattering from and transmission through such surfaces. This work will be reported elsewhere.

ACKNOWLEDGMENTS

The research of T.A.L. and A.A.M. was supported in part by AFRL contract FA9453-08-C-0230. The research of I.S. was supported in part by the Research Council of Norway (Småforsk Grant). We are grateful to NOTUR (the Norwegian Metacenter for Computational Science) for the allocation of computer time.

REFERENCES

1. P. Tran, V. Celli, and A.A. Maradudin, "Electromagnetic scattering from a two-dimensional, randomly rough, perfectly conducting surface: Iterative methods," J. Opt. Soc. Am. A **11**, 1685–1689 (1994).
2. R.L. Wagner, J. Song, and W.C. Chew, "Monte Carlo simulation of electromagnetic scattering from two-dimensional random rough surfaces," IEEE Trans. Antennas Propag. **45**, 235–245 (1997).
3. K. Pak, L. Tsang, C.H. Chan, and J.T. Johnson, "Backscattering enhancement of electromagnetic waves from two-dimensional perfectly conducting random rough surfaces based on Monte Carlo simulations," J. Opt. Soc. Am. A **12**, 2491–2499 (1995).
4. J.T. Johnson, L. Tsang, R.T. Shin, K. Pak, C.H. Chan, A. Ishimaru, and Y. Kuga, "Backscattering enhancement of electromagnetic waves from two-dimensional perfectly conducting random rough surfaces: a comparison of Monte Carlo simulations with experimental data," IEEE Trans. Antennas Propag. **44**, 748–756 (1996).
5. D. Torrungrueng, H.-T. Chou, and J.T. Johnson, "A novel acceleration algorithm for the computation of scattering from two-dimensional large-scale perfectly conducting random rough surfaces with the forward-backward method," IEEE Trans. Geosci. Remote Sensing **38**, 1656–1668 (2000).
6. G. Soriano and M. Saillard, "Scattering of electromagnetic waves from two-dimensional rough surfaces with an impedance approximation," J. Opt. Soc. Am. A **18**, 124–133 (2001).
7. I. Simonsen, A.A. Maradudin, and T.A. Leskova, "Scattering of electromagnetic waves from two-dimensional randomly rough perfectly conducting surfaces: The full angular intensity disribution," Phys. Rev. A **81**, 013806 (1–13) (2010).
8. I. Simonsen, J.B. Kryvi, A.A. Maradudin, and T.A. Leskova, "Light scattering from anisotropic, randomly rough, perfectly conducting surfaces," Comp. Phys. Commun. **182**, 1904–1908 (2011).
9. P. Tran and A.A. Maradudin, "Scattering of electromagnetic waves from a randomly rough 2D metallic surface," Opt. Commun. **110**, 269–273 (1994).
10. L. Tsang, C.H. Chan, and K. Pak, "Backscattering enhancement of a two-dimensional random rough surface (three-dimensional scattering) based on Monte Carlo simulations," J. Opt. Soc. Am. A **11**, 711–715 (1994).
11. K. Pak, L. Tsang, and J.T. Johnson, "Numerical simulations and backscattering enhancement of electromagnetic waves from two-dimensional dielectric random rough surfaces with the sparse-matrix canonical grid method," J. Opt. Soc. Am. A **14**, 1515–1529 (1997).
12. N. Engheta, W.D. Murphy, V. Rokhlin, and M.S. Vassiliou, "The fast multipole method (FMM) for electromagnetic scattering problems," IEEE Trans. Antennas Propag. **40**, 634–641 (1992).
13. V. Jandhyala, B. Shanker, E. Michielssen and W.C. Chew, "Fast algorithm for the analysis of scattering by dielectric rough surfaces," J. Opt. Soc. Am. A **15**, 1877–1885 (1998).
14. I. Simonsen, A.A. Maradudin, and T.A. Leskova, "Scattering of electromagnetic waves from two-dimensional randomly rough penetrable surfaces," Phys. Rev. Lett. **104**, 223904 (1–4) (2010).

15. A.A. Maradudin, T. Michel, A.R. McGurn, and E.R. Méndez, "Enhanced backscattering of light from a random grating," Ann. Phys. (N.Y.) **203**, 255–307 (1990).
16. J.A. Kong, *Electromagnetic Theory*, 3rd ed. (EMW Publishing, Cambridge, MA, 2005), p. 674.
17. W.H. Press, S.A. Teukolsky, W.T. Vetterling, and B. P. Flannery, *Numerical Recipes in Fortran*, 2nd ed. (Cambridge, University Press, New York, 1992), p. 129.
18. H. Van der Vorst, "Bi-CGSTAB: A fast and smoothly converging variant of Bi-CG for the solution of nonsymmetric linear systems," SIAM J. Sci. Stat. Comp. **13**, 631–644 (1992).
19. A.R. McGurn, A.A. Maradudin and V. Celli, "Localization effects in the scattering of light from a randomly rough grating," Phys. Rev. B**31**, 4866–4871 (1985).
20. E.R. Méndez and K.A. O'Donnell, "Observation of depolarization and backscattering enhancement in light scattering from Gaussian random surfaces," Opt. Commun. **61**, 91–95 (1987).
21. D. Torrungrueng and J.T. Johnson, "Numerical studies of backscattering enhancement of electromagnetic waves from two-dimensional random rough surfaces with the forward-backward/novel spectral acceleration method," J. Opt. Soc. Am. A **18**, 2518–2526 (2001).
22. E.I. Chaikina, P. Negrete-Regagnon, V. Ruiz-Cortés, and E.R. Méndez, "Measurements of the hemispherical scattering distribution function of rough dielectric surfaces," Opt. Commun. **205** 215–221 (2002).
23. A.R. McGurn and A.A. Maradudin, "Perturbation theory results for the diffuse scattering of light from two-dimensional randomly rough surfaces," Waves in Random Media **6**, 251–267 (1996).
24. W. Franz, "Zur Formulierung des Huygenschen Prinzips," Z. Naturforsch. **3a**, 500–506 (1948).
25. Ref. 16, pp. 674–675.
26. C. Müller, *Foundations of the Mathematical Theory of Electromagnetic Waves* (Springer-Verlag, Berlin, 1969), Secs. 21 and 23.
27. N. Morita, N. Kumagai, and J.R. Mautz, *Integral Equation Methods for Electromagnetics* (Artech House, Boston, 1990), Sec. 3.5.2.
28. A.A. Maradudin, "The impedance boundary condition at a two-dimensional rough metal surface," Opt. Commun. **116**, 452–467 (1995).
29. P.B. Johnson and R.W. Christy, "Optical Constants of the Noble Metals," Phys. Rev. B **6**, 4370–4379 (1972).
30. J.P. Kotthaus and O.J.F. Martin, "Accurate solution of the volume integral equation for high-permittivity scatterers," IEEE Trans. Antennas Propag. **48**, 1719-1726 (2000).
31. A.A. Maradudin and E.R. Méndez, "The utility of an impedance boundary condition in the scattering of light from one-dimensional randomly rough dielectric surfaces," Opt. Spectrosc. **80**, 409–420 (1996).
32. G.C. Brown, V. Celli, M. Haller, and A. Marvin, "Vector theory of light scattering from a rough surface: unitary and reciprocal expansions," Surf. Sci. **136**, 381–397 (1984).
33. Lord Rayleigh, *The Theory of Sound*, 2nd ed. (Dover, New York, 1945), vol. II, pp. 89-96, pp. 297–311.
34. E. Wolf, "A generalized extinction theorem and its role in scattering theory," in *Coherence and Quantum Optics*, eds. L. Mandel and E. Wolf (Plenum, New York, 1973), pp. 339-357.
35. J.D. Jackson, *Classical Electrodynamics*, 2nd ed. (Wiley, New York, 1962), Section 9.9.
36. T.R. Michel, "Resonant light scattering from weakly rough random surfaces and imperfect gratings," J. Opt. Soc. Am. A **11**, 1874–1885 (1994).
37. T.R. Michel, M.E. Knotts and K.A. O'Donnell, "Scattering by plasmon polaritons on a rough surface with a periodic component," J. Opt. Soc. Am. A **12**, 548–559 (1995).
38. A. Madrazo and A.A. Maradudin, "Numerical solution of the reduced Rayleigh equation for the scattering of electromagnetic waves from a rough dielectric film on perfectly conducting substrates," Opt. Commun. **134**, 251–263 (1997).
39. I. Simonsen and A.A. Maradudin, "Numerical solution of of electromagnetic waves scattered from planar dielectric films deposited on rough perfectly conducting substrates," Opt. Commun. **162**, 99–111 (1999).
40. J.T. Johnson, "Third order small perturbation method for scattering from dielectric rough surfaces," J. Opt. Soc. Am. A **16**, 2720–2736 (1999).
41. A. Soubret, G. Berginc, and C. Bourrely, "Application of reduced Rayleigh equations to electromagnetic wave scattering by two-dimensional randomly rough surfaces," Phys. Rev. B **63**, 245411 (1–20) (2003).

P. A. Letnes, A. A. Maradudin, T. Nordam, and I. Simonsen. "Calculation of all elements of the Mueller matrix for scattering of light from a two-dimensional randomly rough metal surface",
`http://arxiv.org/abs/1108.2599`. ***(accepted, Phys. Rev. A)*** **(2012)**

Paper 7

Calculation of all elements of the Mueller matrix for scattering of light from a two-dimensional randomly rough metal surface

P. A. Letnes,[1] A. A. Maradudin,[2] T. Nordam,[1] and I. Simonsen[1,*]

[1] *Department of Physics, Norwegian University of Science and Technology, NO-7491 Trondheim, Norway*
[2] *Department of Physics and Astronomy, and Institute for Surface and Interface Science, University of California, Irvine, CA 92697 USA*

We calculate all the elements of the Mueller matrix, which contain all the polarization properties of light scattered from a two-dimensional randomly rough lossy metal surface. The calculations are carried out for arbitrary angles of incidence by the use of nonperturbative numerical solutions of the reduced Rayleigh equations for the scattering of *p*- and *s*-polarized light from a two-dimensional rough penetrable surface.

PACS numbers: 42.25.-p, 41.20.-q

All the information about the polarization properties of light scattered from two-dimensional rough surfaces is contained in the Mueller matrix [1–3]. Yet, very few calculations of the elements of this matrix for a two-dimensional randomly rough surface have been carried out to date by any computational approach, largely because calculations of the scattering of light from such surfaces are still difficult to carry out [4–6]. An exception [7] is a calculation of the elements for two-dimensional randomly rough perfectly conducting and metallic surfaces characterized by a surface profile function that is a stationary, zero-mean, isotropic, Gaussian random process, defined by a Gaussian surface height autocorrelation function. These calculations were carried out by a ray-tracing approach on the assumption that the surface was illuminated at normal incidence. In this work it was also shown that due to the assumptions of normal incidence and the isotropy of the surface statistics, the elements of the corresponding Mueller matrix possess certain symmetry properties. Subsequently Zhang and Bahar [8] carried out an approximate analytic calculation of the elements of the Mueller matrix for the scattering of light from two-dimensional randomly rough dielectric surfaces coated uniformly with a coating of a different dielectric material.

In this paper we calculate, for arbitrary angles of incidence, all the elements of the Mueller matrix for the scattering of light from a two-dimensional randomly rough metal surface. The calculations are carried out on the basis of nonperturbative numerical solutions of the reduced Rayleigh equations for the scattering of *p*- and *s*-polarized light from a two-dimensional rough penetrable surface [6, 9].

The system we study consists of vacuum in the region $x_3 > \zeta(\mathbf{x}_\parallel)$, where $\mathbf{x}_\parallel = (x_1, x_2, 0)$, and a metal whose dielectric function is $\varepsilon(\omega)$ in the region $x_3 < \zeta(\mathbf{x}_\parallel)$. The surface profile function $\zeta(\mathbf{x}_\parallel)$ is assumed to be a single-valued function of $\mathbf{x}_\parallel$ that is differentiable with respect to x_1 and x_2, and constitutes a stationary, zero-mean, isotropic, Gaussian random process defined by $\left\langle \zeta(\mathbf{x}_\parallel)\zeta(\mathbf{x}'_\parallel)\right\rangle = \delta^2 W(|\mathbf{x}_\parallel - \mathbf{x}'_\parallel|)$. The angle brackets here and in all that follows denote an average over the ensemble of realizations of the surface profile function, and $\delta = \left\langle \zeta^2(\mathbf{x}_\parallel)\right\rangle^{\frac{1}{2}}$ is the rms height of the surface. Each realization of the surface profile function is generated numerically by a two-dimensional version of the filtering method used in Ref. [10].

We begin by writing the electric field in the vacuum region $x_3 > \zeta(\mathbf{x}_\parallel)$ as the sum of an incident and a scattered field, $\mathbf{E}(\mathbf{x}, t) = [\mathbf{E}^{(i)}(\mathbf{x}|\omega) + \mathbf{E}^{(s)}(\mathbf{x}|\omega)]\exp(-\mathrm{i}\omega t)$, where

$$\mathbf{E}^{(i)}(\mathbf{x}|\omega) = \left[\mathcal{E}_p^{(i)}(\mathbf{k}_\parallel)\hat{\mathbf{e}}_p^i(\mathbf{k}_\parallel) + \mathcal{E}_s^{(i)}(\mathbf{k}_\parallel)\hat{\mathbf{e}}_s^i(\mathbf{k}_\parallel)\right] \times \exp[\mathrm{i}\mathbf{k}_\parallel \cdot \mathbf{x}_\parallel - \mathrm{i}\alpha_0(k_\parallel)x_3], \quad (1a)$$

$$\mathbf{E}^{(s)}(\mathbf{x}|\omega) = \int \frac{\mathrm{d}^2 q_\parallel}{(2\pi)^2} \left[\mathcal{E}_p^{(s)}(\mathbf{q}_\parallel)\hat{\mathbf{e}}_p^s(\mathbf{q}_\parallel) + \mathcal{E}_s^{(s)}(\mathbf{q}_\parallel)\hat{\mathbf{e}}_s^s(\mathbf{q}_\parallel)\right] \times \exp[\mathrm{i}\mathbf{q}_\parallel \cdot \mathbf{x}_\parallel + \mathrm{i}\alpha_0(q_\parallel)x_3]. \quad (1b)$$

Here $\mathbf{k}_\parallel = (k_1, k_2, 0)$, the unit polarization vectors are $\hat{\mathbf{e}}_p^i(\mathbf{k}_\parallel) = (c/\omega)[\alpha_0(k_\parallel)\hat{\mathbf{k}}_\parallel + k_\parallel \hat{\mathbf{x}}_3]$, $\hat{\mathbf{e}}_s^i(\mathbf{k}_\parallel) = \hat{\mathbf{k}}_\parallel \times \hat{\mathbf{x}}_3$, $\hat{\mathbf{e}}_p^s(\mathbf{q}_\parallel) = (c/\omega)[-\alpha_0(q_\parallel)\hat{\mathbf{q}}_\parallel + q_\parallel \hat{\mathbf{x}}_3]$, $\hat{\mathbf{e}}_s^s(\mathbf{q}_\parallel) = \hat{\mathbf{q}}_\parallel \times \hat{\mathbf{x}}_3$, while $\alpha_0(q_\parallel) = [(\omega/c)^2 - q_\parallel^2]^{\frac{1}{2}}$, with $\mathrm{Re}\,\alpha_0(q_\parallel) > 0$, $\mathrm{Im}\,\alpha_0(q_\parallel) > 0$. A caret over a vector indicates that it is a unit vector. In terms of the polar and azimuthal angles of incidence (θ_0, ϕ_0) and scattering (θ_s, ϕ_s), the vectors $\mathbf{k}_\parallel$ and $\mathbf{q}_\parallel$ are given by $\mathbf{k}_\parallel = (\omega/c)\sin\theta_0(\cos\phi_0, \sin\phi_0, 0)$ and $\mathbf{q}_\parallel = (\omega/c)\sin\theta_s(\cos\phi_s, \sin\phi_s, 0)$.

A linear relation exists between the amplitudes $\mathcal{E}_\alpha^{(s)}(\mathbf{q}_\parallel)$ and $\mathcal{E}_\beta^{(i)}(\mathbf{k}_\parallel)$, which we write in the form ($\alpha = p, s$, $\beta = p, s$)

$$\mathcal{E}_\alpha^{(s)}(\mathbf{q}_\parallel) = \sum_\beta R_{\alpha\beta}(\mathbf{q}_\parallel|\mathbf{k}_\parallel)\mathcal{E}_\beta^{(i)}(\mathbf{k}_\parallel). \quad (2)$$

It was shown by Celli and his colleagues [9] that the scattering amplitudes $R_{\alpha\beta}(\mathbf{q}_\parallel|\mathbf{k}_\parallel)$ satisfy the matrix integral

equation (the reduced Rayleigh equation)

$$\int\frac{\mathrm{d}^2q_\parallel}{(2\pi)^2}\,\frac{I\left(\alpha(p_\parallel)-\alpha_0(q_\parallel)|\mathbf{p}_\parallel-\mathbf{q}_\parallel\right)}{\alpha(p_\parallel)-\alpha_0(q_\parallel)}\boldsymbol{\mathcal{N}}_+(\mathbf{p}_\parallel|\mathbf{q}_\parallel)\mathbf{R}(\mathbf{q}_\parallel|\mathbf{k}_\parallel)$$
$$=-\frac{I\left(\alpha(p_\parallel)+\alpha_0(k_\parallel)|\mathbf{p}_\parallel-\mathbf{k}_\parallel\right)}{\alpha(p_\parallel)+\alpha_0(k_\parallel)}\boldsymbol{\mathcal{N}}_-(\mathbf{p}_\parallel|\mathbf{k}_\parallel),\quad(3a)$$

with R_{pp} and R_{ps} forming the first row of the matrix $\mathbf{R}$, where

$$I(\gamma|\mathbf{Q}_\parallel)=\int\mathrm{d}^2x_\parallel\,\exp[-\mathrm{i}\gamma\zeta(\mathbf{x}_\parallel)]\exp(-\mathrm{i}\mathbf{Q}_\parallel\cdot\mathbf{x}_\parallel),\quad(3b)$$

and $\alpha(p_\parallel)=[\varepsilon(\omega)(\omega/c)^2-p_\parallel^2]^{\frac{1}{2}}$, with $\mathrm{Re}\,\alpha(p_\parallel)>0$, $\mathrm{Im}\,\alpha(p_\parallel)>0$. The matrices $\boldsymbol{\mathcal{N}}_\pm(\mathbf{p}_\parallel|\mathbf{q}_\parallel)$ are given by

$$\boldsymbol{\mathcal{N}}_\pm(\mathbf{p}_\parallel|\mathbf{q}_\parallel)=$$
$$\begin{pmatrix} p_\parallel q_\parallel\pm\alpha(p_\parallel)\hat{\mathbf{p}}_\parallel\cdot\hat{\mathbf{q}}_\parallel\alpha_0(q_\parallel) & -\frac{\omega}{c}\alpha(p_\parallel)[\hat{\mathbf{p}}_\parallel\times\hat{\mathbf{q}}_\parallel]_3 \\ \pm\frac{\omega}{c}[\hat{\mathbf{p}}_\parallel\times\hat{\mathbf{q}}_\parallel]_3\alpha_0(q_\parallel) & \frac{\omega^2}{c^2}\hat{\mathbf{p}}_\parallel\cdot\hat{\mathbf{q}}_\parallel\end{pmatrix}.\quad(3c)$$

These equations were solved by generating a realization of the surface profile function on a grid of N_x^2 points within a square region of the x_1x_2 plane of edge L [6]. In evaluating the $\mathbf{q}_\parallel$-integral in Eq. (3a) the infinite limits of integration were replaced by finite ones: $|q_1|<Q/2$, $|q_2|<Q/2$, and the integral was carried out by a two-dimensional version of the extended midpoint rule [12] using a grid in the q_1q_2 plane that is determined by the Nyquist sampling theorem and the properties of the discrete Fourier transform. The values of $\mathbf{q}_\parallel$ and $\mathbf{p}_\parallel$ used in calculating $R_{\alpha\beta}(\mathbf{q}_\parallel|\mathbf{k}_\parallel)$ from Eq. (3a) were given by points on this grid for a given value of $\mathbf{k}_\parallel$, which was also a point on this grid. The resulting matrix equations were solved by LU factorization. In this calculation the function $I(\gamma|\mathbf{Q}_\parallel)$ was evaluated by expanding the integrand in Eq. (3b) in powers of $\zeta(\mathbf{x}_\parallel)$ and calculating the Fourier transform of $\zeta^n(\mathbf{x}_\parallel)$ by the Fast Fourier Transform. The Nyquist sampling theorem requires that $|q_1|$ and $|q_2|$ cannot be larger than $q_c=\pi/\Delta x$ where $\Delta x=L/N_x$ [11]. The components of the vector $\mathbf{Q}_\parallel=\mathbf{p}_\parallel-\mathbf{q}_\parallel$, needed in $I(\gamma|\mathbf{Q}_\parallel)$, are in the interval $[-Q,Q]$, so we have put $Q=q_c$.

The scattering amplitudes $R_{\alpha\beta}(\mathbf{q}_\parallel|\mathbf{k}_\parallel)$ play a central role in the calculation of the elements of the Mueller matrix. In terms of these amplitudes the elements of the Mueller matrix, $\mathbf{M}$, are [13]

$$\begin{aligned}
M_{11} &= C[|R_{pp}|^2+|R_{sp}|^2+|R_{ps}|^2+|R_{ss}|^2]\\
M_{12} &= C[|R_{pp}|^2+|R_{sp}|^2-|R_{ps}|^2-|R_{ss}|^2]\\
M_{13} &= C[R_{pp}R_{ps}^*+R_{sp}R_{ss}^*+R_{ps}R_{pp}^*+R_{ss}R_{sp}^*]\\
M_{14} &= iC[R_{pp}R_{ps}^*+R_{sp}R_{ss}^*-R_{ps}R_{pp}^*-R_{ss}R_{sp}^*]\\
M_{21} &= C[|R_{pp}|^2-|R_{sp}|^2+|R_{ps}|^2-|R_{ss}|^2]\\
M_{22} &= C[|R_{pp}|^2-|R_{sp}|^2-|R_{ps}|^2+|R_{ss}|^2]\\
M_{23} &= C[R_{pp}R_{ps}^*-R_{sp}R_{ss}^*+R_{ps}R_{pp}^*-R_{ss}R_{sp}^*]\\
M_{24} &= iC[R_{pp}R_{ps}^*-R_{sp}R_{ss}^*-R_{ps}R_{pp}^*+R_{ss}R_{sp}^*]\\
M_{31} &= C[R_{pp}R_{sp}^*+R_{sp}R_{pp}^*+R_{ps}R_{ss}^*+R_{ss}R_{ps}^*]\\
M_{32} &= C[R_{pp}R_{sp}^*+R_{sp}R_{pp}^*-R_{ps}R_{ss}^*-R_{ss}R_{ps}^*]\\
M_{33} &= C[R_{pp}R_{ss}^*+R_{sp}R_{ps}^*+R_{ps}R_{sp}^*+R_{ss}R_{pp}^*]\\
M_{34} &= iC[R_{pp}R_{ss}^*+R_{sp}R_{ps}^*-R_{ps}R_{sp}^*-R_{ss}R_{pp}^*]\\
M_{41} &= -iC[R_{pp}R_{sp}^*-R_{sp}R_{pp}^*+R_{ps}R_{ss}^*-R_{ss}R_{ps}^*]\\
M_{42} &= -iC[R_{pp}R_{sp}^*-R_{sp}R_{pp}^*-R_{ps}R_{ss}^*+R_{ss}R_{ps}^*]\\
M_{43} &= -iC[R_{pp}R_{ss}^*-R_{sp}R_{ps}^*-R_{ps}R_{sp}^*-R_{ss}R_{pp}^*]\\
M_{44} &= C[R_{pp}R_{ss}^*-R_{sp}R_{ps}^*-R_{ps}R_{sp}^*+R_{ss}R_{pp}^*]
\end{aligned}$$

where

$$C=\frac{1}{2S}\left(\frac{\omega}{2\pi c}\right)^2\frac{\cos^2\theta_s}{\cos\theta_0},$$

and S is the area of the plane $x_3=0$ covered by the rough surface.

As we are concerned with scattering from a randomly rough surface, it is the average, $\langle\mathbf{M}\rangle$, of the Mueller matrix over the ensemble of realizations of the surface profile function that we seek. In evaluating an average of the form $\langle R_{\alpha\beta}R_{\gamma\delta}^*\rangle$ we can write $R_{\alpha\beta}$ as the sum of its mean value and its fluctuation about the mean, $R_{\alpha\beta}=\langle R_{\alpha\beta}\rangle+[R_{\alpha\beta}-\langle R_{\alpha\beta}\rangle]$. We then obtain the result $\langle R_{\alpha\beta}R_{\gamma\delta}^*\rangle=\langle R_{\alpha\beta}\rangle\langle R_{\gamma\delta}^*\rangle+[\langle R_{\alpha\beta}R_{\gamma\delta}^*\rangle-\langle R_{\alpha\beta}\rangle\langle R_{\gamma\delta}^*\rangle]$. The first term on the right hand side of this equation arises in the contribution to an element of the ensemble averaged Mueller matrix from the light scattered coherently (specularly); the second term arises in the contribution to that ensemble averaged matrix element from the light scattered incoherently (diffusely). It is the latter contribution, $\langle\mathbf{M}\rangle_{\mathrm{incoh}}$, that we calculate.

We have calculated in this way the 16 elements of the Mueller matrix when light of wavelength $\lambda=457.9$ nm is incident on a two-dimensional randomly rough silver surface whose dielectric function at this wavelength is $\varepsilon(\omega)=-7.5+\mathrm{i}0.24$ [14]. The roughness of the surface is defined by a surface height autocorrelation function $W(|\mathbf{x}_\parallel|)=\exp(-x_\parallel^2/a^2)$, where $a=\lambda/4$ and the rms height $\delta=\lambda/40$. For the numerical parameters we used $L=25\lambda$ and $N_x=319$ which implies that $Q=6.4(\omega/c)$. For these parameters, and when the metal is assumed to be non-absorbing [$\mathrm{Im}\,\varepsilon(\omega)\equiv0$], our simulation approach conserved energy within a margin of 1% or better. Moreover, the calculated Mueller matrices were found to be

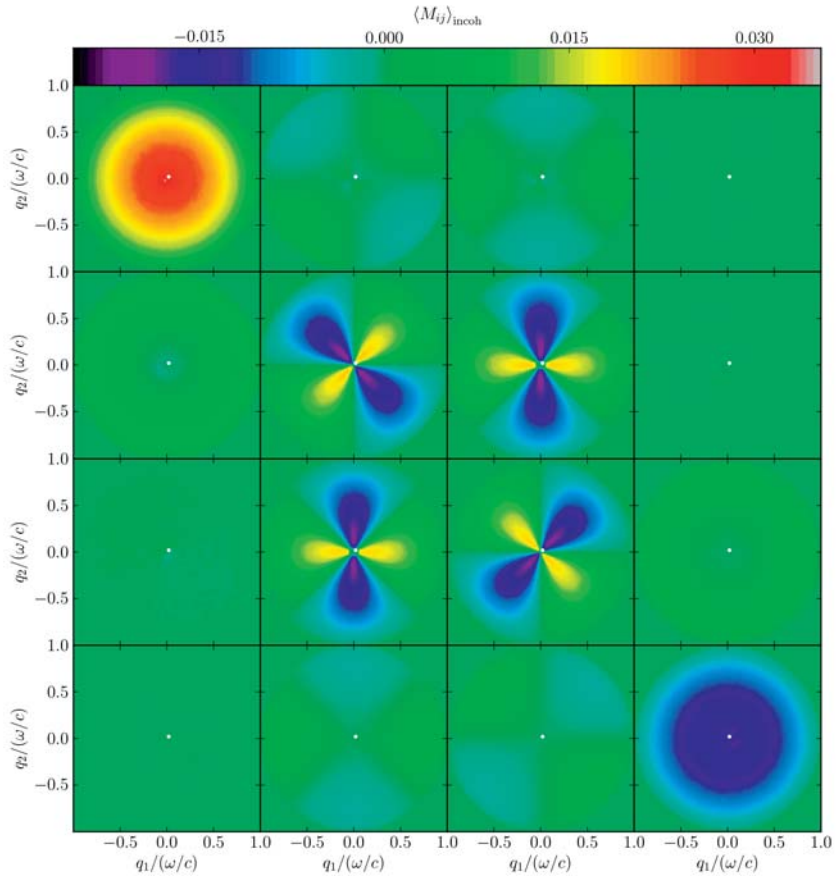

FIG. 1: (Color online) Color-level plots of the contribution to the Mueller matrix elements from the light scattered incoherently as functions of q_1 and q_2 for angles of incidence $(\theta_0, \phi_0) = (2^\circ, 45^\circ)$. An ensemble consisting of $N_p = 10\,000$ surface realizations was used in obtaining these results. The elements, $\langle M_{ij}\rangle_{\rm incoh}$ $(i, j = 1, 2, 3, 4)$, are organized as a matrix with $\langle M_{11}\rangle_{\rm incoh}$ in the top left corner; $\langle M_{12}\rangle_{\rm incoh}$ top row and second column, *etc.* The white spots indicate the specular direction in reflection.

physically realizable and therefore self-consistent by the method of Ref. [15].

The results presented in Fig. 1 were obtained for angles of incidence $(\theta_0, \phi_0) = (2^\circ, 45^\circ)$, *i.e.* for (essentially) normal incidence. The first thing to notice is that the individual matrix elements possess the symmetry properties predicted by Bruce [7]. The elements of the first and last column are circularly symmetric; each element of the second and third columns is invariant under a combined 90° rotation about the origin and a change of sign; and the elements of the second column are 45° rotations of the elements of the third column in the same row [16]. Note that the elements $\langle M_{31}\rangle_{\rm incoh}$, $\langle M_{41}\rangle_{\rm incoh}$, $\langle M_{14}\rangle_{\rm incoh}$, and $\langle M_{24}\rangle_{\rm incoh}$ are zero, at least to the precision used in this calculation.

The results presented in Fig. 2 were obtained for angles of incidence $(\theta_0, \phi_0) = (25^\circ, 45^\circ)$, and display some interesting features. The elements $\langle M_{11}\rangle_{\rm incoh}$, $\langle M_{22}\rangle_{\rm incoh}$, and $\langle M_{33}\rangle_{\rm incoh}$ contain a (weak) enhanced backscattering peak at $\mathbf{q}_\parallel = -\mathbf{k}_\parallel$. The element $\langle M_{44}\rangle_{\rm incoh}$ appears to have a dip in the retroreflection direction. This dip is not present in the results of a calculation based on small-amplitude perturbation theory to the lowest (second) order in the surface profile function, and is therefore a multiple scattering effect, just as the enhanced backscattering peak is. In contrast to what was the case for normal incidence, the elements $\langle M_{31}\rangle_{\rm incoh}$ and $\langle M_{24}\rangle_{\rm incoh}$ are no longer zero.

If we denote the ensemble average of the contribution to a *normalized* element of the Mueller matrix

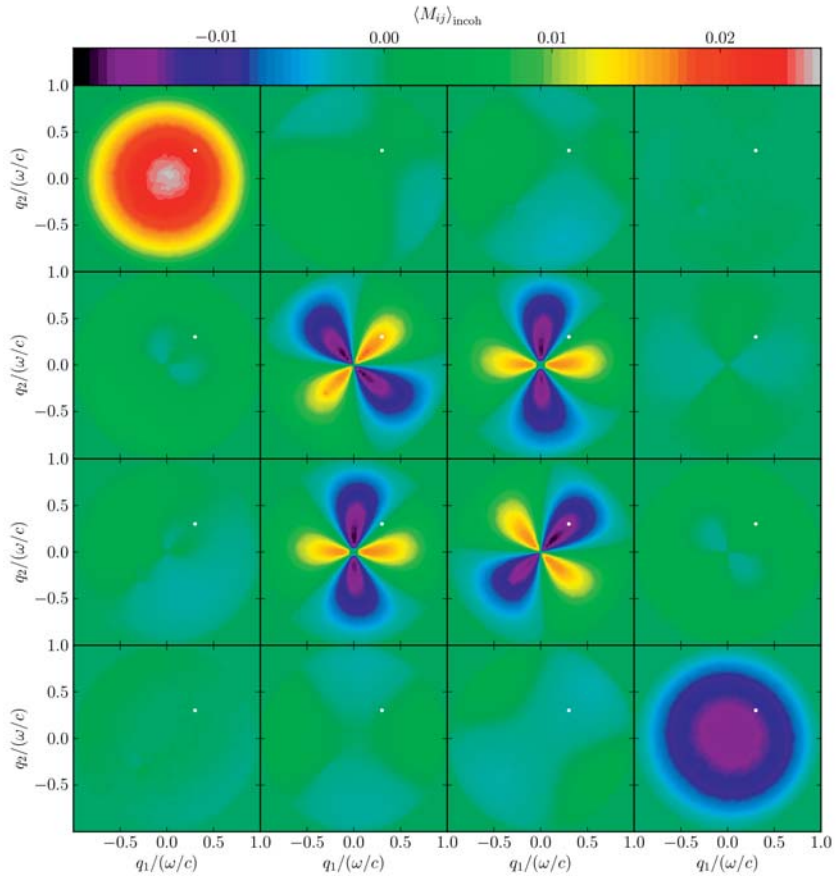

FIG. 2: (Color online) Same as Fig. 1, but now for angles of incidence $(\theta_0, \phi_0) = (25°, 45°)$.

from the light that has been scattered incoherently by $m_{ij} = \langle M_{ij}\rangle_{\rm incoh} / \langle M_{11}\rangle_{\rm incoh}$, we can estimate the order of magnitude of the Mueller matrix elements by calculating the quantities $s_{ij} = \left\langle |m_{ij}(\mathbf{q}_\parallel)| \right\rangle_{\mathbf{q}_\parallel}$, where $\left\langle f(\mathbf{q}_\parallel)\right\rangle_{\mathbf{q}_\parallel} = \int \mathrm{d}^2 q_\parallel \, f(\mathbf{q}_\parallel)/\pi(\omega/c)^2$, and the integral over $\mathbf{q}_\parallel$ is taken over the circular region $0 < q_\parallel < \omega/c$. It was found that s_{11}, s_{22}, s_{23}, s_{32}, s_{33}, s_{44} are of $\mathcal{O}(1)$; s_{12}, s_{13}, s_{21}, s_{34}, s_{42}, s_{43} are of $\mathcal{O}(0.1)$; and s_{14}, s_{24}, s_{31}, s_{41} are of $\mathcal{O}(0.01)$. These results are only weakly dependent on the polar angle of incidence θ_0, for the values of θ_0 assumed in this study.

In conclusion, in this paper we have presented a new approach to the calculation of all sixteen elements of the Mueller matrix for light scattered from a two-dimensional, randomly rough, lossy metal surface, for arbitrary values of the polar and azimuthal angles of incidence. It is based on a rigorous numerical solution of the reduced Rayleigh equation for the scattering of p- and s-polarized light from a two-dimensional rough surface of a penetrable medium, that captures multiple-scattering processes of all orders. The results display multiple scattering effects in certain matrix elements, such as an enhanced backscattering peak in the retroreflection direction, or an unexpected dip in the same direction. The matrix elements also display symmetry properties that, for normal incidence, agree with those predicted by Bruce [7].

The physical implications of the approach and results of this Letter point to better understanding of the polarimetric properties of random surfaces. Such knowledge may be critical for improved photovoltaic and remote sensing applications and has the potential of being used to engineer surface structures with well-defined polarization properties of the light interacting with them.

The authors are grateful for fruitful interactions with

M. Kildemo, I.S. Nerbø, and L.M. Sandvik Aas on Mueller matrices. The research of P.A.L., T.N., and I.S. was supported in part by NTNU by the allocation of computer time. The research of A.A.M. was supported in part by AFRL contract FA9453-08-C-0230.

* Electronic address: Ingve.Simonsen@ntnu.no

[1] H. Mueller, J. Opt. Soc. Am. **38**, 661 (1948).
[2] W.S. Bickel and W.M. Bailey, Am. J. Phys. **53**, 468 (1985).
[3] R.A. Chipman, "Polarimetry" in the *Handbook of Optics* (McGraw-Hill, New York, 1994) Chap. 22.
[4] I. Simonsen, A.A. Maradudin, and T.A. Leskova, Phys. Rev. A **81**, 013806 (2010).
[5] I. Simonsen, A.A. Maradudin, and T.A. Leskova, Phys. Rev. Lett. **104**, 223904 (2010).
[6] T. Nordam, P.A. Letnes, and I. Simonsen (unpublished work).
[7] N.C. Bruce, Waves Random Media **8**, 15 (1998).
[8] Y. Zhang and E. Bahar, IEEE Trans. Antennas Propag. **47**, 949 (1999).
[9] G.C. Brown, V. Celli, M. Haller, and A. Marvin, Surf. Sci. **136**, 381 (1984).
[10] A.A. Maradudin, T. Michel, A.R. McGurn, and E.R. Mendez, Ann. Phys. (N.Y.) **203**, 255 (1990).
[11] W.H. Press, S.A. Teukolsky, W.T. Vetterling, and B.P. Flannery, *Numerical Recipes in C*, 2nd ed. (Cambridge University Press, New York, 1992), p. 135.
[12] Ref. [11], p. 500.
[13] A.A. Maradudin (unpublished work).
[14] P.B. Johnson and R.W. Christy, Phys. Rev. B **6**, 4370 (1972).
[15] S.R. Cloude, Proc. SPIE **1166**, 172 (1989).
[16] It should be noted that the scattering amplitudes f_{sp} and f_{ps} in Bruce's Eq. (1) corresponds to our R_{ps} and R_{sp}, respectively.

T. Nordam, P. A. Letnes, and I. Simonsen. "Numerical simulations of scattering of light from two-dimensional surfaces using the Reduced Rayleigh Equation", `http://arxiv.org/abs/1204.4984` **(2012)**

Paper 8

Numerical simulations of scattering of light from two-dimensional surfaces using the Reduced Rayleigh Equation

T. Nordam,* P. A. Letnes,† and I. Simonsen‡
Department of Physics, The Norwegian University of Science and Technology (NTNU), NO-7491 Trondheim, Norway

A formalism is introduced for the nonperturbative purely numerical solution of the reduced Rayleigh equation for the scattering of light from two-dimensional penetrable rough surfaces. As an example, we in this way study the scattering of p- or s-polarized light from two-dimensional dielectric or metallic randomly rough surfaces by calculating the full angular distribution of the co- and cross-polarized intensity of the scattered light. In particular, we present calculations of the mean differential reflection coefficient for glass and silver surfaces characterized by Gaussian and cylindrical power spectra. We find our results to be in agreement with previous work. The proposed method is found, within the validity of the Rayleigh hypothesis, to give reliable results. In particular, for a non-absorbing metal the conservation of energy is explicitly checked, and found to be satisfied to within 0.03% or better for the simulation results presented.

I. INTRODUCTION

Wave scattering from rough surfaces is an old discipline which keeps attracting a great deal of attention from the scientific and technological community. Several important technologies in our society rely on such knowledge, with radar being a prime example. In the past, the interaction of light with rough surfaces was often considered an extra complication that had to be taken into account in order to properly interpret or invert scattering data. However, with the advent of nano technology, rough structures can be used to design novel materials with tailored optical properties. Examples are: metamaterials [1, 2], photonic crystals [3], spoof plasmons [4], optical cloaking [5–7], and designer surfaces [8, 9]. These developments have made it even more important to have available efficient and accurate simulation tools to calculate both the far- and near-field behavior of the scattered and transmitted fields for any frequency of the incident radiation, including potentially resonant frequencies of the structure.

Lord Rayleigh was the first to perform systematic studies of wave scattering from rough surfaces when, in the late 1800s, he studied the intensity distribution of waves scattered from a sinusoidal surface [10, 11]. More than three decades later, Mandel'shtam studied light scattering from *randomly rough* surfaces [12] thereby initiating the field of wave scattering from surface disordered systems. Since the initial publication of these seminal works, numerous studies on wave scattering from randomly rough surfaces have appeared in the literature [13–19], and several new multiple scattering phenomena have been predicted and confirmed experimentally. These phenomena include the enhanced backscattering and enhanced transmission phenomena, the satellite peak phenomenon, and coherent effects in the intensity-intensity correlation function [19–24].

These studies, and the methods they use, can be categorized as either perturbative, or purely numerical (and non-pertubative). While the former group of methods is limited to weakly rough surfaces, and therefore have limited applicability, the latter group of methods can be applied to a wider class of surface roughnesses. Rigorous numerical methods can in principle be used to study the wave scattering from surfaces of any degree of surface roughness. Such simulations are routinely performed for systems where the interface has a one-dimensional roughness, i.e., where the surface structure is constant along one of the two directions of the mean plane [19, 25]. However, for the practically more relevant situation of a two-dimensional rough surface, the purely numerical and rigorous methods are presently less used due to their computationally intensive nature. The reason for this complexity is the fact that for a randomly rough surface there is no symmetry or periodicity in the surface structure that can be used to effectively reduce the simulation domain. For a periodic surface, however, it is sufficient to simulate a single unit cell, while for a random surface the unit cell is in principle infinite.

A wide range of simulation methods are currently available for simulating the interaction of light with matter, including the finite-difference time-domain (FDTD) method [26], the finite-element method (FEM) [27, 28], the related surface integral equation techniques also known as the boundary element method (BEM) or the method of moments (MoM) [29–33], the reduced Rayleigh equation (RRE) technique [18, 34–40], and spectral methods [32].

The FDTD and FEM methods discretize the whole volume of the simulation domain. Due to the complex and irregular shape of a (randomly) rough surface, it is often more convenient, and may give more accurate results (for the same level of numerical complexity) [41], to base numerical simulations on methods where only the surface itself needs to be discretized. This is the case, for example, for the surface integral technique and the reduced Rayleigh equation methods.

* tor.nordam@ntnu.no
† paul.anton.letnes@gmail.com
‡ Ingve.Simonsen@ntnu.no

The reduced Rayleigh equation is an integral equation where the unknown is either the scattering amplitude or the transmission amplitude. In the former (latter) case one talks about the reduced Rayleigh equation for reflection (transmission). For reflection this equation was originally derived by Brown *et al.* [34], and subsequently by Soubret *et al.* [39, 40]. Later it has also been derived for transmission [42] and film geometries [39, 43, 44].

In the past, the surface integral technique has been used to study light scattering from two-dimensional randomly rough perfectly conducting or penetrable surfaces [33, 45, 46]. However, to date a direct numerical and non-perturbative solution of the two-dimensional reduced Rayleigh equation has not appeared in the literature, even if its one-dimensional analog has been solved successfully numerically and has been used to study the scattering from, and transmission through, one-dimensional rough surfaces [35–37]. The lesson learned from the one-dimensional scattering studies reported in Refs. [35–37] is that simulations based on a direct numerical solution of the reduced Rayleigh equations may give accurate non-perturbative results for systems where alternative methods struggle to give the same level of accuracy. Moreover, the Rayleigh method also requires less memory for the same surface dimensions when compared to, e.g., the rigorous surface integral technique.

The main aim of this paper is to present a numerical method and formalism for the solution of the two-dimensional reduced Rayleigh equation for reflection. While we exclusively consider reflection, the formalism for transmission will be almost identical, and the resulting equation will have a similar form as for reflection. Additionally, the equation for transmission or reflection for a film geometry, i.e., for a film of finite thickness on top of a substrate, where only one interface is rough, will also have a similar form. The method presented will be illustrated by applying it to study the scattering of p- or s-polarized light from two-dimensional metallic or dielectric media separated from vacuum by an isotropic or anisotropic randomly rough surface.

This paper is organized as follows: First, in Sec. II we present the scattering geometry which we consider. We will then briefly outline a derivation of the reduced Rayleigh equation for reflection (Sec. III), followed by details of how the equation was solved numerically (Sec. IV). Next, we will present some results (Sec. V). We then discuss some of the computational challenges of this method (Sec. VI), and, finally, in Sec. VII we draw some conclusions.

II. SCATTERING GEOMETRY

We consider a system where a rough surface separates two regions (Fig. 1). Region 1 is assumed to be vacuum ($\varepsilon_1 = 1$), and region 2 is filled with a metal or dielectric characterized by a complex dielectric function $\varepsilon_2(\omega)$, where the angular frequency is $\omega = 2\pi/\lambda$, with λ being the wavelength of the incident light in vacuum. The height of the surface measured in the positive x_3 direction from the x_1x_2-plane is given by the single-valued function $x_3 = \zeta(\mathbf{x}_\parallel)$, where $\mathbf{x}_\parallel = (x_1, x_2, 0)$, which is assumed to be at least once differentiable with respect to x_1 and x_2. Angles of incidence (θ_0, ϕ_0) and scattering (θ_s, ϕ_s) are defined positive according to the convention given in Fig. 1.

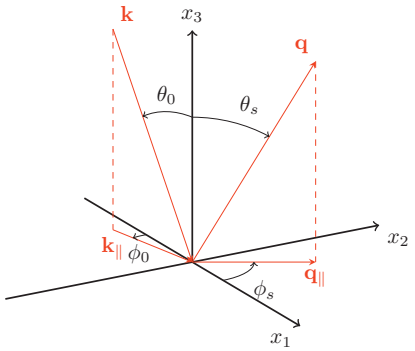

FIG. 1. A sketch of the scattering geometry assumed in this work. The figure also shows the coordinate system used, angles of incidence (θ_0, ϕ_0) and scattering (θ_s, ϕ_s), and the corresponding lateral wavevectors $\mathbf{k}_\parallel$ and $\mathbf{q}_\parallel$, respectively.

In principle, the theory presented in Sec. III can be used to calculate the scattering of light from any surface, provided it is not too rough. However, in this paper, we will consider randomly rough surfaces where $\zeta(\mathbf{x}_\parallel)$ constitutes a stationary random process defined by

$$\begin{aligned} \langle \zeta(\mathbf{x}_\parallel) \rangle &= 0, \\ \langle \zeta(\mathbf{x}_\parallel) \zeta(\mathbf{x}_\parallel{}') \rangle &= \delta^2 W(\mathbf{x}_\parallel - \mathbf{x}_\parallel{}'). \end{aligned} \tag{1}$$

In writing Eqs. (1) we have defined the root-mean-square height of the surface, $\delta = \langle \zeta^2(\mathbf{x}_\parallel) \rangle^{1/2}$, and $W(\mathbf{x}_\parallel - \mathbf{x}_\parallel{}')$ denotes the height-height auto-correlation function of the surface, normalized so that $W(\mathbf{0}) = 1$ [19]. According to the Wiener-Khinchin theorem [47], the power spectrum of the surface profile function is given by

$$g(\mathbf{k}_\parallel) = \int \mathrm{d}^2 x_\parallel \, W(\mathbf{x}_\parallel) \exp\left(-\mathrm{i}\mathbf{k}_\parallel \cdot \mathbf{x}_\parallel\right). \tag{2}$$

The power spectra that will be considered in this work are of either the Gaussian form [33]

$$g(\mathbf{k}_\parallel) = \sqrt{\pi} a_1 a_2 \exp\left(-\frac{k_1^2 a_1^2}{4} - \frac{k_2^2 a_2^2}{4}\right), \tag{3}$$

where a_i $(i = 1, 2)$ denotes the lateral correlation length for direction i, or the cylindrical form [38]

$$g(k_\parallel) = \frac{4\pi}{k_+^2 - k_-^2} \left[\theta(k_\parallel - k_-)\theta(k_+ - k_\parallel)\right], \tag{4}$$

where $k_\parallel = |\mathbf{k}_\parallel|$, θ denotes the Heaviside unit step function, and $k_\pm$ are wavenumber cutoff parameters, with $k_- < k_+$. The cylindrical form in Eq. (4) is a two-dimensional generalization of the power spectrum used in the experiments of West and O'Donnell [21] that confirmed the existence of the enhanced backscattering phenomenon for weakly rough surfaces.

III. SCATTERING THEORY

We consider a linearly p- or s-polarized plane wave which is incident on the surface from region 1, with the electric field given by $\mathbf{E}^{\rm inc}(\mathbf{x};t) = \mathbf{E}^{\rm inc}(\mathbf{x}|\omega)\exp(-{\rm i}\omega t)$ where

$$\mathbf{E}^{\rm inc}(\mathbf{x}|\omega) = \boldsymbol{\mathcal{E}}^{\rm inc}(\mathbf{k}_\parallel)\exp\left[{\rm i}\mathbf{k}_\parallel\cdot\mathbf{x}_\parallel - {\rm i}\alpha_1(k_\parallel)x_3\right], \quad (5a)$$

with

$$\begin{aligned}\boldsymbol{\mathcal{E}}^{\rm inc}(\mathbf{k}_\parallel) = &-\frac{c}{\omega}\left[\hat{\mathbf{k}}_\parallel\alpha_1(k_\parallel,\omega)+\hat{\mathbf{x}}_3 k_\parallel\right]\mathcal{E}_{\rm p}^{\rm inc}(\mathbf{k}_\parallel)\\ &+\left(\hat{\mathbf{x}}_3\times\hat{\mathbf{k}}_\parallel\right)\mathcal{E}_{\rm s}^{\rm inc}(\mathbf{k}_\parallel),\end{aligned} \quad (5b)$$

and

$$\alpha_1(k_\parallel) = \left(\frac{\omega^2}{c^2}-k_\parallel^2\right)^{1/2}, \ \ {\rm Re}\,\alpha_1\geq 0,\ {\rm Im}\,\alpha_1\geq 0. \quad (5c)$$

Here, and in the rest of the paper, a caret over a vector indicates a unit vector. The expressions in front of the amplitudes $\mathcal{E}_\alpha^{\rm inc}(\mathbf{k}_\parallel)$ ($\alpha = {\rm p,s}$) in Eq. (5b) correspond to unit polarization vectors for the incident light of linear polarization α. Moreover, $\mathbf{k}_\parallel = (k_1, k_2, 0)$ denotes the lateral component of the wave vector $\mathbf{k} = \mathbf{k}_\parallel - \alpha(k_\parallel)\hat{\mathbf{x}}_3$. When the lateral wavenumber satisfies $k_\parallel \leq \omega/c$, it is related to the angles of incidence according to

$$\mathbf{k}_\parallel = \frac{\omega}{c}\sin\theta_0\,(\cos\phi_0, \sin\phi_0, 0)\,, \quad (6)$$

where c denotes the speed of light in vacuum and θ_0 and ϕ_0 are the polar and azimuthal angles of incidence, respectively (Fig. 1). When writing the field of incidence [Eq. (5)], we included a harmonic time dependence $\exp(-{\rm i}\omega t)$. For convenience, a similar time dependence will be assumed in all field expressions, but not indicted explicitly.

Above the surface roughness region, i.e., for $x_3 > \max\zeta(\mathbf{x}_\parallel)$, the scattered field can be written as a superposition of *upwards* propagating reflected plane waves:

$$\begin{aligned}\mathbf{E}^{\rm sc}(\mathbf{x}|\omega) = &\int\frac{{\rm d}^2 q_\parallel}{(2\pi)^2}\boldsymbol{\mathcal{E}}^{\rm sc}(\mathbf{q}_\parallel)\\ &\times\exp\left[{\rm i}\mathbf{q}_\parallel\cdot\mathbf{x}_\parallel + {\rm i}\alpha_2(q_\parallel)x_3\right],\end{aligned} \quad (7a)$$

where

$$\begin{aligned}\boldsymbol{\mathcal{E}}^{\rm sc}(\mathbf{q}_\parallel) = &\frac{c}{\omega}\left[\hat{\mathbf{q}}_\parallel\alpha_1(q_\parallel)-\hat{\mathbf{x}}_3 q_\parallel\right]\mathcal{E}_{\rm p}^{\rm sc}(\mathbf{q}_\parallel)\\ &+\left(\hat{\mathbf{x}}_3\times\hat{\mathbf{q}}_\parallel\right)\mathcal{E}_{\rm s}^{\rm sc}(\mathbf{q}_\parallel).\end{aligned} \quad (7b)$$

The integration in Eq. (7a) is over the entire plane, including the evanescent region $q_\parallel > \omega/c$. Therefore, both propagating and evanescent modes are included in $\mathbf{E}^{\rm sc}(\mathbf{x}|\omega)$.

We will assume that a linear relationship exists between the amplitudes of the incident and the scattered fields, and we write (for $\alpha = {\rm p,s}$)

$$\mathcal{E}_\alpha^{\rm sc}(\mathbf{q}_\parallel) = \sum_{\beta={\rm p,s}} R_{\alpha\beta}(\mathbf{q}_\parallel|\mathbf{k}_\parallel)\mathcal{E}_\beta^{\rm inc}(\mathbf{k}_\parallel). \quad (8)$$

Here we have introduced the so-called *scattering amplitude* $R_{\alpha\beta}(\mathbf{q}_\parallel|\mathbf{k}_\parallel)$ which describes how incident β-polarized light characterized by a lateral wave vector $\mathbf{k}_\parallel$ is converted by the surface roughness into scattered light of polarization α and lateral wave vector $\mathbf{q}_\parallel$.

When $q_\parallel \leq \omega/c$, the wave vector $\mathbf{q}_\parallel$ is related to the angles of scattering (θ_s, ϕ_s) by

$$\mathbf{q}_\parallel = \frac{\omega}{c}\sin\theta_s\,(\cos\phi_s, \sin\phi_s, 0)\,. \quad (9)$$

Below the surface region, i.e., for $x_3 < \min\zeta(\mathbf{x}_\parallel)$, the transmitted electric field can be written as

$$\begin{aligned}\mathbf{E}^{\rm tr}(\mathbf{x}_\parallel|\omega) = &\int\frac{{\rm d}^2 p_\parallel}{(2\pi)^2}\boldsymbol{\mathcal{E}}^{\rm tr}(\mathbf{p}_\parallel)\\ &\times\exp\left[{\rm i}\mathbf{p}_\parallel\cdot\mathbf{x}_\parallel - {\rm i}\alpha_2(p_\parallel)x_3\right]\end{aligned} \quad (10a)$$

with

$$\begin{aligned}\boldsymbol{\mathcal{E}}^{\rm tr}(\mathbf{p}_\parallel) = &\frac{1}{\sqrt{\varepsilon_2(\omega)}}\frac{c}{\omega}\left[\hat{\mathbf{p}}_\parallel\alpha_2(p_\parallel)-\hat{\mathbf{x}}_3 p_\parallel\right]\mathcal{E}_{\rm p}^{\rm tr}(\mathbf{p}_\parallel)\\ &+\left(\hat{\mathbf{x}}_3\times\hat{\mathbf{p}}_\parallel\right)\mathcal{E}_{\rm s}^{\rm tr}(\mathbf{p}_\parallel).\end{aligned} \quad (10b)$$

In writing Eqs. (10) we have introduced wave vectors of the transmitted field $\mathbf{p} = \mathbf{p}_\parallel - \alpha_2(p_\parallel)\hat{\mathbf{x}}_3$, where

$$\begin{aligned}\alpha_2(p_\parallel) = &\left[\varepsilon_2(\omega)\frac{\omega^2}{c^2}-p_\parallel^2\right]^{1/2},\\ &{\rm Re}\,\alpha_2\geq 0,\ {\rm Im}\,\alpha_2\geq 0.\end{aligned} \quad (11)$$

In complete analogy to what was done for reflection, a transmission amplitude $T_{\alpha\beta}(\mathbf{p}_\parallel|\mathbf{k}_\parallel)$ may be defined via the following linear relation between the amplitudes of the incident and transmitted fields ($\alpha = {\rm p,s}$)

$$\mathcal{E}_\alpha^{\rm tr}(\mathbf{p}_\parallel) = \sum_{\beta={\rm p,s}} T_{\alpha\beta}(\mathbf{p}_\parallel|\mathbf{k}_\parallel)\mathcal{E}_\beta^{\rm inc}(\mathbf{k}_\parallel). \quad (12)$$

Since the form of the electric fields given by Eqs. (5), (7), and (10) apply far away from the surface region, they are referred as the *asymptotic form* of the electric field. These equations satisfy the boundary conditions at infinity.

In passing we note that once the incident field has been specified, the scattered and transmitted fields are fully specified outside the surface roughness region if the reflection $[R_{\alpha\beta}(\mathbf{q}_\parallel|\mathbf{k}_\parallel)]$ and transmission $[T_{\alpha\beta}(\mathbf{p}_\parallel|\mathbf{k}_\parallel)]$ amplitudes are known. We will now address how the reflection amplitude can be calculated.

A. The Rayleigh Hypothesis

Above the surface, i.e., in the region $x_3 > \max\zeta(\mathbf{x}_\parallel)$, the total electric field is equal to the sum of the incident and the scattered field, $\mathbf{E}^{\rm inc}(\mathbf{x}|\omega) + \mathbf{E}^{\rm sc}(\mathbf{x}|\omega)$. Below the surface, in the region $x_3 < \min\zeta(\mathbf{x}_\parallel)$, it equals the transmitted field, $\mathbf{E}^{\rm tr}(\mathbf{x}|\omega)$. In the surface roughness region, $\min\zeta(\mathbf{x}_\parallel) \leq x_3 \leq \max\zeta(\mathbf{x}_\parallel)$, these forms of the total field will not generally be valid. In particular, when we are above the surface but still below its maximum point, $\zeta(\mathbf{x}_\parallel) \leq x_3 < \max\zeta(\mathbf{x}_\parallel)$, the expression for the scattered field will also have terms containing $\exp\left[\mathrm{i}\mathbf{q}_\parallel\cdot\mathbf{x}_\parallel - \mathrm{i}\alpha_1(q_\parallel)x_3\right]$. Similarly, the transmitted field in the surface region, has to contain an additional term similar to Eq. (10a) but with the exponential function replaced by $\exp\left[\mathrm{i}\mathbf{q}_\parallel\cdot\mathbf{x}_\parallel + \mathrm{i}\alpha_2(q_\parallel)x_3\right]$.

If the surface roughness is sufficiently weak, however, the asymptotic form of the fields, Eqs. (5), (7), and (10), can be assumed to be a good approximation to the total electric field in the surface roughness region. This assumption is known as the *Rayleigh hypothesis* [10, 11, 17], in honor of Lord Rayleigh, who first used it in his seminal studies of wave scattering from sinusoidal surfaces [10, 11]. For a (one-dimensional) sinusoidal surface, $x_3 = \zeta_0\sin(\Lambda x_1)$, the criterion for the validity of the Rayleigh hypothesis, and thus equations that can be derived from it (like the reduced Rayleigh equation to be introduced below), is known to be $\zeta_0\Lambda < 0.448$, independent of the wavelength of the incident light [48, 49]. For a randomly rough surface, however, the absolute limit of validity of this hypothesis is not generally known, though some numerical studies have been devoted to finding the region of validity of this hypothesis for random surfaces [50]. Even if no absolute criterion for the validity of the Rayleigh hypothesis for randomly rough surfaces is known, it remains true that it is a small-slope hypothesis. In particular, if the randomly rough surface is characterized by an rms height, δ, and a correlation length a (see Sec. II and Ref. [19] for details), there seems to be a consensus in the literature on the Rayleigh hypothesis being valid if $\delta/a \ll 1$ [17, 50]. We stress that the validity of the Rayleigh hypothesis does not require the amplitude of the surface roughness to be small, only its slope.

B. The Reduced Rayleigh Equations

Under the assumption that the Rayleigh hypothesis is valid, the total electric field in the surface region, $\min\zeta(\mathbf{x}_\parallel) < x_3 < \max\zeta(\mathbf{x}_\parallel)$, can be written in the form given by Eqs. (5), (7) and (10) [with Eqs. (8) and (12)]. Hence, these asymptotic fields can be used to satisfy the usual boundary conditions on the electromagnetic field at the rough surface $x_3 = \zeta(\mathbf{x}_\parallel)$ [51, 52]. In this way, one obtains the so-called Rayleigh equations, a set of coupled inhomogeneous integral equations, which the reflection and transmission amplitudes should satisfy.

In the mid-1980s, it was demonstrated by Brown *et al.* [34] that either the reflection or transmission amplitude could be eliminated from the Rayleigh equations resulting in an integral equation for the remaining amplitude only. Since this latter integral equation contains only the field above (below) the rough surface, it has been termed the *reduced Rayleigh equation* for reflection (transmission). Subsequently, reduced Rayleigh equations for two-dimensional film geometries, i.e., a film of finite thickness on top of an infinitely thick substrate, where only one interface is rough was derived by Soubret *et al.* [39, 40] and Leskova [43, 44]. Moreover, reduced Raleigh equations for reflection from clean, perfectly conducting, two-dimensional randomly rough surfaces [53] and reduced Raleigh equations for transmission through clean, penetrable two-dimensional surfaces [42] have been derived.

For the purposes of the present study, we limit ourselves to a scattering system consisting of a clean, penetrable, two-dimensional rough surface $x_3 = \zeta(\mathbf{x}_\parallel)$ (Sec. II). If the scattering amplitudes are organized as the 2×2 matrix

$$\mathbf{R}(\mathbf{q}_\parallel|\mathbf{k}_\parallel) = \begin{pmatrix} R_{pp}(\mathbf{q}_\parallel|\mathbf{k}_\parallel) & R_{ps}(\mathbf{q}_\parallel|\mathbf{k}_\parallel) \\ R_{sp}(\mathbf{q}_\parallel|\mathbf{k}_\parallel) & R_{ss}(\mathbf{q}_\parallel|\mathbf{k}_\parallel) \end{pmatrix}, \tag{13}$$

the reduced Rayleigh equation for this geometry can be written in the form [38–40]

$$\int \frac{\mathrm{d}^2 q_\parallel}{(2\pi)^2}\frac{I\left(\alpha_2(\mathbf{p}_\parallel)-\alpha_1(\mathbf{q}_\parallel)|\mathbf{p}_\parallel-\mathbf{q}_\parallel\right)}{\alpha_2(\mathbf{p}_\parallel)-\alpha_1(\mathbf{q}_\parallel)}\mathbf{M}^+(\mathbf{p}_\parallel|\mathbf{q}_\parallel)\mathbf{R}(\mathbf{q}_\parallel|\mathbf{k}_\parallel) = -\frac{I\left(\alpha_2(\mathbf{p}_\parallel)+\alpha_1(\mathbf{k}_\parallel)|\mathbf{p}_\parallel-\mathbf{k}_\parallel\right)}{\alpha_2(\mathbf{p}_\parallel)+\alpha_1(\mathbf{k}_\parallel)}\mathbf{M}^-(\mathbf{p}_\parallel|\mathbf{k}_\parallel), \tag{14a}$$

where

$$I(\gamma|\mathbf{Q}_\parallel) = \int \mathrm{d}^2 x_\parallel \exp\left[-\mathrm{i}\gamma\zeta(\mathbf{x}_\parallel)\right]\exp\left(-\mathrm{i}\mathbf{Q}_\parallel\cdot\mathbf{x}_\parallel\right), \tag{14b}$$

and

$$\mathbf{M}^\pm(\mathbf{p}_\parallel|\mathbf{q}_\parallel) = \begin{pmatrix} p_\parallel q_\parallel \pm \alpha_1(\mathbf{q}_\parallel)\alpha_2(\mathbf{p}_\parallel)\hat{\mathbf{p}}_\parallel\cdot\hat{\mathbf{q}}_\parallel & -\frac{\omega}{c}\alpha_2(\mathbf{p}_\parallel)\left[\hat{\mathbf{p}}_\parallel\times\hat{\mathbf{q}}_\parallel\right]_3 \\ \pm\frac{\omega}{c}\alpha_1(\mathbf{q}_\parallel)\left[\hat{\mathbf{p}}_\parallel\times\hat{\mathbf{q}}_\parallel\right]_3 & \frac{\omega^2}{c^2}\hat{\mathbf{p}}_\parallel\cdot\hat{\mathbf{q}}_\parallel \end{pmatrix}, \tag{14c}$$

where the integrals in Eqs. (14a) and (14b) are over the entire $\mathbf{q}_\parallel$-plane and $\mathbf{x}_\parallel$-plane, respectively.

As mentioned previously, reduced Rayleigh equations for transmission, or film geometries with only one rough interface, will have a similar structure to Eq. (14) [39, 40]. Hence, for the purpose of introducing a formalism for solving the reduced Rayleigh equation numerically, we have decided to treat the simplest geometry consisting of the scattering of light from a clean, penetrable two-dimensional rough surface. Reduced Rayleigh equations corresponding to other geometries can therefore be solved in a completely analogous fashion.

It should be mentioned that the reduced Rayleigh equation can serve as a starting point for most, if not all, perturbation theoretical approaches to the study of scattering from rough surfaces [19]. For example, McGurn and Maradudin studied the scattering of light from two-dimensional rough surfaces based on the reduced Rayleigh equation, going to fourth order in the expansion in the surface profile function, and demonstrating the presence of enhanced backscattering [38].

C. Mean Differential Reflection Coefficient

The solution of the reduced Rayleigh equation determines the scattering amplitudes $R_{\alpha\beta}(\mathbf{q}_\parallel|\mathbf{k}_\parallel)$. While this quantity completely specifies the total field in the region above the surface, it is not directly measurable in experiments. A more useful quantity is the mean differential reflection coefficient (DRC), which is defined as the time-averaged fraction of the incident power scattered into the solid angle $\mathrm{d}\Omega_s$ about the scattering direction $\mathbf{q}$. The mean DRC is defined as [38]

$$\left\langle \frac{\partial R_{\alpha\beta}}{\partial \Omega_s} \right\rangle = \frac{1}{L^2}\frac{\omega^2}{4\pi^2 c^2}\frac{\cos^2\theta_s}{\cos\theta_0}\left\langle \left|R_{\alpha\beta}(\mathbf{q}_\parallel|\mathbf{k}_\parallel)\right|^2 \right\rangle, \quad (15)$$

where L^2 is the area covered by the surface. In this work, we are mainly interested in diffuse (incoherent) scattering. Since we consider weakly rough surfaces, the specular (coherent) scattering will dominate, and it will be convenient to separate the mean DRC into its coherent and incoherent parts. By coherent scattering, we mean the part of the scattered light which does not cancel when the ensemble average of $R_{\alpha\beta}$ is taken, i.e., the part where the scattered field is in phase between surface realizations. Conversely, the incoherent part is the part which cancels in the ensemble average. The component of the mean DRC from incoherent scattering is [38]

$$\begin{aligned}\left\langle \frac{\partial R_{\alpha\beta}}{\partial \Omega_s} \right\rangle_{\text{incoh}} &= \frac{1}{L^2}\frac{\omega^2}{4\pi^2 c^2}\frac{\cos^2\theta_s}{\cos\theta_0} \\ &\times \left[\left\langle \left|R_{\alpha\beta}(\mathbf{q}_\parallel|\mathbf{k}_\parallel)\right|^2 \right\rangle - \left|\left\langle R_{\alpha\beta}(\mathbf{q}_\parallel|\mathbf{k}_\parallel)\right\rangle\right|^2\right].\end{aligned} \quad (16)$$

The contribution to the mean DRC from the coherently scattered light is given by the difference between Eqs. (15) and (16).

D. Conservation of energy

As a way to check the accuracy of our results, it is useful to investigate energy conservation. If we consider a metallic substrate with no absorption, the reflected power should be equal to the incident power. The fraction of the incident light of polarization β which is scattered into polarization α is given by the integral of the corresponding mean DRC over the upper hemisphere:

$$\mathcal{U}_{\alpha\beta} = \int \mathrm{d}\Omega_s \left\langle \frac{\partial R_{\alpha\beta}}{\partial \Omega_s} \right\rangle. \quad (17)$$

For a non-absorbing metal, if we send in light of polarization β, we should have

$$\sum_\alpha \mathcal{U}_{\alpha\beta} = 1, \quad (18)$$

if energy is conserved. While the conservation of energy is useful as a relatively simple test, it is important to note that it is a necessary, but not sufficient condition for correct results.

IV. NUMERICAL SOLUTION OF THE REDUCED RAYLEIGH EQUATION

The starting point for the numerical solution of the reduced Rayleigh equation is a discretely sampled surface, from which we wish to calculate the reflection. We will limit our discussion to quadratic surfaces of size $L \times L$, sampled on a quadratic grid of $N_x \times N_x$ points with a grid constant

$$\Delta x = \frac{L}{N_x}. \quad (19)$$

In this paper, we will present results for numerically generated random surfaces. These are generated by what is known as the Fourier filtering method. Briefly, it consists of generating uncorrelated random numbers with a Gaussian distribution, transforming them to Fourier space, filtering them with the square root of the surface power spectrum $g(\mathbf{k}_\parallel)$, and transforming them back to real space. See, e.g., Refs. [25, 33].

The next step towards the numerical solution of the reduced Rayleigh equation is the evaluation of the integrals $I(\gamma|\mathbf{Q}_\parallel)$ defined in Eq. (14b). These integrals are so-called Fourier integrals and care should be taken when evaluating them due to the oscillating integrands [54]. Using direct numerical integration routines for their evaluation will typically result in inaccurate results. Instead, a (fast) Fourier transform technique with end point corrections may be adapted for their evaluation, and the details of the method is outlined in Ref. [54]. However, these calculations are time consuming, since $I(\gamma|\mathbf{Q}_\parallel)$ must be evaluated for all values of the arguments $\gamma = \alpha_1(\mathbf{p}_\parallel) - \alpha_2(\mathbf{q}_\parallel)$ and $\gamma = \alpha_1(\mathbf{p}_\parallel) - \alpha_2(\mathbf{k}_\parallel)$ [55].

Instead, a computationally more efficient way of evaluating $I(\gamma|\mathbf{Q}_\parallel)$ is to assume that the exponential function $\exp\left[-\mathrm{i}\gamma\zeta(\mathbf{x}_\parallel)\right]$, present in the definition of $I(\gamma|\mathbf{Q}_\parallel)$, can be expanded in powers of the surface profile function, and then evaluating the resulting expression term-by-term by Fourier transform. This gives

$$I(\gamma|\mathbf{Q}_\parallel) = \sum_{n=0}^{\infty} \frac{(-\mathrm{i}\gamma)^n}{n!} \hat{\zeta}^{(n)}(\mathbf{Q}_\parallel), \tag{20a}$$

where $\hat{\zeta}^{(n)}(\mathbf{Q}_\parallel)$ denotes the Fourier transform of the nth power of the profile function, i.e.,

$$\hat{\zeta}^{(n)}(\mathbf{Q}_\parallel) = \int \mathrm{d}^2 x_\parallel \zeta^n(\mathbf{x}_\parallel) \exp\left(-\mathrm{i}\mathbf{Q}_\parallel \cdot \mathbf{x}_\parallel\right). \tag{20b}$$

In practice, the sum in Eq. (20a) will be truncated at a finite value $n = J$, and the Fourier transforms are calculated using a fast Fourier transform (FFT) algorithm.

The advantage of using Eqs. (20) for calculating $I(\gamma|\mathbf{Q}_\parallel)$, rather than the method of Ref. [54], is that the Fourier transform of powers of $\zeta(\mathbf{x}_\parallel)$ can be performed once, and changing the argument γ in $I(\gamma|\mathbf{Q}_\parallel)$ will not require additional Fourier transforms to be evaluated. This will be seen to result in a significant reduction in computational time. The same method has previously been applied successfully to the numerical solution of the one-dimensional reduced Rayleigh equation [35–37].

It should be noted that the Taylor expansion used to arrive at Eq. (20) requires that $\left|\gamma\zeta(\mathbf{x}_\parallel)\right| \ll 1$ to converge reasonably fast, putting additional constraints on the amplitude of the surface roughness which may be more restrictive than those introduced by the Rayleigh hypothesis. Hence, surfaces exist for which the Rayleigh hypothesis is satisfied, but the above expansion method will not converge so that the more time-consuming approach of Ref. [54] will have to be applied.

The next step towards the numerical solution of the reduced Rayleigh equation is to truncate and discretize the integral over $\mathbf{q}_\parallel$ in Eq. (14a). We discretize $\mathbf{q}_\parallel$ on a grid of equidistant points, with spacing Δq, such that

$$\mathbf{q}_{\parallel\, ij} = \left(-\frac{\mathcal{Q}}{2} + i\Delta q, -\frac{\mathcal{Q}}{2} + j\Delta q, 0\right), \tag{21}$$

where $i, j = 0, 1, 2, \ldots, N_q - 1$, and $\mathcal{Q} = 2\Delta q(N_q - 1)$. Here, N_q denotes the number of points along each axis of the grid. Additionally, we limit the integration over $\mathbf{q}_\parallel$ to the region $q_\parallel < \mathcal{Q}/2$. The choice of a circular integration domain reduces the computational cost, and will be discussed in more detail in Sec. VI B. Converting the integral into a sum by using a two-dimensional version of the standard mid-point quadrature scheme, we get the equation:

$$\begin{aligned}\left(\frac{\Delta q}{2\pi}\right)^2 \sum_{q_{\parallel\, ij} \le \mathcal{Q}/2} & \frac{I\left(\alpha_2(\mathbf{p}_\parallel) - \alpha_1(\mathbf{q}_{\parallel\, ij})|\mathbf{p}_\parallel - \mathbf{q}_{\parallel\, ij}\right)}{\alpha_2(\mathbf{p}_\parallel) - \alpha_1(\mathbf{q}_{\parallel\, ij})} \mathbf{M}^+(\mathbf{p}_\parallel|\mathbf{q}_{\parallel\, ij}) \mathbf{R}(\mathbf{q}_{\parallel\, ij}|\mathbf{k}_\parallel) = \\ & - \frac{I\left(\alpha_2(\mathbf{p}_\parallel) + \alpha_1(\mathbf{k}_\parallel)|\mathbf{p}_\parallel - \mathbf{k}_\parallel\right)}{\alpha_2(\mathbf{p}_\parallel) + \alpha_1(\mathbf{k}_\parallel)} \mathbf{M}^-(\mathbf{p}_\parallel|\mathbf{k}_\parallel).\end{aligned} \tag{22}$$

Here, the sum is to be taken over all $\mathbf{q}_{\parallel\, ij}$ such that $q_{\parallel\, ij} \le \mathcal{Q}/2$, where $q_{\parallel\, ij} = \left|\mathbf{q}_{\parallel\, ij}\right|$. This sum yields a matrix equation where the unknowns are the four components of $\mathbf{R}(\mathbf{q}_{\parallel\, ij}|\mathbf{k}_\parallel)$. It is evident from Eq. (8) that if we consider incident light of either p or s polarization, we need only calculate two of the components of the scattering amplitude to fully specify the reflected field. Hence, we solve separately for either p-polarized incident light, i.e., R_{pp} and R_{sp}, or s-polarized incident light, i.e., R_{ss} and R_{ps}. In either case, we have twice as many unknowns as the number of values of $\mathbf{q}_{\parallel\, ij}$ included in the sum in Eq. (22). Note that the coefficient matrix of the equation system is the same for both incident polarizations, and will also remain the same for all angles of incidence, as $\mathbf{k}_\parallel$ only enters at the right hand side of Eq. (22).

In order to solve for all unknowns, we need to discretize $\mathbf{p}_\parallel$ as well, to obtain a closed set of linear equations. Using the same grid for $\mathbf{p}_\parallel$ as for $\mathbf{q}_\parallel$ will give us the necessary number of equations, as Eq.(22) yields two equations for each value of $\mathbf{p}_\parallel$. Since we integrate over a circular $\mathbf{q}_\parallel$ domain, with $\mathbf{q}_\parallel$ discretized on a quadratic grid, the exact number of values of $\mathbf{q}_{\parallel\, ij}$ will depend on the particular values of $\mathcal{Q}$ and N_q, but will be approximately $(\pi/4)N_q^2$.

In order to take advantage of the method for calculating $I(\gamma|\mathbf{Q}_\parallel)$ described by Eq. (20), it is essential that all possible values of $\mathbf{p}_\parallel - \mathbf{q}_\parallel$ and $\mathbf{p}_\parallel - \mathbf{k}_\parallel$ [see Eq. (22)] fall on the grid of wave vectors $\mathbf{Q}_\parallel$ resolved by the Fourier transform of the surface profile we used in that calculation. First, we note that when $\mathbf{p}_\parallel$ and $\mathbf{q}_\parallel$ are discretized on the same grid, the number of possible values for each component of $\mathbf{p}_\parallel - \mathbf{q}_\parallel$ will always be an odd number, $2N_q - 1$. Thus, by choosing N_q such that $2N_q - 1$ equals the number of elements along each axis of the FFT we used to calculate the integrals in Eq. (20b), we ensure

that the required number of points is resolved by the FFT. Hence, we choose

$$N_q = \left\lfloor \frac{N_x + 2}{2} \right\rfloor, \tag{23}$$

where $\lfloor x \rfloor$ is the floor function of x, which is equal to the largest integer less than or equal to x.

Next, we let Δq equal the resolution of the FFT [54], i.e.,

$$\Delta q = \frac{2\pi}{L} \tag{24}$$

and we let $\mathcal{Q}$ be equal to the highest wavenumber resolved by the FFT [54],

$$\mathcal{Q} = \Delta q \lfloor N_x/2 \rfloor. \tag{25}$$

In the end, we get the equation

$$\left(\frac{\Delta q}{2\pi}\right)^2 \sum_{|\mathbf{q}_{\parallel ij}| \le \mathcal{Q}/2} \frac{I\left(\alpha_2(\mathbf{p}_{\parallel kl}) - \alpha_1(\mathbf{q}_{\parallel ij})|\mathbf{p}_{\parallel kl} - \mathbf{q}_{\parallel ij}\right)}{\alpha_2(\mathbf{p}_{\parallel kl}) - \alpha_1(\mathbf{q}_{\parallel ij})} \mathbf{M}^+(\mathbf{p}_{\parallel kl}|\mathbf{q}_{\parallel ij}) \mathbf{R}(\mathbf{q}_{\parallel ij}|\mathbf{k}_{\parallel mn}) = - \frac{I\left(\alpha_2(\mathbf{p}_{\parallel kl}) + \alpha_1(\mathbf{k}_{\parallel mn})|\mathbf{p}_{\parallel kl} - \mathbf{k}_{\parallel mn}\right)}{\alpha_2(\mathbf{p}_{\parallel kl}) + \alpha_1(\mathbf{k}_{\parallel mn})} \mathbf{M}^-(\mathbf{p}_{\parallel kl}|\mathbf{k}_{\parallel mn}), \tag{26}$$

where $\mathbf{q}_{\parallel ij}$, as well as $\mathbf{p}_{\parallel kl}$ and $\mathbf{k}_{\parallel mn}$, are defined on the grid given by Eq. (21), with $i, j = 0, 1, 2, \ldots, N_q - 1$, and where N_q, Δq and $\mathcal{Q}$ are given by Eqs. (23), (24) and (25), respectively.

Evaluating Eq. (26) for all values of $\mathbf{p}_{\parallel kl}$ satisfying $p_{\parallel kl} \le \mathcal{Q}/2$ [with $k, l = 0, 1, 2, \ldots, N_q - 1$], and assuming one value of $\mathbf{k}_{\parallel mn}$ as given by the angles of incidence by Eq. (6), results in a *closed* system of linear equations in $\mathbf{R}(\mathbf{q}_{\parallel ij}|\mathbf{k}_{\parallel mn})$.

By generating a realization of the surface profile function by the method of Refs. [25, 33], the functions $I(\gamma|\mathbf{Q}_\parallel)$ can be calculated from Eq. (20a) as discussed earlier. Hence, the full coefficient matrix and right-hand-side of the linear system can readily be evaluated and its solution is $\mathbf{R}(\mathbf{q}_{\parallel ij}|\mathbf{k}_{\parallel mn})$. With the reflection amplitudes $R_{\alpha\beta}(\mathbf{q}_{\parallel ij}|\mathbf{k}_{\parallel mn})$ available, the contribution to the mean differential reflection coefficient from the light that has been scattered incoherently is obtained from Eq. (16) after averaging over an ensemble of surface realizations.

In passing we note that to avoid loss of numerical precision by operating on numbers with widely different orders of magnitude, we have rescaled all quantities in our problem to dimensionless numbers. When considering an incoming wave of wavelength λ, angular frequency ω and wave vector $\mathbf{k}$, we have chosen to rescale all lengths in our problem by multiplying with ω/c, and all wavenumbers by multiplying with c/ω, effectively measuring all lengths in units of $\lambda/2\pi$, and the magnitude of wave vectors in units of ω/c.

V. RESULTS

To demonstrate the use of the formalism for solving the reduced Rayleigh equation, the first set of calculations we carried out was for two-dimensional randomly rough silver surfaces characterized by an rms-height of $\delta = 0.025\lambda$ and an isotropic Gaussian power spectrum [Eq. (3)] of correlation lengths $a_1 = a_2 = 0.25\lambda$. In Figs. 2 and 3 we present simulation results for the contribution to the mean differential reflection coefficients from light of wavelength (in vacuum) $\lambda = 457.9$ nm that was scattered incoherently from a rough silver surface of size $25\lambda \times 25\lambda$, discretized into 319×319 points. The dielectric function of silver at this wavelength is $\varepsilon_2 = -7.5 + 0.24\mathrm{i}$, and the angles of incidence where $\theta_0 = 18.24^\circ$ and $\phi_0 = 45^\circ$.

Figure 2 shows the in-plane scattering for this system. The enhanced backscattering peak, a multiple scattering phenomenon, is clearly visible, and is as expected strongest in $p \to p$ scattering, since p-polarized light has a stronger coupling to surface plasmon polaritons [19]. Figure 3 shows the full angular distribution of the DRC for the same system. In Figs. 3(a)–(c) and Figs. 3(d)–(e) the incident light was p- and s-polarized, respectively. Figures 3(c) and 3(f) show scattering into s-polarization, Figs. 3(b) and 3(e) show scattering into p-polarization and in Figs. 3(a) and 3(d) the polarization of the scatted light was not recorded. The results presented in Figs. 2 and 3 were obtained by averaging the DRC over an ensemble consisting of $14,200$ surface realizations.

A test of energy conservation was performed with the same parameters as the silver surface presented here, except that Im $\varepsilon_2 = 0$, i.e., a metal surface with no absorp-

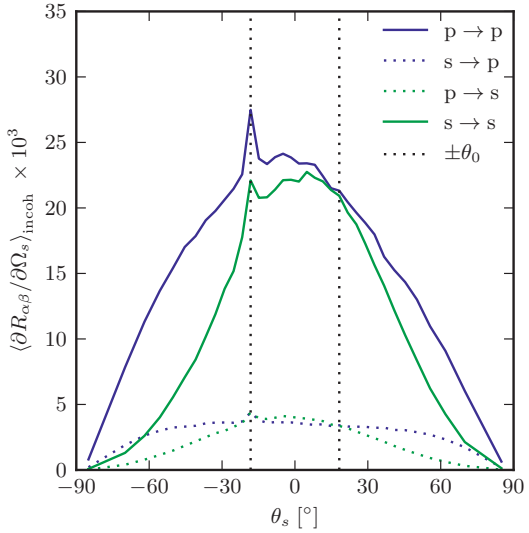

FIG. 2. Incoherent part of the mean differential reflection coefficient [Eq. (16)], showing only the in-plane scattering as a function of outgoing lateral wave vector, averaged over 14200 randomly rough silver surface realizations. The wavelength (in vacuum) of the incident light was $\lambda = 457.9$ nm, and the dielectric function of silver at this wavelength is $\varepsilon_2 = -7.5 + 0.24\mathrm{i}$. The surface power spectrum was Gaussian [Eq. (3)], with correlation length $a_1 = a_2 = 0.25\lambda$ and rms height $\delta = 0.025\lambda$. The angle of incidence was $\theta_0 = 18.24°$, the surface covered an area $L \times L$, where $L = 25\lambda$, and the surface was discretized on a grid of 319×319 points. The position of the specular peak (not present in the incoherent part) and the enhanced backscattering peak are indicated by the vertical dashed lines.

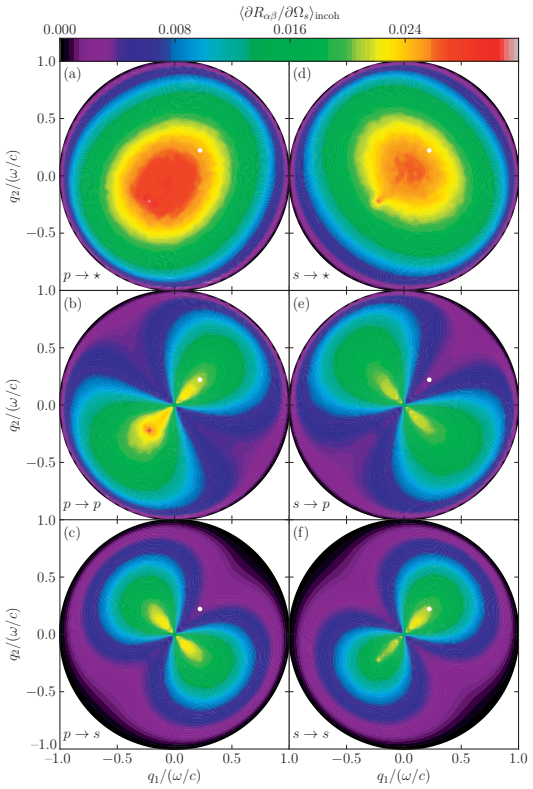

FIG. 3. Incoherent part of the mean differential reflection coefficient [Eq. (16)], showing the full angular distribution as a function of outgoing lateral wave vector. All parameters are the same as in Fig. 2. The specular position is indicated by the white dots.

tion. We found $|\mathcal{U} - 1| \leq 0.0003$, i.e., energy is conserved to within 0.03%. As a further test, we simulated a set of surfaces with the same parameters as those presented in Figs. 2 and 3, except that the rms-roughness δ, was varied between 0.0 and 0.045λ, while the correlation length was held constant at $a_1 = a_2 = 0.25\lambda$. We also did the same set of simulations for the surface with no absorption, i.e., with $\varepsilon_2 = -7.5$. The results of these tests are presented in Fig. 4.

As mentioned previously, the reduced Rayleigh equation is only valid for surfaces with small slopes. We have found that for the parameters described above, our code gives good results for an rms-roughness to correlation-length ratio $\delta/a \lesssim 0.12$. For larger ratios δ/a, the results look qualitatively much the same, but the ratio of reflected to incident power starts increasing past 1, as seen in Fig. 4.

The next set of calculation we performed was for a dielectric substrate, characterized by $\varepsilon_2 = 2.64$. Otherwise, all parameters where the same as for the silver surface presented in Figs. 2 and 3. These results are presented in Fig. 5. Comparing these data to those presented in Fig. 3, we notice that the dielectric has less reflection (the figures show only the incoherent scattering, but the same holds for the coherent part), which is as expected. The ratio of reflected to incident power for these data was $\mathcal{U} = 0.0467$ for p-polarized light at an angle of incidence of $\theta_0 = 18.24°$. Note that for a transparent substrate, it is impossible verify the conservation of energy without also calculating the transmitted field. Additionally, we notice the absence of the enhanced backscattering peak, which is also as expected, since this phenomenon (on a weakly rough surface) depends on surface guided modes.

So far, we have considered surfaces with statistically isotropic roughness. For the results presented in Fig. 6, we simulated scattering from a silver surface with the same parameters as for the surface presented in Figs. 2 and 3, except the surface power spectrum was anisotropic, with correlation lengths $a_1 = 0.25\lambda$ in the x_1 direction and $a_2 = 0.75\lambda$ in the x_2 direction and an

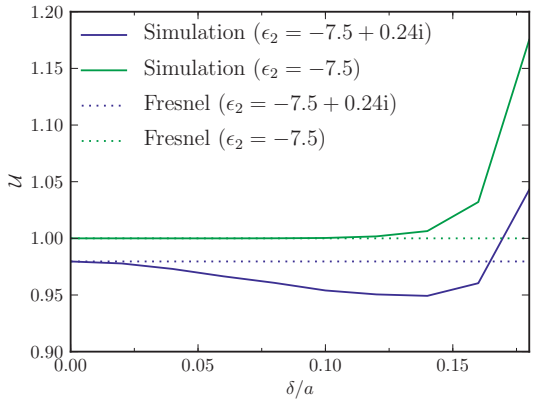

FIG. 4. Ratio of reflected power to incident power, $\mathcal{U}$, as a function of ratio between rms-roughness and correlation length, δ/a. Surface size and resolution were the same as for Fig. 2, and the surface was randomly rough with a Gaussian power spectrum, correlation length was kept constant at $a = a_1 = a_2 = 0.25\lambda$, while the rms-roughness δ was varied from 0.0 to 0.045λ. The Fresnel coefficients have been included for comparison.

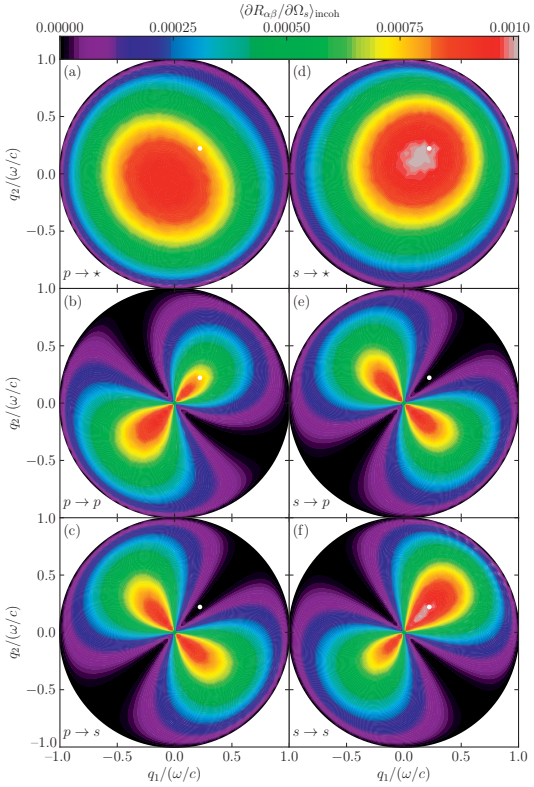

FIG. 5. The same as in Fig. 3, except that $\varepsilon_2 = 2.64$, and the results are averaged over 21800 randomly rough surfaces.

rms-roughness of $\delta = 0.025\lambda$. The figure shows the incoherent part of the mean DRC averaged over 6800 surface realizations. In this case, there is more diffuse scattering along the x_1 direction, which is to be expected, since the shorter correlation length means the height of the surface changes faster when moving along the surface in this direction.

Finally, for the results presented in Fig. 7, we have simulated the scattering of light from a surface of size $25\lambda \times 25\lambda$, discretized into 319×319 points, with $\varepsilon_2 = -16 + 1.088$i, corresponding to silver at $\lambda = 632.8$ nm. The surface power spectrum was cylindrical [See Eq. (4)], with $k_- = 0.82\omega/c$, $k_+ = 1.97\omega/c$ and rms-roughness $\delta = 0.025\lambda$. The figure shows the in-plane, incoherent part of the mean differential reflection coefficient averaged over 7000 surface realizations. The angles of incidence were $(\phi_0 = 45°, \theta_0 = 1.6°)$.

From perturbation theory [17, 19], we know that for an incident wave with lateral wave vector $\mathbf{k}_\parallel$ to be scattered via single scattering to a reflected wave vector $\mathbf{q}_\parallel$, we must have $g(\mathbf{q}_\parallel - \mathbf{k}_\parallel) > 0$, where $g(\mathbf{k}_\parallel)$ is the surface power spectrum [Eq. (2)]. Since the power spectrum in this case was zero for $|\mathbf{q}_\parallel - \mathbf{k}_\parallel| < 0.82\omega/c$, we have no single scattering between $\theta_s = -53.5°$ and $\theta_s = 56.7°$ (for the angles of incidence used here). The enhanced backscattering peak, which is due to double scattering, is still clearly visible.

The results presented here were obtained on shared-memory machines with 24 GB of memory and two six-core 2.4 GHz AMD Opteron processors. Solving for one surface realization required 12 GB of memory, and took approximately 17 CPU minutes.

VI. DISCUSSION

A challenge faced when performing a direct numerical solution of the reduced Rayleigh equation for the scattering of light from two-dimensional surfaces is the numerical complexity. In this section, we detail and discuss some of these issues.

A. Memory

Part of the challenge of a purely numerical solution of the reduced Rayleigh equation in the way described in this paper, is that it requires a relatively large amount of memory. With approximately $\mathcal{N} = (\pi/4)N_q^2$ possible values for $\mathbf{q}_\parallel$, the coefficient matrix of the equation system will contain approximately $(2\mathcal{N})^2$ elements, where the factor 2 comes from the two outgoing polarizations. Hence, the memory required to hold the left hand side of the equation system will be $4\mathcal{N}^2\eta$, where η is the number of bytes used to store one complex number. If each ele-

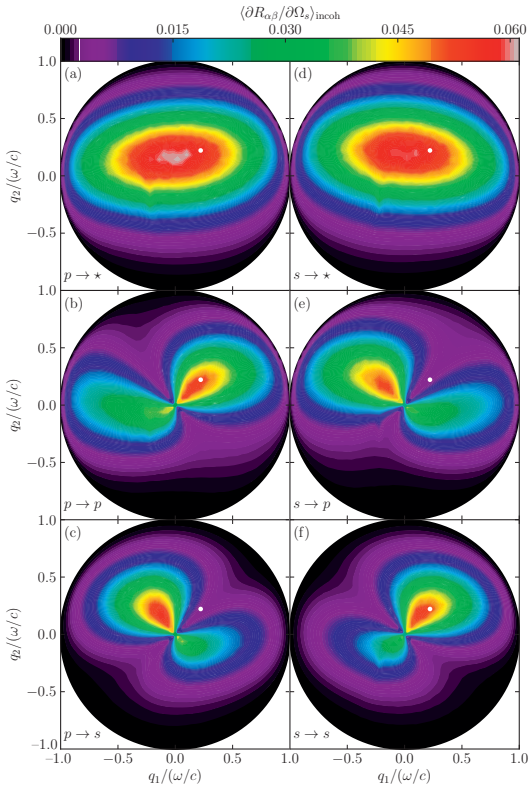

FIG. 6. The same as in Fig. 3, except the correlation length of the Gaussian roughness, which is $a_1 = 0.25\lambda$ in the x_1 direction and $a_2 = 0.75\lambda$ in the x_2 direction, and the results are the average of an ensemble of 6800 surface realizations.

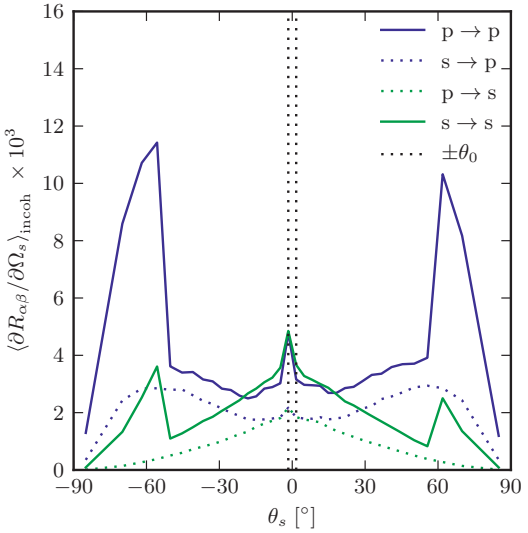

FIG. 7. Incoherent part of the mean differential reflection coefficient [Eq. (16)], showing only the in-plane scattering as function of outgoing lateral wave vector, averaged over 7000 surface realizations with dielectric constant $\varepsilon_2 = -16+1.088\mathrm{i}$, which corresponds to silver at $\lambda = 632.8$ nm. The surface power spectrum was of the cylindrical type [Eq. (4)], with $k_- = 0.82\omega/c$, $k_+ = 1.97\omega/c$, and rms-roughness $\delta = 0.025\lambda$. The angles of incidence were $\theta_0 = 1.6°$ and $\phi_0 = 45°$.

ment is a single precision complex number, which is what was used for the results presented in this paper, then $\eta = 8$ bytes, and the matrix will require approximately $2\pi^2 N_q^4$ bytes of memory. For instance, for $N_x = 319$, which has been used for all the results presented in this paper, the coefficient matrix takes up approximately 12 GB of memory. Note that if we had used a square integration domain for the integral over $\mathbf{q}_\parallel$ in Eq. (**??**), the number of elements in the coefficient matrix would have been $(2N_q^2)^2$. Hence, due to the circular cutoff in the integral over $\mathbf{q}_\parallel$, the memory footprint is reduced by approximately a factor $\pi^2/16 \approx 0.62$.

When determining the system size, we can freely choose the length of the edge of the surface L, and the number of sampling points along each direction N_x. These parameters will then fix the resolution of the surface, Δx, the resolution in wave vector space, Δq, the number of resolved wave vectors, N_q, and the cutoff in the $\mathbf{q}_\parallel$ integral, $\mathcal{Q}$ [see Eqs. (19), (24), (23), and (25)]. The combination of Δq and $\mathcal{Q}$ then determines how many of the resolved wave vectors actually fall inside the propagating region, $|\mathbf{q}_\parallel| < \omega/c$, which is identical to the number of data points used in, e.g., Figs. 5–7.

As we are not free to choose all the parameters, it is clear that some kind of a compromise is necessary. N_x, and by extension N_q, determines the amount of memory needed to hold the coefficient matrix, as well as the time required to solve the system, which means it is likely to be limited by practical considerations. It is then possible to choose L to get good resolution of the surface, at the cost of poor resolution in wave vector space, or vice versa. Note also that changing L will change $\mathcal{Q}$. If $\mathcal{Q}$ is not large enough to include evanescent surface modes, multiple scattering will not be correctly included in the results. The optimal compromise depends on the system to be studied.

B. Time

The simulations presented in this paper were performed on shared-memory machines with 24 GB of memory and two six-core 2.4 GHz AMD Opteron processors, running version 2.6.18-194.32.1.el5 of the Linux operating system. Our program is parallelized with the MPI

TABLE I. Walltime spent to solve the RRE for various N_x on a shared-memory machine with two six-core 2.4 GHz AMD Opteron processors. Included are total time (t_{tot}), time to setup the coefficient matrix of the equation system (t_{LHS}) and the time to solve the equation system (t_{solve}). Also included is the size of the coefficient matrix of the equation system for each run (M_{LHS}).

N_q	t_{LHS}(s)	t_{LU}(s)	t_{tot}(s)	M_{LHS}(GB)
199	9.8	58	69	1.8
239	28	171	200	3.8
279	56	429	486	7.0
319	97	946	1,045	12.0
369	154	1,916	2,074	19.2
399	266	3,625	3,895	29.4

library, and the equation setup runs on all 12 cores in the timing examples given. The solver used was a parallel, dense solver based on LU-factorization (PCGESV from ScaLAPACK), which also runs efficiently on all 12 cores. Setting up the equation system scales almost perfectly to a large number of cores, while the solver scales less well, due to the need for communication. Numerically solving the reduced Rayleigh equation for one surface of 319×319 points, as in the results presented in this paper, uses 12 GB of memory, and takes approximately 17 minutes on the architecture described above. Of this time, approximately 100 seconds is spent setting up the equation system, 950 seconds is spent solving the equation by LU decomposition system, and typically less than 1 second is spent on other tasks, including writing data to disk. See Table I for further timing details.

The ratio of the time spent solving the equation system to the total time increases with increasing system size, as the time to set up the equation system is $\mathcal{O}(N_x^4)$, while the time to solve the system scales as $\mathcal{O}(N_x^6)$. For any surface of useful size, however, the runtime is completely dominated by the time spent in solving the equation.

Since the time to solve the equation system dominates, we investigated whether we could improve the performance by using an iterative solver instead of one based on LU decomposition. For example, Simonsen et al. [56] report good performance using BiCGStab [57] on a dense matrix of a similar size. We found that convergence with BiCGStab was slow and unreliable, though it should be noted we did not use a preconditioning scheme. Additionally, as can be seen from Eq. (14a), changing the angle of incidence or the incident polarization changes the right hand side of the equation only. The advantage of using LU decomposition is that the additional time to solve the system for several right hand sides is negligible, while the time spent with an iterative solver like BiCGStab will scale linearly with the number of right hand sides (and thus angles of incidence). For these reasons, we have chosen to use an LU-based solver.

C. GPU implementation

Currently, performing simulations like those presented in this paper on a single desktop computer is prohibitively time consuming. However, the increasing availability of powerful Graphics processing units (GPUs) has the potential make computing power comparable to that of a powerful parallel machine available at a fraction of the cost. As the most time-consuming part of our simulations is the LU factorization of the system matrix (see Table I), this is where effort should be made to optimize the code, and for this reason the simulation code was adapted to (optionally) employ version 1.0 of the MAGMA library [58] for GPU-based LU factorization. Performance was compared between a regular supercomputing service and a GPGPU (General Purpose GPU) testbed. When our simulations were run on the regular service, the code was running on a single compute node containing two AMD 2.3 GHz 16-core processors and 32 GB of main memory. On the GPGPU testbed, the hardware consisted of a single Nvidia Fermi C2050 processor with 3 GB of dedicated memory and 32 GB of main system memory. For these two computer systems, initial performance testing indicates that the LU factorization took comparable time on the two architectures (the difference was less than 10%) for a system of size $N_q = 100$, including transfer of the system matrix and factorization to and from the Fermi card. This demonstrates that there is a possibility of performing simulations such as those used to generate the figures in this paper without resorting to supercomputing resources.

VII. CONCLUSION

We have introduced a formalism for performing a non-perturbative, purely numerical, solution of the reduced Rayleigh equation for reflection from two-dimensional penetrable rough surfaces, characterized by a complex dielectric function $\varepsilon(\omega)$. We believe this will prove an important addition to the collection of available methods for numerical simulations of the scattering of light from rough surfaces.

As an example, we have used this formalism to carry out simulations of the scattering of p or s polarized light from two-dimensional randomly rough surfaces characterized by Gaussian [Eq. (3)] and cylindrical [Eq. (4)] power spectra. From the scattering amplitude, we calculate the mean differential reflection coefficient, and we obtain the full angular distribution of scattered light, with polarization information.

We have presented the results of these calculations (Figs. 2-7), and we find our simulation code, within the validity of the reduced Rayleigh equation, to give reliable results. In particular, for a non-absorbing metal the conservation of energy is explicitly checked and found, for the physical parameters assumed, to be satisfied within 0.03%, or better. We also observe phenomena such as en-

hanced backscattering which are expected from previous experimental and theoretical work.

ACKNOWLEDGMENTS

We would like to acknowledge the help of Dr. Chris Johnson at the EPCC, University of Edinburgh, for help in parallelizing the code. We are also indebted to Dr. A. A. Maradudin for discussions on the topic of this paper. The work of T.N. and P.A.L. was partially carried out under the HPC-EUROPA2 project (project number: 228398) with support of the European Commission – Capacities Area – Research Infrastructures. The work was also supported by NTNU by the allocation of computer time.

[1] A. Maradudin, ed., *Structured Surfaces as Optical Metamaterials* (Cambridge University Press, New York, 2011).
[2] Y. N. G. V. M. Agranovich, Phys.-Usp. **49**, 1029 (2006).
[3] J. Joannopoulos, S. Johnson, J. Winn, and R. Meade, *Photonic Crystals: Molding the Flow of Light*, 2nd ed. (Princeton University Press, NJ, 2008).
[4] J. Pendry, L. Martín-Moreno, and F. Garcia-Vidal, Science **305**, 847 (2004).
[5] J. B. Pendry, D. Schurig, and D. R. Smith, Science **312**, 1780 (2006).
[6] D. Schurig, J. Mock, B. Justice, S. Cummer, J. Pendry, A. Starr, and D. Smith, Science **314**, 977 (2006).
[7] B. Baumeier, T. Leskova, and A. Maradudin, Phys. Rev. Lett. **103**, 246803 (2009).
[8] A. Maradudin, E. Méndez, and T. Leskova, *Designer Surfaces* (Elsevier Science, New York, 2008).
[9] E. Méndez, E. García-Guerrero, T. A. Leskova, A. A. Maradudin, J. Muñoz-López, and I. Simonsen, Appl. Phys. Lett. **81**, 798 (2002).
[10] Lord Rayleigh, Proceedings of the Royal Society of London. Series A **79**, 399 (1907).
[11] L. Rayleigh, *The Theory of Sound*, 2nd ed., Vol. II (MacMillan, London, 1896) pp. 89, 297–311.
[12] L. Mandelstam, Ann. Phys. (Leipzig) **346**, 609 (1913).
[13] F. Bass and I. Fuks, *Wave Scattering from Statistically Rough Surfaces* (Pergamon, Oxford, UK, 1979).
[14] J. Ogilvy, *Theory of wave scattering from random rough surfaces* (IOP Publishing, Bristol, UK, 1991).
[15] A. Voronovich, *Wave scattering from Rough Surfaces*, 2nd ed. (Springer Verlag, Berlin, 1999).
[16] M. Nieto-Vesperinas, *Scattering and Diffraction in Physical Optics*, 2nd ed. (World Scientific Publishing Company, Singapore, 2006).
[17] A. Maradudin, ed., *Light Scattering and Nanoscale Surface Roughness* (Springer-Verlag, New York, 2007).
[18] A. Zayats, I. Smolyaninov, and A. Maradudin, Phys. Rep. **408**, 131 (2005).
[19] I. Simonsen, Eur. Phys. J.-Spec. Top. **181**, 1 (2010).
[20] A. McGurn, A. Maradudin, and V. Celli, Phys. Rev. B **31**, 4866 (1985), 124; 65; 168.
[21] S. West and K. O'Donnell, J. Opt. Soc. Am. A **12**, 390 (1995), 124; 65; 168.
[22] E. Méndez and K. O'Donnell, Opt. Commun. **61**, 91 (1987).
[23] Z.-H. Gu, R. Dummer, A. Maradudin, A. McGurn, and E. Méndez, Appl. Opt. **30**, 4094 (1991), 38; 172.
[24] V. Freilikher, M. Pustilnik, and I. Yurkevich, Phys. Lett. A **193**, 467 (1994), 175.
[25] A. A. Maradudin, T. Michel, A. R. McGurn, and E. R. Méndez, Ann. Phys. **203**, 255 (1990).
[26] A. Taflove and S. Hagness, *Computational Electrodynamics: The Finite-Difference Time-Domain Method*, 3rd ed. (Artech House, Norwood, MA, 2005).
[27] J. Volakis, A. Chatterjee, and L. Kempel, *Finite Element Method Electromagnetics: Antennas, Microwave Circuits, and Scattering Applications* (IEEE Press, New York, 2001).
[28] J. Jin, *The Finite Element Method in Electromagnetics*, 2nd ed. (Wiley-IEEE Press, New York, 2002).
[29] M. Bonnet, *Boundary Integral Equation Methods for Solids and Fluids* (Wiley, Chichester, England, 1999).
[30] W. Hackbush and B. Verlag, *Integral Equations: Theory and Numerical Treatment* (Birkhauser Verlag, Basel, Switzerland, 1995).
[31] R. Harrington, *Field Computation by Moment Methods*, IEEE Press Series on Electromagnetic Wave Theory (Wiley-IEEE Press, New York, 1993).
[32] J. Boyd, *Chebychev and Fourier Spectral Methods*, 2nd ed. (Dover, New York, 2001).
[33] I. Simonsen, J. B. Kryvi, A. A. Maradudin, and T. A. Leskova, Comp. Phys. Commun. **182**, 1904 (2011).
[34] G. Brown, V. Celli, M. Haller, and A. Marvin, Surface Science **136**, 381 (1984).
[35] A. Madrazo and A. Maradudin, Optics Communications **134** (1997).
[36] I. Simonsen and A. Maradudin, Opt. Commun. **162**, 99 (1999).
[37] I. Simonsen, Phys. Status Solidi B **247**, 2075 (2010).
[38] A. R. Mcgurn and A. A. Maradudin, Waves in Random Media **6**, 251 (1996).
[39] A. Soubret, G. Berginc, and C. Bourrely, Phys. Rev. B **63**, 245411 (2001).
[40] A. Soubret, G. Berginc, and C. Bourrely, J. Opt. Soc. Am. A **18**, 2778 (2001).
[41] A. M. Kern and O. J. Martin, J. Opt. Soc. Am. A **26**, 732 (2009).
[42] A. Maradudin, "The reduced rayleigh equation for transmission of light trough a two-dimensional randomly rough surface," (2012), unpublished.
[43] T. Leskova, "The reduced rayleigh equation for reflection of light from two-dimensional randomly rough films deposited on flat substrates," Unpublished.
[44] T. Nordam, P. Letnes, I. Simonsen, and A. Maradudin, "Satellite peaks in the scattering of light from the two-dimensional randomly rough surface of a dielectric film on a planar metal surface," (2012), submitted.
[45] I. Simonsen, A. A. Maradudin, and T. Leskova, Phys. Rev. A **81**, 013806 (2010).
[46] I. Simonsen, A. A. Maradudin, and T. Leskova, Phys. Rev. Lett. **104**, 223904 (2010).

[47] N. V. Kampen, *Stochastic Processes in Physics and Chemistry*, 3rd ed. (North Holland, 2007).
[48] R. Millar, Proc. Camb. Phil. Soc. **65**, 773 (1969).
[49] R. Millar, Proc. Camb. Phil. Soc. **69**, 217 (1971).
[50] A. Tishchenko, Opt. Express **17**, 17102 (2009).
[51] J. Jackson, *Classical Electrodynamics*, 3rd ed. (John Wiley & Sons, New York, 2007).
[52] J.A.Stratton, *Electromagnetic Theory*, IEEE Press Series on Electromagnetic Wave Theory (Wiley-IEEE Press, New York, 2007).
[53] A. Maradudin, "The reduced rayleigh equation for reflection of electromagnetic waves from two-dimensional, randomly rough perfectly conducting surfaces," (2012), unpublished.
[54] W. H. Press, S. A. Teukolsky, W. T. Vetterling, and B. P. Flannery, *Numerical Recipes in Fortran. The Art of Scientific Computing*, 2nd ed. (Cambridge University Press, Cambridge, 1992).
[55] For the calculations used to generate the results presented in this paper, this would amount to evaluating $I(\gamma|\mathbf{Q}_\parallel)$ on the order of 10^{10} times.
[56] I. Simonsen, A. A. Maradudin, and T. A. Leskova, Phys. Rev. A **81**, 013806 (2010).
[57] H. A. van der Vorst, SIAM Journal on Scientific and Statistical Computing **13**, 631 (1992).
[58] E. Agullo, C. Augonnet, J. Dongarra, M. Faverge, J. Langou, H. Ltaief, and S. Tomov, in *Computer Systems and Applications (AICCSA), 2011 9th IEEE/ACS International Conference on* (IEEE, 2011) pp. 217–224.

T. Nordam, P. A. Letnes, I. Simonsen, and A. A. Maradudin. "Satellite peaks in the scattering of light from the two-dimensional randomly rough surface of a dielectric film on a planar metal surface", pp. 11336–11350. *Opt. Express* 20 (2012)

Paper 9

Satellite peaks in the scattering of light from the two-dimensional randomly rough surface of a dielectric film on a planar metal surface

T. Nordam,[1] P.A. Letnes,[1] I. Simonsen,[1,*] and A.A. Maradudin[2]

[1]*Department of Physics, Norwegian University of Science and Technology (NTNU) NO-7491 Trondheim, Norway*

[2]*Department of Physics and Astronomy, University of California, Irvine CA 92697, USA*

[*]*Ingve.Simonsen@phys.ntnu.no*

Abstract: A nonperturbative, purely numerical, solution of the reduced Rayleigh equation for the scattering of p- and s-polarized light from a dielectric film with a two-dimensional randomly rough surface deposited on a planar metallic substrate, has been carried out. It is found that satellite peaks are present in the angular dependence of the elements of the mean differential reflection coefficient in addition to an enhanced backscattering peak. This result resolves a conflict between the results of earlier approximate theoretical studies of scattering from this system.

OCIS codes: (290.1483) BSDF, BRDF, and BTDF; (290.4210) Multiple scattering; (290.5825) Scattering theory; (290.5880) Scattering, rough surfaces.

References and links

1. A. R. McGurn, A. A. Maradudin, and V. Celli, "Localization effects in the scattering of light from a randomly rough grating," Phys. Rev. B **31**, 4866–4871 (1985).
2. M. Nieto-Vesperinas and J. M. Soto-Crespo, "Monte Carlo simulations for scattering of electromagnetic waves from perfectly conductive random rough surfaces," Opt. Lett. **12**, 979–981 (1987).
3. A. A. Maradudin, E. R. Méndez, and T. Michel, "Backscattering effects in the elastic scattering of p-polarized light from a large-amplitude random metallic grating," Opt. Lett. **14**, 151–153 (1989).
4. I. Simonsen, "Optics of surface disordered systems," Eur. Phys. J.–Spec. Top. **181**, 1–103 (2010).
5. A. McGurn and A. Maradudin, "An analogue of enhanced backscattering in the transmission of light through a thin film with a randomly rough surface," Opt. Commun. **72**, 279–285 (1989).
6. V. Freilikher, E. Kanzieper, and A. Maradudin, "Coherent scattering enhancement in systems bounded by rough surfaces," Phys. Rep. **288**, 127–204 (1997).
7. V. Freilikher, M. Pustilnik, and I. Yurkevich, "Wave scattering from a bounded medium with disorder," Phys. Lett. A **193**, 467–470 (1994).
8. A. McGurn and A. Maradudin, "Perturbation theory results for the diffuse scattering of light from two-dimensional randomly rough metal surfaces," Wave. Random Media **6**, 251–267 (1996).
9. J. T. Johnson, "Third-order small-perturbation method for scattering from dielectric rough surfaces," J. Opt. Soc. Am. A **16**, 2720–2736 (1999).
10. A. Soubret, G. Berginc, and C. Bourrely, "Application of reduced Rayleigh equations to electromagnetic wave scattering by two-dimensional randomly rough surfaces," Phys. Rev. B **63**, 245411 (2001).
11. I. Simonsen, A. A. Maradudin, and T. A. Leskova, "Scattering of electromagnetic waves from two-dimensional randomly rough perfectly conducting surfaces: The full angular intensity distribution," Phys. Rev. A **81**, 013806 (2010).
12. I. Simonsen, A. A. Maradudin, and T. A. Leskova, "Scattering of electromagnetic waves from two-dimensional randomly rough penetrable surfaces," Phys. Rev. Lett. **104**, 223904 (2010).

#165194 - $15.00 USD Received 22 Mar 2012; revised 25 Apr 2012; accepted 27 Apr 2012; published 2 May 2012

13. I. Simonsen, J. B. Kryvi, A. A. Maradudin, and T. A. Leskova, "Light scattering from anisotropic, randomly rough, perfectly conducting surfaces," Comput. Phys. Commun. **182**, 1904–1908 (2011).
14. T. Kawanishi, H. Ogura, and Z. L. Wang, "Scattering of an electromagnetic wave from a slightly random dielectric surface: Yoneda peak and Brewster angle in incoherent scattering," Wave. Random Media **7**, 351–384 (1997).
15. A. Soubret, G. Berginc, and C. Bourrely, "Backscattering enhancement of an electromagnetic wave scattered by two-dimensional rough layers," J. Opt. Soc. Am. A **18**, 2778–2788 (2001).
16. E. R. Méndez, E. I. Chaikina, and H. M. Escamilla, "Observation of satellite peaks and dips in the scattering of light in a double-pass geometry," Opt. Lett. **24**, 705–707 (1999).
17. T. Nordam, P. A. Letnes, and I. Simonsen, "Numerical simulations of scattering of light from two-dimensional surfaces using the reduced Rayleigh equation," http://arxiv.org/abs/1204.4984.
18. T. A. Leskova, P. A. Letnes, A. A. Maradudin, T. Nordam, and I. Simonsen, "The scattering of light from two-dimensional randomly rough surfaces," Proc. SPIE **8172**, 817209 (2011).
19. T. A. Leskova, Department of Physics and Astronomy, University of California, Irvine CA 92697, U.S.A. (personal communication, 2010).
20. J. T. Johnson, "Third-order small-perturbation method for scattering from dielectric rough surfaces," J. Opt. Soc. Am. A **16**, 2720–2736 (1999).
21. A. Maradudin, T. Michel, A. McGurn, and E. Méndez, "Enhanced backscattering of light from a random grating," Ann. Phys. **203**, 255–307 (1990).
22. W. Press, B. Flannery, S. Teukolsky, and W. Vetterling, *Numerical recipes*, 3rd ed. (Cambridge Univ Press, 2007).
23. P. B. Johnson, "Optical constants of the noble metals," Phys. Rev. **6**, 4370–4379 (1972).
24. C. S. West and K. A. O'Donnell, "Observations of backscattering enhancement from polaritons on a rough metal surface," J. Opt. Soc. Am. A **12**, 390–397 (1995).
25. A. Madrazo and A. Maradudin, "Numerical solutions of the reduced Rayleigh equation for the scattering of electromagnetic waves from rough dielectric films on perfectly conducting substrates," Opt. Commun. **134**, 251–263 (1997).
26. I. Simonsen and A. Maradudin, "Numerical simulation of electromagnetic wave scattering from planar dielectric films deposited on rough perfectly conducting substrates," Opt. Commun. **162**, 99–111 (1999).

In the earliest analytic [1] and computer simulation [2, 3] studies of the multiple scattering of light from clean one-dimensional randomly rough surfaces of perfect conductors or of penetrable media, the focus was on the phenomenon of enhanced backscattering. This is the presence of a well-defined peak in the retroreflection direction in the angular dependence of the intensity of the light that has been scattered incoherently (diffusely).

In subsequent work on the multiple scattering of light from free-standing or supported films with a one-dimensional randomly rough surface that support two or more guided waves, new effects were discovered [4]. These include enhanced transmission, which is the presence of a well-defined peak in the anti-specular direction in the angular dependence of the intensity of the light transmitted through the film [5]. Perhaps more interesting was the discovery of satellite peaks in the angular dependence of the intensity of the light scattered from or transmitted through the film. These are well-defined peaks present on both sides of the enhanced backscattering and enhanced transmission peaks, respectively, that arise from the coherent interference of guided waves with the frequency of the incident light, but with different wavenumbers [6].

It should be noted, however, that the prediction of these satellite peaks was first made in the context of the scattering of electromagnetic waves from a dielectric film containing a random distribution of volume scatterers [7], rather than from a randomly rough surface, when the thickness of the film is small compared to the mean free path of the electromagnetic wave in the random medium.

In analytic [8–10] and computer simulation calculations [11–13] of the multiple scattering of light from clean two-dimensional randomly rough surfaces of perfect conductors and penetrable media, enhanced backscattering was observed in the results. However, when attention turned to the scattering of light from a perfectly conducting surface coated with a dielectric film, conflicting results were obtained. In these studies the dielectric-perfect conductor interface was assumed to be planar, while the vacuum-dielectric interface was assumed to be a two-dimensional randomly rough interface. In the first of these studies Kawanishi *et al*. [14]

#165194 - $15.00 USD Received 22 Mar 2012; revised 25 Apr 2012; accepted 27 Apr 2012; published 2 May 2012

applied the stochastic functional approach to this problem and found no evidence for satellite peaks in their results. They suggested that the ensemble averaging of the intensity of the scattered field restores isotropy in the mean scattering plane, and thereby eliminates the occurrence of special scattering angles at which satellite peaks could occur. In subsequent work in which the reduced Rayleigh equation for scattering from this structure [10, 15] was solved in the form of expansions of the amplitudes of the p- and s-polarized components of the scattered field in powers of the surface profile function through terms of third order, satellite peaks were found. However, the contribution to the scattering amplitudes associated with the third-order term was larger than that from the first-order term for the roughness and experimental parameters assumed in that work. It is therefore possible that these values fell outside the ranges for which a perturbative solution of the reduced Rayleigh equation is reliable.

Although satellite peaks were observed in experiments carried out by Méndez *et al.* [16] that utilized the double passage of polarized light through a random phase screen, the experimental conditions were sufficiently different from those studied theoretically in Refs. [10, 14], that these results could not be used to support the predictions of either of these studies.

In an effort to resolve the issue of whether satellite peaks do or do not exist in the scattering of light from a rough dielectric film deposited on the planar surface of a metal, in this paper we carry out a nonperturbative, purely numerical, solution of the reduced Rayleigh equation [17] for the scattering of p- and s-polarized light from a structure consisting of a dielectric film deposited on a metal substrate when the dielectric-metal interface is planar, while the vacuum-dielectric interface is a two-dimensional randomly rough interface. This is an approach that was used successfully in recent calculations of the scattering of p- and s-polarized light from a two-dimensional randomly rough interface between a dielectric and a metal [17, 18], which prompts its application to the present problem.

The system we study consists of vacuum (ε_1) in the region $x_3 > d + \zeta\left(\mathbf{x}_\parallel\right)$, where $\mathbf{x}_\parallel = (x_1, x_2, 0)$; a dielectric film ($\varepsilon_2$) in the region $0 < x_3 < d + \zeta\left(\mathbf{x}_\parallel\right)$; and a lossy metal ($\varepsilon_3$) in the region $x_3 < 0$. The surface profile function $\zeta\left(\mathbf{x}_\parallel\right)$ is assumed to be a single-valued function of $\mathbf{x}_\parallel$ that is differentiable with respect to x_1 and x_2, and constitutes a zero-mean, stationary, isotropic, Gaussian random process defined by

$$\left\langle \zeta(\mathbf{x}_\parallel)\zeta(\mathbf{x}'_\parallel)\right\rangle = \delta^2 W\left(\left|\mathbf{x}_\parallel - \mathbf{x}'_\parallel\right|\right). \tag{1}$$

The angle brackets here denote an average over the ensemble of realizations of the surface profile function, and $\delta = \left\langle \zeta^2\left(\mathbf{x}_\parallel\right)\right\rangle^{1/2}$ is the rms height of the surface roughness.

The electric field in the vacuum $\left[x_3 > d + \zeta\left(\mathbf{x}_\parallel\right)\right]$ is the sum of an incident field and a scattered field, $\mathbf{E}(\mathbf{x};t) = [\mathbf{E}(\mathbf{x}|\omega)_{\rm inc} + \mathbf{E}(\mathbf{x}|\omega)_{\rm sc}]\exp(-{\rm i}\omega t)$, where

$$\begin{aligned}\mathbf{E}(\mathbf{x}|\omega)_{\rm inc} = &\left\{\frac{c}{\omega}\left[\hat{\mathbf{k}}_\parallel \alpha_1(k_\parallel) + \hat{\mathbf{x}}_3 k_\parallel\right] B_{\rm p}(\mathbf{k}_\parallel) + \left(\hat{\mathbf{x}}_3 \times \hat{\mathbf{k}}_\parallel\right) B_{\rm s}(\mathbf{k}_\parallel)\right\} \\ &\times \exp\left({\rm i}\mathbf{k}_\parallel \cdot \mathbf{x}_\parallel - {\rm i}\alpha_1(k_\parallel)x_3\right)\end{aligned} \tag{2a}$$

$$\begin{aligned}\mathbf{E}(\mathbf{x}|\omega)_{\rm sc} = &\int \frac{{\rm d}^2 q_\parallel}{(2\pi)^2}\left\{\frac{c}{\omega}\left[\hat{\mathbf{q}}_\parallel \alpha_1(q_\parallel) - \hat{\mathbf{x}}_3 q_\parallel\right] A_{\rm p}(\mathbf{q}_\parallel) + \left(\hat{\mathbf{x}}_3 \times \hat{\mathbf{q}}_\parallel\right) A_{\rm s}(\mathbf{q}_\parallel)\right\} \\ &\times \exp\left({\rm i}\mathbf{q}_\parallel \cdot \mathbf{x}_\parallel + {\rm i}\alpha_1(q_\parallel)x_3\right),\end{aligned} \tag{2b}$$

while the subscripts p and s denote the p-polarized and s-polarized components of these fields with respect to the local planes of incidence and scattering. A caret over a vector indicates that it is a unit vector, and the vector $\mathbf{k}_\parallel$ is defined as $\mathbf{k}_\parallel = (k_1, k_2, 0)$ (with similar definitions for $\mathbf{q}_\parallel$

#165194 - $15.00 USD Received 22 Mar 2012; revised 25 Apr 2012; accepted 27 Apr 2012; published 2 May 2012

and $\mathbf{p}_\parallel$). The functions $\alpha_i(q_\parallel)$ $(i = 1,2,3)$ are defined by

$$\alpha_i(q_\parallel) = \left[\varepsilon_i \left(\frac{\omega}{c}\right)^2 - q_\parallel^2\right]^{1/2}, \qquad \mathrm{Re}\,\alpha_i(q_\parallel) > 0, \mathrm{Im}\,\alpha_i(q_\parallel) > 0. \tag{3}$$

A linear relation exists between the amplitudes $A_\alpha(\mathbf{q}_\parallel)$ and $B_\beta(\mathbf{k}_\parallel)$ $(\alpha, \beta = \mathrm{p}, \mathrm{s})$, which we write as

$$A_\alpha(\mathbf{q}_\parallel) = \sum_\beta R_{\alpha\beta}(\mathbf{q}_\parallel|\mathbf{k}_\parallel) B_\beta(\mathbf{k}_\parallel) \tag{4}$$

where $R_{\alpha\beta}$ is the scattering amplitude for incident β-polarized light scattered into α-polarized light. The convention we use with respect to the polarization subscripts is

$$\mathbf{R}(\mathbf{q}_\parallel|\mathbf{k}_\parallel) = \begin{pmatrix} R_{\mathrm{pp}}(\mathbf{q}_\parallel|\mathbf{k}_\parallel) & R_{\mathrm{ps}}(\mathbf{q}_\parallel|\mathbf{k}_\parallel) \\ R_{\mathrm{sp}}(\mathbf{q}_\parallel|\mathbf{k}_\parallel) & R_{\mathrm{ss}}(\mathbf{q}_\parallel|\mathbf{k}_\parallel) \end{pmatrix}. \tag{5}$$

It has been shown by Soubret *et al*. [10] and Leskova [19] that the scattering amplitudes $\left[R_{\alpha\beta}(\mathbf{q}_\parallel|\mathbf{k}_\parallel)\right]$ satisfy the matrix integral equation

$$\int \frac{\mathrm{d}^2 q_\parallel}{(2\pi)^2} \mathbf{M}(\mathbf{p}_\parallel|\mathbf{q}_\parallel)\mathbf{R}(\mathbf{q}_\parallel|\mathbf{k}_\parallel) = -\mathbf{N}(\mathbf{p}_\parallel|\mathbf{k}_\parallel), \tag{6}$$

called a *reduced Rayleigh equation* because it is an equation for only the scattered field in the medium of incidence, and not for the fields in the film and in the substrate.The effects of the latter two fields are contained in the elements of the matrices $\mathbf{M}(\mathbf{p}_\parallel|\mathbf{q}_\parallel)$ and $\mathbf{N}(\mathbf{p}_\parallel|\mathbf{k}_\parallel)$. With the shorthand notation $\alpha(q_\parallel, \omega) \equiv \alpha(q_\parallel)$, the elements of these matrices in the forms obtained by

#165194 - $15.00 USD Received 22 Mar 2012; revised 25 Apr 2012; accepted 27 Apr 2012; published 2 May 2012

Leskova [19] are

$$
\begin{aligned}
M_{\mathrm{pp}}(\mathbf{p}_\parallel|\mathbf{q}_\parallel) &= \left[p_\parallel q_\parallel + \alpha_2(p_\parallel)(\hat{\mathbf{p}}_\parallel\cdot\hat{\mathbf{q}}_\parallel)\alpha_1(q_\parallel)\right] \\
&\quad\times \Gamma_{\mathrm{p}}(p_\parallel)\exp\left(-\mathrm{i}\left[\alpha_2(p_\parallel)-\alpha_1(q_\parallel)\right]d\right)\frac{I\left(\alpha_2(p_\parallel)-\alpha_1(q_\parallel)|\mathbf{p}_\parallel-\mathbf{q}_\parallel\right)}{\alpha_2(p_\parallel)-\alpha_1(q_\parallel)} \\
&\quad+\left[p_\parallel q_\parallel - \alpha_2(p_\parallel)(\hat{\mathbf{p}}_\parallel\cdot\hat{\mathbf{q}}_\parallel)\alpha_1(q_\parallel)\right] \\
&\quad\times \Delta_{\mathrm{p}}(p_\parallel)\exp\left(\mathrm{i}\left[\alpha_2(p_\parallel)+\alpha_1(q_\parallel)\right]d\right)\frac{I\left(-\left[\alpha_2(p_\parallel)+\alpha_1(q_\parallel)\right]|\mathbf{p}_\parallel-\mathbf{q}_\parallel\right)}{\alpha_2(p_\parallel)+\alpha_1(q_\parallel)}
\end{aligned}
\tag{7a}
$$

$$
\begin{aligned}
M_{\mathrm{ps}}(\mathbf{p}_\parallel|\mathbf{q}_\parallel) &= -\frac{\omega}{c}\alpha_2(p_\parallel)\left(\hat{\mathbf{p}}_\parallel\times\hat{\mathbf{q}}_\parallel\right)_3 \\
&\quad\left(\Gamma_{\mathrm{p}}(p_\parallel)\exp\left(-\mathrm{i}\left[\alpha_2(p_\parallel)-\alpha_1(q_\parallel)\right]d\right)\frac{I\left(\alpha_2(p_\parallel)-\alpha_1(q_\parallel)|\mathbf{p}_\parallel-\mathbf{q}_\parallel\right)}{\alpha_2(p_\parallel)-\alpha_1(q_\parallel)}\right. \\
&\quad\left.-\Delta_{\mathrm{p}}(p_\parallel)\exp\left(\mathrm{i}\left[\alpha_2(p_\parallel)+\alpha_1(q_\parallel)\right]d\right)\frac{I\left(-\left[\alpha_2(p_\parallel)+\alpha_1(q_\parallel)\right]|\mathbf{p}_\parallel-\mathbf{q}_\parallel\right)}{\alpha_2(p_\parallel)+\alpha_1(q_\parallel)}\right)
\end{aligned}
\tag{7b}
$$

$$
\begin{aligned}
M_{\mathrm{sp}}(\mathbf{p}_\parallel|\mathbf{q}_\parallel) &= \frac{\omega}{c}\left(\hat{\mathbf{p}}_\parallel\times\hat{\mathbf{q}}_\parallel\right)_3\alpha_1(q_\parallel) \\
&\quad\left(\Gamma_{\mathrm{s}}(p_\parallel)\exp\left(-\mathrm{i}\left[\alpha_2(p_\parallel)-\alpha_1(q_\parallel)\right]d\right)\frac{I\left(\alpha_2(p_\parallel)-\alpha_1(q_\parallel)|\mathbf{p}_\parallel-\mathbf{q}_\parallel\right)}{\alpha_2(p_\parallel)-\alpha_1(q_\parallel)}\right. \\
&\quad\left.+\Delta_{\mathrm{s}}(p_\parallel)\exp\left(\mathrm{i}\left[\alpha_2(p_\parallel)+\alpha_1(q_\parallel)\right]d\right)\frac{I\left(-\left[\alpha_2(p_\parallel)+\alpha_1(q_\parallel)\right]|\mathbf{p}_\parallel-\mathbf{q}_\parallel\right)}{\alpha_2(p_\parallel)+\alpha_1(q_\parallel)}\right)
\end{aligned}
\tag{7c}
$$

$$
\begin{aligned}
M_{\mathrm{ss}}(\mathbf{p}_\parallel|\mathbf{q}_\parallel) &= \frac{\omega^2}{c^2}\left(\hat{\mathbf{p}}_\parallel\cdot\hat{\mathbf{q}}_\parallel\right) \\
&\quad\left(\Gamma_{\mathrm{s}}(p_\parallel)\exp\left(-\mathrm{i}\left[\alpha_2(p_\parallel)-\alpha_1(q_\parallel)\right]d\right)\frac{I\left(\alpha_2(p_\parallel)-\alpha_1(q_\parallel)|\mathbf{p}_\parallel-\mathbf{q}_\parallel\right)}{\alpha_2(p_\parallel)-\alpha_1(q_\parallel)}\right. \\
&\quad\left.+\Delta_{\mathrm{s}}(p_\parallel)\exp\left(\mathrm{i}\left[\alpha_2(p_\parallel)+\alpha_1(q_\parallel)\right]d\right)\frac{I\left(-\left[\alpha_2(p_\parallel)+\alpha_1(q_\parallel)\right]|\mathbf{p}_\parallel-\mathbf{q}_\parallel\right)}{\alpha_2(p_\parallel)+\alpha_1(q_\parallel)}\right),
\end{aligned}
\tag{7d}
$$

#165194 - $15.00 USD Received 22 Mar 2012; revised 25 Apr 2012; accepted 27 Apr 2012; published 2 May 2012

and

$$
\begin{aligned}
N_{\mathrm{pp}}(\mathbf{p}_\parallel|\mathbf{k}_\parallel) &= -\left[p_\parallel k_\parallel - \alpha_2(p_\parallel)(\hat{\mathbf{p}}_\parallel\cdot\hat{\mathbf{k}}_\parallel)\alpha_1(k_\parallel)\right] \\
&\quad\times\Gamma_{\mathrm{p}}(p_\parallel)\exp\left(-\mathrm{i}\left[\alpha_2(p_\parallel)+\alpha_1(k_\parallel)\right]d\right)\frac{I\left(\alpha_2(p_\parallel)+\alpha_1(k_\parallel)|\mathbf{p}_\parallel-\mathbf{k}_\parallel\right)}{\alpha_2(p_\parallel)+\alpha_1(k_\parallel)} \\
&\quad-\left[p_\parallel k_\parallel + \alpha_2(p_\parallel)(\hat{\mathbf{p}}_\parallel\cdot\hat{\mathbf{k}}_\parallel)\alpha_1(k_\parallel)\right] \\
&\quad\times\Delta_{\mathrm{p}}(p_\parallel)\exp\left(\mathrm{i}\left[\alpha_2(p_\parallel)-\alpha_1(k_\parallel)\right]d\right)\frac{I\left(-\left[\alpha_2(p_\parallel)-\alpha_1(k_\parallel)\right]|\mathbf{p}_\parallel-\mathbf{k}_\parallel\right)}{\alpha_2(p_\parallel)-\alpha_1(k_\parallel)}
\end{aligned}
\tag{8a}
$$

$$
\begin{aligned}
N_{\mathrm{ps}}(\mathbf{p}_\parallel|\mathbf{k}_\parallel) &= -\frac{\omega}{c}\alpha_2(p_\parallel)\left(\hat{\mathbf{p}}_\parallel\times\hat{\mathbf{k}}_\parallel\right)_3 \\
&\quad\times\left(\Gamma_{\mathrm{p}}(p_\parallel)\exp\left(-\mathrm{i}\left[\alpha_2(p_\parallel)+\alpha_1(k_\parallel)\right]d\right)\frac{I\left(\alpha_2(p_\parallel)+\alpha_1(k_\parallel)|\mathbf{p}_\parallel-\mathbf{k}_\parallel\right)}{\alpha_2(p_\parallel)+\alpha_1(k_\parallel)}\right. \\
&\quad\left.-\Delta_{\mathrm{p}}(p_\parallel)\exp\left(\mathrm{i}\left[\alpha_2(p_\parallel)-\alpha_1(k_\parallel)\right]d\right)\frac{I\left(-\left[\alpha_2(p_\parallel)-\alpha_1(k_\parallel)\right]|\mathbf{p}_\parallel-\mathbf{k}_\parallel\right)}{\alpha_2(p_\parallel)-\alpha_1(k_\parallel)}\right)
\end{aligned}
\tag{8b}
$$

$$
\begin{aligned}
N_{\mathrm{sp}}(\mathbf{p}_\parallel|\mathbf{k}_\parallel) &= \frac{\omega}{c}\left(\hat{\mathbf{p}}_\parallel\times\hat{\mathbf{k}}_\parallel\right)_3\alpha_1(k_\parallel) \\
&\quad\times\left(\Gamma_{\mathrm{s}}(p_\parallel)\exp\left(-\mathrm{i}\left[\alpha_2(p_\parallel)+\alpha_1(k_\parallel)\right]d\right)\frac{I\left(\alpha_2(p_\parallel)+\alpha_1(k_\parallel)|\mathbf{p}_\parallel-\mathbf{k}_\parallel\right)}{\alpha_2(p_\parallel)+\alpha_1(k_\parallel)}\right. \\
&\quad\left.+\Delta_{\mathrm{s}}(p_\parallel)\exp\left(\mathrm{i}\left[\alpha_2(p_\parallel)-\alpha_1(k_\parallel)\right]d\right)\frac{I\left(-\left[\alpha_2(p_\parallel)-\alpha_1(k_\parallel)\right]|\mathbf{p}_\parallel-\mathbf{k}_\parallel\right)}{\alpha_2(p_\parallel)-\alpha_1(k_\parallel)}\right)
\end{aligned}
\tag{8c}
$$

$$
\begin{aligned}
N_{\mathrm{ss}}(\mathbf{p}_\parallel|\mathbf{k}_\parallel) &= \frac{\omega^2}{c^2}\left(\hat{\mathbf{p}}_\parallel\cdot\hat{\mathbf{k}}_\parallel\right) \\
&\quad\times\left(\Gamma_{\mathrm{s}}(p_\parallel)\exp\left(-\mathrm{i}\left[\alpha_2(p_\parallel)+\alpha_1(k_\parallel)\right]d\right)\frac{I\left(\alpha_2(p_\parallel)+\alpha_1(k_\parallel)|\mathbf{p}_\parallel-\mathbf{k}_\parallel\right)}{\alpha_2(p_\parallel)+\alpha_1(k_\parallel)}\right. \\
&\quad\left.+\Delta_{\mathrm{s}}(p_\parallel)\exp\left(\mathrm{i}\left[\alpha_2(p_\parallel)-\alpha_1(k_\parallel)\right]d\right)\frac{I\left(-\left[\alpha_2(p_\parallel)-\alpha_1(k_\parallel)\right]|\mathbf{p}_\parallel-\mathbf{k}_\parallel\right)}{\alpha_2(p_\parallel)-\alpha_1(k_\parallel)}\right).
\end{aligned}
\tag{8d}
$$

In writing Eqs. (7) and (8) we have introduced the functions

$$\Gamma_{\mathrm{p}}(p_\parallel) = \varepsilon_2\alpha_3(p_\parallel,\omega)+\varepsilon_3\alpha_2(p_\parallel,\omega) \tag{9a}$$

$$\Delta_{\mathrm{p}}(p_\parallel) = \varepsilon_2\alpha_3(p_\parallel,\omega)-\varepsilon_3\alpha_2(p_\parallel,\omega) \tag{9b}$$

and

$$\Gamma_{\mathrm{s}}(p_\parallel) = \alpha_3(p_\parallel,\omega)+\alpha_2(p_\parallel,\omega) \tag{10a}$$

$$\Delta_{\mathrm{s}}(p_\parallel) = \alpha_3(p_\parallel,\omega)-\alpha_2(p_\parallel,\omega), \tag{10b}$$

as well as

$$I\left(\gamma|\mathbf{Q}_\parallel\right) = \int \mathrm{d}^2x_\parallel\,\exp\left(-\mathrm{i}\mathbf{Q}_\parallel\cdot\mathbf{x}_\parallel\right)\exp\left[-\mathrm{i}\gamma\zeta\left(\mathbf{x}_\parallel\right)\right]. \tag{11}$$

The scattering amplitudes $\left[R_{\alpha\beta}(\mathbf{q}_\parallel|\mathbf{k}_\parallel)\right]$ play a central role in the present theory because the mean differential reflection coefficient, an experimentally measurable function, can be expressed in terms of these amplitudes. The differential reflection coefficient $(\partial R/\partial\Omega_{\mathrm{s}})$ is defined

#165194 - $15.00 USD Received 22 Mar 2012; revised 25 Apr 2012; accepted 27 Apr 2012; published 2 May 2012

such that $(\partial R/\partial\Omega_s)\mathrm{d}\Omega_s$ is the fraction of the total time-averaged flux incident on the surface that is scattered into the element of solid angle $\mathrm{d}\Omega_s$ about the scattering direction (θ_s,ϕ_s). Since we are studying the scattering of light from a randomly rough surface, it is the average of this function over the ensemble of realizations of the surface profile function that we need to calculate. The contribution to the mean differential reflection coefficient from the incoherent (diffuse) component of the scattered light, when incident light of β polarization whose wave vector has the projection $\mathbf{k}_\parallel$ on the mean scattering surface is scattered into light of α polarization whose wave vector has the projection $\mathbf{q}_\parallel$ on the mean scattering surface, denoted $\left\langle \partial R_{\alpha\beta}/\partial\Omega_s\right\rangle_{\mathrm{incoh}}$, is given by

$$\left\langle\frac{\partial R_{\mathrm{pp}}}{\partial\Omega_s}\right\rangle_{\mathrm{incoh}}=\frac{1}{S}\frac{\sqrt{\varepsilon_1}}{4\pi^2}\frac{\omega}{c}\frac{\alpha_1^2(q_\parallel)}{\alpha_1(k_\parallel)}\left[\left\langle\left|R_{\mathrm{pp}}(\mathbf{q}_\parallel|\mathbf{k}_\parallel)\right|^2\right\rangle-\left|\left\langle R_{\mathrm{pp}}(\mathbf{q}_\parallel|\mathbf{k}_\parallel)\right\rangle\right|^2\right] \tag{12a}$$

$$\left\langle\frac{\partial R_{\mathrm{ps}}}{\partial\Omega_s}\right\rangle_{\mathrm{incoh}}=\frac{1}{S}\frac{\varepsilon_1^{3/2}}{4\pi^2}\frac{\omega}{c}\frac{\alpha_1^2(q_\parallel)}{\alpha_1(k_\parallel)}\left[\left\langle\left|R_{\mathrm{ps}}(\mathbf{q}_\parallel|\mathbf{k}_\parallel)\right|^2\right\rangle-\left|\left\langle R_{\mathrm{ps}}(\mathbf{q}_\parallel|\mathbf{k}_\parallel)\right\rangle\right|^2\right] \tag{12b}$$

$$\left\langle\frac{\partial R_{\mathrm{sp}}}{\partial\Omega_s}\right\rangle_{\mathrm{incoh}}=\frac{1}{S}\frac{1}{4\pi^2\sqrt{\varepsilon_1}}\frac{\omega}{c}\frac{\alpha_1^2(q_\parallel)}{\alpha_1(k_\parallel)}\left[\left\langle\left|R_{\mathrm{sp}}(\mathbf{q}_\parallel|\mathbf{k}_\parallel)\right|^2\right\rangle-\left|\left\langle R_{\mathrm{sp}}(\mathbf{q}_\parallel|\mathbf{k}_\parallel)\right\rangle\right|^2\right] \tag{12c}$$

$$\left\langle\frac{\partial R_{\mathrm{ss}}}{\partial\Omega_s}\right\rangle_{\mathrm{incoh}}=\frac{1}{S}\frac{\sqrt{\varepsilon_1}}{4\pi^2}\frac{\omega}{c}\frac{\alpha_1^2(q_\parallel)}{\alpha_1(k_\parallel)}\left[\left\langle\left|R_{\mathrm{ss}}(\mathbf{q}_\parallel|\mathbf{k}_\parallel)\right|^2\right\rangle-\left|\left\langle R_{\mathrm{ss}}(\mathbf{q}_\parallel|\mathbf{k}_\parallel)\right\rangle\right|^2\right], \tag{12d}$$

where S is the area of the plane $x_3=0$ covered by the rough surface. The two-dimensional wave vectors $\mathbf{k}_\parallel$ and $\mathbf{q}_\parallel$ are defined in terms of the polar and azimuthal angles of incidence (θ_0,ϕ_0) and scattering (θ_s,ϕ_s), respectively, by $\mathbf{k}_\parallel=\sqrt{\varepsilon_1}(\omega/c)\,\sin\theta_0\,(\cos\phi_0,\sin\phi_0,0)$ and $\mathbf{q}_\parallel=\sqrt{\varepsilon_1}(\omega/c)\sin\theta_s(\cos\phi_s,\sin\phi_s,0)$. Thus these wave vectors in Eq. (12) are restricted to the domains $k_\parallel<\sqrt{\varepsilon_1}(\omega/c)$ and $q_\parallel<\sqrt{\varepsilon_1}(\omega/c)$ of the q_1q_2 plane.

Up to now Eq. (6) has been solved by small-amplitude perturbation theory through terms of third order in the surface profile function [10, 20]. Here we present results for the mean differential reflection coefficient and for the full angular distribution of the intensity of the scattered light obtained by a nonperturbative, purely numerical solution of Eqs. (6)–(11), as described in Ref. [17]. This was done by generating a realization of the surface profile function numerically on a grid of N_x^2 points within a square region of the x_1x_2 plane of edge L, so that the (linear) sampling interval was $\Delta x=L/N_x$. A two-dimensional version of the filtering method used in [17, 21] was used to generate the profile function [13]. The function $I(\gamma|\mathbf{Q}_\parallel)$ was then evaluated by expanding the integrand in powers of the surface profile function $\zeta(\mathbf{x}_\parallel)$, and calculating the Fourier transform of $\zeta^n(\mathbf{x}_\parallel)$ by the fast Fourier transform. In evaluating the integral over $\mathbf{q}_\parallel$ in Eq. (6) the infinite limits were replaced by finite ones: $\left(q_1^2+q_2^2\right)^{1/2}\le Q/2$. The Nyquist sampling theorem requires that $|q_1|$ and $|q_2|$ be smaller than $Q_c=\pi/\Delta x$ [22, p. 605]. The components of the vector $\mathbf{p}_\parallel-\mathbf{q}_\parallel$ entering $I(\gamma|\mathbf{p}_\parallel-\mathbf{q}_\parallel)$ lie in the interval $[-Q,Q]$, so we have chosen $Q=Q_c$. A grid with a grid constant $\Delta q_1=\Delta q_2=\Delta q=2\pi/L$ was constructed within the circular region of the q_1q_2 plane where $\left(q_1^2+q_2^2\right)\le Q/2$. The integral over this region in Eq. (6) was carried out by a two-dimensional version of the extended midpoint method [22, p. 161] and the values of $R_{\alpha\beta}(\mathbf{q}_\parallel|\mathbf{k}_\parallel)$ were calculated for values of $\mathbf{q}_\parallel$ at the points of this grid for a given value of $\mathbf{k}_\parallel$, which was also a point on this grid. The resulting matrix equations were solved by LU factorization and backsubstitution. The values of $R_{\alpha\beta}(\mathbf{q}_\parallel|\mathbf{k}_\parallel)$ and $|R_{\alpha\beta}(\mathbf{q}_\parallel|\mathbf{k}_\parallel)|^2$ were then calculated for N_p realizations of the surface profile function. An arithmetic average of the N_p results for each of these functions yielded the averages $\left\langle R_{\alpha\beta}(\mathbf{q}_\parallel|\mathbf{k}_\parallel)\right\rangle$ and $\left\langle|R_{\alpha\beta}(\mathbf{q}_\parallel|\mathbf{k}_\parallel)|^2\right\rangle$, from which the incoherent contribution to the mean differential reflection coefficients were calculated according to Eq. (12).

#165194 - $15.00 USD Received 22 Mar 2012; revised 25 Apr 2012; accepted 27 Apr 2012; published 2 May 2012

We apply this approach to the scattering of p- and s-polarized plane waves, whose wavelength is $\lambda = 633$ nm, incident from vacuum ($\varepsilon_1 = 1$) on a dielectric film ($\varepsilon_2 = 2.6896 + 0.01\mathrm{i}$) coating a silver surface ($\varepsilon_3 = -18.28 + 0.481\mathrm{i}$) [23]. The mean thickness of the film is $d = 0.756\lambda = 478.5$ nm. The roughness of the vacuum-dielectric interface is characterized by a two-dimensional version of the West–O'Donnell power spectrum [24] given by [8]

$$g(|\mathbf{k}_\parallel|) = \frac{4\pi}{k_+^2 - k_-^2}\theta(|\mathbf{k}_\parallel| - k_-)\theta(k_+ - |\mathbf{k}_\parallel|), \tag{13}$$

where $\theta(x)$ is the Heaviside unit step function, and $k_- = 0.82(\omega/c)$, $k_+ = 1.97(\omega/c)$. The rms height of the surface roughness was assumed to be $\delta = \lambda/40 = 15.82$ nm, the surface was discretized on a grid of resolution $\Delta x_1 = \Delta x_2 = 0.123\lambda = 77.6$ nm and the edge of the (quadratic) surface was $L = 55\lambda = 34.8$ μm.

The contribution to the mean differential reflection coefficient $\left\langle \partial R_{\alpha\beta}(\mathbf{q}_\parallel|\mathbf{k}_\parallel)/\partial\Omega_s \right\rangle_{\mathrm{incoh}}$ from single-scattering processes $\left[\text{second order in } \zeta(\mathbf{x}_\parallel)\right]$ is proportional to $g(|\mathbf{q}_\parallel - \mathbf{k}_\parallel|)$ [8]. Since the power spectrum (13) is identically zero for $|\mathbf{k}_\parallel| < k_-$, there is no contribution to the mean differential reflection coefficient from the light scattered incoherently by single-scattering processes when the wave vectors $\mathbf{q}_\parallel$ and $\mathbf{k}_\parallel$ satisfy the inequality $|\mathbf{q}_\parallel - \mathbf{k}_\parallel| < k_-$. The contribution to $\left\langle \partial R_{\alpha\beta}(\mathbf{q}_\parallel|\mathbf{k}_\parallel)/\partial\Omega_s \right\rangle_{\mathrm{incoh}}$ when this condition is satisfied is due only to multiple-scattering processes, including the enhanced backscattering peak and the satellite peaks. These features are more clearly visible in this case because they do not ride on a large background due to single-scattering processes. This is the reason that the calculations whose results are presented here were carried out on the basis of the power spectrum (13).

In Fig. 1(a) we present the contribution to the mean differential reflection coefficient from the light scattered incoherently as functions of the polar scattering angle θ_s for the in-plane ($\phi_s = \phi_0 = 45^\circ$) co-(p→p, s→s) and cross-(p→s, s→p) polarized scattering when a p- or s-polarized plane wave is incident on the dielectric surface at angles of incidence (θ_0, ϕ_0) given by $(0.74^\circ, 45^\circ)$. (In figures showing in-plane or out-of-plane scattering, we depart from the commonly accepted principle of not using negative polar angles, in that we allow for negative θ_s.). An arithmetic average of results obtained for $N_p = 11,165$ realizations of the surface profile function was carried out to produce these figures. In Fig. 1(b) we present the analogous results for out-of-plane ($\phi_s = \phi_0 \pm 90^\circ$) scattering when the roughness and experimental parameters have the values assumed in generating Fig. 1(a).

In the results depicted in Fig. 1(a) [1(b)] single-scattering processes give no contributions to the mean differential reflection coefficient for $-53.8^\circ < \theta_s < 56.4^\circ$ ($-55.08^\circ < \theta_s < 55.08^\circ$). In both figures a well-defined enhanced backscattering peak is seen in the retroreflection direction. In addition, in Fig. 1(a) additional peaks are seen on both sides of the enhanced backscattering peak in the s → s co-polarized scattering contribution to the mean differential reflection coefficient. These peaks are identified as satellite peaks.

We base this identification on the following consideration. It was shown in [6] that in the in-plane co-polarized scattering of light of frequency ω from a one-dimensional randomly rough surface of a film system when the plane of incidence is perpendicular to the generators of the surface, satellite peaks occur at scattering angles given by

$$\sin\theta_s^{(m,n)} = -\sin\theta_0 \pm \frac{c}{\omega\sqrt{\varepsilon_1}}\left[q_m(\omega) - q_n(\omega)\right]. \tag{14}$$

The wave numbers $q_1(\omega), q_2(\omega), \ldots, q_N(\omega)$ are the wavenumbers of the guided waves supported by the film structure at the frequency of the incident light. Not all of the peaks predicted by Eq. (14) may be present in the mean differential reflection coefficient. This happens when the absolute value of the right-hand side of Eq. (14) is greater than unity. Then the corresponding

#165194 - $15.00 USD Received 22 Mar 2012; revised 25 Apr 2012; accepted 27 Apr 2012; published 2 May 2012

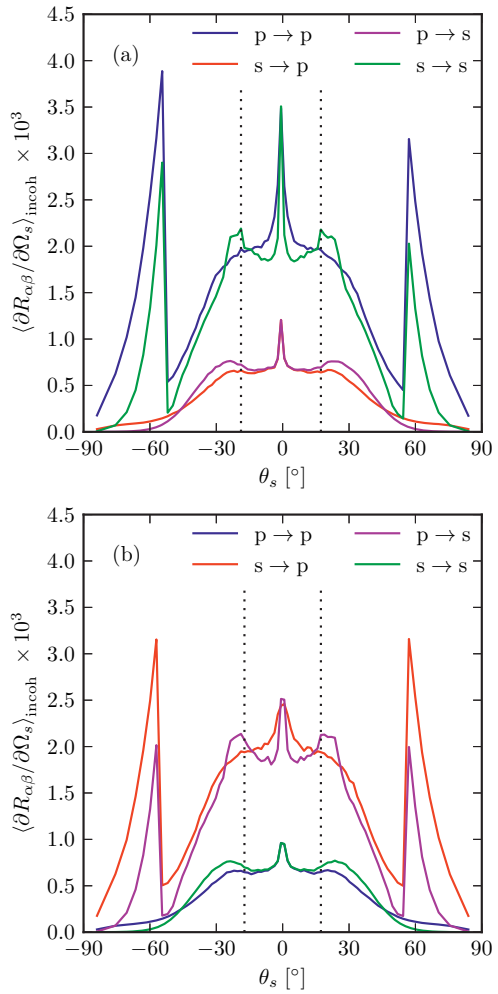

Fig. 1. (a) The contributions to the mean differential reflection coefficient as functions of the polar scattering angle θ_s from the in-plane ($\phi_s = \phi_0$) co-polarized (p→p, s→s) and cross-polarized (p→s, s→p) scattering of light incident on the two-dimensional randomly rough surface of a dielectric film deposited on the planar surface of silver, whose dielectric constant is $\varepsilon_3 = -18.28 + 0.481\mathrm{i}$. The wavelength of the incident light is $\lambda = 633$ nm, the angles of incidence are $(\theta_0, \phi_0) = (0.74°, 45°)$. The dielectric constant of the film is $\varepsilon_2 = 2.6896 + 0.01\mathrm{i}$, and its mean thickness is $d = 478.5$ nm. The roughness of the surface is characterized by the power spectrum in Eq. (13), with $k_- = 0.82(\omega/c)$, $k_+ = 1.97(\omega/c)$, and its rms height is $\delta = \lambda/40 = 15.82$ nm. (b) The same as (a) for out-of-plane ($\phi_s = \phi_0 + 90°$) scattering.

#165194 - $15.00 USD Received 22 Mar 2012; revised 25 Apr 2012; accepted 27 Apr 2012; published 2 May 2012

peak lies in the nonradiative region of the q_1q_2 plane. In addition, among the real satellite peaks that should appear in the radiative region, not all may be sufficiently intense to be observable.

The scattering angles defined by Eq. (14) are expected to give the angles at which satellite peaks occur in the in-plane co-polarized scattering from the two-dimensional randomly rough surface of the film system studied here.

In the absence of absorption and roughness the $\{q_j(\omega)\}$ are the solutions of the dispersion relation

$$\begin{aligned}\alpha_2(q_\parallel,\omega) = \frac{1}{2\varepsilon_1\varepsilon_3}\Big(&\varepsilon_2\left[\varepsilon_1\beta_3(q_\parallel,\omega)+\varepsilon_3\beta_1(q_\parallel,\omega)\right]\cot\left[\alpha_2(q_\parallel,\omega)d\right]\\ &\pm\left\{\varepsilon_2^2\left[\varepsilon_1\beta_3(q_\parallel,\omega)+\varepsilon_3\beta_1(q_\parallel,\omega)\right]^2\cot^2\left[\alpha_2(q_\parallel,\omega)d\right]\right.\\ &\left.+4\varepsilon_1\varepsilon_2^2\varepsilon_3\beta_1(q_\parallel,\omega)\beta_3(q_\parallel,\omega)\right\}^{1/2}\Big)\end{aligned} \tag{15a}$$

in p polarization, and

$$\begin{aligned}\alpha_2(q_\parallel,\omega) = \frac{1}{2}\Big(&\left[\beta_1(q_\parallel,\omega)+\beta_3(q_\parallel,\omega)\right]\cot\left[\alpha_2(q_\parallel,\omega)d\right]\\ &\pm\left\{\left[\beta_1(q_\parallel,\omega)+\beta_3(q_\parallel,\omega)\right]^2\cot^2\left[\alpha_2(q_\parallel,\omega)d\right]\right.\\ &\left.+4\beta_1(q_\parallel,\omega)+\beta_3(q_\parallel,\omega)\right\}^{1/2}\Big)\end{aligned} \tag{15b}$$

in s polarization. In these equations $\beta_i(q_\parallel,\omega) = \left[q_\parallel^2-\varepsilon_i(\omega/c)^2\right]^{1/2}$ for $i=1,3$, while $\alpha_2(q_\parallel,\omega)$ is defined in Eq. (3). The film structure studied in this paper is found to support two guided waves in p-polarization, whose wave numbers are

$$q_1(\omega) = 1.4391(\omega/c), \quad q_2(\omega) = 1.0119(\omega/c), \tag{16a}$$

and two guided waves in s polarization, with wave numbers

$$q_1(\omega) = 1.5467(\omega/c), \quad q_2(\omega) = 1.2432(\omega/c). \tag{16b}$$

These results predict satellite peaks at scattering angles $\theta_s = -25.22^\circ$ and 23.74° in p polarization and at $\theta_s = -18.13^\circ$ and 16.65° in s polarization when we are considering in-plane scattering, assuming the same angles of incidence as in Fig. 1. These scattering angles are indicated by vertical dotted lines in Fig. 1(a). The peaks at $\theta_s = -18.13^\circ$ and 16.65° are seen in the s→s co-polarized scattering contribution to the mean differential reflection coefficient. There is no evidence of satellite peaks at $\theta_s^{(1,2)} = -25.22^\circ$ and 23.74° in the p→p co-polarized scattering contribution to the mean differential reflection coefficient, presumably because they are too weak to be seen. These results disagree with those of [10], in which no satellite peaks were found in the in-plane s→s scattering contribution to the mean differential reflection coefficient (although they are present in this contribution when the dielectric film is deposited on a planar perfectly conducting surface). However, in [10] the surface roughness was characterized by a Gaussian power spectrum, not the West–O'Donnell power spectrum assumed here. The results of earlier calculations [25] of the scattering of p- and s-polarized light from a film with a one-dimensional randomly rough surface characterized by a Gaussian power spectrum that is deposited on a planar perfectly conducting surface, display satellite peaks more weakly than when the roughness is characterized by a West–O'Donnell power spectrum [26].

Turning now to the results for out-of-plane scattering presented in Fig. 1(b), we see that an enhanced backscattering peak is present in each scattering configuration. It is cut off in each configuration. This is an artifact of the present calculation that results from the line defined by

#165194 - $15.00 USD Received 22 Mar 2012; revised 25 Apr 2012; accepted 27 Apr 2012; published 2 May 2012

$\phi_s = \phi_0 \pm 90^\circ$ being exactly one grid point away from the backscattering direction. It is important to note that in out-of-plane scattering the predominant contribution to the differential reflection coefficient is in the cross-polarized part. We see that the satellite peaks are now observed in the p→s scattering configuration, meaning that incident p-polarized light excites both of the s-polarized guided modes with wave vectors in the $\phi = \phi_0 \pm 90^\circ$ directions, which subsequently interfere to cause satellite peaks in out-of-plane scattering. Hence, the well-known "satellite peaks" found in scattering from 1D surfaces turn into a kind of "satellite rings" for scattering from 2D surfaces, where part of the ring is co-polarized (s→s in-plane) and part of the ring is cross-polarized (p→s out-of-plane).

In Fig. 2 we present contour plots of the complete angular distribution of the mean differential reflection coefficient for the light scattered incoherently from the film system studied here. The material and experimental parameters used in producing these results have the same values used in obtaining Fig. 1.

Light of p polarization (left column) or s polarization (right column) is incident on the structure. In Figs. 2(a) and 2(d) all of the scattered light is recorded; in Figs. 2(b) and 2(e) only the p-polarized scattered light is recorded; while in Figs. 2(c) and 2(f) only the s-polarized scattered light is recorded. In Fig. 2(f) we see two regions of high intensity in the in-plane polarized (s→s) intensity distribution, centered at radii of approximately $0.29(\omega/c)$ at $\phi_s = 45^\circ$, and $0.31(\omega/c)$ at $\phi_s = 225^\circ$. These are the satellite peaks seen in the plot of $\langle \partial R_{ss}/\partial\Omega_s \rangle_{incoh}$ presented in Fig. 1(a). No such regions of high intensity are seen in Fig. 2(b) at radii of $0.34(\omega/c)$ at $\phi_s = 45^\circ$ and $0.52(\omega/c)$ at $\phi_s = 225^\circ$, where satellite peaks are predicted by Eq. (14) for in-plane co-polarized scattering of p-polarized incident light. This result is consistent with the absence of satellite peaks in the result for $\langle \partial R_{pp}/\partial\Omega_s \rangle_{incoh}$ presented in Fig. 1(a). The intensity maxima in the out-of-plane cross-polarized (p→s) scattering intensity distribution depicted in Fig. 2(c) correspond to the peaks at $\theta_s \approx 19^\circ$ seen in the plot of $\langle \partial R_{sp}/\partial\Omega_s \rangle_{incoh}$ presented in Fig. 1(b).

The result that satellite peaks are observed in scattering processes in which the scattered light is s polarized, independent of the polarization of the incident light, is an interesting result of the present calculations. It may be connected with the fact that s-polarized light is reflected more strongly from a dielectric surface than is p-polarized light.

In Fig. 3 we present results analogous to those presented in Fig. 1, but for angles of incidence $(\theta_0, \phi_0) = (5.19^\circ, 45^\circ)$. In Fig. 3(a) we present results for the in-plane $(\phi_s = \phi_0)$ co-(p→p, s→s) and cross-(p→s, s→p) polarized scattering, while in Fig. 3(b) we present results for out-of-plane $(\phi_s = \phi_0 \pm 90^\circ)$ co-(p→p, s→s) and cross-(p→s, s→p) polarized scattering. In the results presented in Fig. 3(a) [3(b)] single-scattering processes give no contribution to the mean differential reflection coefficient for $-46.85^\circ < \theta_s < 65.57^\circ$ $(-54.59^\circ < \theta_s < 54.59^\circ)$. The limits of these angular regions are clearly seen in these figures.

A well-defined enhanced backscattering peak is seen in the results plotted in Fig. 3(a). Satellite peaks are predicted by Eq. (14) to occur (in-plane) at $\theta_s^{(1,2)} = -31.18^\circ$ and 19.68° for p-polarized incident light, and at $\theta_s^{(1,2)} = -23.20^\circ$ and 12.30° for s-polarized incident light, when the angles of incidence were the same as in Fig. 3. These scattering angles are indicated by vertical dotted lines in this figure. Peaks at $\theta_s = -23.20^\circ$ and $\theta_s = 12.30^\circ$ are present in the s→s co-polarized scattering contribution to the mean differential reflection coefficient. There is no suggestion of peaks at $\theta_s = -31.8^\circ$ and 19.68° in the p→p co-polarized scattering contribution to the mean differential reflection coefficient, nor any suggestions of peaks in the cross-polarized (p→s, s→p) contribution to it.

The results for out-of-plane scattering presented in Fig. 3(b) show no enhanced backscattering peaks. The reason for this is simply that since the abscissa points along $\phi = \phi_0 \pm 90^\circ$, it does not cut through the backscattering peak, localized at $(\theta_s, \phi_s) = (\theta_0, \phi_0 + 180^\circ)$. We do

#165194 - $15.00 USD Received 22 Mar 2012; revised 25 Apr 2012; accepted 27 Apr 2012; published 2 May 2012

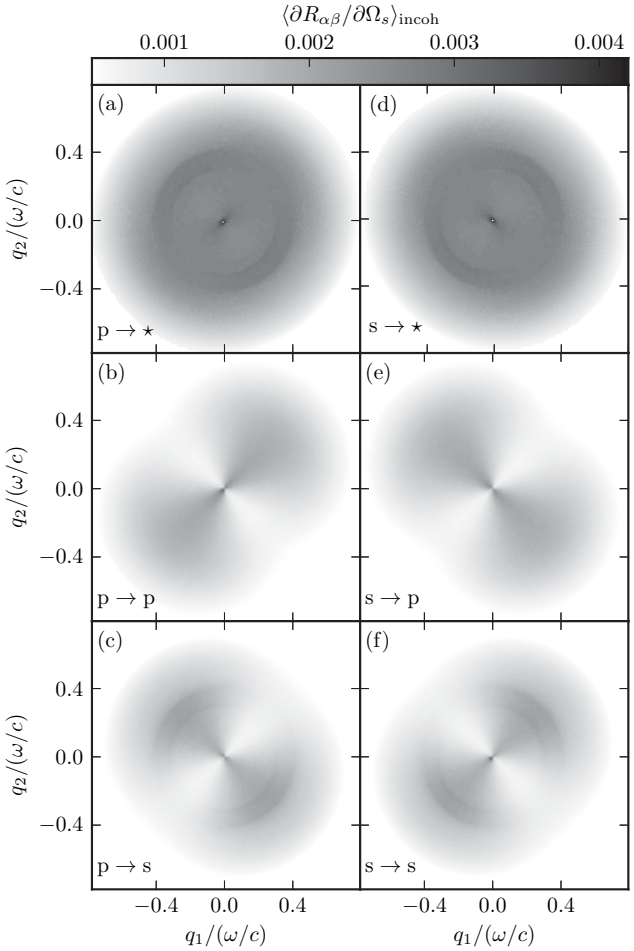

Fig. 2. The complete angular distribution of the mean differential reflection coefficient $\langle \partial R_{\alpha\beta}/\partial\Omega_s \rangle_{\rm incoh}$ for the light scattered incoherently from the film structure. The material and experimental parameters assumed here are those used in obtaining the plots presented in Fig. 1. Light of either p (left column) or s (right column) polarization is incident on the structure. In (a) and (d) all (diffusely) scattered light is recorded. In (b) and (e) only the p-polarized scattered light is recorded, while in (c) and (f) only the s-polarized scattered light is recorded. The dark dot in each panel indicates the enhanced backscattering peak. Note that the gray scale bar is cut at both ends in order to enhance the satellite rings. Also note that the contribution from single scattering is suppressed, i.e. the differential reflection coefficient is artificially set to 0 for $\left|\mathbf{q}_{\|} - \mathbf{k}_{\|}\right| > k_{-}$.

#165194 - $15.00 USD Received 22 Mar 2012; revised 25 Apr 2012; accepted 27 Apr 2012; published 2 May 2012

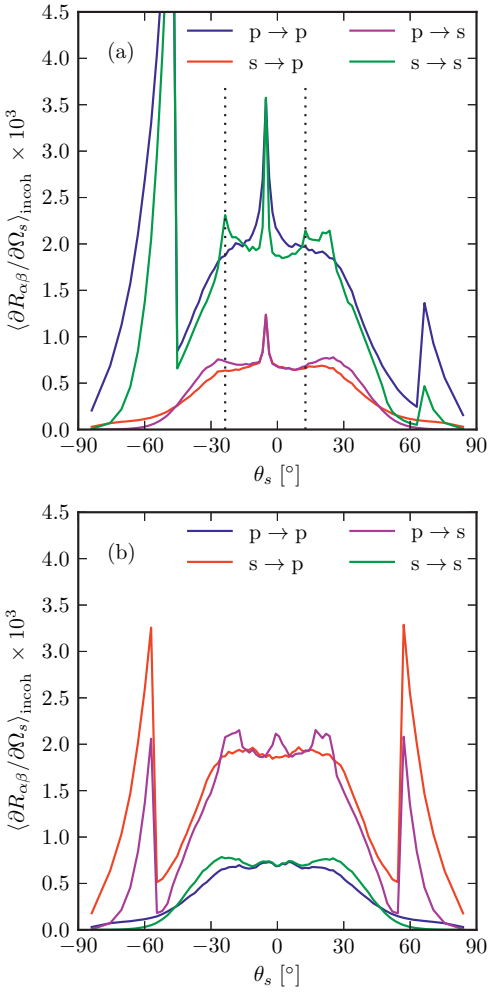

Fig. 3. The same as Fig. 1, but for angles of incidence given by $(\theta_0, \phi_0) = (5.19°, 45°)$.

see some remainders of the satellite ring structure; the low peaks around $\theta_s \approx \pm 20°$ are part of the rings to the upper left in Fig. 4. As the rings decay in strength away from the direction $\phi = \phi_0 \pm 90°$, they are weaker than what is seen in-plane.

As a necessary, but not sufficient, condition of the validity of our simulation results is energy conservation. If all materials in the scattering system are lossless, i.e. $\mathrm{Im}(\varepsilon_i) = 0$ $(i = 1,2,3)$, the power of the scattered light has to be equal to the power of the incident light. Under these conditions, energy was conserved within 0.03% in our simulations.

In conclusion, in this paper we have presented a nonperturbative approach to the solution of

#165194 - $15.00 USD Received 22 Mar 2012; revised 25 Apr 2012; accepted 27 Apr 2012; published 2 May 2012

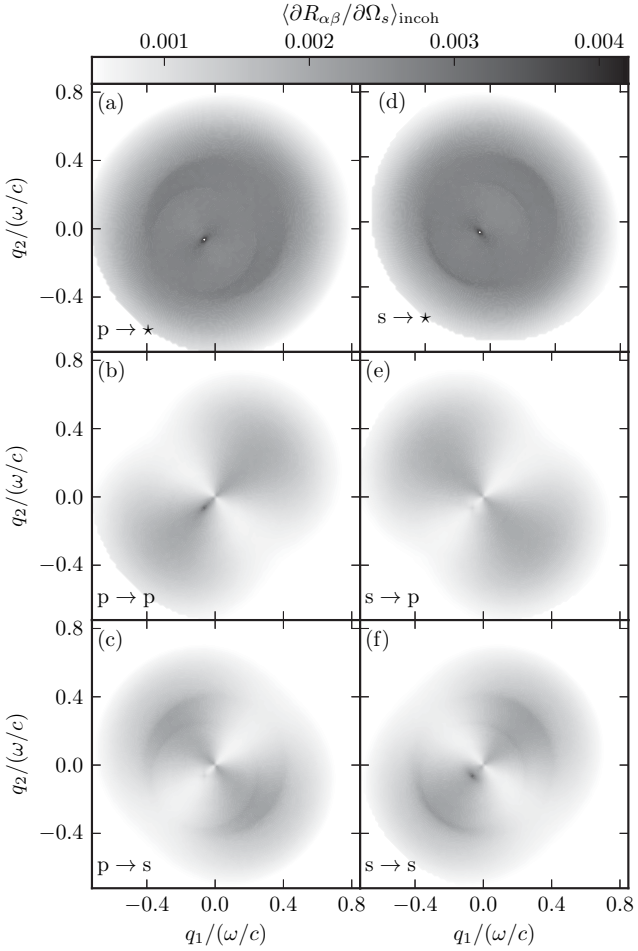

Fig. 4. The same as Fig. 2, but for angles of incidence given by $(\theta_0, \phi_0) = (5.19^\circ, 45^\circ)$. Note that the color bar is cut at both ends in order to enhance the satellite rings. Also note that the contribution from single scattering is suppressed, i.e. the differential reflection coefficient is artificially set to 0 for $\left|\mathbf{q}_\parallel - \mathbf{k}_\parallel\right| > k_-$.

#165194 - $15.00 USD Received 22 Mar 2012; revised 25 Apr 2012; accepted 27 Apr 2012; published 2 May 2012

the reduced Rayleigh equation for the scattering of polarized light from a dielectric film with a two-dimensional randomly rough surface deposited on a planar metallic surface. We have applied this result to calculate the contributions to the mean differential reflection coefficient from the in-plane co- and cross-polarized components of the light scattered incoherently, as well as from the out-of-plane co-and cross-polarized components of the light scattered incoherently. The out-of-plane scattering contributions have not been calculated in earlier perturbative studies of this problem [10, 14]. In addition, we have calculated the full angular distribution of the intensity of the scattered light, which has helped to refine the conclusions drawn from the calculations of the mean differential reflection coefficient. The main physical result obtained in this work is the demonstration that satellite peaks (or rings) can arise in scattering from the film structure studied here. This result is in agreement with the results of Soubret *et al.* [10] but not with those of Kawanishi *et al.* [14]. A detailed study of the conditions under which satellite peaks occur is lacking, but perhaps the approach developed here will be used to determine them. The work reported here also opens the door to the possibility of calculating other properties of the light scattered from the film system studied here, such as all the elements of the associated Mueller matrix, and offers the possibility of designing such structures to possess specified scattering properties. These are problems that have to be left to the future.

Acknowledgements

The research of T.N., P.A.L., and I.S. was supported in part by NTNU by the allocation of computer time. The research of A.A.M. was supported in part by AFRL contract FA9453-08-C-0230. T.N., P.A.L., and I.S. would like to thank Dr. Jamie Cole at the University of Edinburgh for his kind hospitality and fruitful discussions. They would also like to acknowledge the assistance of Dr. Fiona Reid and Dr. Christopher Johnson at the EPCC in parallelizing and optimizing the simulation code. The work by T.N. and P.A.L. was partially carried out under the HPC-EUROPA2 project (project number: 228398) with the support of the European Commission—Capacities Area—Research Infrastructures.

#165194 - $15.00 USD Received 22 Mar 2012; revised 25 Apr 2012; accepted 27 Apr 2012; published 2 May 2012

P. A. Letnes, I. Simonsen, and D. L. Mills. "Plasmonic resonances at interfaces patterned by nanoparticle lattices", `http://arxiv.org/abs/1208.1911` **(2012)**

Paper 10

Plasmonic resonances at interfaces patterned by nanoparticle lattices

P. A. Letnes* and I. Simonsen†
Department of Physics, The Norwegian University of Science and Technology (NTNU), NO-7491 Trondheim, Norway

D. L. Mills
Department of Physics and Astronomy, University of California, Irvine, California 92697, USA
(Dated: July 18, 2012)

We present theoretical studies of the nature of the collective plasmon resonances of surfaces upon which ordered lattices of spherical metallic particles have been deposited. The collective plasmon modes, excited by light incident on the surface, are explored for both square and rectangular lattices of particles. The particular resonances excited by an incident beam of light depend on the frequency, polarization, and angles of incidence. We show that one can create surfaces for which the polarization of the reflected light is frequency dependent. The form of the polarization dependent spectra can be tuned by choosing materials and the parameters of the nanoparticle array.

PACS numbers: 78.67.-n, 78.20.Bh, 78.68.+m, 41.20.Cv

I. INTRODUCTION

It is of great interest to create surfaces whose response to incident light can be controlled to produce desirable effects of various sorts. This may be accomplished in diverse ways. For instance one may modulate the surface profile. Very striking and remarkable reflectivity properties are found in systems containing surfaces whose roughness is prepared according to prescriptions provided by theoretical simulations [1]. We refer the reader to a recent review wherein the scattering of light from roughened surfaces is discussed in detail [2].

In addition to modulating the profile of a surface in a controlled fashion, one may also deposit material onto it in a structured manner. For instance, to enhance photocurrents in solar energy devices, metallic nanoparticles are deposited on or near the surface of solar devices [3, 4]. We remark that the nanoparticle arrays in these systems are very highly disordered. On a related note, disordered structures generated by laser bombardment has been shown to modify the color of metallic surfaces in a profound way [5].

Recently, progress has been made towards using the plasmonic properties of nanowires [6, 7] or nanoparticles [8, 9] as optical polarizers, in a fashion reminiscent of wire-grid polarizers. This work promises to make polarizers that are microscopic in size, and which possess other interesting properties. For instance, the spectral response of nanoparticles can be tuned according to their shape [10] or internal structure [11], allowing the fabrication of optical components with new and interesting properties. In all these studies, the properties of structures on the nanoscale, notably nanoparticles, lead to macroscopic optical effects [12–14].

In this paper, we explore a very different kind of nanoparticle-coated surface, namely, a dielectric substrate upon which an ordered array of sub-wavelength metallic nanoparticles [15] has been deposited [16–18]. As we shall see from the calculations presented below, such a surface exhibits striking optical properties that may be tuned by varying the character of the nanoparticle array.

There are two important features of such an array. First, let ℓ be a length that characterizes the size of the unit cell, and assume that light of wavelength (in vacuum) λ illuminates the structure. If $\lambda/\ell > 1$, a condition satisfied for sub-wavelength arrays, there will only be a single reflected specular beam, very much as realized for a perfectly flat surface. For particle arrays with linear dimensions in the range of the wavelength or larger ($\ell \gtrsim \lambda$), one realizes additional reflected beams in the form of Bragg waves. As the distance between the nanoparticles decreases into the sub-wavelength regime, the additional Bragg waves collapse into evanescent waves confined to the near vicinity of the surface, leaving a single specular reflected beam, once again very much as for a perfectly smooth surface.

A metallic nanoparticle array also supports plasmonic resonances that may be excited by incident light. For an isolated nanoparticle of radius $a \ll \lambda$ made from a "plasmonically active" material such as silver (Ag), the optically active plasmonic (Mie) resonance lies in the ultraviolet (at $\hbar\omega \approx 3.5\,\mathrm{eV}$ for Ag, where ω is the angular frequency of the incident light). Depositing particles onto a substrate will cause inter-nanoparticle and particle-substrate interactions that red-shifts the Mie resonance so it can lie in the visible, as illustrated by previous work; see Fig. 9 in Refs. 19 and 20.

More important for the present study is the role of interactions between nanoparticles in a dense array. These produce collective plasmonic bands whose dispersion relations and effects on polarization are controlled by the properties of the array. As we shall see, these collective plasmon modes can be excited by the incident light, with the consequence that the reflectivity of the surface becomes highly dependent on both the frequency, the

* paul.anton.letnes@gmail.com
† ingve.simonsen@ntnu.no

angles of incidence, and the polarization of the incident light. If the surface is illuminated with unpolarized light, the reflected light will be polarized, but the degree of polarization can be strongly frequency dependent, as illustrated by the calculations presented below. By altering the microstructure of the array, one may in principle tune the polarization characteristics of the reflected light. The purpose of this study is to explore these effects, and to demonstrate how such effects can be simulated in a way that is not computationally demanding.

A classic and frequently used model to obtain the optical response of nanoparticle patterned surfaces is the polarizable dipole model [21]. In this model, each nanoparticle is treated as a polarizable point dipole, and the effect of the substrate is accounted for via image dipoles. For nanospheres with intersphere spacing as small as those of our geometries, such an approximation is very poor. There are highly localized patches of induced charge localized around the points of closest contact between neighboring spheres, and also around the closest point of contact between the sphere and the substrate. One can appreciate this from our previous calculation of the spatial dependence of enhanced fields near an Ag dimer on a dielectric surface, as illustrated in Fig. 10 of Refs. 19 and 20. Also in Fig. 5 of Ref. 22 one sees a detailed presentation of the electric field near the point of closest contact between two spheres when they are excited at their plasmon resonance. It is essential to include higher order multipole moments in the description of interactions between nearby nanospheres, and between nanospheres and a substrate upon which they are deposited, as we have done in the results displayed below.

A more direct approach is that of the discrete dipole approximation (DDA) [23], which can be expanded to include retardation and substrate effects [24]. The DDA is a direct numerical method, relying on discretizing the volume of particles into polarizable dipoles. In contrast, the method used in this work relies on multipole expansion of the quasistatic potential [25]. The advantage of this method is that it gives results closer to analytical mathematics, as well as being computationally efficient, assuming that one does not need to include very high multipole orders.

The organization of this paper is as follows. Section II contains the necessary theoretical formalism. In Sec. III, we present our studies of the plasmon collective modes of arrays of Ag particles supported by an aluminium oxide (alumina, Al_2O_3) substrate, and in Sec. IV we discuss the optical reflectivity of two model systems. Concluding remarks are presented in Sec. V.

II. THEORY

The system we study consists of a periodic array of non-overlapping Ag nanoparticles supported by an Al_2O_3 substrate as depicted in Fig. 1. The global Cartesian coordinate system $\mathbf{r} = (x, y, z)$ is chosen such that the plane $z = 0$ coincides with the (flat) surface of the substrate that is located in the region $z < 0$ and characterized by the dielectric function $\varepsilon_-(\omega)$. The ambient ($z > 0$) is assumed to be vacuum, and therefore $\varepsilon_+ \equiv 1$.

A set of identical Ag nanospheres of radius a are arranged on a regular lattice close to the surface of the substrate. For each spherical nanoparticle, we associate a position vector $\mathbf{R}_{ij} = (x_{ij}, y_{ij}, h + a)$ pointing from the origin of the (global) coordinate system to the center of each particle, where the particles are indexed $i, j = 0, \pm1, \pm2, \ldots$. For later convenience, we assume a small but finite positive value for the parameter h [Fig. 1(b)]. The particle $i = j = 0$ is assumed to be located on the z-axis so that $\mathbf{R}_{00} = (0, 0, a + h)$. Furthermore, each sphere ij has associated with it a (local) coordinate system $\mathcal{S}_{ij}$ that has its origin located at the center of that sphere and its axes oriented parallel to those of the main coordinate system. The position vector in $\mathcal{S}_{ij}$ we denote by $\mathbf{r}_{ij} = (r_{ij}, \theta_{ij}, \phi_{ij})$.

The Ag nanospheres are characterized by the dielectric function $\varepsilon(\omega)$. Corrections to the dielectric function of the particles due to, e.g., finite size and temperature effects are necessary in order to obtain good agreement between theoretical predictions and experimental measurements [26]. This will not be done here, however, since comparison to experimental data will not be our main concern. Hence, for reasons of simplicity, we have assumed bulk values for all dielectric functions.

In the following we shall consider both square and rectangular lattice structures. Without loss of generality, the coordinate system can be oriented so that the lattice constants b_x and b_y, corresponding to the directions $\hat{\mathbf{x}}$ and $\hat{\mathbf{y}}$, respectively, obey $b_x \leq b_y$ [see Fig. 1(a)]. Here, a caret above a vector indicates that it is a unit vector. Furthermore, since the spheres are non-overlapping, we also have that $2a < b_x$.

Although in general square lattices are formally a subset of rectangular lattices, we will here restrict the term "rectangular lattice" to lattices for which $b_x < b_y$. A comparison between square and rectangular lattices will provide us with an assessment of the range of electrostatic coupling between the spheres in the lattice. Moreover, in the limit $b_y \gg a$, where interactions between the spheres in the $\hat{\mathbf{y}}$ direction safely can be neglected, the system essentially consists of non-interacting, parallel, linear chains of nanoparticles [27]. Moreover, the word "chains" will be used about the lines of spheres parallel to the x axis, as $b_x < b_y$.

A. Multipole expansion

In this work we will focus on systems for which $b_y \ll \lambda$, where the *quasistatic approximation* applies [25]. Then, if all materials are assumed to be non-magnetic, the electromagnetic properties of the system is fully described by the electrostatic potential, $\psi(\mathbf{r})$, satisfying the Laplace

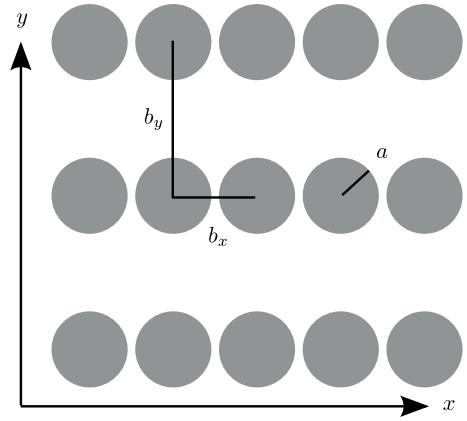

(a) The nanoparticle lattice seen in the xy plane.

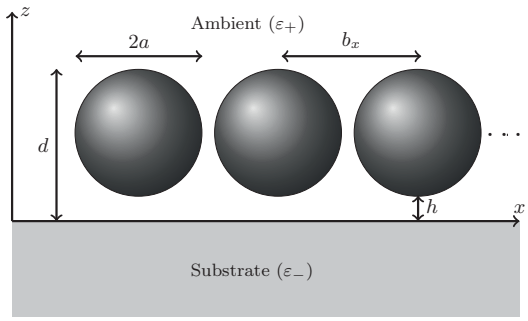

(b) A view of the lattice in the xz plane.

FIG. 1. (a) Nanospheres of radius a are arranged on a rectangular lattice with lattice constants b_x and b_y. The z axis points out of the substrate, and we always assume $b_x \leq b_y$. (b) The ambient-substrate interface is located at $z = 0$. The definitions of d, the effective film thickness; a, the sphere radius; b_x, the lattice constant along $\hat{\mathbf{x}}$; and the parameter h are indicated. The spheres are all characterized by the dielectric function $\varepsilon(\omega)$. Note that h is exaggerated for clarity.

equation:

$$\nabla^2\psi(\mathbf{r}) = 0.$$

Also, the appropriate boundary conditions [25] on the surfaces of each sphere and at the interface between the substrate and the ambient have to be fulfilled. By definition, the electric field can be calculated from $\mathbf{E}(\mathbf{r}) = -\nabla\psi(\mathbf{r})$ [25]. Finally, we assume that the incident optical radiation can be modeled as a spatially uniform electric field $\mathbf{E}_0$ of angular frequency $\omega = 2\pi c/\lambda$. As we are employing the quasistatic approximation, ω only appears in the frequency dependence of the dielectric functions $\varepsilon_\pm(\omega)$ and $\varepsilon(\omega)$.

In what follows, we adapt the *multipole expansion* formalism presented in detail in Ref. 19, only modifying it where necessary to take into account the symmetries and the infinite nature of the lattice. The structure of the lattice requires the potential to satisfy the Bloch–Floquet theorem [28]. Let $\psi_{ij}(\mathbf{r}_{ij})$ denote the scalar potential of the particle located at $\mathbf{R}_{ij}$ (in the global coordinate system) and expressed in terms of its local coordinate system, $\mathbf{r}_{ij}$. We assume that the potential from each nanoparticle, ψ_{ij}, is identical save for a phase factor, due to the phase of the incident electric field:

$$\psi_{ij}(\mathbf{r}_{ij}) = \psi_{00}(\mathbf{r}_{ij})\mathrm{e}^{\mathrm{i}\mathbf{k}_\parallel\cdot\Delta\mathbf{R}_{ij}}. \tag{1}$$

In writing Eq. (1), we have introduced the lattice vector $\Delta\mathbf{R}_{ij} \equiv \mathbf{R}_{ij} - \mathbf{R}_{00} = (ib_x, jb_y, 0)$ describing the periodic array of spheres, and $\mathbf{k}_\parallel$ denotes the component of the wave vector $\mathbf{k}$ of the incident electric field that is parallel to the xy plane: $\mathbf{k}_\parallel = \hat{\mathbf{x}}k_x + \hat{\mathbf{y}}k_y$. Equation (1) signifies that once the scalar potential of sphere $i = j = 0$ is known, it is essentially known for all spheres of the lattice. This is a consequence of the Bloch–Floquet theorem, and the form (1) is similar to the tight binding description of electron energy bands in solids. The Bloch phase factor is also assumed to be present in the potential of the corresponding image multipole. In passing, we note that Eq. (1) also predicts that the potential $\psi_{ij}(\mathbf{r}_{ij})$ is invariant under a replacement of $\mathbf{k}_\parallel$ by $\mathbf{k}_\parallel + \mathbf{G}_{mn}$ where $\mathbf{G}_{mn} = 2\pi(m/b_x, n/b_y, 0)$ denotes a reciprocal lattice vector (with m and n integers). This invariance follows from the fact that a scalar product of a primitive lattice vectors from direct space, and one from reciprocal space, equals an integer multiple of 2π [28]. Hence, for the sake of the calculation of the potentials, it suffices to consider wave vectors $\mathbf{k}_\parallel$ in the first Brillouin zone. Moreover, since this work considers the limit $\lambda \gg b_y \geq b_x$, one may when calculating the potentials take the limit $|\mathbf{k}_\parallel| \to 0$.

In the formalism presented in Ref. 19, the total potential in the ambient, $\psi_+(\mathbf{r})$, is expressed as a superposition of the potential corresponding to the background electric field ($\mathbf{E}_0$), the potential scattered from each nanoparticle, and the potential from an image multipole designed to take the substrate into account:

$$\psi_+(\mathbf{r}) = -\mathbf{r}\cdot\mathbf{E}_0 + \sum_{i=-\infty}^{\infty}\sum_{j=-\infty}^{\infty}\psi_{ij}(\mathbf{r}_{ij}) + \sum_{\bar{i}=-\infty}^{\infty}\sum_{\bar{j}=-\infty}^{\infty}\psi_{\bar{i}\bar{j}}(\mathbf{r}_{\bar{i}\bar{j}}).$$

Here the indices $\bar{i}$ and $\bar{j}$ indicate that the quantity $\psi_{\bar{i}\bar{j}}$ represents contribution to the potential from image multipoles associated with the sphere ij, and $\mathbf{r}$ is the position vector in the global coordinate system. With the shorthand notation $\sum_{lm} = \sum_{l=0}^{\infty}\sum_{m=-l}^{l}$, the multipole expansion we use for the scalar potential is given by [25]:

$$\psi_{00}(\mathbf{r}_{00}) = \sum_{lm} A_{lm} r_{00}^{-l-1} Y_l^m(\theta_{00}, \phi_{00}),$$
$$\psi_{\bar{0}\bar{0}}(\mathbf{r}_{\bar{0}\bar{0}}) = \sum_{lm} A_{lm}^{(R)} r_{\bar{0}\bar{0}}^{-l-1} Y_l^m(\theta_{\bar{0}\bar{0}}, \phi_{\bar{0}\bar{0}}).$$

Here, the symbols A_{lm} and $A_{lm}^{(R)}$ are multipole expansion coefficients to be determined. The symbol Y_l^m refers to the spherical harmonic functions as described by Ref. 25. By symmetry arguments and by matching the boundary conditions at $z = 0$ [29], the coefficients A_{lm} are related to the coefficients $A_{lm}^{(R)}$ by the relation

$$A_{lm}^{(R)} = (-1)^{l+m} \frac{\varepsilon_+ - \varepsilon_-}{\varepsilon_+ + \varepsilon_-} A_{lm}.$$

We note that the sum over l for practical reasons has to be truncated at a finite value $L_{\max}$, meaning that only terms for which $l \leq L_{\max}$ are included in the sum. It should be stressed that local fields may not have converged fully for this cutoff; however, the observed collective resonances and reflectivity are less sensitive to the details of the local fields. This is especially true when considering large arrays of metallic nanoparticles, in which the interparticle interactions are stronger than the particle-substrate interactions. The potential originating from other nanoparticles (and images), ψ_{ij}, can be found from ψ_{00} and Eq. (1). In order to determine the A_{lm} coefficients, one forms a linear system of equations which couples all multipole orders l. How to form and solve this system of equations is given in detail in Ref. [19].

Although we are working with lattices that have discrete translational symmetry with respect to the lattice vector, there is little to be gained by use of a Fourier representation of the relevant lattice sums. In mathematical terms, the vector $\mathbf{R}_{\bar{i}\bar{j}} - \mathbf{R}_{kl}$ pointing from sphere kl to image $\bar{i}\bar{j}$ does not lie in the xy plane: Its polar angle will vary depending on the relative position of the image multipoles and the sphere on the z-axis. Hence, the presence of the substrate, and thus the image multipoles, leads to terms in the lattice sums lacking the symmetry needed to use the Fourier transform. For this reason, the necessary sums over spheres [19] are performed directly in real space, up to $N = 10$ unit cells away from the sphere on the z-axis. We stress that these sums include both nanoparticles and nanospheres out to N unit cells.

In all of our simulations, we have kept a finite value of the parameter h to ensure convergence of the spherical harmonics expansion. This is because a singularity arises at the bottom of the sphere if we choose $h = 0$ [30]. In the simulations we present here, we have elevated the layer of spheres off the substrate by the amount $h = 0.01a$. We then find very good convergence in terms of the collective excitations and reflectivity behavior. It should be stressed that global behavior, such as the reflectivity of the lattice, does not depend on the details of h, even though the convergence of the local fields is more sensitive to the parameters $L_{\max}$ and h.

As a proxy for the optical response of nanoparticles or clusters of nanoparticles, we use the dipole moment, $\mathbf{p}$, or its dimensionless analog defined as (in SI units) [19]

$$\bar{\mathbf{p}}(\omega) = \frac{\mathbf{p}(\omega)}{a^3 \varepsilon_0 E_0}, \tag{3a}$$

and its absolute value

$$\bar{p}(\omega) = \left(\bar{\mathbf{p}}^\dagger \bar{\mathbf{p}}\right)^{1/2}, \tag{3b}$$

where the superscript † on a quantity indicates its Hermitian conjugate. The components of the dipole moment vector can be found from [19]

$$\bar{p}_x = \left(\frac{3}{8\pi}\right)^{1/2} \frac{A_{1,-1} - A_{1,1}}{a^2}, \tag{4a}$$

$$\bar{p}_y = -\mathrm{i}\left(\frac{3}{8\pi}\right)^{1/2} \frac{A_{1,-1} + A_{1,1}}{a^2}, \tag{4b}$$

and

$$\bar{p}_z = \left(\frac{3}{4\pi}\right)^{1/2} \frac{A_{1,0}}{a^2}. \tag{4c}$$

The ith component of the dipole moment is related to the incident electric field ($\mathbf{E}_0$) in the vicinity of the particle by

$$p_i = \sum_{j=1}^{3} \alpha_{ij} E_{0,j}, \tag{5}$$

where α_{ij} denotes the polarizability tensor of one of the nanoparticles.

In passing we note that even though the dipole moment only depends on the lowest order ($l = 1$) expansion coefficients, it carries information on higher order resonances, as the system of equations for the A_{lm} coefficients couple coefficients of all orders [19]. Moreover, for ease of comparison, we will below always refer to the dipole moment of a single particle.

B. Surface reflectivity

The most readily observable quantity that gives an indication of plasmonic activity is the surface reflectivity. The reflectivity of the system we consider can be calculated via several routes. The first approach that will be mentioned is due to Bedeaux and Vlieger [29] (see also Refs. 26, 31–35). It introduces an equivalent geometry consisting of the same ambient and substrate as the original geometry, but without the nanoparticles. The influence of the latter is accounted for through effective boundary conditions for the electromagnetic field on the ambient–substrate interface. These boundary conditions depend on so-called surface susceptibilities that contain, for instance, the effect of the size, shape, aspect ratio, and location of the nanoparticles. The surface susceptibilities are obtained from the multipole coefficients A_{lm} that were shown above how to calculate. The approach of Bedeaux and Vlieger [29, 31, 33] has proven to produce accurate results for the surface reflectivity that compares quantitatively well to experimental measurements [31, 33, 35]. It has been used successfully to interpret and invert experimental reflectivity data [26, 35].

Recently, this has opened for the possibility of detailed *in situ* and real time studies of the growth of supported nanoparticles during deposition [35]. However, the accuracy of the Bedeaux–Vlieger method comes at a cost: The approach is somewhat technical, and may be challenging to grasp for those not familiar with it.

Since our main concern in this study is not quantitative interpretation of experimental reflectivity measurements, we will instead follow a simpler and more qualitative route towards obtaining the surface reflectivity. To this end, we define above the substrate a thin film region of thickness d [Fig. 1(b)] that contains the nanoparticles, and when it is homogenized [36–38], an effective medium results. The classic Maxwell Garnett theory [36–40] or the Bruggeman theory [41] for such films are essentially only sensitive to the volume fraction of particles and the (bulk) dielectric functions of the materials of the particles and substrate, and not to the shape and environment (e.g., the ambient-substrate interface) surrounding the particles of the lattice. Instead of employing the Maxwell Garnett or Bruggeman theories directly, we construct an effective medium theory that does depend on other parameters, such as the local environment, via the calculated polarizability of the metallic particles. The starting assumption of our effective medium model is that the lattice of nanospheres can be represented as an anisotropic thin film of thickness $d = 2a + h \approx 2a$ [Fig. 1(b)].

Due to the symmetry properties of the two-dimensional rectangular (or square) lattice, the dielectric tensor ($\overleftrightarrow{\varepsilon}$) will in our choice of coordinate system be diagonal:

$$\overleftrightarrow{\varepsilon} = \begin{pmatrix} \varepsilon_x & 0 & 0 \\ 0 & \varepsilon_y & 0 \\ 0 & 0 & \varepsilon_z \end{pmatrix}. \tag{6}$$

where ε_x, ε_y, and ε_z are the principle dielectric constants. Hence, the polarizability tensor, $\overleftrightarrow{\alpha}$, must also be diagonal. The macroscopic polarization, $\mathbf{P}$, defined as the total dipole moment per unit volume, is thus given by

$$P_i = \frac{1}{b_x b_y d} \sum_{j=1}^{3} \alpha_{ij} E_{0,j}, \tag{7}$$

where P_i denotes the ith component of $\mathbf{P}$, and subscript indices $i = 1, 2, 3$ correspond to subscripts x, y, z, respectively. Moreover, $b_x b_y d$ is the volume of the effective thin film covering one unit cell of the 2D lattice. In SI units, the displacement field, $\mathbf{D}$, is given by

$$\mathbf{D} = \varepsilon_0 \mathbf{E} + \mathbf{P}. \tag{8}$$

By inserting Eq. (7) into Eq. (8), we obtain

$$\begin{aligned} D_i &= \varepsilon_0 E_{0,i} + P_i = \varepsilon_0 \left(E_{0,i} + \frac{1}{b_x b_y d} \sum_{j=1}^{3} \alpha_{ij} E_{0,j} \right) \\ &= \sum_{j=1}^{3} \varepsilon_0 \left(\delta_{ij} + \frac{1}{b_x b_y d} \alpha_{ij} \right) E_{0,j} = \sum_{j=1}^{3} \varepsilon_0 \varepsilon_{ij} E_{0,j}, \end{aligned}$$

so that we get for the component of the dielectric tensor

$$\varepsilon_{ij} = \delta_{ij} \ + \frac{1}{b_x b_y d} \alpha_{ij}. \tag{9}$$

The polarizability tensor components, α_{ij}, that appears in Eq. (9), can be related to the multipole coefficients A_{lm} by comparing Eq. (5) to the multipole expansion of $\psi(\mathbf{r})$ [25]. This yields the formulas

$$\alpha_{xx} = \left(\frac{3}{2\pi} \right)^{1/2} A_{1,-1}, \tag{10a}$$

$$\alpha_{yy} = -\mathrm{i} \left(\frac{3}{2\pi} \right)^{1/2} A_{1,-1}, \tag{10b}$$

$$\alpha_{zz} = \left(\frac{3}{4\pi} \right)^{1/2} A_{1,0}, \tag{10c}$$

and $\alpha_{ij} = 0$ for $i \neq j$. Note that the formula for α_{xx} [Eq. (10a)] is only valid for $\mathbf{E}_0 \parallel \hat{\mathbf{x}}$, and the same applies to the pairs $(\alpha_{yy}, \mathbf{E}_0 \parallel \hat{\mathbf{y}})$ and $(\alpha_{zz}, \mathbf{E}_0 \parallel \hat{\mathbf{z}})$. Hence, each component of the polarizability tensor is determined by one simulation each. This is the reason why Eq. (10) seems to disagree with Eq. (4). After determining the elements of the dielectric tensor, standard theory can be applied to the model thin film system in order to determine reflectivity from the nanoparticle lattice on top of the substrate.

After determining all components of the dielectric tensor describing the (effective medium) thin film, the reflectivity of the system can be readily calculated from standard theory [40]. In the following, we will denote the surface reflectivity $R_\beta(\omega)$ where the subscript $\beta = p, s$ indicates the linear polarization of the incident light. Finally, we note that whereas we can assume $\left|\mathbf{k}_\parallel\right| = 0$ for the solution of the Laplace equation, the lateral wave vector enters as

$$\mathbf{k}_\parallel = \frac{\omega}{c} \sin\theta_0 (\cos\phi_0, \sin\phi_0, 0)$$

in the reflectance formulas. This is a consequence of the well known fact that the reflectance in general depends on the angle of incidence.

III. THE COLLECTIVE PLASMON MODES OF NANOPARTICLE ARRAYS

In order to estimate how the interactions between the nanoparticles influence their plasmonic resonances, we compare the dimensionless dipole moment [Eq. (3)] of an Ag nanoparticle when it is situated in various environments in Fig. 2. The dipole moment of a single Ag nanoparticle (with no substrate present) is shown in Fig. 2(a) and it exhibits a peak at $\hbar\omega \approx 3.5\,\mathrm{eV}$. This is the well-known Mie resonance [42] in the quasistatic regime. We note that in obtaining the results of Fig. 2 a cutoff of $L_{\max} = 30$ was used in the calculations. Moreover, the same value of $L_{\max}$ was assumed in obtaining all results that will be presented in this paper.

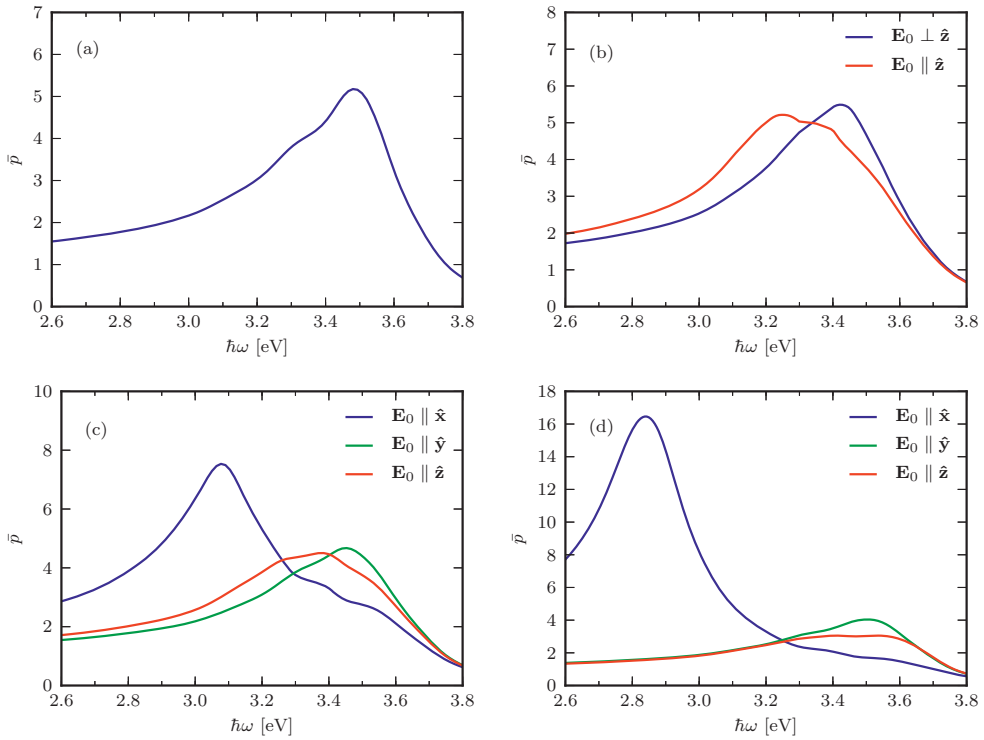

FIG. 2. The absolute value of the dimensionless dipole moment of a single nanosphere in the following environments: (a) "hovering" in vacuum, (b) supported by an Al_2O_3 substrate, (c) in an Ag dimer with an interparticle center-center distance of $2.2a$ on top of an Al_2O_3 substrate, (d) in an Ag lattice [Figs. 1(a) and 1(b)] with $b_x = 2.2a$ and $b_y = 4b_x$ supported by an Al_2O_3 substrate. For comparison, a perfect metal sphere (of radius much smaller than λ) in vacuum excited by a homogeneous $\mathbf{E}_0$ has $\bar{p}(\omega) \equiv 1$. The parameters common to all subfigures were $h = 0.01a$ and $L_{\max} = 30$.

When the Ag monomer is supported by a semi-infinite Al_2O_3 substrate ($\varepsilon_- \approx 2.76$ at 3 eV, with little dispersion), its dipole moment response is as shown in Fig. 2(b). By comparing Figs. 2(a) and 2(b), it is observed that the presence of the substrate leads to a red-shift of the Mie resonance when the electric field is perpendicular to the substrate ($\mathbf{E}_0 \parallel \hat{\mathbf{z}}$), but is almost unchanged in the case when the electric field is parallel to the substrate ($\mathbf{E}_0 \perp \hat{\mathbf{z}}$). The Mie resonance splits due to the breaking of symmetry caused by the presence of a substrate. Note that in this case, full convergence was not obtained. Nevertheless, the results are shown for easy comparison with the other subfigures of Fig. 2. For a detailed discussion of this system, see Ref. [43].

Next, we consider two supported Ag particles placed in a dimer configuration with the distance between the particle centers being $2.2a$ and the dimer axis being oriented along the x axis. We also assume that it is "hovering" $h = 0.01a$ above an Al_2O_3 substrate. We observe that the resonance for $\mathbf{E}_0 \perp \hat{\mathbf{z}}$ splits into two resonances, located at different photon energy for $\mathbf{E}_0 \parallel \hat{\mathbf{x}}$ relative to the $\mathbf{E}_0 \parallel \hat{\mathbf{y}}$ case [Fig. 2(c)]. This happens because we no longer have rotational symmetry about the z axis. If instead the incident electric field is oriented along the dimer axis ($\mathbf{E}_0 \parallel \hat{\mathbf{x}}$), one gets a redshift of approximately 0.45 eV (relative a corresponding isolated particle) and a significant enhancement of the resonance. The particle-substrate interactions are not particularly strong for the Al_2O_3 substrate we consider; it only leads to a small redshift and broadening of the resonance when the incident electric field is directed normal to the surface ($\mathbf{E}_0 \parallel \hat{\mathbf{z}}$). When the incident electric field is directed normal to both the surface of the substrate and the dimer axis, i.e., $\mathbf{E}_0 \parallel \hat{\mathbf{y}}$, the spectrum looks very similar to the case $\mathbf{E}_0 \perp \hat{\mathbf{z}}$ of an isolated nanoparticle supported by the same substrate [Fig. 2(b)].

Finally, we study the case when the neighborhood of the particle becomes a two-dimensional rectangular lattice of (identical) nanoparticles with lattice constants $b_x = 2.2a$ and $b_y = 4b_x$, supported by an Al_2O_3 substrate ($h = 0.01a$). In this case, the Mie resonance for $\mathbf{E}_0 \parallel \hat{\mathbf{x}}$ undergoes further redshift and enhancement [Fig. 2(d)].

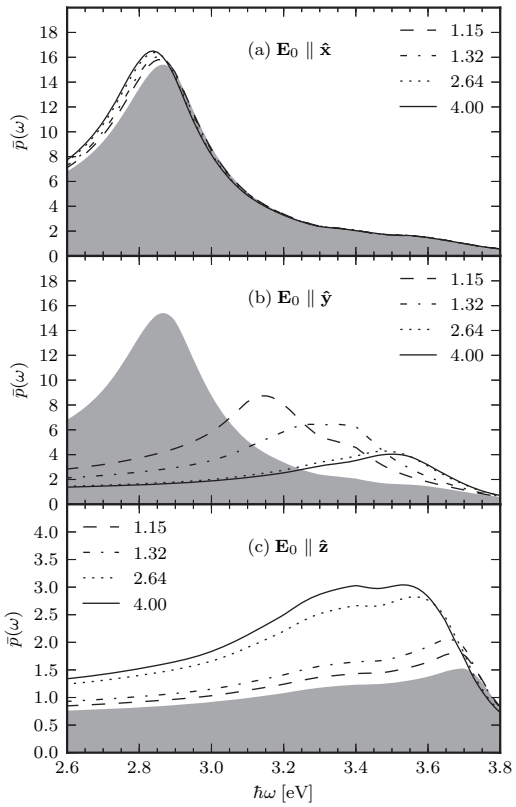

FIG. 3. The absolute value of the dimensionless dipole moment for a sphere in a rectangular lattice, with anisotropy parameters $b_y/b_x = 1.15$ to $b_y/b_x = 4$; b_x was kept constant at $2.2a$. For reference, the dipole moment of a sphere in a square lattice ($b_x = b_y$) is shown in gray shade. In each plot, the exciting electric field is directed along different axes: (a) $\mathbf{E}_0 \parallel \hat{\mathbf{x}}$, (b) $\mathbf{E}_0 \parallel \hat{\mathbf{y}}$, and (c) $\mathbf{E}_0 \parallel \hat{\mathbf{z}}$. Note that the scale of the second axis in (c) is different from the scales used for the equivalent axes of the other two subfigures.

As expected, successively longer chains of particles cause stronger interactions between the particles, causing more redshift and resonance enhancement. When the incident electric field is transverse to the chains and to the surface normal, i.e., $\mathbf{E}_0 \parallel \hat{\mathbf{y}}$, the interactions between the "chains of particles" are rather weak and cause no significant redshift. Finally, for $\mathbf{E}_0$ normal to the substrate ($\mathbf{E}_0 \parallel \hat{\mathbf{z}}$), the particle-substrate interactions mainly serve to kill off the resonance. This may be understood by recalling that the induced dipole in the particle and the image dipole in the substrate will have opposite directions and therefore partly cancel the effect of each other.

By comparing the results for the different ratios b_y/b_x shown in Fig. 2, we see that the local environment can significantly alter the optical response of nanoparticles. In particular, periodic lattices strongly influence the optical response of nanoparticles to an incident electric field. In Sec. IV, we will discuss how this can be observed in a reflectivity experiment.

By studying the dipole moment of a single nanosphere in a rectangular lattice, one aims at better understanding how the lattice affects the strength and position of particle resonances and under which conditions the rectangular lattice turns into a collection of non-interacting chains. Hence, in Fig. 3 we show the (single particle) dipole moment as a function of the anisotropy parameter b_y/b_x of the lattice. As this parameter increases, the intersphere interactions along the y-axis weaken [Fig. 3(b)], leading to reduced resonance strength and less red-shift of the resonance. We observe that from $b_y/b_x = 2.64$ to $b_y/b_x = 4$, there is little change in both resonance strength and position. Results for intermediate values, i.e., $2.64 < b_y/b_x < 4$, are virtually indistinguishable from those of $b_y/b_x = 4$. From this result, we conclude that for $b_y \geq 4b_x$, one may ignore interactions between the nanosphere chains altogether (at least for our choice of b_x).

When examining Fig. 3(a), it is clear that if the electric field is directed along $\hat{\mathbf{x}}$, the change in b_y does not affect the plasmon resonances significantly. This is because the interactions between neighbouring particles is strongest along the direction of the incident field. For the case when $\mathbf{E}_0 \parallel \hat{\mathbf{z}}$ [Fig. 3(c)], however, the anisotropy affects the plasmonic resonances by increasing the resonance strength. This effect is mainly caused by the reduced density of particles on the substrate, as neighbouring particles cause damping of the resonance. This damping effect can be explained in a "hand-waving" fashion by considering the fact that side-by-side parallel dipoles counteract polarization of each other.

Simulations have also been run for lattices where the anisotropy was kept at $b_y/b_x = 4$, but b_x (and thus, b_y) was increased. As would be expected, increasing the lattice constants reduces interparticle interactions, and the dipole moment behavior becomes more similar to that of Fig. 2(b). Hence, for lattice constants larger than what has been explored here, one can safely assume that a lattice with $b_y/b_x > 4$ can be approximated as a set of non-interacting linear chains of nanoparticles.

Finally, we have investigated the effects of finite $|\mathbf{k}_\parallel|$. While the effects of a phase difference between neighbouring particles can be significant, we do not include any results in this paper. The reason is that we are primarily interested in optical fields, where $|\mathbf{k}_\parallel| \ll \pi/b_y$. Results of simulations for small, but finite, $|\mathbf{k}_\parallel|$, indicate that the approximation $|\mathbf{k}_\parallel| = 0$ is a good one.

IV. REFLECTIVITY OF NANOPARTICLE ARRAYS

The reflectivity of an interface is an experimentally accessible quantity for probing the nanoparticle sys-

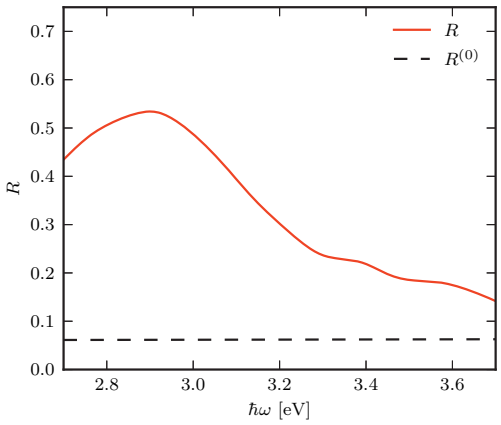

(a) $\theta_0 = 0°$

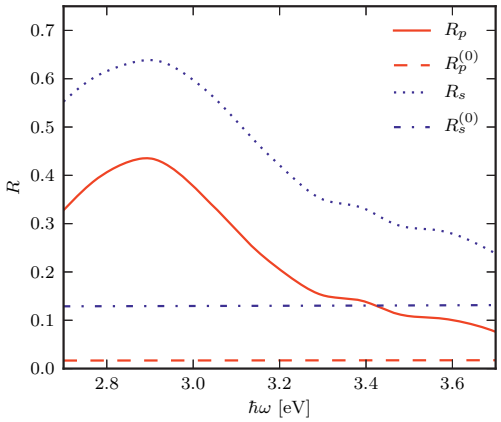

(b) $\theta_0 = 45°$

FIG. 4. Reflectivity of a square lattice of spheres supported by an Al_2O_3 substrate for angles of incidence (a) $(\theta_0, \phi_0) = (0°, 0°)$ and (b) $(\theta_0, \phi_0) = (45°, 0°)$. The lattice parameters were $a = 10\,\text{nm}$ and $b_x = b_y = 2.2a$. The isotropic nature of the square lattice means that the reflectivity is identical for p-polarized and s-polarized light at normal incidence. The dashed lines shows the reflectivity of a substrate with no nanoparticles.

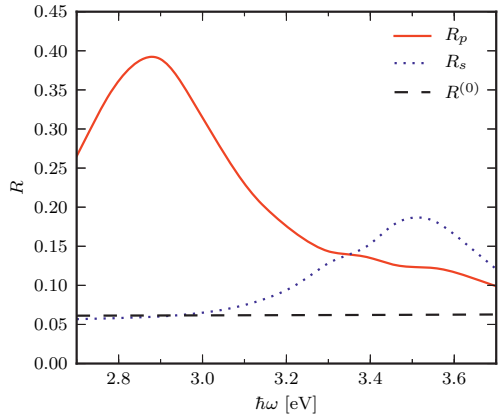

(a) $(\theta_0, \phi_0) = (0°, 0°)$

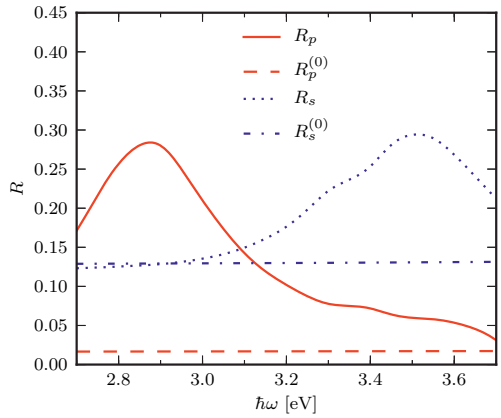

(b) $(\theta_0, \phi_0) = (45°, 0°)$

FIG. 5. Reflectivity of a rectangular lattice of spheres on top of an Al_2O_3 substrate. The lattice parameters were $a = 10\,\text{nm}$, $b_x = 2.2a$, and $b_y = 2b_x$. The dashed lines shows the reflectivity of a substrate with no nanoparticles. (a) At normal incidence $[(\theta_0, \phi_0) = (0°, 0°)]$ we define p-polarized light to be polarized along the x-axis, and (b) $(\theta_0, \phi_0) = (45°, 0°)$.

tem. Optical methods have the advantage of being non-destructive, and can be used *in situ* in various challenging environments, e.g., vacuum chambers. For these reasons, we have calculated the surface reflectivity of a square and a rectangular two-dimensional lattice of Ag nanoparticles supported by an Al_2O_3 substrate. In these calculations, the incident field is assumed to be a plane wave that is either p- or s-polarized. At normal incidence, we define a p-polarized (s-polarized) field by $\mathbf{E}_0 \parallel \hat{\mathbf{x}}$ ($\mathbf{E}_0 \parallel \hat{\mathbf{y}}$). The lattice constants were $b_x = b_y = 2.2a$ for the square lattice and $b_x = 2.2a$, $b_y = 2b_x$ for the rectangular lattice. In both cases, $a = 10\,\text{nm}$ was the radius of the spheres.

First we address normal incidence. Figures 4(a) and 5(a) present the calculated reflectivity [Sec. II B] for the square and rectangular lattices, respectively, at angles of incidence $(\theta_0, \phi_0) = (0°, 0°)$. The red solid curve in Fig. 4(a) depicts the reflectivity from the square lattice at normal incidence, whereas the dashed line shows the reflectivity from a flat, clean Al_2O_3 surface. From this figure it is observed that there is no difference (at normal incidence) between p- and s-polarized reflected light, as is to be expected due to the symmetry of the lattice. Moreover, the presence of the metallic particles cause the reflectivity to increase relative to the reflectivity of the clean dielectric substrate. This increase is

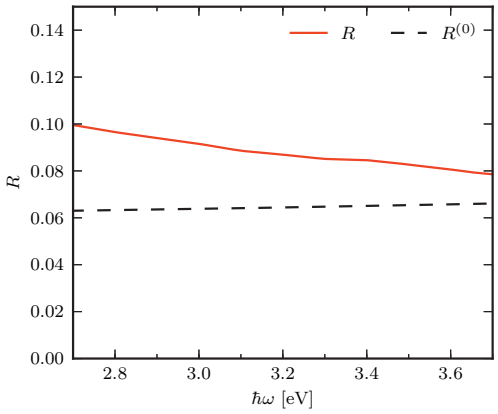

(a) $\theta_0 = 0°$

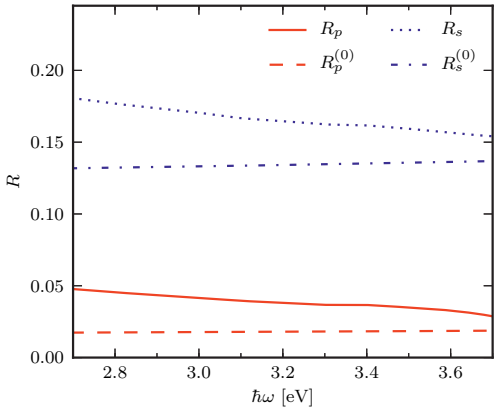

(b) $\theta_0 = 45°$

FIG. 6. The reflectivity of an isotropic and homogeneous Ag film at angles of incidence (a) $\theta_0 = 0°$ and (b) $\theta_0 = 45°$ (as the film is isotropic, ϕ_0 is irrelevant). The film thickness was assumed to be 4.3 nm, which is equivalent to the mass thickness of the rectangular lattice shown in Fig. 5.

especially pronounced near the redshifted Mie resonance.

For the rectangular lattice at normal incidence, the reflectivity of p-polarized light looks rather different from the reflectivity of s-polarized light [Fig. 5(a)], caused by $b_x \neq b_y$. Since $b_y = 2b_x$ was assumed, the particles will interact more strongly along the x-direction than along the y-direction. Based on what was found in Fig. 3, the system can be thought of as a set of weakly interacting linear chains oriented along the x-axis. Along the chain, the interactions are strong (p-polarized light has a component along $\hat{\mathbf{x}}$), whereas between the chains (s-polarized light is polarized along $\hat{\mathbf{y}}$) the interactions are much weaker. This can be seen directly in the reflectivity curves: for p polarization, a large red shift relative to the isolated, single particle Mie resonance is observed due (mainly) to interparticle interactions. However, for s polarization there is essentially no redshift, meaning that the resonance occurs close to the single particle Mie resonance. Note that the interparticle interactions along the chain ($\hat{\mathbf{x}}$) in p polarization produce a much stronger resonance, and hence higher reflectivity, than the interchain interactions in s polarization.

We now turn to non-normal incidence, $(\theta_0, \phi_0) = (45°, 0°)$, for which results are presented in Figs. 4(b) and 5(b). In this case, the two polarization states give rise to different reflectivity curves even for the square lattice. From Fig. 4(b), it is observed that the reflectivity for s polarization is systematically higher than the reflectivity for p polarization. Moreover, the difference between the two curves is almost independent of energy, and the relative change in the reflectivity as a function of energy follows closely that of normal incidence. This behavior is due to the difference in reflectivity at non-normal incidence for the two linear polarizations, as indicated by the dashed lines in Figs. 4(b) and 5(b).

For the same angles of incidence $[(\theta_0, \phi_0) = (45°, 0°)]$, Fig. 5(b) shows that the reflectivity from the rectangular lattice is both quantitatively and qualitatively different from that of the square lattice. As the interactions between the particles are now significantly stronger for electric fields polarized along the x axis, the p-polarized reflectivity still has a significantly redshifted peak. For s-polarized light, however, the redshift is negligible. This means that this surface acts as a spectral polarizer: it reflects predominantly p polarized light at around 2.9 eV, whereas at around 3.5 eV, s-polarized light dominates. The reflectivity can be increased by simply using a greater "mass thickness" (the equivalent thickness of a homogeneous Ag thin film) of Ag, i.e., by using larger nanoparticles. However, the results will be affected by retardation effects if the nanoparticle radius increases too much.

For comparison, we present in Fig. 6 the reflectivity of a continuous, isotropic, and homogeneous Ag film of thickness 4.3 nm. This is the equivalent mass thickness of the rectangular lattice with $b_y = 2b_x$. By comparing the results of Figs. 5(b) and 6 it is readily observed that the corresponding reflectivity curves are rather different. Thus, it is feasible to separate the case of a continuous thin film from that of isolated metallic island films through reflectance measurements. In fact, the reflectivity of the thin continuous film is much closer to the reflectivity of the clean substrate, where few features of interest can be observed.

V. CONCLUSION

In this paper, we have investigated the collective excitations in square and rectangular two-dimensional lattices of Ag nanoparticles supported by a dielectric (Al_2O_3) substrate. In particular, we have established

that for lattices where the lattice constant is greater than approximately 4 sphere diameters ($b_y/b_x > 4$), the system can be approximated as a collection of independent, non-interacting linear chains. It has also been demonstrated that if the incident field is polarized along the shortest lattice vector, the anisotropic nature of the lattice leads to collective resonances that are significantly redshifted relative to the single particle Mie resonance.

We have also presented results showing the reflectivity of surfaces patterned by such nanoparticle lattices. If the lattice is rectangular, the surfaces exhibit the interesting property that the reflected light possesses different colors in the two linear polarizations (p and s). It is reasonable to assume that similar behavior will be apparent in transmission. For technological applications, the advantage of the rectangular lattice configuration is that no control is necessary over the nanoparticle orientation (cf. anisotropic particles on a square lattice), and that resonance positions can be tuned via the lattice constants.

Since rectangular lattices of nanoparticles leave much room for tunability of the plasmonic and polarization characteristics of an interface, we believe further studies are in order to gain more insight. Tunability can further be extended by employing other materials; nanoshells, which allow for tunability through the core and shell radii; or through use of truncated spheres or otherwise anisotropic particles. For spherical nanoshells, the theory sketched in this paper could be applied with relatively straightforward modifications. The effects of randomness on the properties of such lattices is also a topic of interest [44], relevant to experimental conditions in which some element of randomness is inevitable. The approach here is not very computationally demanding, and should thus be suited for exploration of random effects.

ACKNOWLEDGMENTS

The authors would like to acknowledge the Norwegian University of Science and Technology for the allocation of computer time.

P.A.L. would like to thank Dr. Ingar S. Nerbø, Lars Martin Sandvik Aas, Tor Nordam, and Dr. Jamie Cole for interesting discussions. Moreover, I.S. acknowledges fruitful discussions with Dr. Rémi Lazzari.

We used the freely available computer library SHTOOLS authored by Dr. Mark Wieczorek to evaluate the associated Legendre functions.

[1] A. Maradudin, E. Méndez, and T. Leskova, *Designer surfaces* (Elsevier Science, Amsterdam, 2008).
[2] I. Simonsen, Eur. Phys. J.–Spec. Top. **181**, 1 (2010).
[3] S. Pillai, K. R. Catchpole, T. Trupke, and M. A. Green, J. Appl. Phys. **101**, 093105 (2007).
[4] H. A. Atwater and A. Polman, Nat. Mater. **9**, 205 (2010).
[5] A. Y. Vorobyev and C. Guo, Appl. Phys. Lett. **92**, 041914 (2008).
[6] X. Zhang, H. Liu, J. Tian, Y. Song, and L. Wang, Nano Lett. **8**, 2653 (2008).
[7] Z. Ghadyani, I. Vartiainen, I. Harder, W. Iff, A. Berger, N. Lindlein, and M. Kuittinen, Appl. Opt. **50**, 2451 (2011).
[8] S. G. Moiseev, Proc. SPIE **7993** (2010).
[9] L. M. S. Aas, I. S. Nerbø, M. Kildemo, D. Chiappe, C. Martella, and F. B. de Mongeot, Proc. SPIE **8082** (2011).
[10] S. Link and M. A. El-Sayed, Int. Rev. Phys. Chem. **19**, 409 (2000).
[11] Y. B. Martynov, R. G. Nazmitdinov, I. A. Tanachev, and P. P. Gladyshev, JETP Lett. **95**, 138 (2012).
[12] U. Kreibig and M. Vollmer, *Optical properties of metal clusters* (Springer-Verlag, Berlin, 1995).
[13] H. C. van de Hulst, *Light scattering by small particles* (Dover Publications Inc., New York, 1981).
[14] C. F. Bohren and D. R. Huffman, *Absorption and Scattering of Light by Small Particles* (Wiley-VCH Verlag GmbH, Berlin, 2007).
[15] M. Pelton, J. Aizpurua, and G. Bryant, Laser Photonics Rev. **2**, 136 (2008).
[16] J. Tang, E. V. Ponizovskaya, A. M. Bratkovsky, D. R. Stewart, Z. Li, and R. S. Williams, Nanotechnology **19**, 415702 (2008).
[17] C. E. Cross, J. C. Hemminger, and R. M. Penner, Langmuir **23**, 10372 (2007).
[18] J. Liu, J. C. Barnard, K. Seeger, and R. E. Palmer, Appl. Phys. Lett. **73**, 2030 (1998).
[19] P. A. Letnes, I. Simonsen, and D. L. Mills, Phys. Rev. B **83**, 075426 (2011).
[20] P. A. Letnes, I. Simonsen, and D. L. Mills, Phys. Rev. B **85**, 149901 (2012).
[21] T. Yamaguchi, S. Yoshida, and A. Kinbara, Thin Solid Films **21**, 173 (1974).
[22] P. Chu and D. L. Mills, Phys. Rev. B **77**, 045416 (2008).
[23] E. M. Purcell and C. R. Pennypacker, Astrophys. J. **186**, 705 (1973).
[24] R. Schmehl, B. M. Nebeker, and E. D. Hirleman, J. Opt. Soc. Am. A **14**, 3026 (1997).
[25] J. D. Jackson, *Classical Electrodynamics*, 3rd ed. (John Wiley, New York, 1998).
[26] R. Lazzari, I. Simonsen, and J. Jupille, Europhys. Lett. **61**, 541 (2003).
[27] R. Arias and D. L. Mills, Phys. Rev. B **68**, 245420 (2003).
[28] C. Kittel, *Introduction to solid state physics*, 7th ed. (Wiley, New York, 1976).
[29] D. Bedeaux and J. Vlieger, *Optical Properties of Surfaces* (Imperial College Press, London, 2004).
[30] I. Romero, J. Aizpurua, G. W. Bryant, and F. J. García de Abajo, Opt. Express **14**, 9988 (2006).
[31] I. Simonsen, R. Lazzari, J. Jupille, and S. Roux, Phys. Rev. B **61**, 7722 (2000).
[32] R. Lazzari, I. Simonsen, D. Bedeaux, J. Vlieger, and J. Jupille, Eur. Phys. J. B **24**, 267 (2001).
[33] R. Lazzari, S. Roux, I. Simonsen, J. Jupille, D. Bedeaux,

and J. Vlieger, Phys. Rev. B **65**, 235424 (2002).
[34] R. Lazzari and I. Simonsen, Thin Solid Films **419**, 124 (2002).
[35] R. Lazzari and J. Jupille, Nanotechnology **22**, 445703 (2011).
[36] T. C. Choy, *Effective medium theory* (Oxford University Press, New York, 1999).
[37] G. W. Milton, *The theory of composites* (Cambridge University Press, Cambridge, 2002).
[38] D. J. Bergman, Phys. Rep. **43**, 377 (1978).
[39] J. C. Maxwell Garnett, Phil. Trans. R. Soc. Lond. A **203**, 385 (1904).
[40] R. M. A. Azzam and N. M. Bashara, *Ellipsometry and polarized light* (North Holland, Amsterdam, 1977).
[41] D. A. G. Bruggeman, Ann. Phys. (Leipzig) **24**, 636 (1935).
[42] G. Mie, Ann. Phys. (Leipzig) **330**, 377 (1908).
[43] C. Noguez, J. Phys. Chem. C **111**, 3806 (2007).
[44] R. Esteban, R. W. Taylor, J. J. Baumberg, and J. Aizpurua, Langmuir **28**, 8881 (2012).

P. A. Letnes, T. Nordam, and I. Simonsen. "Coherent effects in the scattering of light from two-dimensional rough metal surfaces". *(unpublished)* (2012)

Paper 11

Coherent effects in the scattering of light from two-dimensional rough metal surfaces

P. A. Letnes,* T. Nordam,† and I. Simonsen‡
Department of Physics, The Norwegian University of Science and Technology (NTNU), NO-7491 Trondheim, Norway

We investigate numerically multiple light scattering phenomena in two-dimensional randomly rough metallic surfaces, where surface plasmon polaritons mediate several surface scattering effects. The scattering problem is solved by numerical solution of the reduced Rayleigh equation for reflection. The multiple scattering phenomena of enhanced backscattering and enhanced forward scattering are observed in the same system, and their presence is dependent on surface plasmon polariton excitation. The numerical results discussed are qualitatively different from previous results for one-dimensionally rough surfaces, as one-dimensional surfaces have a limited influence on the polarization of light.

PACS numbers: 42.25.-p, 41.20.-q, 78.20.-e, 78.20.Bh

I. INTRODUCTION

A hot topic in the electronics and photonics community is plasmonics, due to the prediction that surface plasmon polaritons (SPP) can carry information faster and with less energy loss than electronic circuits [1]. Surface plasmon polaritons can have a penetration depth in metal on the order of 10 nm, i.e., two orders of magnitude smaller than the wavelength of visible light in vacuum. This means that plasmonics allows light to be concentrated and manipulated by structures well below the diffraction limit from classical optics.

Surface plasmon polariton excitation is also being investigated as a way to improve the performance of photovoltaic devices. For thin solar cells, with a thickness on the order of 1 µm, the path length of light travelling through the cell is insufficient to absorb more than a small fraction of the incident energy. By converting light into SPPs which can propagate along the dielectric-metal interface at the back of the photovoltaic cell, it is possible to absorb a larger fraction of the incident energy [2].

Since SPPs propagate along the interface of a metal, they are sensitive to conditions on the surface, making SPPs well suited for sensor applications. Such devices are often called surface plasmon resonance (SPR) sensors, and can be used for, e.g., microarray analysis of proteins [3] or DNA [4].

At a flat interface, incident light cannot couple to SPPs due to momentum mismatch. By manipulating the surface roughness, however, it is possible to control the coupling of incident light into SPPs. In this paper, we will consider light reflected from randomly rough surfaces with particular statistical properties, and look at multiple scattering phenomena which arise due to SPPs. Several multiple scattering phenomena have been predicted theoretically and/or confirmed experimentally. For example, enhanced backscattering was predicted by McGurn et al. [5] and later confirmed experimentally by West and O'Donnell [6]. The enhanced backscattering phenomenon is a double scattering phenomenon, caused by constructive interference between a wave scattered (at least) twice by the surface, and its time-reversed partner. Usually, the excitation of SPPs is involved in this process. For weak (low rms) surface roughness, scattering processes are usually dominated by single scattering. Hence, West and O'Donnell designed a surface whose roughness had a power spectrum which suppresses single scattering in a certain angular range, allowing multiple scattering effects to be seen more clearly [6]. The surface in question had a surface profile function dependent on only one of the axes in the surface plane; colloquially, we refer to such surfaces as "one-dimensional". This power spectrum is now known as the West–O'Donnell spectrum or the rectangular spectrum.

Enhanced forward scattering was first predicted theoretically by O'Donnell [7], who termed it the enhanced specular peak phenomenon. O'Donnell investigated the scattering of light from surfaces with weak, one-dimensional roughness by the use of perturbation theory, and reported an enhancement in the specular direction of the intensity of the light scattered diffusely by the rough surface. To lowest order in the surface profile function, this phenomenon appears as an eight-order contribution to the intensity within perturbation theory, and for one-dimensional surface roughness it is caused by constructive interference between counterpropagating SPPs; see Fig. 10 of Ref. 7. To confirm these findings, O'Donnell and Méndez studied surface scattering from one-dimensional surfaces by direct solution of the one-dimensional reduced Rayleigh equation [8]. Their findings were later confirmed by Simonsen [9] who also performed a detailed numerical study of this phenomenon, focusing on the competition between how light couples into and out from SPPs, and how one SPP can couple to another counterpropagating SPP.

Up till now, the enhanced forward scattering phenomenon has not been studied for two-dimensional randomly rough surfaces neither by perturbation theory nor by computer simulations. Also, only a few numerical studies of enhanced backscattering have appeared in the

* paul.anton.letnes@gmail.com
† tor.nordam@ntnu.no
‡ Ingve.Simonsen@ntnu.no

literature for two-dimensional roughness. In this paper, we investigate light scattering from two-dimensionally rough surfaces by means of large scale computer simulations, with a focus on phenomena caused by the excitation and interference of SPPs. In particular, we are interested in the enhanced backscattering phenomenon and the less studied phenomenon of forward scattering enhancement. The understanding of such phenomena could be useful for the understanding and tweaking light-plasmon coupling in plasmonic circuits. Furthermore, two-dimensional surface roughness leads to significant polarization effects that cannot be taken into account in a one-dimensional model.

This paper is organized as follows. In Sec. II, we discuss the relevant theory, including how the statistical properties of the surface roughness decide which scattering processes are allowed. Section III presents results from numerical simulations, exhibiting enhanced forward scattering and enhanced backscattering. Finally, concluding remarks are found in Sec. IV.

II. THEORY

The system under study consists of a metallic substrate with a vacuum cladding [Fig. 1(a)]. We assume that the vacuum-metal interface has a randomly rough structure, and the metal is characterized by a complex dielectric function $\varepsilon_2(\omega)$. Since the cladding is vacuum, its dielectric constant is $\varepsilon_1 \equiv 1$. The height of the surface is given by the single-valued function $x_3 = \zeta(\mathbf{x}_\parallel)$, where $\mathbf{x}_\parallel = (x_1, x_2, 0)$ is the lateral component of the position vector, $\mathbf{x}$. We assume that $\zeta(\mathbf{x}_\parallel)$ is at least once differentiable with respect to x_1 and x_2. The angles of incidence (θ_0, ϕ_0) and scattering (θ_s, ϕ_s) are defined positive according to the convention given in Fig. 1(b).

In this paper, we will consider randomly rough surfaces where $\zeta(\mathbf{x}_\parallel)$ constitutes a stationary random process defined by

$$\left\langle \zeta(\mathbf{x}_\parallel) \right\rangle = 0, \tag{1a}$$

$$\left\langle \zeta(\mathbf{x}_\parallel)\zeta(\mathbf{x}'_\parallel) \right\rangle = \delta^2 W(\mathbf{x}_\parallel - \mathbf{x}'_\parallel), \tag{1b}$$

where the angle brackets denote an average over an ensemble of surface realizations. In writing Eq. (1) we have defined the root-mean-square height of the surface, $\delta = \left\langle \zeta^2(\mathbf{x}_\parallel) \right\rangle^{1/2}$, and $W(\mathbf{x}_\parallel - \mathbf{x}'_\parallel)$ denotes the height-height auto-correlation function of the surface, normalized so that $W(\mathbf{0}) = 1$ [11]. In the discussion below, and when generating realizations of the surface profile function, it is more convenient to work with the power spectrum of the surface, rather than using the auto-correlation function directly. The power spectrum, $g(\mathbf{k}_\parallel)$, of the surface profile function is defined by

$$g(\mathbf{k}_\parallel) = \int \mathrm{d}^2 x_\parallel \; W(\mathbf{x}_\parallel) \exp\left(-\mathrm{i}\mathbf{k}_\parallel \cdot \mathbf{x}_\parallel\right), \tag{2}$$

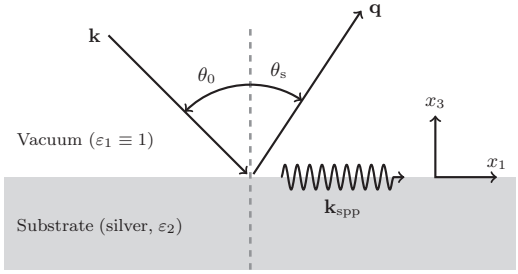

(a) System sketch, seen in the x_1x_3 plane.

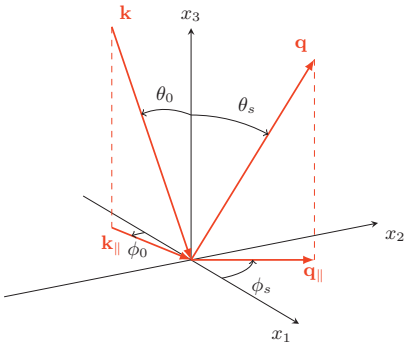

(b) Definition of wave vectors and polar angles.

FIG. 1. (Color online) Sketches of the system under study (surface roughness not shown). (a) The light of wave vector $\mathbf{k}$ incident on the surface causes scattering into various propagating modes (of wave vector $\mathbf{q}$) and the excitation of surface plasmon polaritons ($\mathbf{k}_{\mathrm{spp}}$). In this study, we assume $\varepsilon_1(\omega) \equiv 1$, and $\varepsilon_2(\omega)$ is taken from Ref. 10. (b) Definition of the lateral wave vectors ($\mathbf{k}_\parallel$ and $\mathbf{q}_\parallel$) as well as the polar angles of incidence and scattering.

where $\mathbf{k}_\parallel = (k_1, k_2, 0)$ is the lateral component of the wave vector, $\mathbf{k}$. The power spectra that will be considered in this work are of the cylindrical form, where

$$g(k_\parallel) = \gamma_1 g_1(k_\parallel) + \gamma_2 g_2(k_\parallel) \tag{3a}$$

and g_i $(i = 1, 2)$ are given by [12]

$$g_i(k_\parallel) = \frac{4\pi}{k_+^2 - k_-^2} \theta\left(k_\parallel - k_-^{(i)}\right) \theta\left(k_+^{(i)} - k_\parallel\right). \tag{3b}$$

In Eq. (3a), γ_1 and γ_2 are real constants defined such that $\gamma_1, \gamma_2 \geq 0$ and $\gamma_1 + \gamma_2 = 1$. Furthermore, $k_\parallel = \left|\mathbf{k}_\parallel\right|$, $\theta(\cdot)$ denotes the Heaviside unit step function, and $k_\pm^{(i)}$ are wavenumber cutoff parameters, with $k_-^{(1)} < k_+^{(1)} < k_-^{(2)} < k_+^{(2)}$. The Heaviside step functions in Eq. (3b) cause each of the g_i's to have a cylindrical shape: g_i is zero for $k_\parallel < k_-^{(i)}$, a positive constant for $k_-^{(i)} \leq k_\parallel < k_+^{(i)}$, and zero for $k_\parallel \geq k_+^{(i)}$. The constants γ_i determine the relative balance between the outer and inner cylindrical

parts of the power spectrum. The power spectrum described by Eq. (3) is a two-dimensional generalization of the one used by O'Donnell and Méndez [8] and Simonsen [9] in their previous numerical investigations of enhanced forward scattering from one-dimensional randomly rough surfaces. The power spectrum used by West and O'Donnell [6] in their experimental confirmation of enhanced backscattering is a one-dimensional special case of Eq. (3), with $\gamma_1 = 1$ and $\gamma_2 = 0$.

A. The reduced Rayleigh equation

The electric field in the vacuum above the surface $\left[x_3 > \max\zeta\left(\mathbf{x}_\parallel\right)\right]$ can be expressed as the sum of an incident field and a scattered field,

$$\mathbf{E}(\mathbf{x}|t) = \left[\mathbf{E}^{(0)}(\mathbf{x}|\omega) + \mathbf{E}^{(\mathrm{s})}(\mathbf{x}|\omega)\right]\exp\left(-\mathrm{i}\omega t\right), \tag{4}$$

where ω is the angular frequency of the incident (and scattered) light. The superscripts (0) and (s) on the electric field vectors indicate the incident and scattered field, respectively. Furthermore,

$$\mathbf{E}^{(0)}(\mathbf{x}|\omega) = \left\{-\frac{c}{\omega}\left[\hat{\mathbf{k}}_\parallel\alpha_1(k_\parallel) + \hat{\mathbf{x}}_3 k_\parallel\right]\mathcal{E}_{\mathrm{p}}^{(0)}(\mathbf{k}_\parallel) + \left(\hat{\mathbf{x}}_3\times\hat{\mathbf{k}}_\parallel\right)\mathcal{E}_{\mathrm{s}}^{(0)}(\mathbf{k}_\parallel)\right\}\exp\left[\mathrm{i}\mathbf{k}_\parallel\cdot\mathbf{x}_\parallel - \mathrm{i}\alpha_1(k_\parallel)x_3\right], \tag{5a}$$

$$\mathbf{E}^{(\mathrm{s})}(\mathbf{x}|\omega) = \int\frac{\mathrm{d}^2 q_\parallel}{(2\pi)^2}\left\{\frac{c}{\omega}\left[\hat{\mathbf{q}}_\parallel\alpha_1(q_\parallel) - \hat{\mathbf{x}}_3 q_\parallel\right]\mathcal{E}_{\mathrm{p}}^{(\mathrm{s})}(\mathbf{q}_\parallel) + \left(\hat{\mathbf{x}}_3\times\hat{\mathbf{q}}_\parallel\right)\mathcal{E}_{\mathrm{s}}^{(\mathrm{s})}(\mathbf{q}_\parallel)\right\}\exp\left[\mathrm{i}\mathbf{q}_\parallel\cdot\mathbf{x}_\parallel + \mathrm{i}\alpha_1(q_\parallel)x_3\right], \tag{5b}$$

where $\mathcal{E}_\alpha^{(0)}(\mathbf{q}_\parallel)$ and $\mathcal{E}_\beta^{(\mathrm{s})}(\mathbf{k}_\parallel)$, with $\alpha,\beta = \mathrm{p},\mathrm{s}$, are the amplitudes for the α-polarized and β-polarized components of these fields with respect to the local planes of incidence and scattering, respectively. The wave vector of the incident light is $\mathbf{k}$, which is of length $|\mathbf{k}| = \omega/c$, where c is the speed of light in vacuum. The expressions in front of the field amplitudes are the unit polarization vectors. The wave vector of the scattered light, $\mathbf{q}$, has lateral component $\mathbf{q}_\parallel = (q_1, q_2, 0)$, and is related to the angles of scattering as indicated by Fig. 1(b). A caret over a vector indicates that it is a unit vector. Finally, the functions $\alpha_i(q_\parallel)$, $i = 1, 2$ are defined by

$$\alpha_i(q_\parallel) = \left[\varepsilon_i\left(\frac{\omega}{c}\right)^2 - q_\parallel^2\right]^{1/2}, \qquad \mathrm{Re}\,\alpha_i(q_\parallel) > 0,\ \mathrm{Im}\,\alpha_i(q_\parallel) > 0. \tag{6}$$

A linear relation is assumed to exist between the amplitudes $\mathcal{E}_\alpha^{(\mathrm{s})}(\mathbf{q}_\parallel)$ and $\mathcal{E}_\beta^{(0)}(\mathbf{k}_\parallel)$ $(\alpha,\beta = \mathrm{p},\mathrm{s})$, which we express in terms of the scattering amplitudes $R_{\alpha\beta}(\mathbf{q}_\parallel|\mathbf{k}_\parallel)$ [13]:

$$\mathcal{E}_\alpha^{(\mathrm{s})}(\mathbf{q}_\parallel) = \sum_{\beta=p,s} R_{\alpha\beta}(\mathbf{q}_\parallel|\mathbf{k}_\parallel)\mathcal{E}_\beta^{(0)}(\mathbf{k}_\parallel).$$

In order to obtain an equation for the scattering amplitudes, we first write down an expression for the transmitted field, $\mathbf{E}^{(\mathrm{t})}(\mathbf{x}|\omega)$, that is valid in the region $x_3 < \min\zeta(\mathbf{x}_\parallel)$ below the surface. We then assume the Rayleigh hypothesis, which states that for a sufficiently smooth surface, $\left|\nabla\zeta(\mathbf{x}_\parallel)\right| \ll 1$, these asymptotic expressions for the fields are valid also in the surface roughness region $[\min\zeta(\mathbf{x}_\parallel) < x_3 < \max\zeta(\mathbf{x}_\parallel)]$ [14, 15], and can be used to fulfill the boundary conditions satisfied by the electric and magnetic fields at the surface $x_3 = \zeta(\mathbf{x}_\parallel)$. From the resulting set of coupled matrix integral equations, it is possible to eliminate the amplitudes of the transmitted (reflected) field so that a single matrix integral equation results for the amplitudes corresponding to the field above (below) the surface. The resulting equation is known as the reduced Rayleigh equation for reflection (transmission). For details regarding the derivation of the reduced Rayleigh equation, we refer to Refs. 13 and 16.

If the scattering amplitudes are organized as the 2×2 matrix

$$\mathbf{R}(\mathbf{q}_\parallel|\mathbf{k}_\parallel) = \begin{pmatrix} R_{\mathrm{pp}}(\mathbf{q}_\parallel|\mathbf{k}_\parallel) & R_{\mathrm{ps}}(\mathbf{q}_\parallel|\mathbf{k}_\parallel) \\ R_{\mathrm{sp}}(\mathbf{q}_\parallel|\mathbf{k}_\parallel) & R_{\mathrm{ss}}(\mathbf{q}_\parallel|\mathbf{k}_\parallel)\end{pmatrix}, \tag{7}$$

the reduced Rayleigh equation for reflection from a two-dimensional surface can be written in the form [12, 16, 17]

$$\int\frac{\mathrm{d}^2 q_\parallel}{(2\pi)^2}\frac{I\left(\alpha_2(p_\parallel) - \alpha_1(q_\parallel)|\mathbf{p}_\parallel - \mathbf{q}_\parallel\right)}{\alpha_2(p_\parallel) - \alpha_1(q_\parallel)}\mathbf{M}^+(\mathbf{p}_\parallel|\mathbf{q}_\parallel)\mathbf{R}(\mathbf{q}_\parallel|\mathbf{k}_\parallel) = -\frac{I\left(\alpha_2(p_\parallel) + \alpha_1(k_\parallel)|\mathbf{p}_\parallel - \mathbf{k}_\parallel\right)}{\alpha_2(p_\parallel) + \alpha_1(k_\parallel)}\mathbf{M}^-(\mathbf{p}_\parallel|\mathbf{k}_\parallel), \tag{8a}$$

where

$$I(\gamma|\mathbf{Q}_\parallel) = \int \mathrm{d}^2 x_\parallel \exp\left[-\mathrm{i}\gamma\zeta(\mathbf{x}_\parallel)\right] \exp\left(-\mathrm{i}\mathbf{Q}_\parallel \cdot \mathbf{x}_\parallel\right), \tag{8b}$$

and

$$\mathbf{M}^{\pm}(\mathbf{p}_\parallel|\mathbf{q}_\parallel) = \begin{pmatrix} p_\parallel q_\parallel \pm \alpha_2(p_\parallel)\hat{\mathbf{p}}_\parallel \cdot \hat{\mathbf{q}}_\parallel \alpha_1(q_\parallel) & -\frac{\omega}{c}\alpha_2(p_\parallel)\left[\hat{\mathbf{p}}_\parallel \times \hat{\mathbf{q}}_\parallel\right]_3 \\ \pm\frac{\omega}{c}\left[\hat{\mathbf{p}}_\parallel \times \hat{\mathbf{q}}_\parallel\right]_3 \alpha_1(q_\parallel) & \frac{\omega^2}{c^2}\hat{\mathbf{p}}_\parallel \cdot \hat{\mathbf{q}}_\parallel \end{pmatrix}. \tag{8c}$$

Equation (8a) is valid for an arbitrary value of the lateral wave vector $\mathbf{p}_\parallel$, which is a quantity used only for mathematical purposes. The integral in Eq. (8b) is evaluated by expanding the exponential $\exp\left[-\mathrm{i}\gamma\zeta(\mathbf{x}_\parallel)\right]$ in powers of its argument, and integrating the resulting series term-by-term by the fast Fourier transform (FFT). In practice, the sum is truncated at a finite order ($n = 20$ was used in this work). The integration domain used for the integral in Eq. (8a) is truncated to cover the circular region $q_\parallel \leq \mathcal{Q}/2$, and the integration was converted to a finite sum over this domain by a two-dimensional version of the standard mid-point quadrature scheme. From this sum, we can obtain a linear system of equations (one for each value of $\mathbf{p}_\parallel$), which can be solved to find $R_{\alpha\beta}(\mathbf{q}_\parallel|\mathbf{k}_\parallel)$.

For the simulations presented in this paper, we have used numerically generated, discrete realizations of the surface profile function. These realizations covered a square area of size $L \times L$ of the x_1x_2 plane, determining the integration limits in Eq. (8b). The surface realizations were discretized onto a quadratic, equidistant grid of $N_x \times N_x$ points. Each realization was generated by a two-dimensional version of the Fourier filtering method presented in, e.g., Refs. 18 and 19. For a detailed discussion of how one can proceed to solve the reduced Rayleigh equation numerically, we refer to Ref. 20.

B. Mean differential reflection coefficient

When the incident field is known, the quantity $R_{\alpha\beta}(\mathbf{q}_\parallel|\mathbf{k}_\parallel)$ completely specifies the total electromagnetic field in the region above the surface. However, $R_{\alpha\beta}(\mathbf{q}_\parallel|\mathbf{k}_\parallel)$ is not directly measurable in experiments. A quantity well suited for experimental studies is the mean differential reflection coefficient (MDRC), $\langle \partial R_{\alpha\beta}/\partial\Omega_\mathrm{s}\rangle$, which is defined as the time-averaged fraction of the incident power scattered into the solid angle $\mathrm{d}\Omega_s$ about the scattering direction, $\hat{\mathbf{q}}$. The relationship between $R_{\alpha\beta}(\mathbf{q}_\parallel|\mathbf{k}_\parallel)$ and the MDRC can be written as [12]

$$\left\langle \frac{\partial R_{\alpha\beta}}{\partial\Omega_s} \right\rangle = \frac{1}{L^2}\frac{\omega^2}{4\pi^2c^2}\frac{\cos^2\theta_s}{\cos\theta_0}\left\langle \left|R_{\alpha\beta}(\mathbf{q}_\parallel|\mathbf{k}_\parallel)\right|^2 \right\rangle. \tag{9}$$

Since we are studying weakly rough surfaces, light scattered coherently (specularly) by the rough surface will dominate. However, some of the light incident on the surface will also be scattered incoherently (diffusely) by the rough surface. In theoretical and numerical studies, it is advantageous to separate these two contributions.

By light scattered coherently by the surface, we mean scattered light that is in phase from one surface realization to the next, so that the intensity of light scattered coherently (from β to α polarization) will be proportional to $\left|\left\langle R_{\alpha\beta}(\mathbf{q}_\parallel|\mathbf{k}_\parallel)\right\rangle\right|^2$. The contribution to the MDRC from the light that has been scattered *incoherently* by the rough surface is defined as [12]

$$\begin{aligned}\left\langle \frac{\partial R_{\alpha\beta}}{\partial\Omega_s} \right\rangle_\mathrm{incoh} &= \frac{1}{L^2}\frac{\omega^2}{4\pi^2c^2}\frac{\cos^2\theta_s}{\cos\theta_0} \\ &\times \left[\left\langle \left|R_{\alpha\beta}(\mathbf{q}_\parallel|\mathbf{k}_\parallel)\right|^2 \right\rangle - \left|\left\langle R_{\alpha\beta}(\mathbf{q}_\parallel|\mathbf{k}_\parallel)\right\rangle\right|^2\right].\end{aligned} \tag{10}$$

The contribution to the MDRC from the light scattered *coherently* is therefore given by the difference between Eqs. (9) and (10). We will see below that enhanced backscattering and enhanced forward scattering are both phenomena observed in the *incoherent component* of the MDRC, even if in the case of enhanced forward scattering it is observed in the *specular direction*.

We also note that the quantity $R_{\alpha\beta}(\mathbf{q}_\parallel|\mathbf{k}_\parallel)$ can be used to construct the Mueller matrix for reflection from a rough surface [21]. The Mueller matrix contains all linear transformations of the polarization of light undergoing scattering from a rough surface, including polarization and depolarization.

C. Surface plasmon polaritons

Surface plasmon polaritons are electromagnetic modes that are confined to dielectric-metal interfaces, where the dielectric function of the cladding is positive and the (real part of the) dielectric function of the substrate is smaller than the negative of the dielectric function of the cladding [22]. The dispersion relation of SPPs at a flat vacuum-metal interface is [22]

$$k_\mathrm{spp}(\omega) = \frac{\omega}{c}\left(\frac{\varepsilon_2(\omega)}{\varepsilon_2(\omega)+1}\right)^{1/2} \tag{11}$$

where $k_\mathrm{spp}(\omega)$ is the length of the wave vector of the SPP mode. For silver at wavelength $\lambda = 457.9\,\mathrm{nm}$ (in vacuum), for which the dielectric function is $\varepsilon_2(\omega) = -7.5{+}0.24\mathrm{i}$ [10], it follows that $k_\mathrm{spp} = (1.074{+}0.003\mathrm{i})\omega/c$

($\omega = 2\pi c/\lambda$). The imaginary part of $k_{\rm spp}$ can be interpreted as an inverse decay length of the SPP mode, whereas the real part corresponds to the wave number of the mode.

Multiple scattering phenomena such as the enhanced backscattering and enhanced forward scattering are, for weakly rough surfaces, typically caused by the incident light exciting SPPs that are subsequently scattered zero or more times before coupling into a mode propagating away from the surface [11]. In particular, in one-dimensional small-amplitude perturbation theory, the lowest order contribution to the enhanced forward scattering peak in the mean DRC has its origin in quadruple scattering processes [7, Fig. 10].

D. Allowed and forbidden scattering processes

From small amplitude perturbation theory [11, 23], it can be shown that a *single* scattering event from lateral wave vector $\mathbf{k}_\parallel$ to $\mathbf{q}_\parallel$ is allowed only if the power spectrum evaluated at the wave vector transfer $\mathbf{k}_{\rm sc}$ is non-zero, i.e.,

$$g\left(\mathbf{k}_{\rm sc}\right) > 0, \qquad \mathbf{k}_{\rm sc} = \mathbf{q}_\parallel - \mathbf{k}_\parallel. \tag{12}$$

This condition holds for scattering between propagating modes; between evanescent modes; and from propagating to evanescent modes, and vice versa. For isotropic power spectra, such as those studied in this paper [Eq. (3)], the requirement (12) simplifies to

$$g\left(|\mathbf{k}_{\rm sc}|\right) > 0. \tag{13}$$

To better understand the physical implications of condition (13), and to facilitate our interpretation of the simulation results presented later in this paper, we present a visual model for discussing relevant scattering processes in Fig. 2. Before starting the discussion, we remind the reader that modes for which $k_\parallel \leq \omega/c$ are propagating in the vacuum, whereas for $k_\parallel > \omega/c$, the corresponding fields are evanescent. Moreover, at the wavelength $\lambda = 457.9\,\text{nm}$, assumed in the simulations presented below, the vacuum-silver interface supports surface plasmon polaritons of lateral wave vector $k_{\rm spp} = 1.074\omega/c$ (see Sec. II C). For simplicity, we have neglected the imaginary part of the wave number, as it is small compared to its real part.

In passing, we note that the polarization state of light can be modified at each scattering event, subject to the requirement that SPPs are always p-polarized. We will, however, not discuss polarization effects of single scattering events in this section.

We will now discuss Fig. 2, which was produced under the assumption that the surface power spectrum was identical to that in Eq. (3), and characterized by the values for $k_\pm^{(i)}$ to be used in later simulations (Sec. III). The annular regions, indicated by blue shaded regions in Fig. 2, represent the nonzero parts of the surface roughness power spectrum.

First, we consider the scattering process $\mathbf{k}_\parallel \rightarrow \mathbf{q}_\parallel$ [Fig. 2(a)] that corresponds to the lateral wave vector (or momentum) transfer $\mathbf{k}_{\rm sc}$. In Fig. 2(a) the incident lateral wave vector, $\mathbf{k}_\parallel$, is placed so that it starts at the origin of wave vector space, O; the same is done for $\mathbf{q}_\parallel$. We superpose blue shaded regions representing the power spectrum so that the center of the power spectrum is located at the end of $\mathbf{k}_\parallel$. Thus, if $\mathbf{k}_{\rm sc}$ indicates a point inside the blue shaded regions (the power spectrum), the scattering process $\mathbf{k}_\parallel \rightarrow \mathbf{q}_\parallel$ is allowed. Moreover, at the same time, if $q_\parallel \leq \omega/c$, the process $\mathbf{k}_\parallel \rightarrow \mathbf{q}_\parallel$ results in a scattered mode that can propagate away from the surface. On the assumption that both $\mathbf{k}_\parallel$ and $\mathbf{q}_\parallel$ are propagating in vacuum, one realizes that $\mathbf{k}_\parallel$ [for the value of $\mathbf{k}_\parallel$ used in Fig. 2(a)] can be converted into $\mathbf{q}_\parallel$ through a single interaction with the surface roughness (single scattering) only within a *crescent-like* region. This region is defined by the shaded blue region which resides inside the circle $q_\parallel = \omega/c$, indicated in black in Fig. 2(a). Outside this crescent region, the scattering process is either not allowed or $q_\parallel > \omega/c$, meaning that the mode is evanescent (non-propagating). When later studying the full angular distribution of the scattered light (Fig. 3), we will see that this observation is important.

We now turn to the possibility of exciting SPPs by the incident light, a situation addressed in Fig. 2(b). The excitation $\mathbf{k}_\parallel \rightarrow \mathbf{k}_{\rm spp}$ of SPPs is subject to the constraints in Eq. (13). In particular, we have that the excitation of a surface plasmon polariton by the incident field characterized by $\mathbf{k}_\parallel$ is only allowed if

$$k_-^{(1)} < \left|\mathbf{k}_{\rm spp} - \mathbf{k}_\parallel\right| < k_+^{(1)} \tag{14}$$

or (less relevant for the parameters used in this study, due to the large θ_0 required)

$$k_-^{(2)} < \left|\mathbf{k}_{\rm spp} - \mathbf{k}_\parallel\right| < k_+^{(2)}. \tag{15}$$

Consequently, it is only possible to excite surface plasmon polaritons for small (or very large) angles of incidence. The excitation of a surface plasmon polariton is shown in Fig. 2(b). The black ring indicates the length of the possible SPP wave vectors. In the plane of incidence, surface plasmon polaritons cannot be excited for angles of incidence $\theta_0 > 17^\circ$. For out of plane scattering, however, SPP excitation is allowed also for $\theta_0 > 17^\circ$. This is qualitatively different from scattering from a one-dimensionally rough surface.

E. Enhanced backscattering

For weakly rough surfaces, the presence of the enhanced backscattering phenomenon typically requires the excitation of surface plasmon polaritons. On the other hand, for strongly rough surfaces it can take place through a multiple scattering effect [24, 25]. For the weakly rough surfaces discussed here, the SPP channel

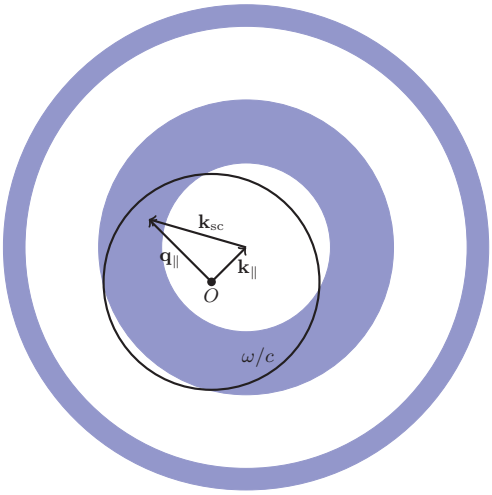

(a) Scattering from wave vector $\mathbf{k}_\parallel$ into wave vector $\mathbf{q}_\parallel$. The scattered mode is propagating, since $|\mathbf{q}_\parallel| < \omega/c$, with ω/c indicated by the black ring.

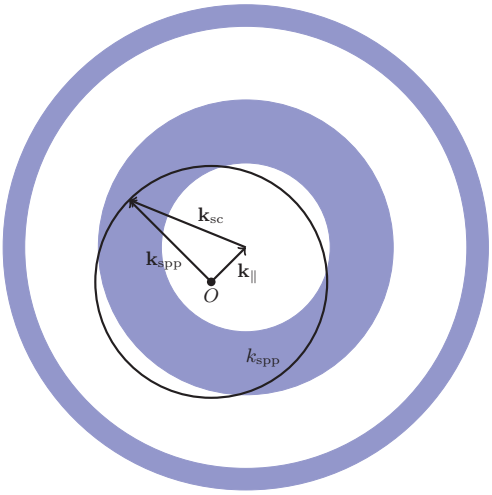

(b) Excitation of a surface plasmon polariton by incident light. The surface plasmon polariton is not propagating in vacuum, as $k_{\rm spp} > \omega/c$. The parts of the black ring (of radius $k_{\rm spp}$) which lie in the blue region represent legal SPP excitation processes.

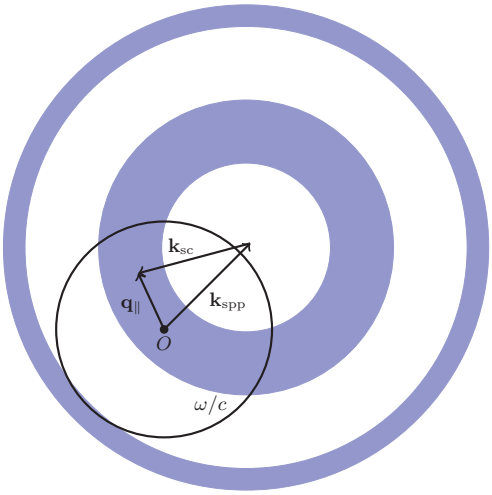

(c) Scattering of a surface plasmon polariton into a bulk propagating mode. Legal propagating modes are those for which $\mathbf{q}_\parallel$ lies inside the blue region and $q_\parallel < \omega/c$.

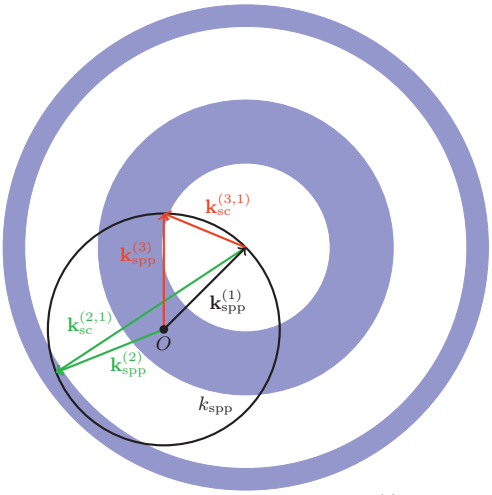

(d) Scattering of a surface plasmon polariton ($\mathbf{k}_{\rm spp}^{(1)}$). Two legal scattered modes ($\mathbf{k}_{\rm spp}^{(2)}$ and $\mathbf{k}_{\rm spp}^{(3)}$) are shown. The black ring indicates legal wave vectors for SPPs.

FIG. 2. (Color online) Four scattering processes important for understanding the results of this study. A detailed discussion of the figure is found in the text. All subfigures 2(a)–(d) are drawn to correct and identical scale for the parameters $k_\pm^{(i)}$ and ε_2 used throughout this study. The blue annular regions indicate the non-zero parts of the power spectrum, i.e., the ranges of $\mathbf{k}_{\rm sc}$ allowed by the power spectrum. The lengths of $\mathbf{k}_\parallel$ in Figs. 2(a) and (b) correspond to $(\theta_0, \phi_0) = (27°, 45°)$.

is by far the dominant contribution to the backscattering enhancement. As such, the presence of the enhanced backscattering phenomenon requires first that incident light can couple to SPPs, i.e., $g\left(\left|\mathbf{k}_{\rm spp} - \mathbf{k}_\parallel\right|\right) > 0$, as discussed in the previous paragraph. Second, the existence of enhanced backscattering requires that SPPs can couple out into the anti-specular direction, i.e., that $g\left(\left|-\mathbf{k}_\parallel - \mathbf{k}_{\rm spp}\right|\right) > 0$. This implies, with the power spec-

trum used here, that

$$k_-^{(1)} < \left|\mathbf{k}_{\rm spp} + \mathbf{k}_\parallel\right| < k_+^{(1)}. \tag{16}$$

Coupling from SPPs to vacuum propagating modes is illustrated in Fig. 2(c). The outer cylindrical part of the power spectrum essentially does not contribute to the scattering process $\mathbf{k}_{\rm spp} \to \mathbf{k}_\parallel$, as $k_-^{(2)} \approx \omega/c + k_{\rm spp}$.

For one-dimensionally randomly rough surfaces [7, 9], the scattered wave vectors are confined to the plane of incidence, and all quantities in Eqs. (12)–(16) can be written as scalars. Thus, there is a sharp and well-defined angular cutoff for the excitation of surface plasmon polaritons in this case. For two-dimensionally rough surfaces, however, incident light can couple to SPPs which do not propagate in the plane of incidence. This can allow scattering processes which would be forbidden in the one-dimensional case, and any limits derived using the one-dimensional model will become "fuzzy" for two-dimensional surfaces.

F. Enhanced forward scattering

For SPPs to contribute to enhanced forward scattering, it is required that the power spectrum allows both the excitation and counterpropagation of surface plasmon polaritons, as well as coupling from SPPs to vacuum propagating modes in the specular direction.

For the scattering of an SPP of wavevector $\mathbf{k}_{\rm spp}^{(1)}$ to an SPP of wavevector $\mathbf{k}_{\rm spp}^{(2)}$ to be allowed, it is required that $g\left(\left|\mathbf{k}_{\rm spp}^{(2)} - \mathbf{k}_{\rm spp}^{(1)}\right|\right) > 0$. For the power spectrum used in this study, this condition is fulfilled if

$$k_-^{(1)} < \left|\mathbf{k}_{\rm spp}^{(2)} - \mathbf{k}_{\rm spp}^{(1)}\right| < k_+^{(1)}, \tag{17}$$

or

$$k_-^{(2)} < \left|\mathbf{k}_{\rm spp}^{(2)} - \mathbf{k}_{\rm spp}^{(1)}\right| < k_+^{(2)}. \tag{18}$$

The counterpropagation requirement is the rationale for adding the outer annulus to the power spectrum (3). This annulus is narrow, and centered at $k_\parallel = 2k_{\rm spp}$, meaning that it facilitates scattering where $|\mathbf{k}_{\rm sc}| \approx 2k_{\rm spp}$, i.e., counterpropagation of SPPs. This corresponds to the fulfillment of Eq. (18), and is illustrated by the green vectors in Fig. 2(d).

We note that for two-dimensionally rough surfaces it is possible for an SPP to be scattered out-of-plane by the g_1 part of the power spectrum. This can happen when Eq. (17) is fulfilled, as shown in red in Fig. 2(d), where the resulting lateral wave vector is denoted $\mathbf{k}_{\rm spp}^{(3)}$.

The principles discussed above are also valid for systems consisting of a metallic substrate on which a dielectric thin film has been deposited, with a vacuum or lossless dielectric cladding, where either interface of the film is randomly rough [26]. The generalization to different power spectra should also be obvious. We note that if the power spectrum of the randomly rough surface is, e.g., Gaussian, the single scattering contribution to the MDRC is typically dominant. In such cases, it can be challenging to separate single scattering effects from multiple scattering effects.

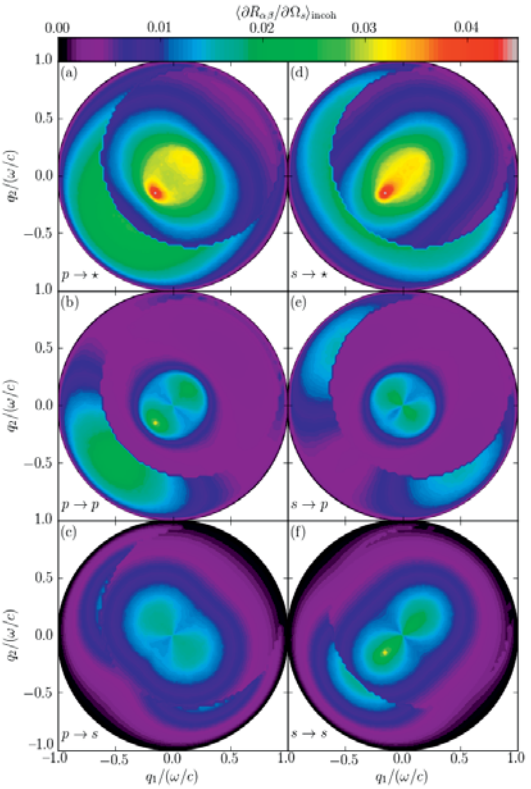

FIG. 3. (Color online) The full angular distribution of the incoherent contribution to the MDRC, assuming the surface properties stated in the text. The angles of incidence were $(\theta_0, \phi_0) = (12.5°, 45°)$. The subplots show scattering (b) from p polarization to p polarization, (e) s → p, (c) p → s, and (f) s → s. In (a), the incident light was p-polarized, but the polarization of the scattered light was not recorded, and in (d) the incident light was s-polarized. The enhanced forward scattering peak is most easily seen in the p → p configuration (b). The sharp circular edge, centered on $\mathbf{k}_\parallel$, is caused by the suppression of single scattering due to the form of the power spectrum; see Eq. (3) and Fig. 2(a).

III. RESULTS

In this section, we present results for the MDRC when light is scattered from rough silver surfaces. For all the results presented here, the (vacuum) wavelength of

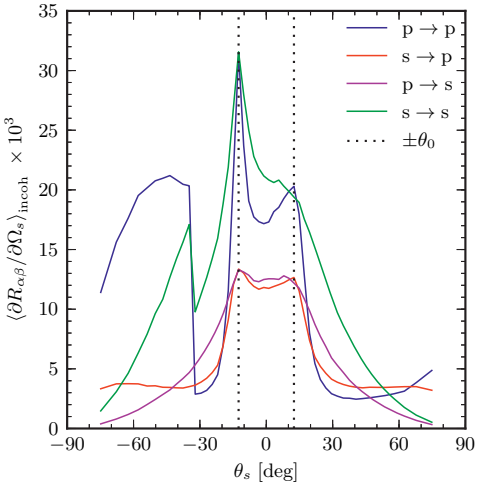

FIG. 4. (Color online) The in-plane (i.e., for $\phi_s = \phi_0$) part of the MDRC for light scattered from a rough silver surface with rms roughness $\delta = 0.025\lambda$. The angles of incidence were $(\theta_0, \phi_0) = (12.5^\circ, 45^\circ)$. The results were obtained by averaging over $10,825$ surface realizations. The most prominent enhanced forward scattering peak is in p → p polarization, but a small contribution in s → p polarization can also be seen. Enhanced backscattering is observed in all polarization combinations.

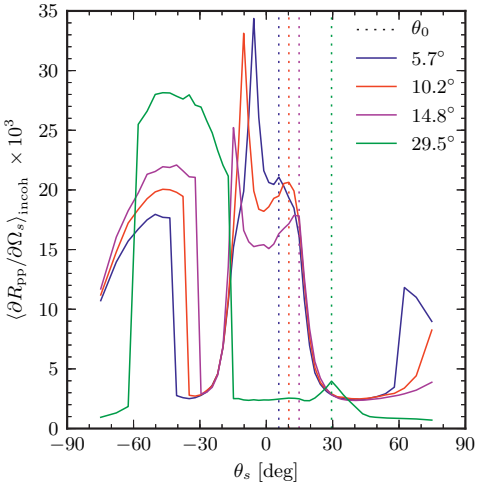

FIG. 5. (Color online) The p → p contribution to the MDRC for the same surface properties as in Fig. 4, for several different angles of incidence. In all cases, we observe the enhanced forward scattering peak. The effect is most powerful in the vicinity of $\theta_0 \approx 12^\circ$. For polar angle of incidence $\theta_0 = 29.5^\circ$, it is not possible to achieve enhanced forward scattering through the in-plane SPP channel; hence, the peak at $\theta_s = 29.5^\circ$ has a different explanation.

the incident light was $\lambda = 457.9\,\text{nm}$, and the dielectric function of the Ag substrate (cladding) at this wavelength is $\varepsilon_2 = -7.5 + 0.24\text{i}$ ($\varepsilon_1 = 1$). The rough surfaces were characterized by the power spectrum (3), defined by the wavenumber parameters: $k_-^{(1)} = 0.782\omega/c$, $k_+^{(1)} = 1.366\omega/c$, $k_-^{(2)} = 2.048\omega/c$, and $k_+^{(2)} = 2.248\omega/c$. Furthermore, the amplitudes γ_i were $\gamma_1 = 0.57$ and $\gamma_2 = 0.43$, and the rms surface roughness was taken to be $\delta = 0.025\lambda$; the edge of the square region covered by the rough surface was $L = 36\lambda$; and this region was discretized at a grid of $N_x = 359$ points along each of the x_1 and x_2 directions.

As the Nyquist theorem [27] relates resolution in position space and wave vector space, the values of N_x and L lead to the following numerical parameters: The wavenumber cutoff in the integral in Eq. (8a) was $\mathcal{Q}/2 = 2.493\omega/c$; the resolution in $\mathbf{q}_\parallel$ was $\Delta q = 0.0279\omega/c$; and $N_q = 180$ values of $\mathbf{q}_\parallel$ were resolved along each of the q_1 and q_2 axes [20]. The results presented were obtained by averaging the results over an ensemble of $10,825$ surface realizations. For a discussion of the details of how the calculations were performed, we refer to Ref. 20, where an estimate of the computing resources required can also be found.

In Fig. 3, we show the full angular distribution of the MDRC, including polarization effects. Figure 3(a)–(c) shows the MDRC for p-polarized incident light, and in Fig. 3(d)–(f) the incident light was s-polarized. In the upper row, the polarization of the scattered light was not recorded; in the second row, only the p-polarized component of the scattered light was recorded; and in the third row, only the s-polarized component of the scattered light was recorded. The full angular intensity distribution displays important information, hidden from the reader of in-plane or out-of-plane cuts of the MDRC (e.g., Fig. 4). Notably, we observe that the intensity distribution depends on which linear polarization is used to illuminate the surface, as well as which linear polarization is recorded in the (simulated) detector. Furthermore, the crescent regions of the MDRC of high intensity show for which angles of scattering single scattering is allowed, as per the theoretical discussion in Sec. II D.

One of the significant differences between the light scattering from one-dimensional and two-dimensional rough surfaces is the absence of polarization effects in the former case (assuming the plane of incidence to be perpendicular to the grooves of the surface). Notably, for light scattering from rough two-dimensional surfaces, the light scattered out-of-plane is significantly cross-polarized.

The enhanced forward scattering phenomenon expresses itself as a peak in the specular direction of the intensity of the light scattered incoherently by the rough surface. For this reason, in Figs. 4 and 5 we present the incoherent component of the MDRC in the plane of incidence (i.e., for $\phi_s = \phi_0$).

Figure 4 shows the incoherent component of the MDRC for $\theta_0 = 12.5^\circ$, for all combinations of incident

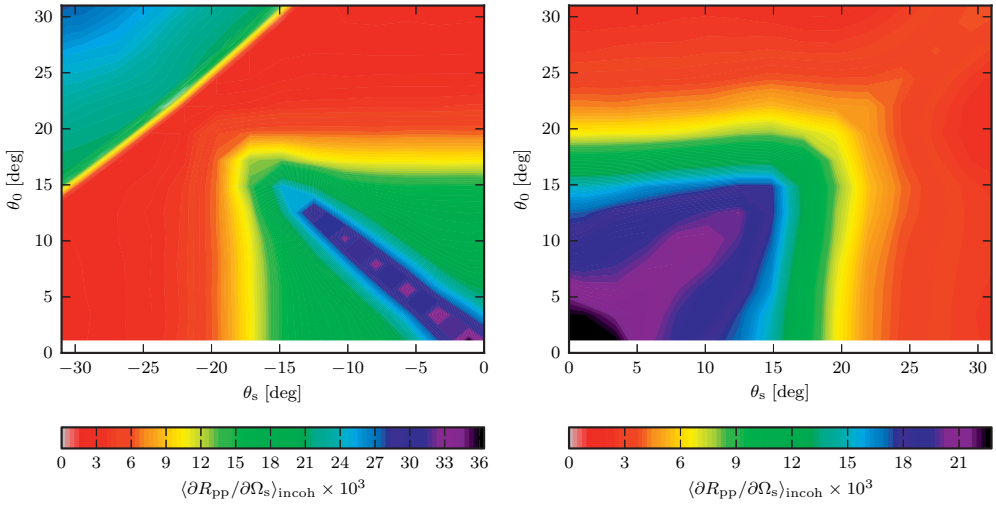

(a) $\theta_s < 0$. (b) $\theta_s > 0$.

FIG. 6. (Color online) Contour plots of the incoherent, in-plane, and p → p part of the MDRC as a function of angle of incidence (θ_0) and scattering (θ_s). We assume $\phi_s = \phi_0$ in these figures. (a) The enhanced backscattering peak is shown as a purple "ridge" at $\theta_s = -\theta_0$. (b) The enhanced forward scattering peak is shown as a purple "ridge" at $\theta_s = \theta_0$. Note that the color map has been truncated [cf. (a)] to show the peak more clearly.

and scattered polarizations. Since SPPs can only be excited in p-polarization, it is reasonable to assume that light scattered through the temporary creation of an SPP will be predominantly p-polarized. When examining Fig. 4, we only observe enhanced forward scattering, i.e., a peak in the forward direction, for p → p and s → p scattering. We also note that the enhanced forward scattering peak is much more well-defined in p → p than in s → p scattering. It is worth noting that for angles $\theta_s > -34.4°$, in-plane single scattering of light is forbidden due to the power spectrum used [Eq. (3) and Fig. 2]. Consequently, the "edge" seen at the left hand side of Fig. 4 is mainly caused by the single scattering of light for angles $\theta_s \leq -34.4°$.

By studying the θ_0 dependence of $\langle \partial R_{pp}/\partial \Omega_s \rangle$ (Fig. 5), several effects caused by the shape of the power spectrum can be observed. The positions of the "edges" caused by the suppression of single scattering is directly related to the power spectrum: To leading order in the surface profile function, the intensity of single scattering is proportional to the power spectrum of the surface [11, 23]. For the surface parameters assumed here, single scattering is forbidden for $\left|\mathbf{q}_\parallel - \mathbf{k}_\parallel\right| < k_-^{(1)} = 0.782\omega/c$. Thus, the cylindrical shape of the power spectrum leads to a region around $\mathbf{k}_\parallel$ into which less light is scattered, as single scattering is suppressed here.

A sharp edge is observed for the case of $\theta_0 = 29.5°$, at $\theta_s \approx -60°$. The location of this edge is given by the outer edge of the inner cylinder of the power spectrum, $k_+^{(1)}$. Due to the the power spectrum vanishing between the inner and outer cylinder [Eq. (3)], single scattering is forbidden for $\theta_s < -60°$.

Of greater interest, and one of the main points of this paper, are the peaks observed in the forward and backward directions. The vertical dotted lines in Figs. 4 and 5 show the expected positions of the enhanced forward scattering peaks, and we see that in each case, these coincide with the observed peaks. The effect is most pronounced for the polar angle of incidence around $\theta_0 \approx 12°$. For angles of incidence above 17°, it is not possible for surface plasmon polaritons to be excited in the plane of incidence, since the power spectrum (3) is zero for $k_\parallel + k_{spp} > k_+^{(1)}$ for in-plane scattering [9]. Nevertheless, a peak in the incoherent part of the MDRC and in the specular direction is visible for $\theta_0 = 29.5°$. Our interpretation is that the origin of this peak is the presence of the g_2 part of the power spectrum; see Fig. 7(b) and the corresponding discussion.

In accordance with previous work on light scattering from two-dimensionally randomly rough surfaces [16–18, 20, 21, 26], we observe enhanced backscattering in Figs. 4 and 5. The enhanced backscattering peak is located exactly at the direction of incidence, $\theta_s = -\theta_0$. The effect is present in both co-polarized and cross-polarized scattering. This is in contrast to the case of one-dimensional surface roughness, where enhanced backscattering can only be observed in the p → p polarization configuration.

A complete scan of the angles of incidence for which one observes enhanced backscattering and enhanced for-

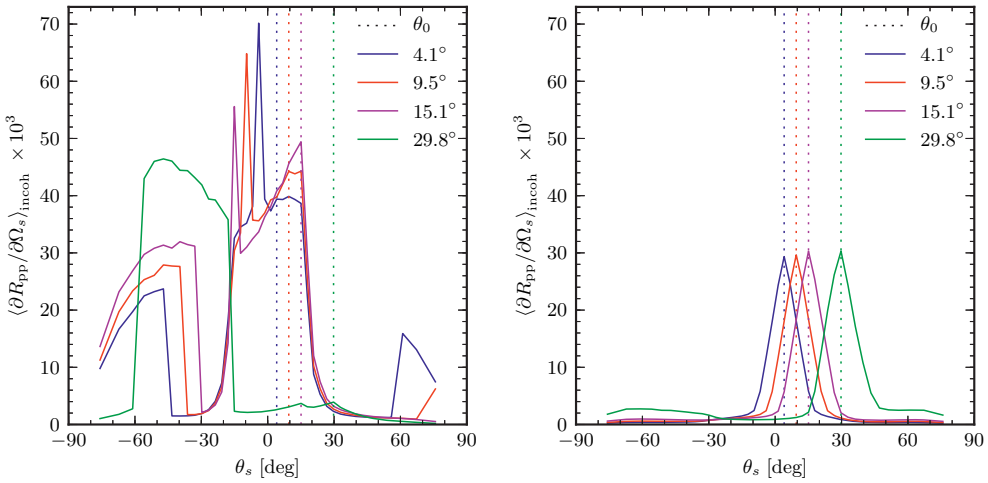

(a) In-plane part of the p → p contribution to the MDRC for a power spectrum with $\gamma_1 = 1$ and $\gamma_2 = 0$.

(b) In-plane part of the p → p contribution to the MDRC for power spectrum with $\gamma_1 = 0$ and $\gamma_2 = 1$.

FIG. 7. (Color online) In plane p → p scattering for power spectra with (a) $\gamma_1 = 1, \gamma_2 = 0$ and (b) $\gamma_1 = 0, \gamma_2 = 1$. With $\gamma_1 = 0, \gamma_2 = 1$, coupling into SPPs is suppressed. With $\gamma_1 = 1, \gamma_2 = 0$, coupling into SPPs is allowed, but not scattering from an SPP to a counterpropagating SPP. This allows enhanced backscattering, but not enhanced forward scattering.

ward scattering is presented in Fig. 6. In these figures, the enhanced backscattering peak and the enhanced forward scattering peak are shown as "ridges" in the color map. As the ridges follow the $\pm\theta_{\rm s}$ directions very well, we conclude that they indeed represent the phenomena enhanced backscattering and enhanced forward scattering. For enhanced forward scattering, which is a quadruple scattering effect, the peak is somewhat broader than the enhanced backscattering peak, which is a double (or higher order) scattering effect. Briefly put, the two-dimensional nature of the rough surface allows for more freedom in the choice of scattered wave vectors, leading to a wider peak.

For comparison with the results shown in Fig. 5, we have also performed simulations for the cases where either $\gamma_1 = 1, \gamma_2 = 0$ [Fig. 7(a)], or where $\gamma_1 = 0, \gamma_2 = 1$ [Fig. 7(b)]. In the former case, only the inner annulus of the power spectrum is present, and in the latter case, only the outer annulus is present. The other simulation parameters were as follows. The edges of the simulation domain in the x_1x_2 plane was $L = 30\lambda$, and was discretized at $N_x = 319$ points along each of the lateral axes. The dielectric function, the power spectrum parameters $k_{\pm}^{(i)}$, and the rms surface roughness parameters were the same as before. The parameters N_x and L were reduced for these simulations in order to save computer resources. This also leads to a different discrete set of $\theta_{\rm s}$ being resolved (cf. Fig. 5).

The results for $\gamma_1 = 1, \gamma_2 = 0$ are presented in Fig. 7(a). In this case, incident light can couple to SPPs, but it is not possible to couple from an SPP to an SPP traveling in the opposite direction (counterpropagation). Thus, enhanced backscattering, which to lowest order is a double scattering process, is allowed. Enhanced forward scattering, on the other hand, is a quadruple scattering process, dependent on scattering from SPP to counterpropagating SPP. Hence, there is no enhanced forward scattering peak when $\gamma_2 = 0$. The shoulder visible in Fig. 7(a) does not move as θ_0 increases, meaning that it is not related to the enhanced forward scattering phenomenon, but is a result of the shape of the power spectrum.

In Fig. 7(b), we show the results for $\gamma_1 = 0, \gamma_2 = 1$. In this case, both single scattering and coupling from incident light to SPPs are prohibited. Instead, incident light will excite evanescent modes which are not resonant modes of the surface. These may be scattered several times before coupling out to vacuum propagating modes. The width of the triangular structure seen in the MDRC in Fig. 7(b) is determined by the width of the outer annulus of the power spectrum.

In order to verify the correctness of the numerical results, the total reflected power normalized by the total incident power was calculated. In all cases it was found to be lower than 1. If one (artificially) assumes the substrate to be lossless, the normalized reflected power should in principle be identical to 1. For the surface parameters used in this study, and with $\mathrm{Im}(\varepsilon_2) = 0$, the normalized total reflected power was 1.000 ± 0.007 for all angles of incidence. We stress that the conservation of energy is a necessary, but not sufficient, criterion for the validity of the simulation results [20].

IV. CONCLUSION

In conclusion, we have surveyed two phenomena observed in rough surface scattering, namely enhanced forward scattering and enhanced backscattering. These are both phenomena observed in the diffuse (incoherent) part of the mean differential reflection coefficient, and are caused by constructive interference between surface plasmon polaritons propagating along a vacuum-metal interface. In particular, the observation of enhanced forward scattering has not previously been reported for systems containing two-dimensionally rough surfaces. The two-dimensional nature of the rough surface studied here gives significantly more freedom in the allowed scattering channels when compared to one-dimensionally rough surfaces, giving less sharp "cutoffs" caused by the power spectrum.

A simple visual model for determining which scattering processes are allowed in two-dimensionally rough surfaces has also been given (Fig. 2). This model can be used to determine for which combinations of angles of incidence and scattering enhanced backscattering and enhanced forward scattering can be observed.

The enhanced forward and backward scattering phenomena are dependent on the presence of surface guided modes. Enhanced backscattering has already been observed in a thin film system in both polarizations [26]. We expect that enhanced forward scattering can also be observed in thin film systems for all polarization combinations, as such structures support surface guided modes in both p and s polarizations. We leave this investigation to future work, as the required computational effort is significant.

ACKNOWLEDGMENTS

The authors would like to acknowledge Dr. A.A. Maradudin for fruitful interactions.

[1] E. Ozbay, Science **311**, 189 (2006).
[2] H. A. Atwater and A. Polman, Nat. Mater. **9**, 205 (2010).
[3] A. Savchenko, E. Kashuba, V. Kashuba, and B. Snopok, Anal. Chem. **79**, 1349 (2007).
[4] A. Savchenko, E. Kashuba, V. Kashuba, and B. Snopok, Sens. Lett. **6**, 705 (2008).
[5] A. R. McGurn, A. A. Maradudin, and V. Celli, Phys. Rev. B **31**, 4866 (1985).
[6] C. S. West and K. A. O'Donnell, J. Opt. Soc. Am. A **12**, 390 (1995).
[7] K. A. O'Donnell, J. Opt. Soc. Am. A **18**, 1507 (2001).
[8] K. A. O'Donnell and E. R. Mendéz, J. Opt. Soc. Am. A **20**, 2338 (2003).
[9] I. Simonsen, phys. status solidi (b) **247**, 2075 (2010).
[10] P. B. Johnson and R. W. Christy, Phys. Rev. **6**, 4370 (1972).
[11] I. Simonsen, Eur. Phys. J.-Spec. Top. **181**, 1 (2010).
[12] A. R. McGurn and A. A. Maradudin, Wave. Random Media **6**, 251 (1996).
[13] G. C. Brown, V. Celli, M. Haller, and A. Marvin, Surf. Sci. **136**, 381 (1984).
[14] Lord Rayleigh, Proc. R. Soc. Lon. Ser-A **79**, 399 (1907).
[15] A. G. Voronovich, *Wave scattering from Rough Surfaces*, 2nd ed. (Springer Verlag, Berlin, 1999).
[16] A. Soubret, G. Berginc, and C. Bourrely, J. Opt. Soc. Am. A **18**, 2778 (2001).
[17] A. Soubret, G. Berginc, and C. Bourrely, Phys. Rev. B **63**, 245411 (2001).
[18] A. A. Maradudin, T. Michel, A. R. McGurn, and E. R. Méndez, Ann. Phys. **203**, 255 (1990).
[19] I. Simonsen, J. B. Kryvi, A. A. Maradudin, and T. A. Leskova, Comp. Phys. Commun. **182**, 1904 (2011).
[20] T. Nordam, P. A. Letnes, and I. Simonsen, http://arxiv.org/abs/1204.4984 (2012).
[21] P. A. Letnes, A. A. Maradudin, T. Nordam, and I. Simonsen, http://arxiv.org/abs/1108.2599 (accepted, Phys. Rev. A) (2012).
[22] V. Agranovich and D. Mills, eds., *Surface Polaritons: Electromagnetic Waves at Surfaces and Interfaces* (North-Holland Publishing Company, Amsterdam, 1982).
[23] A. A. Maradudin, ed., *Light Scattering and Nanoscale Surface Roughness* (Springer-Verlag, New York, 2007).
[24] I. Simonsen, A. A. Maradudin, and T. A. Leskova, Phys. Rev. Lett. **104**, 223904 (2010).
[25] I. Simonsen, A. A. Maradudin, and T. A. Leskova, Phys. Rev. A **81**, 013806 (2010).
[26] T. Nordam, P. A. Letnes, I. Simonsen, and A. A. Maradudin, Opt. Express **20**, 11336 (2012).
[27] W. H. Press, S. A. Teukolsky, W. T. Vetterling, and B. P. Flannery, *Numerical Recipes: The Art of Scientific Computing*, 3rd ed. (Cambridge University Press, Cambridge, New York, 2007).